Exsolved base metal catalyst systems with anchored nanoparticles for carbon monoxide (CO) and nitric oxides (NO_x) oxidation

By

WAN KHAIRUNNISA BINTI WAN RAMLI

A Thesis Submitted for the Degree of Doctor of Philosophy (PhD) in Chemical Engineering at Newcastle University, United Kingdom

School of Chemical Engineering and Advanced Materials

July 2017

ABSTRACT

Noble metals notably platinum (Pt), is a major element of heterogeneous catalysts, excel in catalysing an extensive number of important catalytic reactions in chemical and automotive industries. Since the increased use of these metals is severely limited because of their high cost and scarcity's, there is therefore an urgent need for the search of alternative base metal catalysts that are cheaper and more widely available. This can only be practical if the main drawbacks of base metals such as the agglomeration of particles under high temperatures operational conditions and irreversible sulphur poisoning can be overcome, and their activity enhanced, such that they can directly replace Pt on a weight-to-weight basis. However, most previous studies have been restricted to low temperature reaction conditions and have not compared their activity directly to that of Pt, whether in terms of active sites or on a weight-to-weight basis. Moreover, most researchers have not investigated extensively the long-term stability of their base metal catalysts, since the longest was at most around 200 hours and at relatively low temperatures, for example at room temperature. It is proposed that long term stability can be achieved by producing uniformly distributed nano-sized socketed and strained base metal particles via the exsolution method. The main objective of this thesis is to produce exsolved base metals catalyst systems rivalling Pt on a weight-to-weight basis in two base reactions; CO and NO oxidation. NO oxidation was also chosen as our model reaction in this research since most Pt in the automotive industry are used in the lean NO_x trap (LNT) or a combination of LNT and selective catalytic reduction (SCR), which demand the high conversion of NO to NO_2 at low temperatures to work effectively. Initial screening experiments were performed to evaluate the potential CO oxidation activities and long-term stability at 520 °C of two different exsolved metal pellet systems namely lanthanum-doped ceria nickel titanates to exsolve nickel (Ni) metal ($La_{0.8}Ce_{0.1}Ni_{0.4}Ti_{0.6}O_3$) and lanthanum-doped strontium iron nickel titanates to exsolve iron-nickel (FeNi) alloy ($La_{0.5}Sr_{0.4}Fe_{0.1}Ni_{0.1}Ti_{0.6}O_3$). Exsolved FeNi pellet system gives high and stable turnover frequencies (TOFs) of 10^3 s^{-1} at 520 °C for almost 170 hours, which confirms the potential of these stable exsolved metal systems for CO oxidation. Sixty exsolved metal powder systems with various metal formulations were produced to enable direct activity comparison to Pt on a weight-to-weight basis. Most exsolved metal systems displayed increasing CO_2 production rates with increasing CO partial pressures (P_{CO}) and reversible sulphur poisoning with exsolved CoNi powder system showing remarkable stability at 200 °C for 655 hours (one month). This exsolved CoNi system also showed enhanced activity for CO oxidation upon exposure to CO-rich environment, as a result of the restructuring of particles

into metal oxide nanocubes anchored onto nanosockets within the support surface. The CO_2 production rates of the activated exsolved CoNi powder system at 200 and 520 °C were 0.13 x 10^{-4} and 1.5 x 10^{-4} mol s^{-1} g^{-1} compared to its initial rate of around 0 (below the detected limit of 0.007 x10^{-4} mol s^{-1} g^{-1}) and 0.8 x 10^{-4} mol s^{-1} g^{-1} prior to activation. These active spinel $(CoNi)_3O_4$ cubic structures were seen planted at an angle of ~55°, at the edge of an empty socket with mediocre features for CO oxidation, such as rich in Co^{2+} with exposed (100) planes that had only 44 cubes μm^{-2} compared to its initial 144 particles μm^{-2} particle population. Above 450 °C, the main active sites for CO oxidation were thought to be close to or at the metal-support interface of the exsolved CoNi systems. Comparable NO_2 production rates to those of commercial Pt catalyst was achieved with only ± 5 % of difference at each measured point within the temperature range used (100-440 °C) over exsolved CoNi system by exploiting the effect of having two particle size ranges (10 and 30 nm). These results confirm the dual functionality of the activated exsolved CoNi system and its huge potential to be commercialised as an alternative catalyst to Pt in two oxidation reactions; CO and NO oxidation.

In general, a simple procedure that induces high, long-lasting activity in a base metal catalyst, rivalling platinum for CO and NO oxidation on a weight-to-weight basis was demonstrated. The nature of this activation by tracking individual nanoparticles was successfully elucidated to link their microstructural evolution to their catalytic and kinetic behaviour. This research also illustrates new strategies for enhancing and tailoring the catalytic activity of base metal systems towards replacing platinum.

ACKNOWLEDGEMENTS

In the name of Allah, the most beneficent, the most merciful

The writing of this thesis has been the most significant yet challenging task that I have ever had to face. Without the support, patience and guidance of the following people, this thesis would not have been completed. It is to them that I owe my deepest gratitude.

First and foremost, I would like to express my gratitude to my supervisor, Professor Ian S. Metcalfe for his endless support, enthusiasm and compassion in helping me to understand and look at my research in different ways and finally finishing my PhD. Your support was essential to my success. I would also like to thank the post-docs that have helped me over the years. In particular, huge thanks go to Dr Evangelos Papaioannou for all the things he did just to help me, from the essential research advice and huge expectations (just kidding!) to being my chauffeur after finishing the lab works late at night. I would never forget these things and I hope we can still stay in touch in the future. Congratulations on your lectureship, by the way! I am so proud of you. My appreciation goes a long way to Dr Dragos Naegu and Prof John T.S. Irvine from St Andrews University for always quick to supply the materials for my research, which in other words, have made me the most hardworking and determined ever in my life. Thanks for teaching me almost everything you guys know about these materials and I am most grateful for that. I also would not have survived the lab without these guys; Dr Samuel Zhang, Dr Wei Chen and Dr Ana Gil. Thanks a lot!

To all the members of my research group, I would like to thank them all for helping me throughout my years of my PhD. I truly enjoyed all the group meetings, particularly the pizzas and of course the input that I have received each time. To my best lab buddy, Danny, your help in every aspect of my research was imperative to the completion of my thesis. Thank you so much for always being there when I needed you and those little things like the free Starbucks vouchers which always cheer me up through the long hours in the lab. I would also like to thank Sotiria, Chenyang, Maria and Stephen for the chitchat and gossip sessions in the lab that would brighten up my day amidst the long list of works. Much of my experimental work would not have been completed without the help of the technical and administrative staffs at CEAM. My particular thanks go to Bryan, Stewart, Ian, Rob and Simon for always find times to help me. To Justine, thanks for always complimenting me on how colourful I look every time we met and of course for the never ending supports and smiles. To Gayle and Debbie who have helped me with all the quick queries especially on the deliveries of my orders, I could not have done it without your help.

To my beloved mum (Fae'za Hamid) and dad (Wan Ramli Wan Daud), thanks for always supporting me in whatever I do. You guys have always been my strongest pillar in life and even though I haven't been expressing my love to you that doesn't mean I don't love you. I am also forever grateful to my siblings (Wan Nurliyana and Wan Muhammad Faris) and I love all of you with all my heart. To Jeka, Alia, Bella and kak Sheila, all those coffee sessions meant a lot to me and your friendship was crucial in keeping my sanity throughout the years.

I would also like to thank the Ministry of Education, Malaysia and Universiti Malaysia Perlis for the scholarship throughout the three years of my PhD.

TABLE OF CONTENTS

NOMENCLATURE

List of abbreviations

TOF	Turnover frequency
TWC	Three-way-catalyst
LD	Light-duty diesel
HD	Heavy-duty diesel
LG	Light-duty gasoline
NRMM	Non-road mobile machinery
AFR	Air-to-fuel ratio
LNT	Lean nitric oxide trap
SCR	Selective catalytic reduction
CRT	Continuously regenerating technology
NSR	Nitric oxides storage-reduction
PM	Particulate matter
YSZ	Yttria stabilised zirconia
SEM	Scanning electron microscopy
HIM	Helium ion microscopy
TEM	Transmission electron microscopy
FIB	Focused ion beam
EDX	Energy dispersive X-Ray analysis
XPS	X-Ray photoelectron spectra
XRD	X-Ray diffraction
BET	Brunauer–Emmett–Teller
STP	Standard temperature and pressure
MFC	Mass flow controller
IR	Infrared
NTP	Normal temperature and pressure
GHSV	Gas hourly space velocity

List of symbols

Symbol	Description	Unit
r_{CO_2}	CO_2 production rate per pellet area decorated with exsolved particles	mol s^{-1} m^{-2}
$r^*_{CO_2}$	CO_2 production rate per weight of active catalyst	mol s^{-1} g^{-1}
y_{CO_2}	Measured CO_2 concentrations at the gas outlet	ppm
$\dot{n}$	Mol of CO_2 produced	mol
A_{pe}	Pellet area decorated with exsolved particles	cm^{-2}
A_p	Area of exposed particle are per unit surface	m^{-2}
a	Unit cell parameter	nm
k	Average number of active sites per unit cell parameter	unitless
N_A	Avogadro's number	atom mol^{-1}
w_p	Weight of active catalyst	g
r_{NO_2}	NO_2 production rate per pellet area decorated with exsolved particles	mol s^{-1} m^{-2}
$r^*_{NO_2}$	NO_2 production rate per weight of active catalyst	mol s^{-1} g^{-1}
y_{NO_2}	Measured NO_2 concentrations at the gas outlet	ppm
T	Temperature	°C
P_{CO}	Partial pressure of CO	kPa
P_{NO}	Partial pressure of NO	kPa
P_{CO_2}	Partial pressure of O_2	kPa
F_t	Total flow rate	ml min^{-1}

LIST OF FIGURES

LIST OF TABLES

1 CHAPTER 1: INTRODUCTION

1.1 Research background

Platinum (Pt) is the most versatile metal among the noble metals, and serves as an efficient, multifunctional catalyst for oxidation, hydrogenation and dehydrogenation reactions [1], finding numerous applications in the chemical and petrochemical industries [2, 3]. More than one third of the globally produced Pt is consumed by the primary user of Pt, catalytic converters in the automotive industry alone [4], where Pt acts as an oxidation and reduction catalyst to control the emission of exhaust gases, namely carbon monoxide (CO), unburned hydrocarbon (HC), and nitric oxides (NO_x) from petrol and diesel powered vehicles, especially for the oxidation of NO_x to NO_2 [5, 6]. This is expected, owing to its exceptional catalytic activity and great thermal stability, low reaction affinity with support materials and high resistance towards sulphur [1]. However, the limited supply of Pt leads to high price and its increased demand remains as one of the major obstacles limiting its large scale applications in current and new technologies, such as fuel cells [4, 7].

For the past decades, researchers have been trying to find cheaper alternatives such as base metals to substitute Pt and attempts have been made to use base-metal catalysts in CO and NO_x oxidation, respectively [8, 9]. Cobalt (Co) has been found to have good oxidation activity under CO oxidation [10-12] and NO oxidation [13, 14] at low temperatures, although they showed some deactivations at room temperatures, and even more so at high temperatures [9, 15]. Co oxides displayed reversible sulphur poisoning under stoichiometric CO and HC oxidation at higher temperatures (550 °C and above) and the degree of recovery increases with temperatures [16] while the combination of Co, K and TiO_2 demonstrated good resistance towards sulphur under NO oxidation [17].

The activities of these base metals are of a similar order of magnitude to those of Pt at relatively low temperature; e.g. at room temperature, but the approaches for catalyst activity comparison tend to be weak [18], and most studies eluded the direct activity comparison to that of Pt, especially under CO oxidation. Despite being researched extensively, these base metal catalysts are still inferior in terms of rates per metal area or on a weight-to-weight basis, and turnover frequencies (TOFs) under CO and NO oxidation in comparison to Pt. They also have lower stability to sintering and poisoning [19, 20], and easily react with support materials [21, 22]. The catalytic and stability investigations at high temperatures, and the direct activity comparison to that of Pt are still limited and are not well-described.

1.2 Aim & objectives

The main aim of this research is to develop base metal catalysts e.g. exsolved base metals particles perovskites systems rivalling Pt in two distinct base reactions; CO and NO_x oxidation. The reactions were chosen as the key reactions due to their importance in various industries, especially in automotive and newly emerged technologies such as fuel cells.

The objectives of this research are as follows:

1. To investigate the catalytic activities of base metals in exsolved metal system formulations that can possibly compete with state-of-the-art commercial Pt on alumina (Pt/ Al_2O_3) powder catalyst in terms of carbon dioxide (CO_2) production rates under CO oxidation on a weight-to-weight basis.
2. To thoroughly investigate the catalytic activity of the active exsolved metal system under CO oxidation, attained from the first objective, in terms of temperature and its stability against time and poisoning both by CO or sulphur, and to also perform preliminary temperature investigation under NO oxidation.
3. To link the catalytic and kinetic behaviour of the active exsolved metal system to their particle characteristics by monitoring the microstructural changes of the metal particles system at nanoscale at each key stage of catalytic experiments via particle tracking experiments.
4. To investigate the effect of metal-support interface length on the activity of the active exsolved metal system under both key reactions; CO and NO oxidation.

1.3 Research scope

The scope of research will mainly focus on the investigations of the catalytic performance of exsolved base metals catalyst systems, mostly under CO oxidation and NO oxidation. These exsolved metal systems were prepared via the exsolution method, employing an A-site deficient perovskites system which has been proven to produce uniform, well-distributed metal nanoparticles on the catalyst surface. This is beneficial, especially for several important heterogeneous catalysis, for example in oxidation reactions. The main aim of this research is to investigate the exsolved base metal systems which can perform well in two key reactions; CO and NO_x oxidation in comparison to commercial Pt catalyst on a weight-to-weight basis as a key requirement for application as industrial catalysts. Most studies did not compare the activities of their base metal catalysts to those of Pt, especially on a weight-to-weight basis which then hindered their application, especially in terms of quantity since the exact activities per catalyst weight are unknown. The reaction conditions for CO and NO oxidation employed

throughout this thesis mirrored the condition that Pt catalyst would face in the exhaust converter, as potential application for these exsolved metal systems. However, since the aim of this investigation is not to fully simulate the exhaust reactions, but only to study the reactions as based reactions; e.g. CO oxidation, we did not investigate the effect of water or HC oxidation, which is also present in the exhaust converter. Nevertheless, past investigations have revealed that these exsolved metal systems showed good activity under HC oxidation and tolerance against coking [23].

1.4 Thesis outline

The overall structure of this thesis takes the form of six chapters. This thesis begins with the first chapter, which contextualises the research by giving background information on the problem at hand; that is to replace Pt with cheaper alternative catalysts by listing the research's aims and scope in order to solve the problem. Following this chapter, Chapter Two begins by laying out the theoretical dimensions of the research, and looking at noble metals as the major industrial catalysts worldwide. In particular, Pt is used to catalyse several key catalytic reactions such as oxidation and hydrogenation which are reviewed in detail in terms of its major user and drawbacks towards its future application. It also gives a brief summary on the automotive industry as the major user of Pt, and its characteristics as successful exhaust catalysts and their relation to base metals as possible alternatives are pointed out. The third chapter describes the methodology employed for this research. The preparation method of the exsolved metal systems utilised in this thesis is briefly described. Chapter Three also explains the materials and experimental methods involved throughout the study. In this chapter, the experimental setups and all catalytic experiments performed throughout this research are described appropriately. This includes the surface and elemental characterisation methods involved; brief explanation on how the instruments work and the analysis technique of our materials. The surface characterisations described include the scanning electron microscopy (SEM) or helium ion microscopy (HIM), and transmission electron microscopy (TEM), while the elemental characterisations include the X-ray powder diffraction (XRD) and X-ray photoelectron spectroscopy (XPS). The equations to calculate the reaction rates in terms of CO_2 production and turnover frequencies, TOFs are also included.

The outcomes of this research are divided into two separate chapters. The investigations on exsolved base metal systems in comparison to that of commercial Pt on a weight-to-weight basis are described in detail in Chapter Four, starting from the preliminary catalytic testing to screen their potential using pellet systems under CO oxidation. For practical applicability, the exsolved metal systems are then prepared in powder form and their catalytic activities; in terms

of CO_2 production rates per weight of active catalyst, $r^*_{CO_2}$, are first assessed and compared to a state-of-the-art Pt/Al_2O_3 catalyst on a weight-to-weight basis under a temperature-effect experiments. Their stability against poisons, such as CO and sulphur is also probed to address the disadvantages of base metals in these atmospheres.

The fifth chapter presents the findings of the research, focusing on the active exsolved metal combination, cobalt-nickel (CoNi) systems under CO oxidation. Due to the nature of Co, which is likely to go through surface change upon oxidation, particle tracking experiment is employed as a tool to closely monitor the particles at several key experimental stages. This also serves to provide information as to link its catalytic and kinetic behaviour towards its microstructural changes and comprehensive analysis are reported. The resulted active structures of Co, induced by the exposure to CO-rich environment which then led to the activities enhancement, comparable to that of Pt are analysed in detail to explain the origin of the high activities. The mechanism of this restructuring is explained by a phenomenon known as the Kirkendall effect and through this, we managed to identify the active morphologies in tuning base metal oxides systems to rival Pt. The effects of the interface length are also addressed. The activities of the active exsolved CoNi powder system, having the active structures are tested under another key reaction; i.e. NO oxidation. This is performed to screen the functionality of this exsolved system under another key reaction and a preliminary temperature effect experiment is later performed. The change in structures is also explored briefly, although due to the introductory nature of these experiments, further in-depth investigations and experimentation into this reaction are strongly recommended.

The final chapter of this thesis draws together the various key findings and conclusion throughout the thesis and to reflect on the implication of the research to future tailoring of these exsolved systems to have high activities in two main reactions; i.e. CO and NO oxidation. This chapter also provides gathered data to address each research aims highlighted in the first chapter. Future works such as to investigate the detailed reaction mechanism under both reactions; CO and NO oxidation using this exsolved systems are also included to fully understand the system, among others.

2 CHAPTER 2: LITERATURE SURVEY

2.1 Introduction

More than 80 % of the industrial chemical, petrochemical and biochemical processes are based on catalytic processes that employ materials known as catalysts to accelerate reactions, which would be otherwise unobtainable or prohibitively expensive to achieve. Catalysts serve a vital role in manufacturing an extensive range of products since the early 1890s when catalytic hydrogenation of vegetable oil was first introduced. Besides manufacturing processes, the importance of catalysis has found its way in pollution abatement with successful application in the automotive industry and is predicted to increase in the near future. Most of these catalytic processes are naturally heterogeneous, which typically involve a solid catalyst, normally known as heterogeneous catalyst and gas- or liquid-phase reactants. Other main types of catalysis include homogeneous and bio catalysis.

Catalysis is an occurrence by which when a suitable material, known as catalyst is added into a chemical reaction, the total reaction rates and selectivity are enhanced without itself being consumed and it leaves the reaction equilibrium unaffected. These materials are used to increase the reaction rates and accelerates the completion of the reaction equilibrium in a chemical reaction without altering the thermodynamic equilibrium of the process. This catalyst offers an alternative reaction path with lower activation energies, E_a for the formation of the product from the reactants so that the reaction can reach its equilibrium much faster and easier. The two different reaction paths (catalysed and uncatalysed reaction) are shown in **Figure 2-1** below.

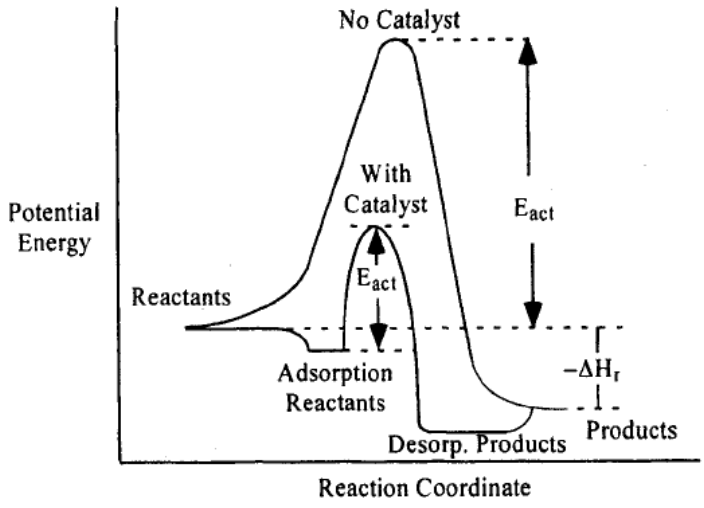

Figure 2-1 Potential energy profile for exothermic reaction, showing lower activation energy, Ea of the catalysed reaction [24].

Heterogeneous catalysts are widely used as industrial catalysts, including in hydrocarbon refining, production of bulk chemicals, automobile pollution control and fuel-cell technologies. This is due to their advantages over other catalysts especially on the simplicity of catalysts' preparation and product separation, which can prevent the formation of impurities (e.g. inorganic) that can deactivate the catalyst. Thus, the catalyst that is highly stable and tolerant under severe operating conditions and that can be reused or otherwise, can be cost consuming. Typical metal catalysts used in the industries are normally in the form of highly porous, high surface area oxide with dispersed metal phase, which is known to be active for catalytic reactions [25]. The performance of these kinds of catalysts in terms of activity, selectivity and their stability contributes towards their feasibility in specific applications, which is controlled by a number of factors such as the type and nature of the active metals, the effect of the support and its interactions, metal particle sizes, electronic structure, catalyst promoters and treatments, as well as the reaction conditions [26].

There are several critical properties that a catalyst should possess, which determine its feasibility as industrial catalysts. These properties are as follows [27]:

i. Activity (in terms of moles of products per volume per hour, turnover frequencies (TOFs) or of reactants conversion) and selectivity
ii. Catalysts' lifetime
iii. Ease of regeneration and reproducibility of the catalyst in order to increase its life time
iv. Price

Noble metals notably platinum (Pt) serve as efficient, multifunctional catalysts for a variety of reactions including oxidations, hydrogenation and dehydrogenation reactions [1], as well as in catalytic cracking for crude oil refinery and petrochemical industries [2-4]. This is due to the fact that Pt has shown exceptional catalytic activity and great thermal stability, low reaction affinity with support materials and highly resistant toward sulphur. However, due to the limited resources and the high cost of Pt, which have remained as major obstacles limiting its large scale applications in current and new technologies, there has been a growing number of research to develop highly selective alternative base metal catalysts that are capable of replacing Pt.

This chapter provides a general overview of noble metals, particularly Pt as the main industrial catalysts. The overview on Pt reviews its history and explains why it is expensive and what makes it an excellent catalyst, especially as the main catalyst in automotive exhaust converters. This is then followed by introducing base metals as the potential alternative catalysts in two main Pt-catalysed reactions, namely CO and NO_x oxidation in exhaust converters in both petrol

and diesel engines. Conventional preparation methods of supported base metal catalysts are discussed and their limitations in terms of activity and stability are also identified in relation to its preparation parameters. Last but not least, the exsolution method is introduced as the main preparation method in this research and its advantages over the conventional preparation method are also mentioned.

2.2 Noble metals

Noble metals have been acknowledged as vital catalysts that are dominantly used in several major industries, such as in the chemical, petrochemical, automotive after-treatment process and fuel cells, which are attributable to their excellent activity and stability [28-30]. These metals are highly sought after as commercial catalysts because of their superior chemical and physical properties. These properties include their high resistance towards corrosion and thermal ageing, and their good mechanical strength and ductility. Not only that, these metals are called "noble" because of their propensity to remain metallic even under harsh reaction conditions since they are less reactive, compared to other metallic-state elements. **Table 2-1** lists some of the physical properties of noble metals and nickel that are heavily used as current automotive catalysts.

Table 2-1 Physical properties of some selected noble metals, nickel and their oxides relevant to their behaviour in automotive catalysts [31]

Metal	Symbol	Atomic number	Atomic weight	Density (g cm^{-3})	Melting point (K)	Oxide stability under operating conditions
Platinum	Pt	77	195.08	21.45	2045	Unstable oxides
Iridium	Ir	46	192.22	22.56	2683	Moderately stable oxides
Palladium	Pd	45	106.42	12.02	1825	Stable oxides
Rhodium	Rh	76	102.91	12.41	2239	Stable oxides
Osmium	Os	44	190.2	22.59	3327	Very volatile oxides
Ruthenium	Ru	29	101.07	12.37	2583	Very volatile oxides
Nickel	Ni	28	58.69	8.908	1728	Volatile oxides

These noble metals are used in various applications, mainly as catalysts in chemical and petrochemical industries, among others. Apart from gold (Au) and silver (Ag), Pt has also been used to make jewellery and coins, thanks to its resistant against corrosion at high temperatures, good mechanical strength and ductility. These metals are also used in the glass, electric,

electronic and dentistry industries. For example, Ir has been used in spark plugs for aircraft and in machinery parts like spinneret because of its hardness and highly resistance towards corrosion. Ru is used in various applications from strengthening alloys in Pt and Pd, to improving the resistance of titanium towards corrosion and also as a biological stain for nucleic acids and pectin. The primary uses of these noble metals, mainly Pt, Pd and Rh, are as automobile catalysts to reduce the emission of toxic exhaust gases such as CO, unburned HC and NO_x. The demand for these metals is expected to rise in the near future, especially due to the stricter emission regulations and the increasing number of developing countries opting for reduced emission levels. Not only that, fuel cells, a newly emerged technology that also uses platinum-coated electrodes and is pollution-free, is expected to be a major technology in the future, which in turn is expected to increase the use of Pt as well. Nickel on the other hand, are used in the preparation of alloys such as stainless steel, which accounts for approximately 67% of all nickel used in manufacture due to its hardness, high ductility and highly resistant towards corrosion because of its slow rate of oxidation at room temperature. However, due to its being considered as carcinogens, its usage has been reduced. It also boasts a high melting point and is magnetic at room temperature. Other nickel alloys also have important applications such as a component of the tubing used in the desalination of sea water. Nickel steel is used in the manufacture of armour plates and burglar proof vaults. Nickel alloys are especially valued for their strength, resistance to corrosion and in the case of stainless steel for example, aesthetic value. Other applications of nickel include coinage, transportation and construction, petroleum industry, machinery and household appliances and also as catalysts in the chemical industry.

2.3 Platinum

As the most common and the most versatile noble metal, Pt has been widely used as catalysts, since it can function efficiently in the abatement of pollution, especially in the automotive industry. Pt consists of six natural isotopes: ^{190}Pt, ^{192}Pt, ^{194}Pt, ^{195}Pt, ^{196}Pt, and ^{198}Pt, with ^{195}Pt being the most abundant, comprising of around 33.83 wt.% and has a maximum oxidation state of +6, but the oxidation states of +2 and +4 are the most stable under the earth surface environment. Pt is an inert, i.e. the least reactive among the noble metals, refractory metal with high boiling and melting points, which makes it highly resistant towards oxidation and corrosion. However, surface corrosion can occur in the presence of halogens, cyanides, thiosulfate, other potential sulphur compounds and organic acids. Pt is also insoluble in hydrochloric and nitric acid but it can dissolve in hot aqua regia. Pt and other noble metals can be dissolved in strong, alkaline oxidising agents and molten bases such as sodium (Na), phosphorus (P), silicon (Si), arsenic (As), antimony (Sb) and lead (Pb). As previously

mentioned, Pt is widely employed as catalysts in the automotive industry, owing to its ability to chemisorb simple gaseous components such as CO and oxygen (O_2). These characteristics, combined with significant metal coverage and a fairly weak surface desorption ability of the gaseous components produce the superior reaction rates of Pt [32, 33].

2.3.1 Major industries of Pt and its disadvantages

Pt is typically used as catalysts in oxidation, hydrogenation, halogenation, and isomerisation reactions. Pt is also being used in newly emerged technologies such as fuel cells though its extensive commercialization is yet to be successful, owing to the high cost, which is caused by the high loading of Pt needed in the fuel cells [34, 35]. **Figure 2-2A** shows the major consumers of Pt in the year 2016 (up to May 2016), which corroborates the widespread industrial uses of Pt. Automotive catalyst consumes more than one-third (40 %) of the world's Pt supply due to the introduction of the three-way-catalyst (TWC) in the automotive gaseous after-treatment process. This is attributed to the growth of light-duty diesel (LD) sector where the consumption rose by 10 % in 2015, compared to the previous year, especially in Europe. Automotive catalysts can be divided further into four main categories, such as light-duty diesel (LD), heavy-duty diesel (HD), light-duty gasoline (LG), motorcycles and non-road mobile machinery (NRMM).

From **Figure 2-2B,** it is evident that more than half of the world's Pt supply are used as the automotive catalysts in the LD market and this mostly reflects the increase in LD market in Europe, while the use of LD gradually increases in other parts of the world, such as Japan. The increase of the LD market in Europe is mainly due to the establishment of the stricter Euro-6b emission standards, focusing on diesel NO_x emissions. This then requires a Pt-rich lean NO_x trap (LNT) or a combination of LNT and selective catalytic reduction (SCR). As a result, the consumption of Pt increases in order to meet these emission limits. Heavy-duty diesel (HD) also contributed to the rise of Pt usage in recent years. However, the Pt growth slowed down in 2015, as a result of the general cutback of catalyst content and by the greater use of palladium in heavy duty catalysis. Pt is also used in the jewellery sector, as the second largest consumer of Pt. This sector comprises of around 33.76 % of Pt demand, owing to its properties, such as highly resistance towards corrosion at high temperatures. Other major sectors include the petrochemical industries, in which Pt is used to catalyse various reactions, for example, in naphtha reforming. It is also being used in the medical and dental sectors, in which Pt has been exploited in cancer treatment and the preparation of dental fillings [36].

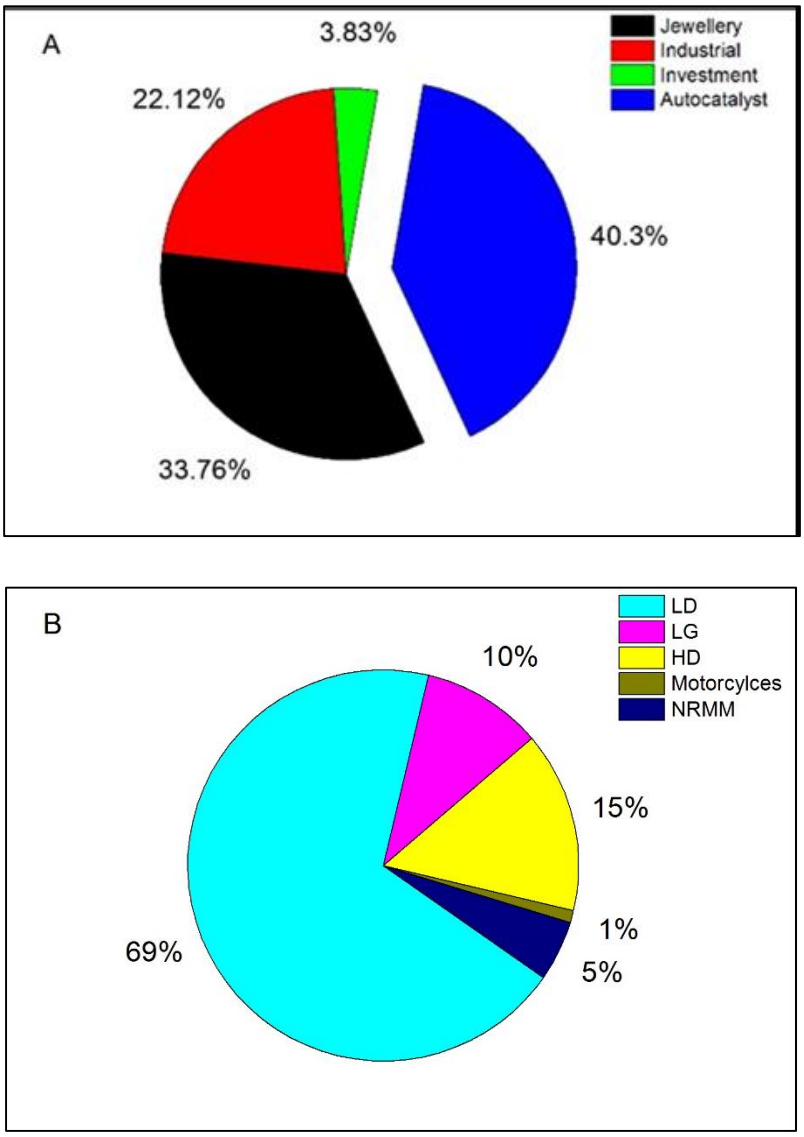

Figure 2-2 Platinum demand by (A) main industries with automotive catalyst reported the highest demand for Pt and (B) shows the demand by various auto sectors in the year 2016, comprising the 40.3 % of Pt demand in automotive catalyst industries. Note: LD: Light duty diesel, LG: Light duty gasoline, HD: Heavy duty diesel and NRMM: Non-road Mobile Machinery [36]

The worldwide production of Pt has been growing steadily since the 1970s, although the demand of Pt intensifies with the introduction of automotive catalysts, containing several noble metals such as Pt, Pd and Rh in order to abate pollution due to the increased emission of toxic exhaust gases such as CO, HC and NO_x. Pt as the major noble metal in these catalysts is of the greatest concerns, since they typically contain ~0.08 wt.% of Pt, 0.04 wt.% Pd and 0.06 wt.% Rh [37]. In the recent years, due to the more stringent automotive emission regulation and the increase in vehicle production, more Pt is required to accommodate this need in petrol and diesel converters. From 2013 to 2015, the total demand for Pt only rose by a small margin of ~10 %, which most of them are used to accommodate the need of Pt as automotive catalysts, as a result of the constrained supply from the major supplier, South Africa. Pt is mainly mined in

South Africa, Russia, North America, Zimbabwe and others, with South Africa monopolising the majority of the supply sector with almost three-quarter of the world's Pt production in 2015 (**Figure 2-3B**). Although the supply of Pt is abundant in the past, the recent mining strike in South Africa in 2014 has resulted in declining Pt supply, which by far was the most damaging supply-side vents for years. The primary supplies fell by 12 % in 2014, and following the prolonged industrial action by the three major companies which then resulted in around 40 % decline of global Pt production combined. This wage-related strike was the longest (22 weeks) in the South Africa's history, following the 2012 strike, which some have argued on its long-term reliability of the world's largest Pt producing country. These concerns were the turning point which the major consumer sectors have started to seek for alternative to mitigate this potential supplier risk. Although the Pt price is expected to rise during this supply-constrained period, the price however, failed to rise, owing to the consumers who opted to outsource to other production countries and secondary suppliers such as recycling to mitigate these supply problems [38].

Even though the supply constrains have been resolved, the possibility of the scarcity of noble metals and its high price are still considered as major concerns, which might affect its consumption in various industries. This then requires for the development of alternative metal-based catalysts, which have similar characteristics and activities to those of Pt, to be able to replace Pt, especially as automotive catalysts.

A

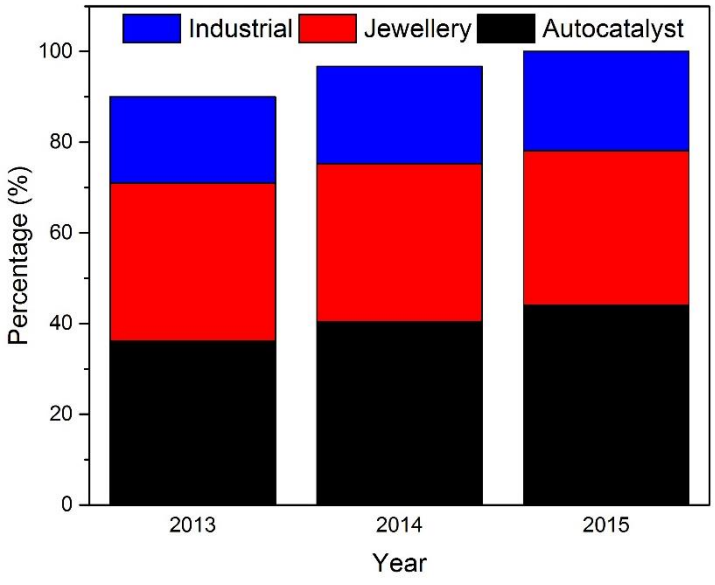

B

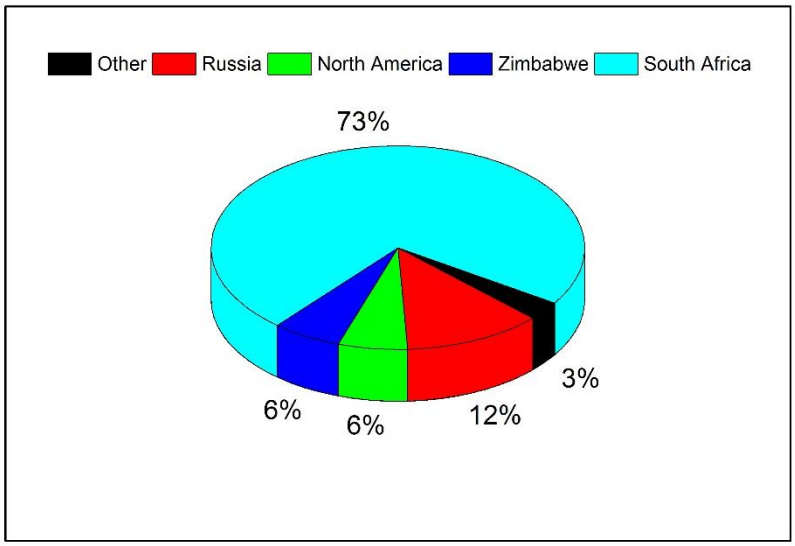

Figure 2-3 (A) Demand data (in percentage) for Pt from 2013 to 2015 by the application and (B) the global Pt production by country in 2015. Data from Johnson Matthey Market data tables and Metal price history charts [4]

2.3.2 Automotive catalytic converter

Due to the increased air pollution generated by the incomplete combustion in the engine exhaust which result in some toxic exhaust gas emissions, stringent exhaust gas emission standards were established, starting in the USA in the late '60s. These exhaust gases contained primarily of three main pollutants such as the unburned or partially burned hydrocarbon (HC), carbon monoxide (CO) and nitric oxides (NO_x), plus several other compounds such as water (H_2O), hydrogen (H_2), nitrogen (N_2) and oxygen (O_2). Not only that, traces of sulphur oxides (principally SO_2) are also present as they normally accumulate in the system and can only be removed by reducing them into elemental sulphur. Due to the different nature of these pollutants, the development of the catalytic exhaust gas after-treatment is focused on the simultaneous conversion of these pollutants into nontoxic gases via a variety of reactions (reduction and oxidation) over several metal catalysts, known as the exhaust catalysts. Some of the desirable reactions are listed in **Table 2-2** below and since it is possible for other detrimental reactions to occur such as the reduction of NO_x to ammonia, high selectivity towards the desirable reactions is greatly required. Noble metals were found to be very active and the fact that they can remain metallic in most operating conditions without forming volatile oxides which can cause metal loss made them the commonly used exhaust catalysts since the early years of these automotive catalyst systems. However, the use of high noble metal loadings is considered inefficient since they promote sintering at high temperatures, leading to the deactivation of the exhaust catalysts and also causing the cost of these catalytic converters to rise steeply.

Table 2-2 Reactions occurring in a three-way-catalysts (TWC) of the catalytic exhaust gas after treatment [5, 29] and the catalysts used for each reaction, with typical wt.% of 0.08, 0.04 and 0.006 of Pt, Pd and Rh, respectively [37]

Reactions	Conversion involved	Reaction equations	Catalysts
Oxidation			
CO	$CO \rightarrow CO_2$	$2CO + O_2 \rightarrow CO_2$	Pt/ Pd
HC	$HC \rightarrow CO_2, H_2O$	$HC + O_2 \rightarrow CO_2 + H_2O$	
Reduction			
NO_x	$NO_x \rightarrow N_2 + CO_2/ H_2O$	$NO_x + CO \rightarrow N_2 + CO_2$ $NO_x + H_2 \rightarrow N_2 + H_2O$ $NO_x + HC \rightarrow N_2 + CO_2 + H_2O$	Rh/ Pd
Additional reactions			
Water-gas-shift		$CO + H_2O \rightarrow CO_2 + H_2O$	
Steam reforming		$HC + H_2O \rightarrow CO_2 + H_2O$	

Since the 1970s, the first commercial automotive catalyst has been introduced in passenger cars to meet the stringent exhaust gas emission standards which require the use of catalytic exhaust gas after treatment systems. A "two-way" device is first introduced to remove CO and HC emissions caused by the incomplete fuel combustion while the NO_x emissions are controlled by the recirculation of the exhaust gases, but the robustness of this technology has been compromised. This new technology produces nontoxic N_2, O_2 and water with a few toxic gases such as volatile organic compounds (VOCs), HC and CO due to the O_2 deficient engine environment and NO which is caused by the reversible reaction of NO and O_2 at high temperatures [39]. This then leads to the development of catalytic converters in order to lower the NO_x emissions. A dual-bed catalytic converter was first built to operate with excess fuel to reduce NO_x to N_2 over the first catalyst in the reducing conditions. The secondary catalyst was used to oxidise CO and HC to carbon dioxide (CO_2) and water in the oxidising condition. This technology was found to be efficient in removing toxic exhaust gases although it is cost ineffective due to its failure to control the air to fuel ratio (AFR) at stoichiometric conditions. A closed loop engine management system using oxygen sensors was then developed to balance the exhaust gas compositions at the optimum stoichiometric point of AFR=14.6 to simultaneously oxidise CO and HC, and reduce NO_x over a single catalyst up to 99 % efficiencies, which is now known as the three-way catalyst (TWC) [40, 41]. Typical TWC components are shown in **Figure 2-4** below.

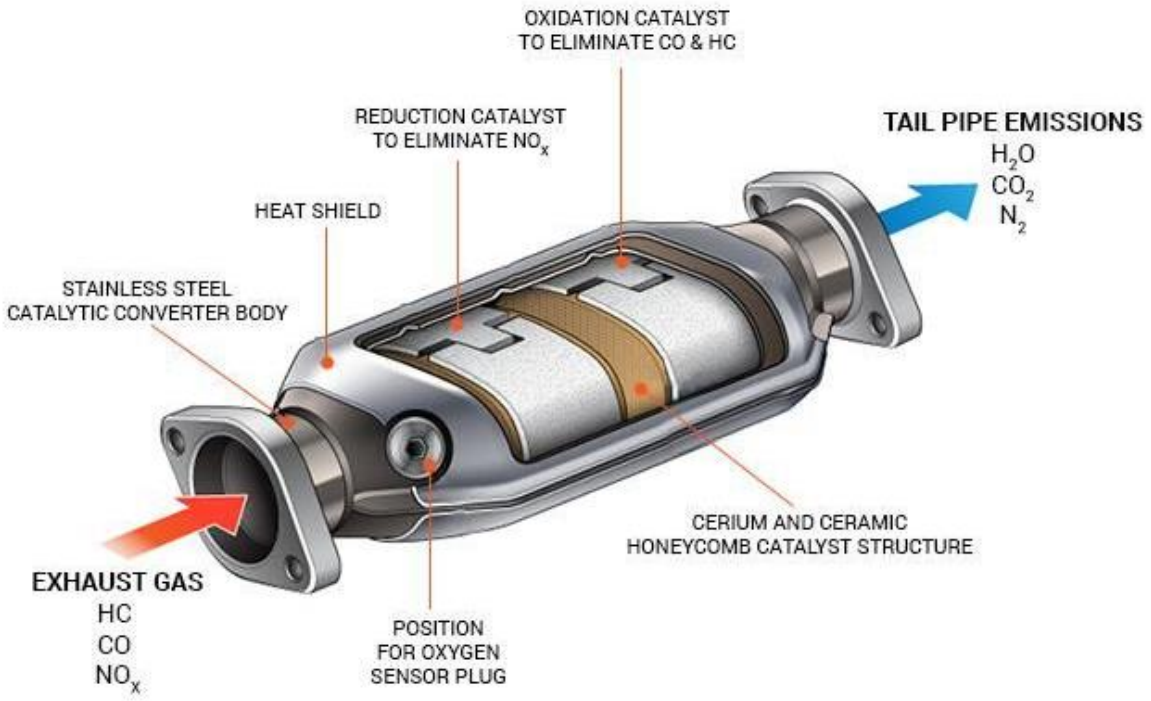

Figure 2-4 Diagram of a typical catalytic converter for a petrol engine, showing the important components; including the three-way-catalyst (TWC) and the position for the oxygen sensor to keep the exhaust gases compositions at the optimum point (AFR=14.6) [41].

This petrol catalytic converter generally consists of several crucial components including the TWC system in the form of metallic or ceramic honeycomb monolith structure and an oxygen sensor to keep the exhaust gases concentrations at the optimum AFR point of 14.6. This so-called three-way catalyst (TWC) system makes use of certain noble metals combinations such as Pt, Pd and Rh, which could then simultaneously oxidise CO and HC and reduce NO_x near the stoichiometric conditions (AFR=~14.6). For this system to work, the AFR needs to be maintained within a narrow margin of ± 0.05, near the stoichiometric AFR (14.6) at all times. This is controlled by the oxygen sensor, positioned right before the catalyst system. TWC are principally consists of around 0.15 wt.% noble metals with Pt to Rh ratio of 5:1, supported (or wash coated) on alumina (γ-Al_2O_3), admixed with varying concentrations of bulk CeO_2 for instance, in order to promote the oxygen storage. In order to maintain the high surface area in varying reaction conditions such as at different temperatures, the wash coat is stabilised with lanthanum (La_2O_3) and/or barium (BaO) oxides, and is then deposited on a ceramic honeycomb structure to obtain the finished catalyst system.

This TWC system are designed to simultaneously convert three toxic exhaust gases (CO, HC and NO_x) into nontoxic gas emissions (CO_2, H_2O, N_2). Upon start-up, both the engine and the catalysts are cold, which then require some heat or temperature on the catalyst surfaces for the reaction in **Table 2-2** to occur. After the start-up, the heat of combustion is transferred from the

engine and the exhaust piping begins to heat up. A specific temperature, known as the lightoff temperature is then reached within the catalysts which then initiates the catalytic reactions. This temperature and the concurrent reaction rate is kinetically controlled, which depends on the chemistry of the catalyst due to the fast transport reactions. Typically, the CO reaction initiates first, followed by the HC and NO_x reactions and when all three reactions occurring simultaneously, the term TWC is used. Upon further heating, the chemical reaction rates become fast and the overall conversions are then controlled by pore diffusion and/or bulk mass transfer [42]. **Figure 2-5** shows the fuel consumption and the three-way performance of petrol engine as a function of the engine air to fuel ratio. The normal 14.5:1 (stoichiometric) ratio produces exhaust gas that contains correct balance of CO, H_2 and HC to reduce NO_x and O_2. Lean-burn engines, which operate at air–fuel (A/F) ratios of 25:1 and above, are effectively improve the fuel efficiency of petrol vehicles, but produce oxygen-rich exhaust gases, which then suffer from the extremely difficult removal of NO_x in lean engines.

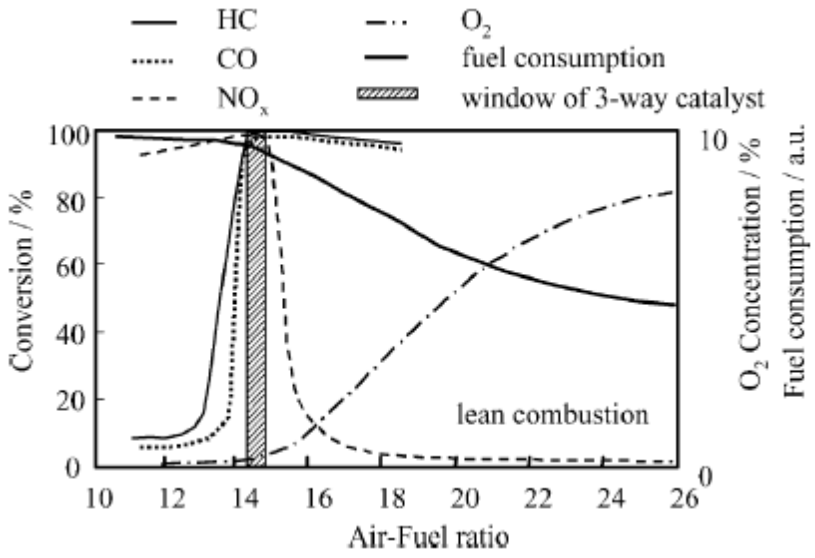

Figure 2-5 Fuel consumption and three-way performance of a petrol engine as a function of the air–fuel (A/F) ratio [43].

Although these catalysts system are able to achieved significant reductions of toxic gases, the operating conditions to which these catalysts were subjected often cause them to become thermally, chemically and/ or mechanically deactivated. This then caused the removal of active sites from the catalytic surfaces, thereby causing the decrease in their catalytic performance. Thermal deactivation which involves the deactivation at high temperatures is a physical processes caused by sintering which are a loss of catalytic surface area due to crystalline growth of the catalytic phase or the loss of washcoat area due to the collapse of the pore structure. Solid-solid phase transitions are also occurring in TWC at very high temperatures (> 900 °C)

whereby it involves the chemical transformations of catalytic phases to non-catalytic phases. Catalytic converters are also prone to poisons and/or impurities containing lubricants oils, for example, which even at low levels can completely cover the catalysts' active sites. These common poisons include lead, sulphur, phosphorus and zinc.

Certainly, this system has been highly effective in pollution abatement due to its continuous improvement of the catalytic performance and the durability of the catalysts over the years. However, due to the more rigorous emission regulations, particularly in lowering HC emissions in the recent years, the concern relating to the cold-start emissions became more critical, at which around 80-90 % of HC emissions from petrol cars, equipped with this TWC system occurred during the cold-start. Because of this, the development of new alternative catalysts shows high conversion efficiency even at low, near ambient temperature [44] with tremendous thermal stability, exceeding 1100 °C are gaining attention worldwide, in both noble or non-noble metals, particularly for the removal of CO and HCs.

Lean diesel engines are still popular, especially in Europe due to their high operating efficiencies, relatively low emission, excellent durability and cost efficient. Unlike the traditional stoichiometric spark-ignited petrol engine, in a compressed-ignition diesel engine, the engine is operated in significantly leaner (excess O_2) conditions and at lower temperatures of around 30 to 650 °C due to the nature of the process, in which only sufficient fuel is injected into the compressed hot air to power the engine. The exhaust emissions from both petrol and diesel-powered engines contained similar major toxic chemical species although they are present in different concentrations as shown in **Table 2-3** below. The lower amount of HC and CO emission in diesel engine can be easily removed by oxidation due to the abundance of O_2. However, this makes it particularly challenging to control the NO_x emissions under the lean condition even though only a very low level of NO_x is present. This is due to the fact that the metallic catalyst has a higher affinity towards O_2 than that of N_2, which leads to metal surfaces covered by strongly bonded O_2, preventing the adsorption of NO to complete the reaction. However, this can be reversed by using a reducing species in the catalyst formulation such as zeolite although a significantly large amount of these reductants is needed to reduce NO_x under this lean conditions, thus it is not cost effective. Therefore, it is definitely challenging to reduce NO_x emissions under highly oxidising conditions, which are readily oxidised to form NO_2. Despite the successful establishment of lean NO_x-trap systems which exploited the easiness to oxidise NO in to NO_2 rather than the reduction of NO under highly oxidised conditions, we are still in dire need of active low temperature NO_x oxidation catalysts [45].

Table 2-3 Literature survey on exhaust conditions for TWC and diesel engines [46-49]

Exhaust components and conditions	Four-stroke spark ignited-engine, equipped with TWC	Lean-burn diesel engine
CO	0.1-6 %	300-1200 ppm
O_2 (%)	0.2-2	10-15
HC (ppm)	500-5000	50-330
NO_x (ppm)	100-4000	350-1000
H_2O	10-12	1.4-7
CO_2 (%)	10-13.5	7
SO_x (ppm)	15-60	10-100
PM (mg m^{-3})	-	65
Temperature (°C)	RT-1100	RT-650
Gas hourly space velocity, GHSV (h^{-1})	30000-100000	30000-100000
A/F ratio	14.7	26

The important role of NO_2 in NO_x storage and reduction (NSR) catalyst is first identified by the research in Toyota [50, 51], which makes use of a supporting oxides catalyst consisting of dispersed Pt metals (Pt/ Rh) on γ-Al_2O_3 and a basic component such as BaO for the adsorption of NO_x [52]. This combines with ammonia (NH_3) or HC as the reducing agent can be used to reduce NO to N_2, especially in the selective catalytic reduction (SCR) process [53]. Successive lean and rich phases are attained to remove these NO_x by first oxidising NO to NO_2 on Pt and these nitrates are stored in BaO during the lean phase. In the following short rich phase, NO_x is released and reduced into N_2 on Pt/ Rh by the reducing species. The amount of NO_2 in the exhaust has also been shown to substantially increase the selectivity of this SCR process, most prominent at low temperatures of around 200-300 °C, indicating the importance of NO_2 as the intermediate components towards the activity of these systems [54].

Not only that, diesel engines also formed significant particulate matter (PM) emissions which can be lessened by the use of a particulate filter that is adequate in meeting the existing emission standards. For that reason, Johnson Matthey has proposed the use of a continuous regenerating trap (CRT) to continuously oxidise the soot collected on a particulate filter at comparably low temperatures. This again called for the need of low temperature NO_x oxidation catalysts since both systems require additional NO_2 to successfully convert toxic NO_x to N_2. The main drawback of these diesel engines is also due to the sulphate emissions which are almost twofold the emission from petrol engines. Since these sulphates are not removed during the exhaust after-treatment and can only be reduced to elemental sulphur by minimising the sulphur content in the fuel itself, they posed a serious problem in diesel engines. This is due to the lower

operating temperature range, which makes it difficult to desulphurise (at temperatures above 650 °C) and if not removed from the system, it can deactivate the catalysts.

To summarise, both petrol and diesel-powered engines pose similar problem, in which for both systems, the need to develop an alternative active low-temperature catalyst (<100 °C), with extreme thermal stability (>1000 °C) and the ability to withstand sulphur poisoning is considered critical. Especially, in the recent years, due to the more stringent emission regulations worldwide.

2.3.3 History of noble metals as oxidation catalysts and catalysts' improvement

Since noble metals are limited and costly, Pt is expected to be greatly affected since it is used in both petrol and diesel engines, and also in several newly emerged technologies like fuel cells, because of its great physical and chemical properties [55]. Aside from the exhaust converter, Pt-catalysed CO oxidation is also used in chemical sensors, CO_2 lasers, residential and automotive air cleaning technologies and gas masks for mining applications, among others [56]. In order to accommodate these various applications, various catalyst improvements are introduced in order to reduce the dependency on Pt while still able to accommodate the needs of using these metals. There are two ways of tackling this problem, to formulate catalysts which use less Pt or to develop non-noble metal catalysts which can rival Pt in activity and stability. Activity deterioration of these noble metal catalysts in TWC also worsened as a result of the installation of the catalytic converter closer to the engine to ensure immediate conversion of exhaust gases during start-up, which demands for extreme thermal resistance of the catalysts. Repeated exposure towards sintering causes the agglomeration and the growth of metal particles, causing the overall surface area to decrease, resulting in severe drop of activities of these noble metals. To compensate this, excess loading of noble metals is then used, leading to the overuse of noble metals.

The addition of the perovskite structures into noble metals catalysts formulation have been investigated since the 1970s, especially for catalytic converters due to its recognised wide-ranging properties such as its high thermal stability [57]. The concept of "intelligent" catalysts has been introduced by Nishihata et al. [58] and has been used as automotive catalysts in Japan ever since. These catalysts can self-regenerate its metal particles during redox cycles in automotive engines, hence can be recyclable which then leads to the reduce use of Pt following metal particles agglomeration. This is particularly crucial for Pd, which displayed the biggest deterioration among the other two metals, owing to its lower melting point. Pd-perovskites oxide, $LaFe_{0.57}Co_{0.38}Pd_{0.05}O_3$ was found to perform well over ~100 hours with minimal

deactivations under CO-NO_x redox conversion, owing to its ability to suppress the growth of metal particles during redox reaction by the reversible movements of Pd particles into and out of the perovskite lattice. In order to market this technology, $LaFe_{0.95}Pd_{0.05}O_3$ was investigated and despite Co being removed from the catalyst formulation due to its possible carcinogenic properties, this Pd-perovskites showed similar self-regeneration and excellent overall activity even at low temperatures (100-300 °C) [59]. Since then, catalytic improvements, particularly in terms of catalysts formulation and preparations have gained increased attention worldwide, which are considered to be crucial in reducing our dependency on noble metals. This technology is also being applied to Pt and Rh since the limited availability of these metals is more serious than those posed by Pd. Pt- and Rh-doped $CaTiO_3$ are found to exhibit similar self-regeneration properties, which in turn can supress the growth of particles, consequently maintaining the catalytic activities of these catalysts [60]. These materials are able to tackle two main problems posed by noble metal catalysts that are to use less and to have extreme thermal resistance.

Improvement on immediate activation of these metals is also on the rise for the cold-start process, setting up a foundation on the search for low-temperature oxidation catalysts worldwide, which is also desirable in other oxidation reaction processes. Again, due to its interesting oxygen storage capacity (OSC) and the support's oxygen release ability of supported Pd catalysts which are considered crucial in low-temperature CO oxidation, it has been widely used as alternative low-temperature oxidation catalyst to Pt. CeO_2-supported Pd has shown impressive low-temperature activity under CO oxidation, achieving ~95 % of CO conversion at 150 °C, compared to other supported Pd, owing to the above-mentioned features and their strong electronic interaction [61]. This also leads to investigations focusing on the effect of preparation methods of this CeO_2-supported Pd catalysts in order to further decrease the light-off temperatures of these catalysts [62, 63]. The lowest temperature of 75 °C was achieved by Gulyaev et al., using CeO_2-supported Pd prepared via the plasma arc method, resulting in high surface area and high defects concentrations, causing the activation of the catalyst at low temperature [64]. Metal oxides doped CeO_2 supports have also been investigated as a way to increase the OSC of the CeO_2 support. Wang and his colleagues reported the catalytic properties enhancement which can be attributed to the addition of Mn and Sn in a CeO_2-supported Pd catalysts, showing almost ~90 % of CO conversion at room temperature, with reversible sulphur poisoning above 200 °C and remarkable hydrothermal stability [65]. Along with Ce, Fe is also known for their oxygen storage ability which can then be manipulated to produce catalysts that are active under low-temperature CO oxidation due to its ability to provide additional adsorption sites for oxygen. A comparable TOF value of 0.151 s^{-1} to Au-based catalysts is

reported (0.4 s^{-1}) when FeO_x is used as the support for Pt, Pd catalysts, highlighting the capability of Fe as additional adsorption sites for O_2 [66]. The temperature for the total oxidation of CO over Fe-supported Pt/ SiO_2 was reduced to 140 °C from 230 °C, over the conventional Pt/ SiO_2. However, the excess Fe amount can deactivate the catalysts due to the formation of iron oxides [67].

In terms of NO_x oxidation, in order to improve the activity of the most active catalysts, Pt, under NO oxidation and/or to at least reduce the dependency on Pt, various investigations, especially in terms of catalysts formulation have been performed. This includes investigations on the role of different supports, Pt loading and the effect of sulphur on the NO oxidation activities of Pt catalysts. Pt/ SiO_2 has been found to be more active than Pt/ Al_2O_3 and Pt/ ZrO_2, although all three catalysts exhibited increased activities with increasing Pt loading [68]. This study also reveals the size-dependency of these catalysts that opened up the possibility to tailor their particle morphology to attain higher activities. Binary oxides such as TiO_2-ZrO_2 has also been utilised as support for supported Pt catalysts for NO oxidation by Liu and co-workers. They have found that the acidity of the support plays a key role in preventing SO_2 adsorption and a more acidic support such as TiO_2-ZrO_2 can result in better resistivity towards sulphur in comparison to the conventional Ba/Al_2O_3 [69, 70]. The beneficial nature of potassium, which formed a more stable K-based nitrate than the typical Ba-based nitrate, especially at high temperatures has been considered as a better prospective nitrate storage, especially in the lean-NO_x trap (LNT) catalysts [71].

As the first step to reduce dependency on Pt, many works have been carried out in assessing the effect of the addition of transition metals in conventional Pt catalysts [72-75]. The addition of Co oxides, in particular, Co_3O_4 can enhance the NO_x storage ability of the Pt catalysts due to its high oxidation capability. However, this shows no effect on the activities following the sulphur poisoning-regenerating process. Zou et al. [76] found that the addition of Co in the previously mentioned Pt catalyst supported on TiO_2-ZrO_2 can greatly improve their oxidation ability, but they suffer from a slight deactivation upon sulphur poisoning due to the formation of the detrimental bulk sulphates and Pt oxides. The detrimental effect of these Pt oxides in the NO oxidation has also been investigated by Lira et al. [77]. Based on the literature reported above, Pt is still the leading catalysts in NO oxidation although it is costly and demonstrates poor thermal stability in highly oxidised conditions. Since it is still the best oxidation catalysts, the growing researchers are still focusing on how to tackle the problems with Pt, instead of trying to find comparable alternative catalysts.

To summarise, noble metals, especially Pt are critical in many aforementioned existing and newly emerged technologies. However, their limited availability and high cost enforce the development of noble-free catalytic systems with enhanced activity and improved stability. In particular, the utilisation of base metals as catalysts which are much cheaper is considered as an obvious choice although several setbacks in tailoring these metals need to be addressed.

2.4 Base metal catalysts

The development of noble metal-free catalysts is also growing rapidly worldwide in order to meet this urgent need posed by the limited availability of the precious metals. Stringent emission regulations and the evolution in catalyst technology also lead to the possibility to shift from using precious metals towards the utilisation of cheaper base metals as the catalysts. However, the challenges posed by base metals intensified because the application of base metals as automotive exhaust catalysts is hindered, mainly due to its well-known sensitivity to poisoning by trace amounts of sulphur [78], which are always present in the exhaust gases [79]. Therefore, the weaknesses of base metals such as their limited activity (refer **Table 2-4** for the relative activity for several noble and base metals), thermal stabilities and low resistivity towards poisons, in particular, sulphur need to be tackled.

Table 2-4 Relative activity of noble metals and base metals oxide catalysts under CO oxidation at 300 °C, with 1 % CO in excess O_2 [80, 81]

Active phase	Pd	Pt	Co_2O_3	CuO	CuO/ Cr_2O_3	$LaCoO_3$	Au	MnO_2	Fe_2O_3	Cr_2O_3	NiO
Relative activity	500	100	80	45	40	35	15	4.4	0.4	0.03	0.013

For practical applicability, their performance needs to be comparable to that of the precious metals' [5, 82], in terms of catalytic activity per metal or on a weight-to-weight basis and thermal stability in similar operating conditions as those applied in a TWC. As displayed in **Table 2-4**, noble metals are more active than base metals although some oxides, especially those with Co or Cu, have exhibited promising activity for CO oxidation. However, their comparison to Pt is seldom eluded. What is more, in order to reduce the consumption of fuel in the automotive industry, for instance, these materials also need to perform in a wider range of operation conditions including at low temperatures for cold start operation and highly oxidised condition in diesel engine.

2.4.1 History in CO and NO oxidation

In the literature, there is a massive number of studies employing base metals as catalysts in CO oxidation and the details of these studies are presented in **Table 2-5** below. The catalytic activities for these materials are listed in terms of their temperature upon achieving 100 % of CO conversion, T_{100} shown in the far right column of the table. For the catalyst to be beneficial as the alternative to Pt in practical applicability, it should have performed better or at least comparable to Pt on a weight-to-weight basis or on their site activities, for example, in terms of turnover frequencies, TOFs. As previously stated, since Co and Cu showed relatively high activities for CO oxidation, they have been chosen as the main base metals in the growing catalytic investigations (refer **Table 2-4**), although several reports also investigate the use of other metals such as Ni.

As one of the promising candidates, cobalt oxides (Co_3O_4) has been extensively investigated in CO oxidation with various structures and preparation methods, for example, nanorods [9] and nanosheets [83] due to its high activity at room temperature. These low-temperature oxidation catalysts are beneficial in many applications such as in the automotive industry, especially during the cold start period and in diesel engines. However, under realistic conditions, these catalysts are unable to perform well due to the presence of water/ moisture and sulphur which act as poisons and deactivate their activities [12]. The relative stability of these kinds of catalysts is also compromised even without these so-called poisons due to either the formation of surface carbonates, carbonyls or surface restructuring which might cause the inactivity of the Co ions for CO adsorption [84, 85]. The catalytic activities of Co-based catalysts are also said to be dependent on their morphology, phase, plane exposure and synthesis procedure [86] and since it has been proven to be crucial as low-temperature oxidation catalyst, different structures of cobalt oxides and supported cobalt oxides catalysts have been widely investigated, mostly for CO oxidation. Particularly for Co_3O_4, different nanostructures are prepared via various routes including hydro- and solvothermal, precipitation-oxidation, wetness impregnation and combustion synthesis methods, among others. Among the reported studies, Co oxides spinel nanorods prepared by Xie et al. [9] exhibited high CO oxidation activities at a very low temperature of -77 °C with increased moisture stability even under realistic practical conditions. They also revealed the importance of exposing (110) plane, favouring the formation of the active Co^{3+} ions, which is thought to promote the activities. In another study by Yu et al., Co oxides catalyst also showed significant high activities at -67 °C with higher stability at ambient temperature, although in their study, they have highlighted the importance of pre-treatment of the catalysts [15]. This was performed to produce active phases and planes, which emphasise

on the morphology dependency of these catalysts in tailoring their CO oxidation activities. However, most studies suffer from deactivation even at room temperature, mainly due to the surface restructuring of the metal ions at high temperature, highlighting the thermal stability limitation of these metal catalysts [15, 87-89].

Much attention has also been directed towards copper (Cu), in particular, Cu-CeO_2 [90, 91], Cu-chromite [92] and Cu-manganese [93]. Zheng and co-workers revealed in their study that high CuO concentrations in CuO-CeO_2 catalysts, prepared by the sol-gel/ impregnation method can influence their activities at the low-temperature region of CO oxidation, due to the higher CuO dispersion achieved, in comparison to the commercial CuO-CeO_2 catalyst, with measured temperature at 50 % CO conversion, T_{50} of 140 °C [90]. Hasegawa et al. demonstrated a more active copper-based catalyst than the previous study, employing amorphous mesoporous Cu-Mn oxides, prepared via the sol-gel method, with T_{50} of 83 °C under similar reaction conditions [94]. They also discovered that this higher CO oxidation activity is caused by the different nature of the lattice oxygen present, having high redox ability, which was easily removed and reintroduced. From these studies, the effect of the preparation method seemed to play a significant role among other parameters, such as the type of support and the particle size in tailoring copper-based catalysts, as previously studied by Hutchings et al. [95].

Since Fe and Ni are less active under CO oxidation, there are fewer investigations using these metals for this reaction. The fact that NiO are volatile even at low temperatures of around 50 °C and the high toxicity of Ni complexes, such as nickel tetracarbonyl, $Ni(CO)_4$ also contributed to the lack of catalytic studies using this metal, although this carbonyl decomposes at around 230 °C. Ni-doped CeO_2 nanorods showed low activity in comparison to Co- and Mn-doped CeO_2 and its activities are almost similar to that of an undoped CeO_2, caused by the formation of metallic Ni species, which is thought to be inactive in CO oxidation [96]. NiO nanorings prepared by the hydrothermal method has exhibited an active low-temperature region with T_{50} of ~125 °C in comparison to other NiO nanocrystals [97], emphasising on the importance of particles morphology in tailoring NiO catalysts. In contrast, Fe is known for its major disadvantages which include the low activity at low temperatures, low thermal stability and the crystal growth resulting in the loss of surface area which then limits its use as CO oxidation catalysts. However, its excellent redox ability which can catalyse CO oxidation either with or without oxygen by losing its lattice oxygen has been previously considered as a good quality to be used as potential metal catalyst. To overcome this, Fe has been added or alloyed into another base metals catalysts formulation and it has been discovered that the synergistic effect between Fe and other metals, especially Co and Cu is capable of producing higher CO oxidation

activities in comparison to pure Fe catalysts [98, 99]. Cu-Fe composite oxide catalyst, prepared by the co-precipitated method shows total oxidation of CO at low temperature of 100 °C although it is discovered that this activity is subjected to few other preparation and morphology parameters such as calcination temperature, Cu: Fe molar ratio and particle size, etc. [100]. Biabani-Ravandi et al. have discovered that Co addition into Fe-oxides catalysts resulted in a huge increase of activities, especially at the low-temperature region with measured T_{50} of ~60 °C in comparison to 75 and 225 °C for pure cobalt and iron oxides, respectively [98].

NO oxidation has been widely investigated using base metal catalysts; e.g. supported-Co_3O_4 [13] and supported Co [45]. Several mixed oxides which include MnO and CuO have been investigated for this reaction, though they reveal poor activities and the fact that the catalysts need to operate effectively at fairly low temperatures (<300 °C) in highly oxidised atmospheres making it even harder to find active alternative catalysts. Co_3O_4/ SiO_2 and Co_3O_4 demonstrated higher oxidation activities than those Pt-based catalysts, achieving more than 50 % of NO conversion at 300 °C, compared to 350 °C for the Pt-based catalyst, revealing the superior oxidation ability of Co [101]. The reaction mechanism on Co- based catalysts are similar to that of Pt and Pd, in which the O_2 adsorption on the oxygen atom vacancies is revealed to be the kinetically important step for NO oxidation. Weiss et al. also revealed the size dependency of Co_3O_4, with larger cluster size in the range of 40 to 100 nm that showed higher turnover rates in comparison to the small clusters by preparing abundant O_2 vacancies, needed for O_2 activation, hence increasing the activities of the catalyst [102]. A more recent study by Shao et al. reveal the effect of alloying Co into Fe-based catalysts, in which the activities are improved with the total oxidation of NO is achieved at a low temperature of 170 °C, in comparison to its pure Fe catalysts at 250 °C. They also observed similar crucial catalytic steps, and the Co ability to increase the amount of Fe ions, surface oxygen and oxygen activity aided the reactants adsorption and desorption of products resulting in marked improvement of the activities [103].

Table 2-5 Literature survey on transition metal-based catalysts for CO oxidation with various reaction conditions

Catalyst formulation	Catalyst geometry	Catalyst weight (g)	Gas composition		Inlet total flowrate, F_t (ml min^{-1})	Operating temperature (°C)	Temperature at CO conversion, X_{co}=100 % (T_{100}), (°C)	Ref.
			P_{O_2} (kPa)	P_{CO} (kPa)				
Co-supported SiO_2	Powder	0.04	10	4	25	RT-300	150	[104]
Co-supported Al_2O_3	Powder	0.04	10	4	25	RT-300	200	[104]
Co-doped CeO_2	Microspheres	0.1	15	0.24	100	80-550	300	[105]
Co-doped CeO_2	Nanorods	0.1	6	1	48	30-550	308	[96]
Co oxides	Nanocrystalline	0.05	20	0.8	100	30-200	<90	[106]
Co_3O_4		0.15	excess	1	150	-100-140	-40	[84]
Co_3O_4	Nanotubes	0.2	2.5	1	50	-80-30	~25	[89]
Co_3O_4	Rods	0.08	21	3.4	42	-120-30	-50	[88]
Co_3O_4	Wires	0.08	21	3.4	42	-120-30	-50	[88]
Co_3O_4	Rod-wires	0.08	21	3.4	42	-120-30	20	[88]
Co_3O_4-CeO_2	Core shells		10	1	50	80-200	140	[107]
Co_3O_4		0.15	excess	1	50	-110-50	-80	[15]
Co_3O_4	Mesoporous	0.2	excess	1	60	-40-160	30	[108]
Co_3O_4/ TiO_2		0.2	10	1	20	-100-80	-50	[87]
Co_3O_4		0.075	2.4	2.4	20	RT-380	<175	[86]
Cu-doped CeO_2	Microspheres	0.1	15	0.24	100	80-550	300	[105]
Cu-doped CeO_2		0.05-0.1	16	2	15-100	RT-600	80	[109]
CuO-CeO_2		0.05	0.5	1	100	RT-350	200	[110]
CuO/ TiO_2		0.1	1	1	20	50-310	175	[111]
Ni-doped CeO_2	Microspheres	0.1	15	0.24	100	80-550	350	[105]
Ni-doped CeO_2	Nanorods	0.1	6	1	48	30-550	430	[96]
$LaBaCoNiO_3$		0.5	4	1	250	150-400	200	[112]

2.4.2 Challenges of base metal catalysts

Despite the growing number of research in synthesising base metal catalysts as alternative CO oxidation catalysts, these types of catalysts have not been commercialised as of yet in industrial application due to some major concerns that can lead to catalysts deactivation. These major concerns are coking, and irreversible poisoning of sulphur. These crucial aspects are not well-described in most reports on base metal catalysts for CO oxidation that are considered extremely important in catalysis. Catalyst deactivation or the loss of catalytic activity and/or selectivity over time is a huge and continuous problem in the practice of industrial catalytic process. Typically, the deactivation occurs fairly slowly and its rate varies depending on the process. Although it is present in most processes such as steam reforming, fortunately, it can be prevented or even delayed. Two major mechanisms that can cause deactivation, especially for base metals are sulphur poisoning and coking, as described in **Table 2-6.** The following literature review would mostly involve base metal catalysts in other reaction processes; e.g. steam reforming since not much has been reported on sulphur poisoning deactivation of base metals in CO and NO oxidation reactions.

Table 2-6 Mechanisms of catalyst deactivation

Mechanism	Type	Brief definition
Poisoning	Chemical	Strong chemisorption of species on catalytic sites, blocking sites for catalytic reaction
Fouling/ coking	Mechanical/ chemical	Physical/ chemical deposition of species from fluid phase onto the catalytic surface and in catalyst pores
Sintering	Thermal	Thermally induced loss of catalytic surface area, support area, and active phase–support reactions

Of the two mechanisms, fouling or the so-called catalyst coking is perhaps the primary focus for deactivation investigations of base metals catalysts. The coking usually occurs as a side reaction due to the degradation of reactants/products, resulting in covered active catalytic sites and activity loss. Extreme coking might result in pore blockage, leading to the removal of active sites that prevents the completion of the reaction; e.g. particle uplifting due to the formation of carbon whiskers. It can also cause the inter-particle coke growth which may then increase the pressure drop of the fixed bed reactor, causing the blockage of fluid flow in the reactor. This has been considered as a perennial problem for Ni catalysts since the early years, especially in steam reforming since the rate of formation of C-C bond on Ni is high, leading to rapid

deposition of carbon, which then deactivates the catalyst. The formation of coke depends on the operating temperatures and catalyst formulation which can cause at least three different kinds of coke species; i.e. the encapsulated particles, whisker-like carbon and pyrolytic-type carbon depending on the coked mechanisms and operating conditions. The carbon tolerance of Ni catalysts can be improved by alloying, which then reduces the binding energy of carbon on the uncoordinated surface sites [113].

The methanation activity of several base metal catalysts including Fe, Ni and Co has shown strong and rapid poisoning by H_2S in the range of 15-100 parts per billion (ppb), which in this case, deactivation occurs as a result of sulphur (S) accumulation onto the catalytic sites, reducing the sites quite rapidly due to the intense interaction between S and the active sites even at low concentration. This corroborates the earlier study by Maxted, which found that the typical poisons for transition metals (Group VIII: Fe, Co, Ni, Pd, Pt, etc.) are molecules containing elements such as S and O among others although metal oxides are more resistant than its metal counterpart towards these poisons. In an attempt to tackle this problem, various studies have resorted to employing various approaches including manipulating the operating conditions in order to have as minimal amount of poisons as possible. Matsuzaki et al. found that at least three operating parameters can be manipulated to alter the effect of sulphur poisoning on Ni-YSZ electrode, such as S concentrations and poisoning temperatures. S components are easily adsorbed on Ni at low temperature due to the stronger adsorption at these temperatures, causing a more complicated desulphurisation process compared to poisoning at higher temperatures [114]. Ashrafi et al. in their paper supporting the previous work, found that the poisoning of Ni can be reversed at higher temperature of 800 °C, simply by removing the sulphur source [115]. Literature has shown significant improvement in sulphur tolerance of Ni by alloying [116]. Saha et al. observed reversible sulphur poisoning of Ni/CaO supported catalysts at higher temperature of 900 °C although a slight decrease in temperature to 800 °C resulted in severe deactivation [116]. A most recent study revealed the effect of alloying Co into Ni-spinel catalysts, suggesting that faceting can improve the sulphur tolerant of these type of catalysts with strong CO_2 adsorption on highly faceted edge sites causing the improved oxidative sulphur removal [117].

2.4.3 Fabrication of supported base metals catalysts

The fabrication method of base metal catalysts has also been found to be critical in tailoring their catalytic activities under specific reaction, especially for supported dispersed metal catalysts. This is due to the fact that the properties of base metal catalysts; e.g. cobalt can be

influenced by several vital factors including the nature of the support, the metal-support interactions, particle or crystal size of active phases, and the surface structures among others. Specifically, the metal-support interaction can be altered to significantly enhance the catalytic activity of the catalysts [104, 118]. These properties can be manipulated via the fabrication method and depending on the nature of the fabrication method, catalysts with various properties can be synthesised. For supported metal catalysts, active metal components are deposited or dispersed on the surface of a highly porous and thermostable support, which provides higher surface area and mechanical stability. This can promote higher metal dispersion and increase the thermal stability of the catalysts, hence prolonging the catalysts life. For supported metal catalysts, the common preparation method involves at least three different unit operations including the introduction of metal precursor on the support, drying or calcination and reduction. The key methods used to introduce the metal precursor to the support are impregnation and precipitation methods, among others. These methods involve the deposition of metal catalyst precursor onto the surface of a support via thermal treatment [118].

In the impregnation method, the support is contacted with a solution containing the metal precursor prior to heating treatment, followed by drying and calcination. The metal solution, typical salt is used and depending on the volume of the metal solution, impregnation can be classified into two main types. Incipient-wetness or dry impregnation method employs adequate metal concentration with less volume of metal solution, i.e. the volume is equal or slightly less than the pore volume of the support. The metal solution is sprayed on the support while stirring, provided that the trapped air in the pores has been removed beforehand to allow deeper penetration of the solution into the pores. This also resulted in better metal precursor's distribution on the support since the pore volume is known. The major benefits of this method are the simplicity of the method and its cost effectiveness since only a small amount of the metal solution is used, especially when using expensive active metal. It can also replicate the metal loading and successive impregnation steps can be performed to increase the metal concentrations on the support if required. On the other hand, wet or soaked impregnation method employs excess volume of metal solution with respect to the pore volume of the support. The system is then heated under continuous stirring for a longer period of time preceding the filtration and drying processes. The drying process is crucial in removing the excess metal solution. Another parameter that can affect the nature of the dispersed metal produced by this method is the type or concentration of adsorption sites present at the support surface that promotes the important metal-support interaction of the catalysts, which is thought to enhance their activities in comparison to their single metal counterparts [119].

In the co-precipitation method, solution containing sufficient metal and support components, depending on the required loading is mixed with an alkaline or base solution to precipitate the metal in the form of hydroxides and/ or carbonyls. This is performed since the hydroxides are insoluble and often unstable, and can easily form oxides upon heating. Principally, the co-precipitation method is capable of producing catalysts with uniform distribution of different active metals on a molecular scale. It has also been found that the interaction between hydroxide ions group and the metal ions serves a vital role in determining the nature of the active phases formed on the support, which is directly associates with the preparation parameters. These parameters include the choice of metal salts-alkali solutions and the efficient mixing between the two solutions, the external operating parameters such as temperatures, ageing time, filtering and washing procedures among others. Not only that, the pH of the solution also needs to be controlled efficiently to prevent precipitation at different sequence which can then result in different final structure of the catalysts. These problems intensify upon scaling up, which then limits the use of this method to produce commercial catalysts that demand catalysts having well-dispersed uniformly sized metal. Despite the drawbacks previously discussed, this method has found application in producing catalysts for two chemical industries; steam reforming (Ni/Al_2O_3) and methanol synthesis (Cu-Zn oxide/ alumina). A rather similar fabrication method to the precipitation method, namely the deposition-precipitation method involves the precipitation of a metal hydroxide on the particles of a powder support via a reaction between the metal and the base solution. In order to produce well-dispersed small particles on the support, precipitation inside the pores is required to promote the particles nucleation and growth on the support. This is difficult due to the rapid nucleation and growth in the solution bulk, forming particles larger than the pore causing the precipitation to occur outside the pores. This resulted in uneven distributions of larger crystallites, which are unfavourable under catalysis. After this step, the materials are subjected to similar after-treatment process including the filtration and drying [119, 120].

Although some of these methods have been used to commercially produce industrial catalysts, there are still several setbacks following these approaches, mainly due to their limited control over the deposited particles size and distributions. The particles anchorage is usually compromised during calcination or during reaction, leaving only a few active metals for catalysis, resulting in activity loss during catalytic reaction. These methods are also lengthy and pricey, which are considered critical from the industrial point of view. This called for a better preparation method aiming to tackle the setbacks posed by the conventional method. The stoichiometric exsolution method has been employed by several groups in their attempt to

reduce the use of noble metals, employing perovskite as the support and the reducibility of the metal, especially during reaction. This method can also be used to exsolve cheaper base metals which then require the use of deficient perovskite systems as the driving force for exsolution since most base metals such as Co are harder to reduce. The following section will elaborate the exsolution method in detail, for both the stoichiometric and deficient exsolution method.

2.5 Metal exsolution method

As an alternative method to prevent the setbacks posed by the conventional preparation approaches, incorporation of metal catalysts as a dopant within the perovskite host (support) during synthesis in air is employed and via the subsequent reduction, the metals are exsolved at the surface in the form of catalytically active metallic nanoparticles [121]. This so-called in-situ growth of metallic nanoparticles from the parent perovskite resulted in surfaces decorated with uniformly dispersed pinned metal nanoparticles, which are deemed crucial in many fields, especially catalysis. Not only that, this process is also time and cost effective, and its reversibility indicates that agglomeration can be reversed or avoided through re-oxidation, enhancing the lifetime of the catalysts, especially for the stoichiometric exsolution of Pt.

2.5.1 Utilisation of perovskite support

As the primary component in the realisation of this exsolution concept, the utilisation of perovskite as the ideal support is explained. The increased research which employ perovskite as the catalysts framework have been observed worldwide, owing to their promising catalytic activity in the redox reactions and their outstanding thermal stability and high poisons resistivity [122]. This perovskites structure is also of particular interest, especially in catalysis due to its flexibility to accommodate various components via partial substitution of A and/or B cations, leading to materials with wide range of properties to suit specific application, like as a possible catalyst rivalling Pt [123]. An ideal perovskites structure (**Figure 2-6A**), $SrTiO_3$, having general formula of ABO_3 can be described best as a continuous network packing of AO_3 with the B-site cations occupying 100 % of the resultant BO_6 oxygen octahedral which connect through corner sharing [124].

Although the multicomponent can be substituted into the perovskite lattice, the cubic structure needs to be fulfilled (in relation to their ionic radii) and the deviation from the ideal cubic structures can be measured using a tolerance factor, *t* by Goldsmith:

$$t = \frac{(r_A + r_O)}{\sqrt{2}(r_B + r_O)} \qquad \text{Equation 2-1}$$

where r_A is the radius of the A-site cation, r_B is the radius of the B-site cation and r_O is the radius of the lattice oxygen anion. A value of t in between 0.75 to 1.05 needs to be fulfilled in order to adapt the perovskite structures, especially at room temperature and the value beyond this range will result in severe distortion and segregation, leading to destabilisation of the structures. For example, if the sizes of either the A-site or B-site cations are huge or small then the necessary sizes following the value of t, it may result in strained or loose structure, which then destabilised the whole perovskites structure. Besides that, the other requirement that needs to be satisfied is the electroneurality of the structures which means that the equality between the sum of A and B charges to the total charge of the oxygen anions needs to be satisfied. This can be achieved by appropriate charge distribution between the A and B cations or partial substitution of A and B-site cations, while preserving the perovskite structure. However, numerous oxide compounds are non-stoichiometric in nature, resulting in the excess cation or anion defects [125], which are often necessary, allowing the movement of cations since the ideal structure of perovskite is incapable of conducting oxides ions [126]. The A-site vacancies can be manipulated to offer non-stoichiometry, unlike the B-site vacancies, which are not thermodynamically favoured due to the larger charge and smaller size of the B-site cations. These defects are attributed to several factors, including the partial substitution of the A-site cations and the variation of A/B ratio or oxygen stoichiometry that has been considered important in catalysis [127].

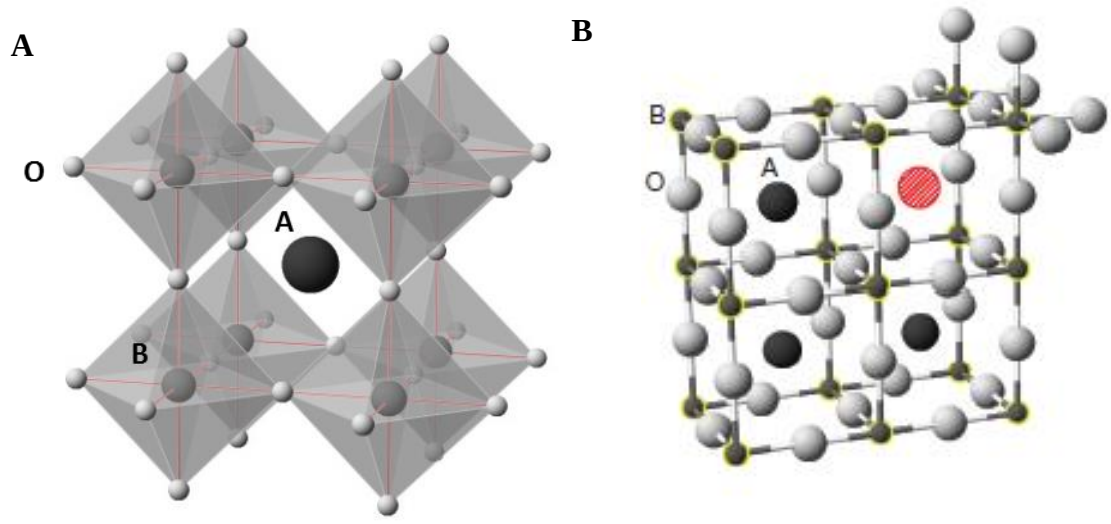

Figure 2-6 Schematic diagrams of the (A) ideal perovskite structure of ABO_3 and (B) A-site deficient structure, in which following the different exsolution routes of the B-site species [128]. The large red hashed circle represents the A-site vacancies.

The two cations have different roles in the perovskite system. The A-site is normally occupied by a rare-earth ion, commonly altered (or substituted) to introduce or modify concentration of

oxygen vacancy while transition metals ions as the B-site cations are used to control the overall electronic conductivity, making it simpler to manipulate their cation composition and non-stoichiometry [129]. Based on these properties of perovskite, several principles in designing perovskite catalyst have been identified. The selection of B-site cation, i.e. the transition metals plays the most cardinal part in determining the catalytic activity of the catalysts and the vacancy, and the valency of the B-site can be manipulated via partial substitution of A-site to achieve the desired B-site valence to enhance the activity. This has been observed for the substitution of Sr and Ce for La in $LaCoO_3$ systems [130], forming the abnormal Co^{3+}, which tends to be reduced by releasing oxygen from the perovskite lattice, improving the redox ability of the materials. Not only that, its ability to have alloyed B-site metal cations also brought about the occurrence of the synergistic effects between two metals, which can function to accommodate different steps of the catalytic reactions [131].

2.5.2 Stoichiometric exsolution

A similar concept was first introduced by Nishihata et al., which involved integrating Pd in a stoichiometric perovskites lattice, in which it self-regenerates upon exposure under redox cycle, preventing any agglomeration, and resulting in stable activity over a long time [58, 60, 132, 133]. These self-regenerative catalysts have been commercialised as automotive catalysts since 2002 in Japan, and as solid oxide fuel cells (SOFC) anodes, catalysts for steam reforming of HC fuels and organic synthesis. In SOFCs, the anode's tendency to deactivate upon coarsening can be avoided by regenerating the initial low resistance via anode redox cycles, in which the metal particles are dissolved in the oxides upon oxidation and under the following reduction, the fresh particles are re-nucleated. However, this concept marked only the sole importance of B-site cations exsolution, in which the only driving force for exsolution is cation reducibility to metals, limiting to only easily reducible catalytically active cations such as Ni^{2+}, Rh^{2+}, Pd^{4+} and Pt^{4+}. Furthermore, exsolution in these systems favourably occurs within the bulk, rather than on the surface, making them unreachable for catalysis [134-136], hence lowering the effectiveness of the concept [137].

Exsolution followed a modified solid state synthesis route, involving the release of metal particles from the crystal lattice on the surface upon exposure to a hydrogen atmosphere (reduction by hydrogen), following the oxidation of the solid solution which embeds the active metal in the crystal lattice as the catalysts' backbone. However, only stoichiometric perovskites have been used with A/B=1, limiting the exsolution of other B-site cations; i.e., other active base metals like Co. With similar concept in mind, Naegu and his colleagues introduced the use

of a highly A-site deficient perovskite (A/B<1) systems (**Figure 2-6B**), which promote the exsolution of hardly reducible cations (e.g. Fe, Co) with preferred surface exsolution [128]. This signified the use of base metals with added advantages that come with the concept itself, like enhanced lifetime and stability against thermal ageing (no agglomeration upon exposure to high temperatures). Thus, the A-site deficiency acts as the general driving force to initiate the B-site exsolution, producing a wider range of metal nanoparticles with superior surface coverage [138]. Furthermore, by introducing the A-site deficiency ($A_{1-\alpha}$ BO_3, with α denoted as the A-site deficiency), B-site exsolution serves as a tool to revert the perovskite towards the stable, defect-free ABO_3 structure without producing undesirable A-site cation-containing phases. Additionally, owing to the redox nature of the process, exsolved particles may be produced within minutes electrochemically, enabling quick 'switching on' of high performance solid oxide fuel or electrolysis cells [139], which then makes them more time effective and are considered highly potential to be commercialised [139].

2.5.3 B-site cation exsolution using A-site deficient perovskite

The influence of reducing an A-site deficient perovskite ($A_{1-\alpha}$ BO_3) is schematically explained using the diagram shown in **Figure 2-7** below. Upon reducing an A-site deficient perovskite system with the presence of A-site vacancy (yellow striped circle in A), oxygen vacancies are introduced (red circle) with δ denoting the degree of reduction, or the number of oxygens removed per formula unit of perovskites. The presence of these vacancies (A, O vacancies) destabilised the perovskite lattice structure, causing the spontaneous B-site exsolution to reinstate the stoichiometry of the perovskite structures.

$$A_{1-\alpha}BO_{3-\delta} \xrightarrow{Exsolution} (1-\alpha)ABO_3 + \alpha B \qquad \text{Equation 2-2}$$

These A, O-site deficient perovskite can also be viewed as a B-site excess perovskite, which explains the predominant exsolution of B-site cations in filling up the vacancies and the high concentration of A-site vacancies (V_A") that facilitated the B-cation migration due to the lowered migration repulsion between these cations [140]. This indicates the role of A-site cations and its vacancies in promoting the B-site exsolution, which then can be manipulated to improve the surface particles exsolution. Upon reduction, the oxygens are removed from the perovskite cell with the V_A" (yellow striped circle in A), causing the isolation of the B-site cations (red circles) from the main perovskite structure (with no vacancies), progressing them towards exsolution (B). Whilst the cell without A vacancy remain unaffected, the excess B-site cations residing in the A-site deficient perovskite cell are forced out to the surface along (011) plane, whereas the A-site cations simultaneously fill the vacancies, producing rigid surfaces.

These surfaces will then limit the A- and B-site cation diffusion and exsolution, lodging the particles into place, producing uniformly distributed anchored nanoparticles. This anchorage or pinned characteristics of the particles produced are attributed to the strong adhesion between the particles and the perovskites phases during the exsolution process.

This anchored property of the exsolved particles has been investigated by Naegu et al. [23], and they have discovered that the particles are certainly embedded to significant depth inside the parent perovskites as shown in **Figure 2-8A**, with the metallic particles located epitaxial to the parent perovskite, which is not the case with particles produced via the deposition method (**Figure 2-8B**). Not only that, the increased adhesion between the particles and the perovskite support is believed to originate from the increased inter-diffusion between the metal and the oxide lattice due to the fact that these particles grow from the bulk, further improving the anchorage of the particles [141]. The strong adhesion between the particles and the oxide support brings several advantages such as increased stability against coking and agglomeration, owing to the particles' strong grip onto the support [142], inhibiting particle movement and uplifting from their original position although the adhesion decreases with the increase of particle size.

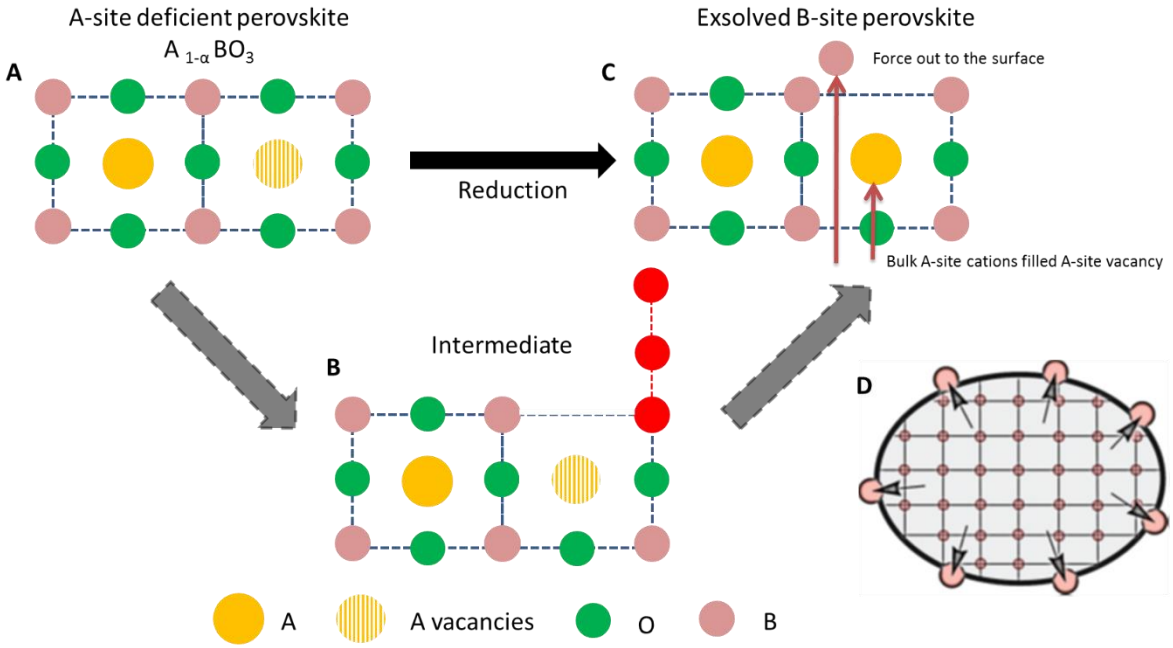

Figure 2-7 Schematic representation of the exsolution of B-site cations from A-site-deficient perovskite unit cells. By removing oxygen from the A-site-deficient unit cell through reduction, some B sites are locally secluded from the parent perovskite, progressing them for surface exsolution (B), resulting in simultaneous B-site cation surface exsolution and A-site cations diffusion to fill the A-site vacancies (C and D) [128].

The introduction of these defect structures through non-stoichiometry and manipulation of cation composition provides additional driving force for the exsolution of wider range of B-site cations. Through non-stoichiometry, inherent surface restructuring can be controlled which is found to be vital in exsolution, with terrace and edge surfaces restraining the B-site exsolution by hampering particle nucleation which normally develops in an O-deficient composition. Whilst A-site deficient formulation is found to promote particle nucleation of B-site cations, producing small and uniformly distributed surface particles, the type of A-site cations and the optimum concentration of A-site deficiency, α value are also crucial in order to promote particle nucleation over growth, depending on the particle size and surface coverage required. External factors can also influence the degree of B-site exsolution from an A-deficient perovskite system, which includes insufficient reducing atmospheres, reduction time and temperatures, and samples containing component that are harder to reduce, such as Sr^{2+}, which promote the formation of the detrimental Ruddlesden–Popper phases [143] towards particle nucleation. This concept can also be broadened to other types of perovskites with various A-site concentrations and/or alloyed B-site metal cations, which are beneficial in preventing coke deposition during application [144], to tailor these materials to fit any application requiring surfaces with uniformly dispersed catalytically active metal nanoparticles, including heterogeneous catalysis or fuel cells.

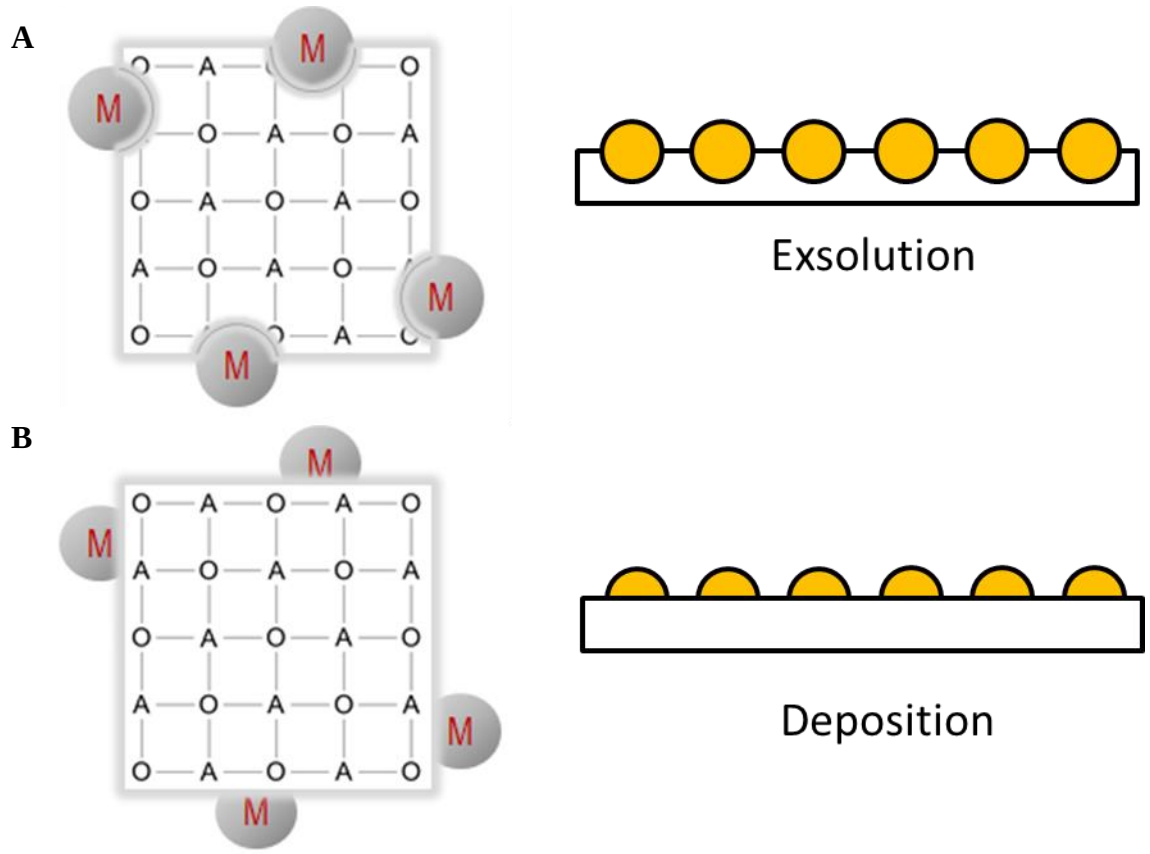

Figure 2-8 The anchorage characteristics of the exsolved particles, compared to the particles produced via the conventional techniques [23]

2.6 Summary

Earlier in this chapter, we have reviewed the importance of noble metals, mainly Pt as heterogeneous catalysts across various industries, in particular in the automotive industry due to their preferable noble characteristics; superior chemical and physical properties, highly resistant towards corrosion, thermal ageing and good mechanical strength. As the major user of noble metals, mainly Pt, Pd and Rh, the automotive industry uses almost one-third of the world Pt in 2015, which is believed to increase even more in coming years due to the more stringent emission regulations worldwide. Due to the limited availability of Pt and its high price, the researches in finding alternative catalysts to Pt have also increased in recent years, targeting the cheaper and more abundant base metals.

Among the base metals, Co and Cu are seen to show high low-temperature CO oxidation activity, evident from the plenty of studies summarised in this chapter, although most of these studies did not present direct comparison of the activity of their catalysts to Pt, either in terms of active sites or on weight-to-weight basis. These catalysts also suffered from deactivation, caused by sintering under reaction at high temperatures, which are detrimental for application at high temperatures, for instance in exhaust converter at temperatures ranging from ~700 to

1100 °C. Not only that, they also suffered from irreversible sulphur poisoning and coking which makes them less favourable to be used as exhaust catalysts. Another key oxidation reaction that uses Pt is the highly oxidised NO oxidation, present in diesel engine due to the need to oxidise NO_x to NO_2 at relatively low temperature before the reaction is thermodynamically limited at high temperatures. This then calls for low temperature NO oxidation catalysts in which Co_3O_4 is seen to show promising NO oxidation activities, in comparison to that of Pt.

The exsolution method or the ability to self-regenerate in the redox reactions have been employed to reduce the use of noble metals, such as Pd although this can only be used using the stoichiometric perovskites systems and easily-reduced cations, which then limit the use of base metals such as Fe or Co. These limitations can be addressed by employing an A-site deficient perovskites systems, enabling the exsolution of harder reducible cations. This method will be used in this research to produce base metal-based catalysts (exsolved metal catalyst systems) via the exsolution method for CO and NO oxidation, mimicking a rather similar reaction condition to that of Pt would face in catalytic converter. However, since the aim of this investigation is not to fully simulate the exhaust reactions, but only to study one reaction as a base reaction such as in CO oxidation, we will not investigate the effect of water or hydrocarbons (HC) oxidation, which is also present in the exhaust converter. We also target to tackle the aforementioned disadvantages of base metals; i.e. irreversible sulphur poisoning, thermal and long-term stability using these exsolved metal catalyst systems, exploiting the socketed property of these materials.

3 CHAPTER 3: METHODOLOGY

3.1 Introduction

This chapter describes the methods used in this thesis that include the synthesis of the exsolved base metal systems, employing three different exsolved metals, i.e. nickel (Ni), iron (Fe) and cobalt (Co), which will be used to produce catalysts whose catalytic activities parallel the state-of-the-art platinum on alumina (Pt/ Al_2O_3) catalyst and the materials characterisations involved. Previously reported exsolved pellet systems, involving nickel (Ni) and iron-nickel (FeNi) as the exsolved metals were first tested in preliminary CO oxidation studies since they showed promising activities in fuel cells and hydrocarbon oxidation with higher tolerance against coking, which is attributed to their socketed properties. This is performed to assess their potential as CO oxidation catalysts prior to comparing their activity to that of Pt on a weight-to-weight basis. Brief explanation on all characterisation methods are included; e.g. for scanning electron microscopy, SEM and helium ion microscopy, HIM. The catalytic experimental setup is reviewed, employing two different reactor setups for pellet and powder systems, and the catalytic experiments procedures involving two key reactions; CO and NO oxidation are also explained.

3.2 Materials synthesis

3.2.1 Catalysts synthesis

Exsolved metal nanoparticles catalysts samples are prepared by Dr Dragos Naegu from John T.S. Irvine's group in St Andrews University, Scotland via a method known as the modified solid-state synthesis. The synthesis of these exsolved catalysts were based on the preparation method described in their paper and the intrinsic parameters such as the exsolved metals (B-site cations substitutions) and/or the partial substitution of different A-site cations and/or the extrinsic parameters in particular, the reduction atmospheres and/or milling processes were varied because these parameters have been previously reviewed to influence the nature of the exsolved metal particles and distribution. Since this was our first attempt in formulating these exsolved metal systems with Co and/or in powder form, preparation parameters were varied; e.g. the milling methods and reduction parameters used, which then resulted in exsolved metal powder systems with various particle characteristics [128, 138]**.** Because of this, an example of catalysts preparation for the exsolved cobalt-nickel (CoNi) is presented as follows.

High purity precursors including lanthanum oxide (La_2O_3) from Pi-Kem (> 99.99 %), ceria oxide (CeO_2) from Alfa Aesar (> 99.99 %), TiO_2 from Alfa Aesar (> 99.6 %), cobalt (III) oxides

(Co_3O_4) from Aldrich (> 99.5 %) and nickel (II) nitrate hexahydrate ($Ni(NO_3)_2*6H_2O$) from Acros (> 99%) were used in the appropriate stoichiometric molar ratios, following the balanced perovskites formula. The oxides were dried at different temperatures (TiO_2 at 300 °C, La_2O_3 at 800 °C) and weighed while still warm. The dried powders were transferred into a beaker and mixed with acetone and ~0.05 wt. % Hypermer KD1 dispersant. An ultrasonic Hielscher UP200S probe was utilised to produce homogenous and stable dispersion of the mixture. The acetone was later evaporated at room temperature under continuous stirring and the content of the beaker was transferred to a crucible and calcined at 1000 °C for 12 hours. The calcined powder was then pressed into pellets (~1.5 g of powder per pellet) and fired in air at 1390 °C for 16 hours to form the perovskite phase in dense pellet form (pore density > 95 %). The as-prepared pellets were further processed via two routes either as pellet or powder. For the preparation of powder, the as-prepared pellets were crushed and ball-milled to produce a powder with a total specific surface area of ~0.5-1.5 $m^2 g^{-1}$ prior to any reduction process. For the preparation of pellet, the pellets were first polished on one side (top side) to enable uniform exsolution of metal particles on one side of the pellet only and to prevent the formation of terraces and/or edges surfaces which can supress the exsolution. Polishing was carried out with a Metaserv 2000 polisher. Initially, MetPrep P1200 polishing paper was used, followed by cloth polishing with MetPrep 6, 3 and 1 μm diamond paste, respectively. The samples were cleaned in between each steps with acetone in an ultrasonic bath.

Finally, in order to exsolve metal particles on the surface, the samples (pellet and powder) were reduced in a controlled atmosphere furnace, under continuous flow (20 ml min^{-1}) of 5 % H_2/Ar at different temperatures with heating and cooling rates of 5 °C min^{-1}, depending on the particle size required and type of exsolved metals [138]. For instance, the reducing conditions used for several pellet systems are as follows: 860 °C and 30 h for exsolved cobalt-nickel (CoNi) pellet system with 30 nm particles, 830 °C and 30 h for exsolved Ni pellet system with 30 nm particles and 550 °C and 30 h for exsolved CoNi pellet system with 10 nm particles.

Commercially purchased Pt/Al_2O_3 (pellet and powder form, 1 wt. % Pt loading) and nickel on alumina silica, Ni/Al_2O_3 SiO_2 (powder form, 60 wt. % Ni loading) from Alfa Aesar were used without any further processing. The characteristics of these reference powders are listed as follows:

Table 3-1 Reference catalyst powders used, the supplier and the corresponding catalytic experiments

Materials	Characteristics	Provider	Experiments involved
Pt/Al_2O_3	1 wt. % Pt loading	Alfa Aesar	CO oxidation NO oxidation
$Ni/Al_2O_2\ SiO_2$	60 wt. % Ni loading	Alfa Aesar	CO oxidation
Al_2O_3	99 wt. % γ-alumina	Sigma Aldrich	CO oxidation NO oxidation

3.2.2 Synthesis and catalytic testing of the exsolved metal systems

Figure 3-1 shows the flow chart of the synthesis and the catalytic testing involved for the exsolved base metal catalysts reported in this thesis. All catalyst samples (pellets and powders) were prepared by our collaborators, Dr. Dragos Naegu from St. Andrews University as explained in the previous subsection. Each sample will then undergo catalytic performance testing which includes the effect of temperature, also known as light-off and the effect of CO partial pressures. The activities were then compared to our reference systems, Pt/Al_2O_3 and $Ni/Al_2O_3\ SiO_2$ and the improvements were made based on their activity are discussed in the following chapter (Refer Chapter 4). All catalytic experiments were performed at Newcastle University.

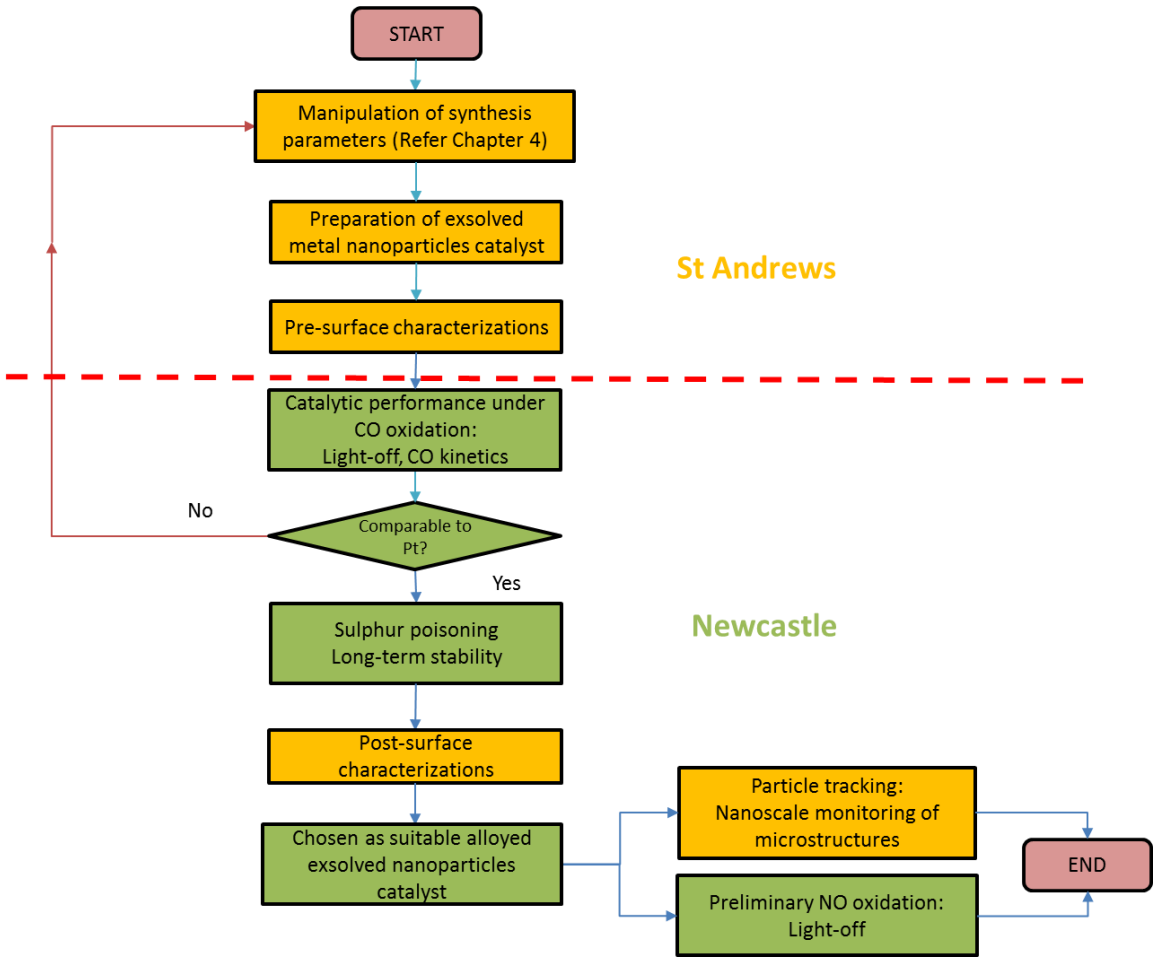

Figure 3-1 Flow chart of the synthesis and catalytic testing of the exsolved base-metal catalyst systems for CO and NO oxidation, and the work distribution between two universities; yellow for St Andrews and green for Newcastle University.

3.3 Materials characterisation

3.3.1 Scanning Electron Microscopy, SEM

A JEOL JSM-5600 scanning electron microscopy (SEM) system was used to analyse the microstructure of the samples. A SEM (**Figure 3-2**) is a machine which comprises of a source of electrons called the electron gun, a column which the electron beam travels through, a series of lenses to shape the electron beam, the sample chamber at the base and a series of pumps to keep the system under vacuum. This SEM utilises a high energy electron beam generated by an electron gun and processed by magnetic lenses to focus on the specimen surface and systematically scan across the surface of a specimen. As the beam interacts with the sample's surface, electrons lose energy due to the absorption and scattering by the sample which resulted in high energy and secondary electrons being produced (along with electromagnetic radiation). The secondary electrons generated by the ionisation caused by the primary electrons have energy less than 50 eV and the backscattered electrons which have energy greater than 50eV

were detected and converted into an image on the viewing screen. The backscattered electrons can also be used to detect areas of the sample with different chemical compositions i.e. high atomic number elements which appear brighter in the image produced.

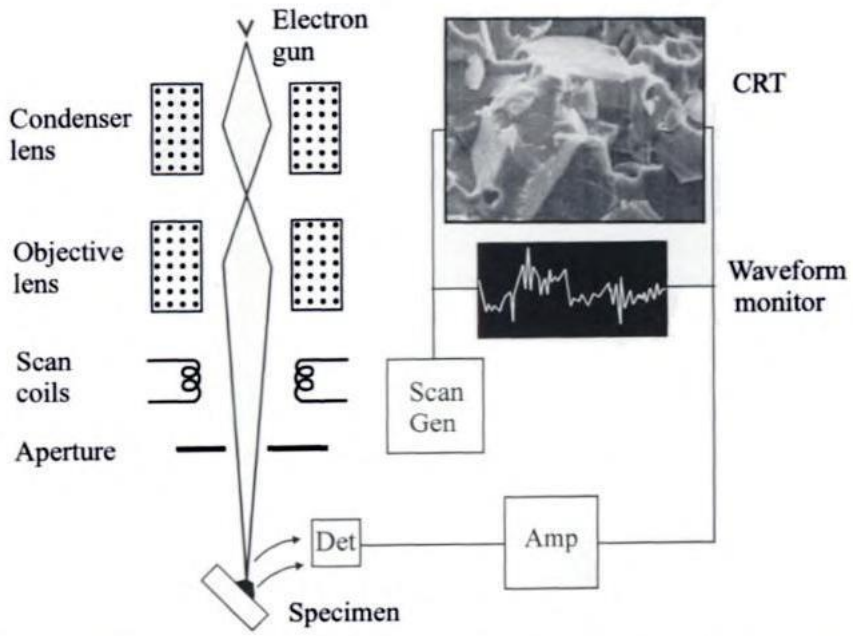

Figure 3-2 The general concept of how SEM works **[145]**

The scanning was conducted on all samples (pellet and powder) from all batches under high vacuum mode and at 1-15 kV without any pre-treatment to determine the surface morphology of this type of catalysts. The surface of the fresh and used samples from the best performed powders were analysed to quantify their particle sizes and its distribution on the samples to link it to their contribution towards catalytic activity. The changes in surface morphology on targeted area (also known as particle tracking) were also performed using pellet via SEM after each catalytic experiment in order to monitor the changes in potential active sites/planes towards its catalytic activity.

3.3.2 Helium Ion Microscopy, HIM

Helium Ion Microscopy, HIM is a new type of microscope that uses helium ions for surface imaging and analysis, but instead of electrons as in SEM, it uses a focused beam of helium ions. These helium ions can focus into smaller probe size and provide smaller interaction volume at the sample surface as compared to electrons, which then resulted in higher resolution images with better material contrast and improved depth of focus. The layout of the ion-optical column is quite similar to the ones in SEM (**Figure 3-3**). Two key technologies featured in this microscope are the ion source and the nature of the interaction between the beam and the

samples. A sharpened needle was held at high positive voltage and low temperature in helium gas. Field ionisation creates a very bright ion beam at the needle's tip, so that it has only three atoms (trimer) and when the electric field becomes intense enough, an electron was stripped from the gas atoms occupying the surface and emitted as ions. The ion beams were then transmitted through two electrostatic lens in ion-column onto the sample surface. An Everhardt-Thornley (ET) detector for secondary electron collection along with an electron flood gun, and an image signal was later accomplished. These secondary particle signals resulted from the interaction of the beam with the sample produced provide the image information that is novel in several aspects.

He-ion microscopy (HIM) was carried out at NEXUS, Newcastle University on a Zeiss ORION NanoFab instrument, using a 25 keV He^+ beam with 0.2 pA beam current. This instrument was used particularly to image CoNi-10nm pellet system due to its small particles which could not be seen under high resolution SEM.

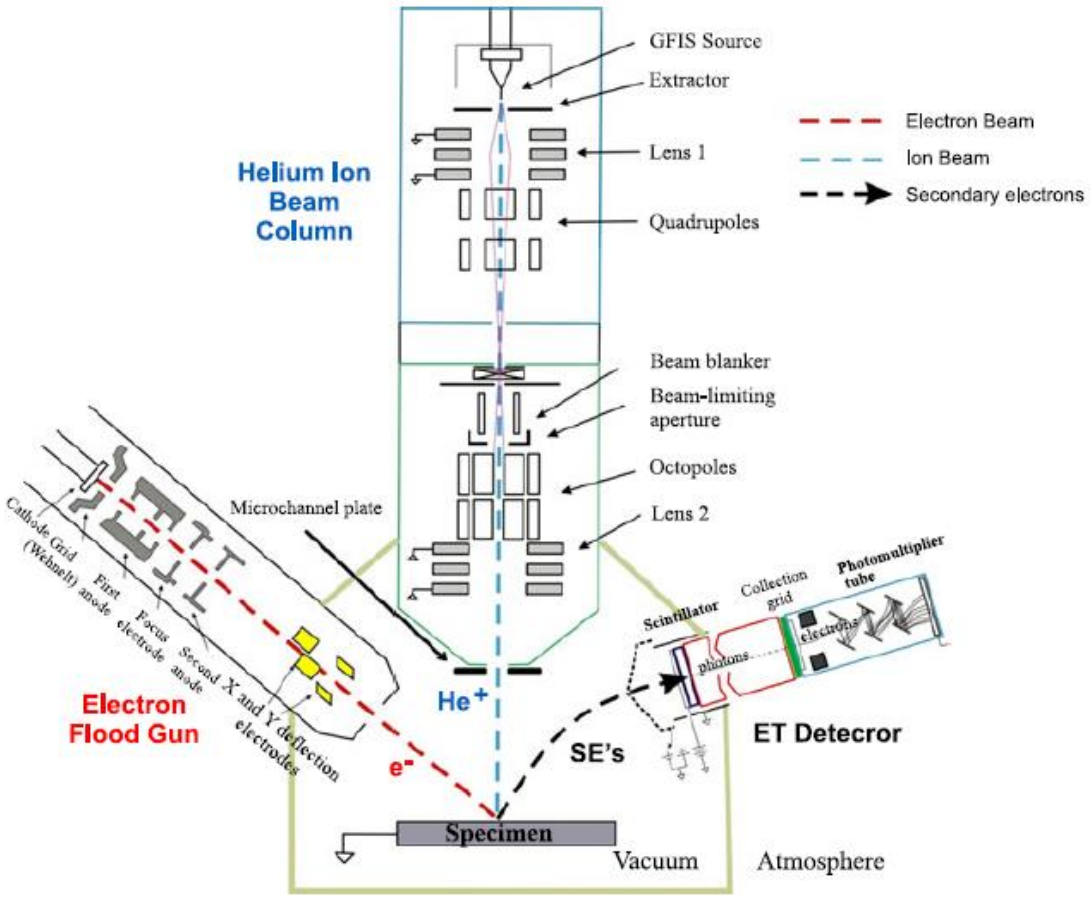

Figure 3-3 Layout of the ion-optical column in Helium Ion Microscope [146]

3.3.3 Specific Surface Area Measurement

The BET surface area was calculated and the total pore volume was determined by the estimation from the nitrogen uptake at P/ Po→1, where Po is the saturation vapour pressure of the adsorptive and P is the pressure of the vapour. In spite of the oversimplification of the model on which the theory is based on, this is the most widely used standard procedure for the determination of surface area of finely divided and porous material. The BET equation uses the information from the isotherm to determine the surface area of the sample, where X is the weight of N_2 adsorbed at a given relative pressure (P/ Po), X_m is the monolayer capacity, which is the volume of gas adsorbed at STP, where STP is defined as 273 K and 1 atm while C is the BET constant. This constant, C is related to the enthalpy of adsorption in the first adsorbed layer and gives information about the magnitude of adsorbent-adsorbate interaction energy [4].

$$\frac{1}{X[(P_o/P)-1]} = \frac{1}{X_m C} + \frac{C-1}{X_m C}\left(\frac{P}{P_o}\right) \qquad \text{Equation 3-1}$$

The total surface area of the catalyst powders was obtained from the adsorption-desorption isotherm of nitrogen at 77 K. An amount of 30-50 mg of pure catalyst was used each time. Prior to any measurement, the sample must be degassed to remove any moisture and other contaminants before the surface area can be accurately measured. The samples were degassed in vacuum at high temperature (< 300 °C) to shorten the degassing time prior to any analysis. Liquid nitrogen is used to cool the sample and maintain it at a constant temperature, preferably at low temperature to ensure measurable amount of adsorption can occur due to its weak interaction between the gas molecules and the surface of the samples. The BET surface area was calculated and the total pore volume was determined by estimation from the nitrogen uptake at P/ Po → 1. Adsorption isotherms are obtained by plotting the volume of nitrogen adsorbed (ccg^{-1} at STP) against the equilibrium relative pressure (P/ Po) where P is the actual gas pressure and Po is the vapour pressure of the adsorbing gas, N_2, at the temperature of which the test is conducted. The plots reveal greatly about the porous texture of the adsorbent catalyst simply from their shapes. The total surface area, S_t can then be calculated by using the calculated X_m (From Eq. 1) and the following equation;

$$S_t = \frac{X_m L_{av} A_m}{M_v} \qquad \text{Equation 3-2}$$

where L_{av} is the Avogadro's number, A_m is the cross sectional area of the adsorbate (0.162 nm^2 for an adsorbed nitrogen molecule, and M_v is the molar volume, where at STP equals to 22.4 L.

3.3.4 Carbon monoxide, CO chemisorption

Metal dispersion on supported metal catalysts is considered crucial in catalysis since it can affect the number of effective active sites or the contribution of metal particles located on the edge and corner towards the reaction activity. Metal dispersion is evaluated by measuring the chemisorption of H_2 and CO on the metal supported catalysts. The CO pulse measurement method is widely recognised as a straightforward measurement method for noble metal surface area determination. The active site is an adsorption point with the surface of the catalyst where the chemical adsorption first initiated, which includes the surface of metal nanoparticles and its neighbouring surface on their catalyst support in metal-supported catalyst. The total metal surface area is obtained from the adsorbed amount of CO and occupation area of an adsorbed amount of CO molecule. The dispersion ratio and average particle size of a noble metal can also be estimated from the total surface area. Metal dispersion ratio corresponded to the ratio of exposed metal atoms in the total amount of its loading while the metal particles is assumed to be cubic of similar size in order to estimate their sizes [147].

Analysis was performed to investigate the Pt metal surface area. The machine is designed to perform several experiments including pulse chemisorption, temperature programmed reduction and desorption. The Pt/ Al_2O_3 sample (50 mg) was suspended in between quartz wools in a straight wall quartz tube, which was later placed inside the furnace. The sample was exposed to a pre-treatment procedure before the CO pulse chemisorption is carried out. The pre-treatment procedure follows the steps illustrated in **Figure 3-4** below. After the pre-treatment, he sample was cooled down in He to room temperature to initiate the CO pulse injection. The CO gas was introduced by fixed pulse dosing and the quantity of unadsorbed CO was simultaneously measured by using the stoichiometric CO/ Pt ratio of 1. This step was repeated until the pulse area no longer changes, which indicates the saturation of CO adsorption on metal surfaces. The amount of adsorbed CO is calculated from the difference between the injected and saturated CO pulses. The total surface area was then calculated and will be used to plot the TOFs profile for all catalytic experiments.

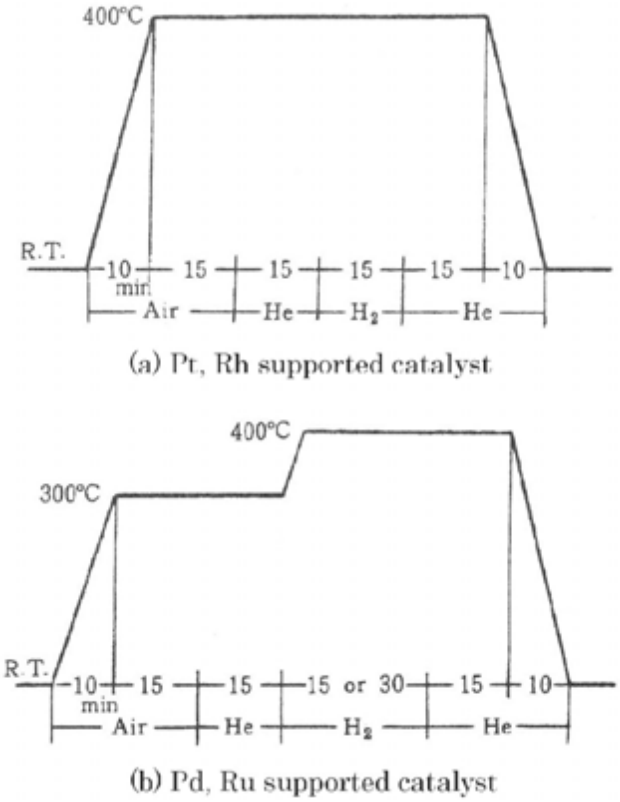

Figure 3-4 Pre-treatment pattern for selected metals supported catalyst **[148]**

3.3.5 Transmission Electron Microscopy, TEM

Transmission Electron Microscopy (TEM), which utilises energetic electrons is considered a vital characterisation tool for direct imaging of nanomaterials in order to obtain quantitative measures of particle and/or grain size, size distribution, and morphology. TEMs are usually used to probe the internal, ultra-structures of the tested samples since the electron beam can pass through the samples and they offer higher resolution images up to 10 nm. **Table 3-2** below listed the major similarities and differences between SEM and TEM as follows. TEMs normally consist of several components such as an electron source, thermionic gun, electron beam, electromagnetic lenses, vacuum chamber, condensers, a sample stage, and a phosphor screen, and it functions under similar basic principles as a light microscope, but uses electrons instead. Due to the smaller wavelength of electrons compared to light, it can reach optimal resolution of many orders magnitude higher than that of a light microscope. A beam of electrons is transmitted through an ultra-thin specimen, and the interaction between the electrons and the atoms is used to observe features such as the crystal structure and grain boundaries. As a result, a black and white image is formed, and is magnified and focused onto imaging device such as a phosphor screen or to be detected by a charge coupled device (CCD) camera. The darker areas of the image represent the areas of the sample in which fewer electrons are transmitted through

while the lighter areas of the image signify those areas of the sample where more electrons transmitted through.

Table 3-2 Similarities and the major differences between SEM and TEM

Similarities		
	SEM	TEM
Source of radiation	Electron	
Medium	High vacuum	
Differences		
	SEM	TEM
Type of samples investigations	Excellent for studying the surface morphology of samples	1. Investigations on ultrastructure of samples 2. Can provides details on the internal compositions of any suitable materials/ samples
Scanning area	Surface scans only	Electron beam pass through the samples
Type of electron	Scattered electrons	Transmitted electrons
Resolution	Comparatively low resolution of around 2 nm	High resolution up to around 10 nm
Field depth	High	Moderate
Specimen contrast	Electron adsorption	Electron scattering
Images	3-D black and white images	2-D black and white images

The exsolved catalyst was prepared for TEM using JEOL JIB-401 multi beam focused ion beam (FIB) SEM system (FEI Titan Themis). The nanoparticles and surfaces were preserved by the deposition of a protective carbon layer, before milling and thinning using gallium focused ion beam. Further electron diffraction characterisation was carried out on a JEOL JEM-2010 TEM. The preparation of the lamella for TEM by FIB is shown in **Figure 3-5**. A small fragment of a pellet was grounded with some silver paste (**Figure 3-5** (A) and (B)) prior to the deposition of carbon protective layer (**Figure 3-5**(C)) at the area of interest. A layer of Pt was then deposited to protect the top portion of the fragment and to mark the position of the target area. After cutting two trenches with ion beams, the final lamella which looks like the letter 'H' (**Figure 3-5**(F)) was then extracted, mounted on a Pt needle (**Figure 3-5**(G)) and transferred onto a TEM copper grid (**Figure 3-5** H)). Subsequently, the lamella was thinned and polished, and only then, the surface of the sample became apparent (**Figure 3-5**(I)) [149].

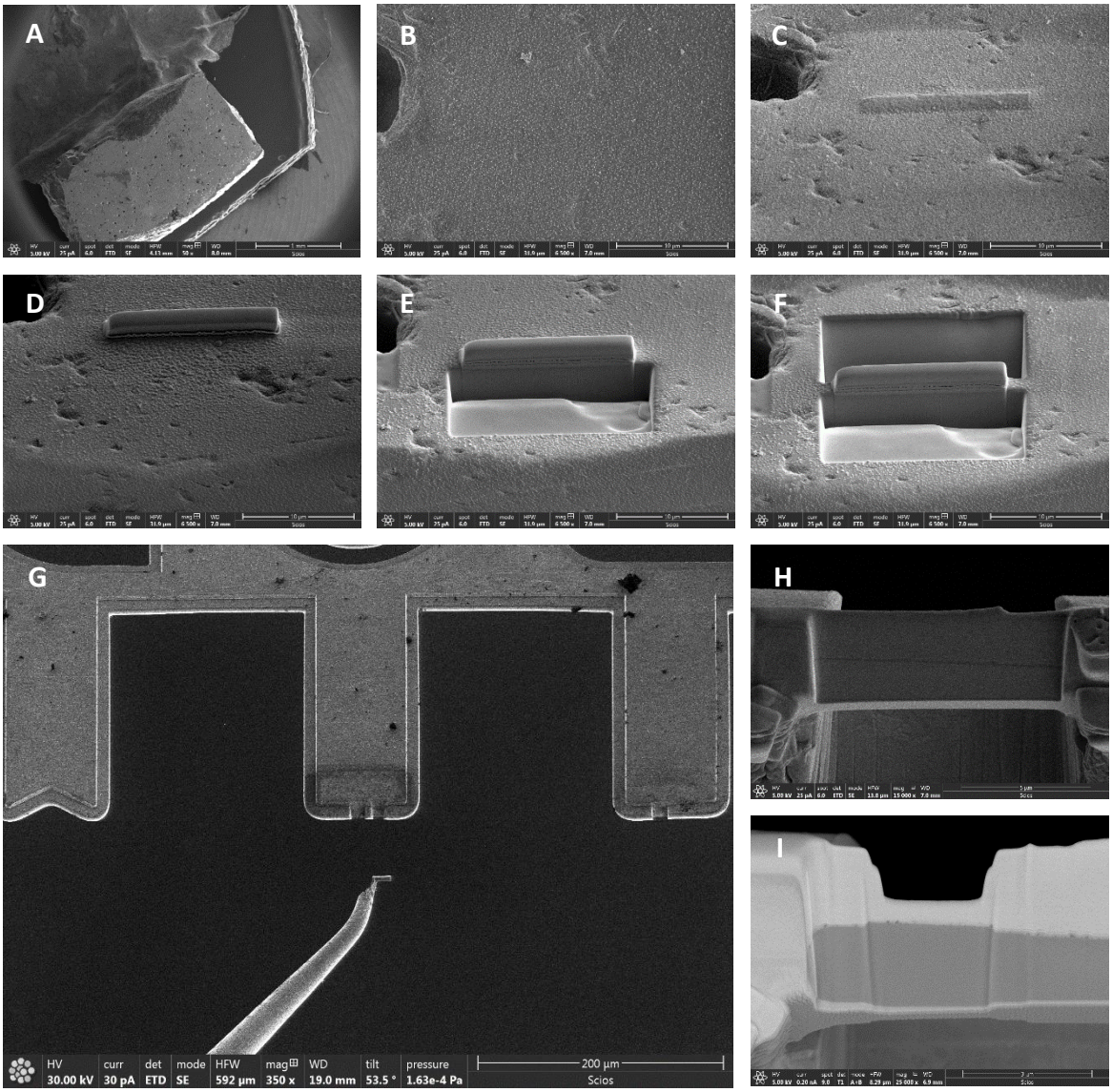

Figure 3-5 Preparation of a lamella for TEM by FIB as explained. (A) A small fragment from sample was grounded with some silver paste. (B) Detail from the surface of the sample shown in A. (C) A thin (< 100 nm), protective layer of carbon was deposited on the area of interest. (D) A layer of Pt (~1 µm) was then deposited. (E) and (F) trenches were formed on either sides of the area of interest with the help of the ion beam. (G) the lamella was then cut loose, mounted on a Pt needle and docked into a TEM copper grid. (H) the lamella as mounted on the TEM grid. (I) the lamella after thinning and polishing with the focused ion beam; the surface features in the sample become apparent.

3.3.6 X-ray photoelectron spectra, XPS

X-ray photoelectron, XPS is considered as one of the most important surface-sensitive analysis techniques in catalysis, which can provide information on the elemental compositions and the oxidation state of the surface elements. This photoelectron spectroscopy utilises photo-ionisation and analysis of the kinetic energy distribution of the emitted photoelectrons to study the composition and electronic state of the surface region of a sample. The basic requirement of this instrument includes a source of fixed-energy radiation (an x-ray source), an electron

energy analyser (which can disperse the emitted electrons according to their kinetic energy, and thereby measure the flux of emitted electrons of a particular energy) and a high vacuum environment (to enable the emitted photoelectrons to be analysed without interference from gas phase collisions). The sample surface was irradiated with x-rays and the emitted photo electrons are measured. When atom absorbs a photon of energy h_v, a core or valence electron with binding energy E_b is ejected with kinetic energy, E_k:

$$E_k = h_v - E_b - \varphi \qquad \text{Equation 3-3}$$

where, E_k is the kinetic energy of the photoelectron, h is Planck's constant, v is the frequency of the exciting radiation, E_b is the binding energy of the photoelectron with respect to the Fermi level of the sample and φ is the work function of the spectrometer.

Each element will give rise to a characterised set of binding energies peaks associated with each core of atomic orbital. The presence of peaks at particular binding energies indicates the presence of specific element, whereas the peak intensities represent the concentration of the element within the sample. Thus, this technique can provide both the qualitative and quantitative elemental analysis of the surface composition. Information about the oxidation states of the element can also be achieved in XPS by monitoring the shifts in binding energies. This chemical shifts are typically in the range of 0-3 eV, but the most commonly employed are the Mg-Kα (1253.6 eV) and the Al-Kα (1486.6 eV), which are produced from a standard X-ray tube and the peaks detected in XPS spectra corresponding to the bound core-level electron of the sample.

The oxidation states of the sample were performed using XPS (Thermo Scientific K-Alpha instrument), equipped with monochromatic Al X-ray source. The data were analysed using the CasaXPS software. Quantification was performed based on the area of peaks of interest (Ce 3p, La 3d 5/2, Ti 2p, Co 2p) after the subtraction of background of appropriate shape.

3.3.7 X-ray diffraction, XRD

X-Ray Diffraction, XRD is a non-destructive analytical technique which can yield the unique fingerprints of Bragg reflections associated with specific crystal structure. It has been used to identify bulk phases, monitor the kinetics of bulk formations and can also be used to estimate the particle size. In an XRD instrument, a continuous beam of X-rays, with wavelength ($\lambda \sim 0.5$ - 2 Å), is incident on the sample specimen and is then diffracted in certain directions by the crystalline phases in the specimen according to Bragg's Law, providing the conditions for constructive interference as follows:

$$\lambda = 2d\ sin\theta$$ Equation 3-4

where d is the lattice spacing between atomic of the crystalline phase and θ is the diffraction angle. The intensity of the diffracted X-rays is detected and measured as a function of the diffraction angle 2θ and the specimen's orientation. This diffraction pattern is used to identify the specimen's crystalline phases and to measure its structural properties, which are unique for every material. This instrument consists of five main components; the X-ray source, double crystal monochromator, sample holder, crystal analyser and a detecting system as displayed in the schematic in **Figure 3-6** below. XRD data can be used more effectively for quantitative analysis of the crystalline phases in a mixture and also for the determination of structural parameters as summarised in **Table 3-3** below.

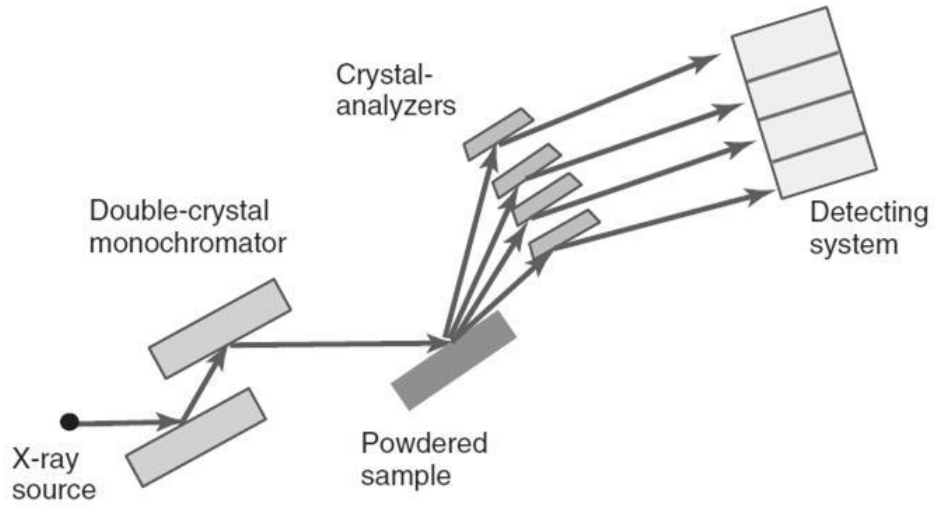

Figure 3-6 Schematic diagram of XRD

Table 3-3 Typical applications of XRD methods **[150]**

Determination of crystallographic parameters	Determination of physical/ morphological features
Unit cell dimensions and lattice symmetry Atomic coordinates and thermal parameters Isomorphous substitution in lattice sites Infra-lattice porosity (zeolites, microporous materials)	Crystallite size Crystallinity Lattice strain (stacking faults, dislocations, microtwinning) Preferred orientation of the crystallites (texture)

The phase purity and crystal structure of the prepared exsolved system were confirmed by room temperature X-ray diffraction (XRD), using a PANalytical Empyrean X-ray diffractometer

operated in reflection mode. Diffraction patterns were produced by employing CuKα radiation (λ= 0.154098 nm) at 40 kV and 40 mA generated by a diffraction X-ray tube on the samples that were mounted on samples holder, and the basal spacing was determined via powder technique. The samples were scanned at the range 2θ, starting from θ =10 – 80 °. The values of the lattice parameter, a, and the d-spacing were then calculated.

3.4 Catalytic experimental setup

3.4.1 Experimental rig

In this section, the standard reaction procedures are described. The reaction conditions especially in CO oxidation, were chosen based on our previous literature review (refer **Table 2-3)** on the reaction conditions of a three-way-catalyst (TWC) and were adhered to throughout the course of this thesis. The primary objective of this thesis is to test the catalytic performance of these materials and therefore, the reaction conditions were maintained for all types of experiments, including sulphur poisoning and long term stability unless stated otherwise. The oxidation reactions; CO and NO oxidation were conducted in a conventional continuous flow reactor, which is equipped with an online IR gas analyser (X-Stream, Emerson/Rosemount) with a minimum measured value of 1 ppm CO_2 to quantify the production of CO_2. Outlet gases were sampled directly after the reaction gases were exposed to the catalyst, before entering the gas analyser. The infrared (IR) analyser was employed to measure the concentration of CO_2 in the outlet gas streams, which utilised an IR technique. Every gas line is equipped with a mass-flow controller (MFC) and a shut-off valve. The inlet gases line is equipped with a carbonyl remover (pre-reactor), consisting of a quartz tube with inert Al_2O_3, heated at 90 °C in order to remove possible carbonyl (i.e. rust or iron carbonyls) from the gas cylinders which decompose at around 40-70 °C [151]. Following the pre-reactor, the gases were equipped with a pre-heating zone to provide faster heating of the gases upon entering the main reactor for reaction. A general schematic of the experimental rig is shown in **Figure 3-7** below. Helium (He) was used as a balance gas throughout the experiments.

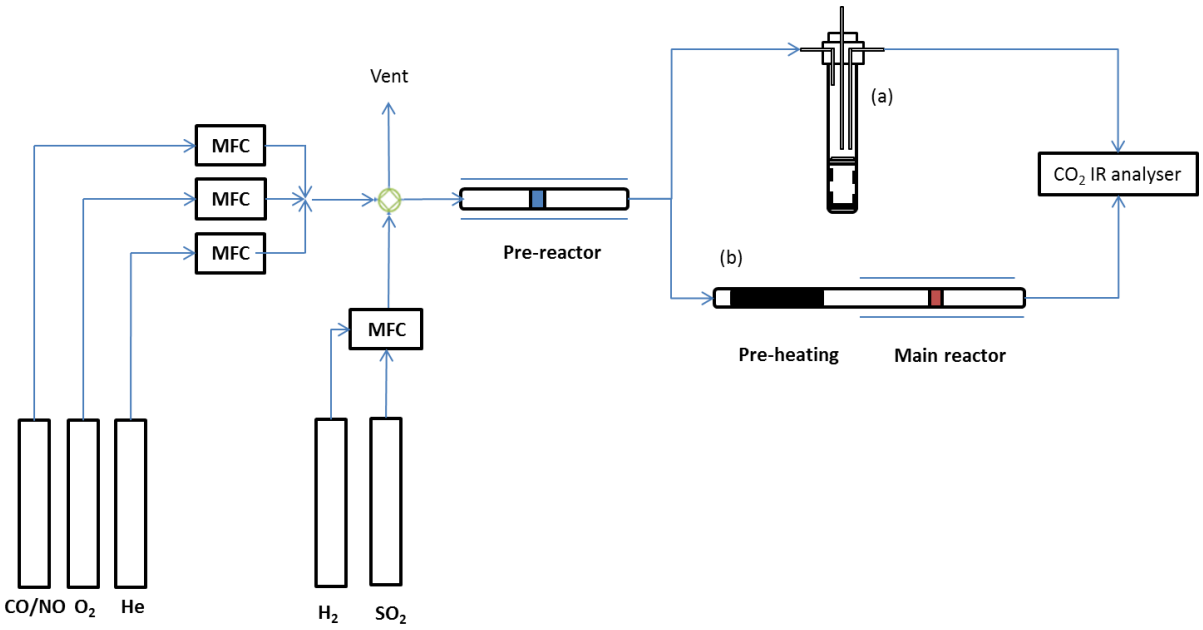

Figure 3-7 Experimental setup for catalytic experiments with either (A) pellet or (B) powder catalysts

3.4.2 Experimental reactors

Two types of reactors were used throughout this research; a continuous flow single chamber reactor (pellet) for preliminary and particle tracking experiments, and a fixed-packed bed reactor for catalytic experiments with powders (**Figure 3-8(B)**). Preliminary experiments were performed in a single chamber reactor with a pellet holder to place the pellet exactly in the middle of the furnace. The schematic diagrams of the reactors are shown in **Figure 3-8(A)**. The exsolved metal nanoparticle pellets were tested in this reactor to check for any measureable catalytic activity. A pellet was placed on top of the pellet holder and the different parts of the reactor were connected using ultra-high-vacuum compression fittings in order to minimise leaks from the atmosphere. A K-type thermocouple was placed in proximity to the pellet surface, of around 0.5 cm to measure the temperature of the sample. Flow rates of 150 ml min^{-1} were used (flow rates are given at normal temperature and pressure (NTP)) and the outlet flowrates were also measured using a Varian digital flow meter (1000 series). Temperature profile and flow rates tests were performed to confirm the isothermal region and the uniformity of temperature and composition inside the reactor within the isothermal region at several flow rates. For pellet reactor, we have found that the distance for the first contact between the feed gases and the pellet should not be more than 0.6 cm, hence, 0.5 cm was chosen. Also, a total flow rates of 150 ml min^{-1} was chosen as it shows the lowest experimental error of around ±1 % in reaching steady state condition

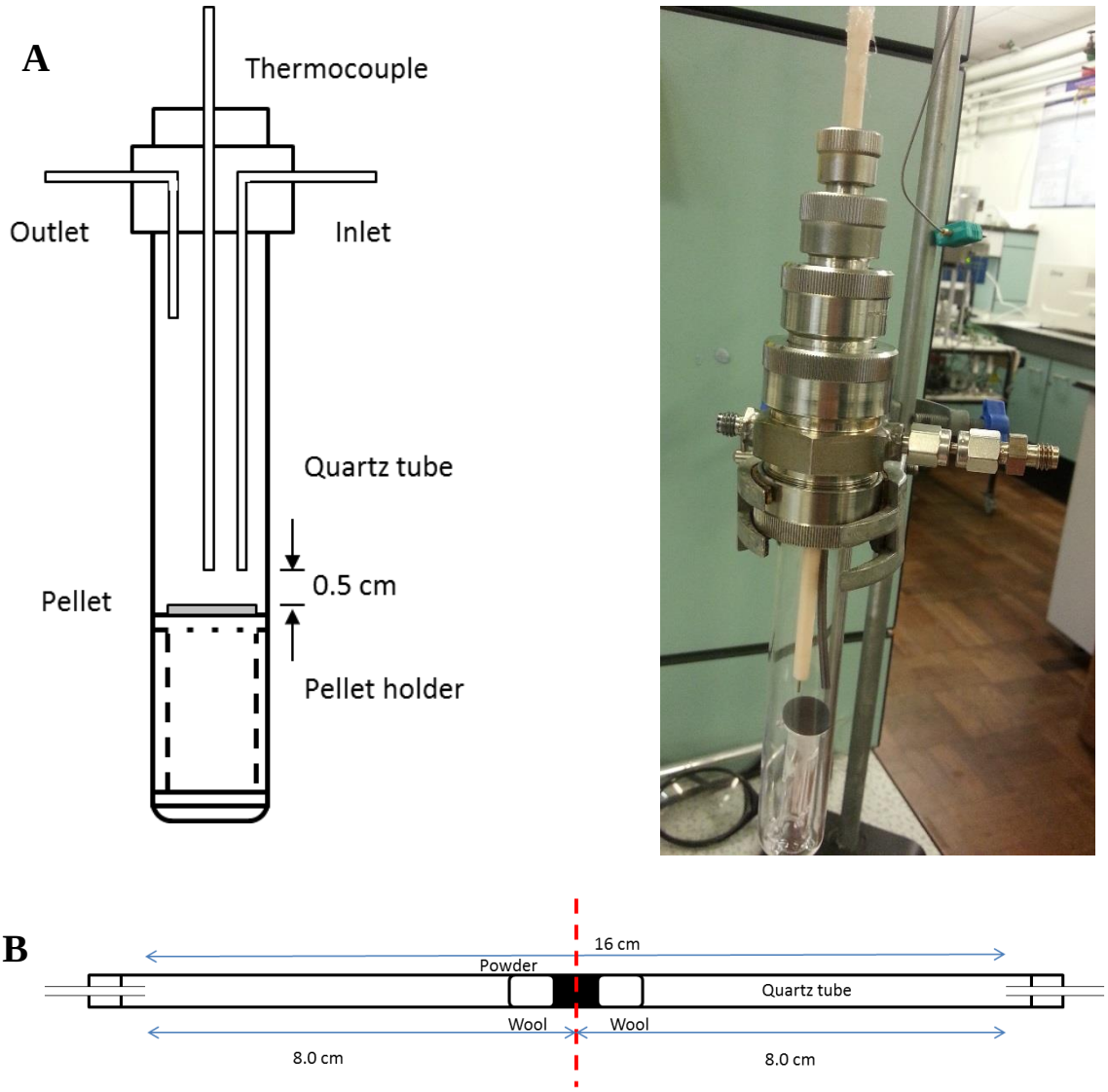

Figure 3-8 Schematic diagrams of the single chamber catalytic reactor; both for (A) pellet and (B) powder reactors

On the other hand, the powder reactor itself consists of a quartz reactor tube, with an inner diameter of 7 mm and was held inside a furnace for a maximum temperature of 520 °C which offered an isothermal zone of about 5 cm. The heating tape and insulation were wrapped around the reactor outside the furnace to ensure minimal heat losses and for fast heating of the gases to the required reaction temperature. Volumetric dilution was made within the catalyst bed by mixing the catalyst powder with alumina powder (10 wt. % of each catalyst was diluted with Al_2O_3 to obtain a total weight of 100 mg). The mixture was then placed inside the centre of the quartz reactor tube, supported by two equal amounts of quartz wool above and below the catalyst. Total flow rates of 450 ml min^{-1} are used (flow rates are given at normal temperature and pressure (NTP)) and the outlet flowrates were also measured using a Varian digital flow meter (1000 series). Flow rate tests were performed to confirm the uniformity of temperature

and composition inside the reactor at several flow rates and a total flow rates of 450 ml min^{-1} was chosen as it shows the lowest experimental error of around ±2 % in reaching steady state condition. **Figure 3-9** shows the temperature profile and its distance from the reactor inlet where the inlet gases were introduced into the reactor. The red region highlighted in the graph shows the isothermal region and the first point of contact of the feed gases from the inlet in the reactor will be made within the isothermal region of the furnace which is in between 7.5 to 8.5 cm from the inlet of the furnace.

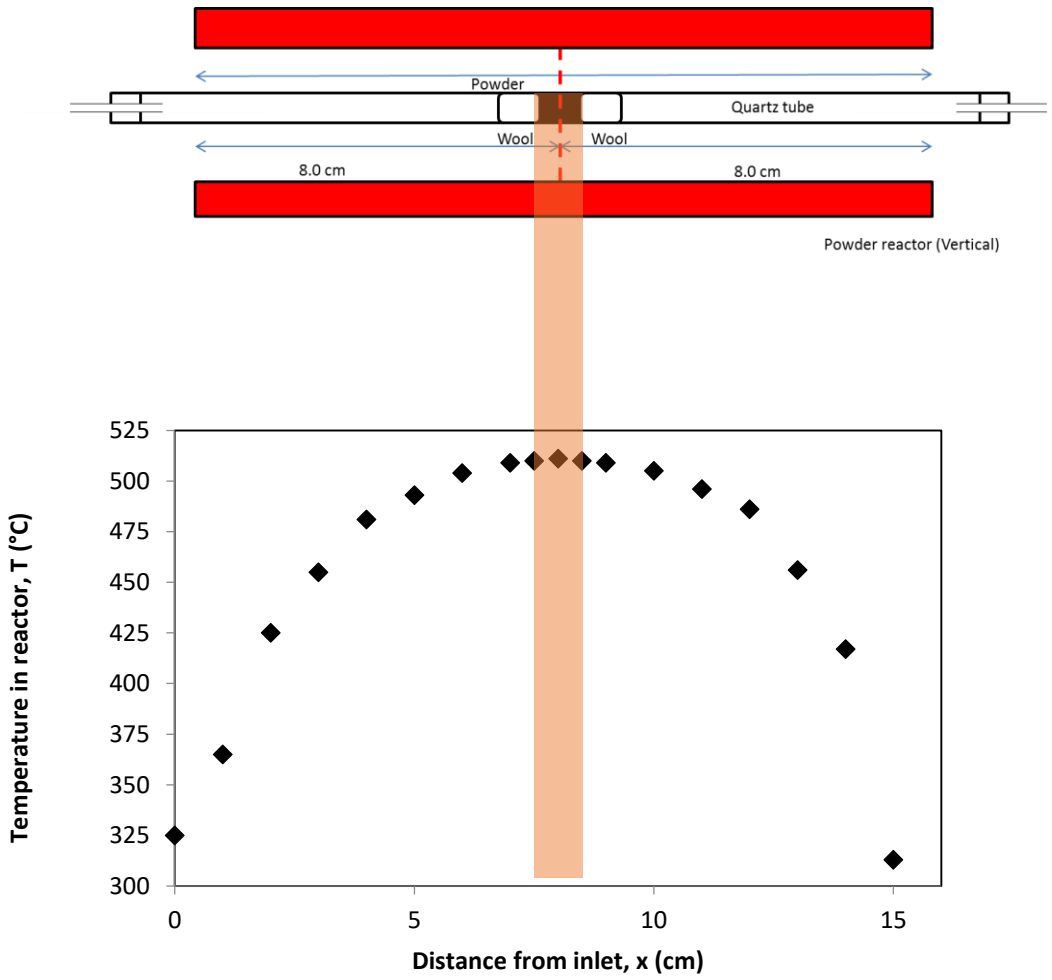

Figure 3-9 Temperature profile of the furnace showing isothermal region and how the powder is positioned in the reactor tube and furnace according to the temperature profile

3.4.3 Gas analysis

An infrared (IR) analyser by Emerson (Xstream, Rosemount) was used to analyse the composition of outlet gases from the catalytic reactor. This analyser measures the trace gases by determining the absorption of an emitted infrared light source through a certain air sample. Each substance has its unique infrared spectrum which makes the detection and analysis by this analyser very accurate in chemical and industrial applications. The entire device consists of two

parallel chambers; one sample chamber for measuring the wavelengths of the sample gas and the second reference chamber is used as a reference for comparison purposes, an infrared source (lamp) and an optical filter. The reference chamber is filled with a non-absorbing gas (non-polar gases) such as nitrogen, N_2 while the sample chamber contains the gas sample that needs to be analysed. In a simple IR instrument (**Figure 3-10**), the IR energy passes through the two identical tubes, placed in parallel chambers with each other before it hits the detector. The first chamber is the reference cell and is filled with non-absorbing gas such as N_2 and the second chamber is the measurement cell which contains the gas sample to be analysed. In this case, the gas samples are CO_2 and NO_2 in their respective IR analysers.

Continuous IR waves were sent from an IR source through the gas chambers and the detector will then measure the intensity of the two different wavelengths; one at the sample gas absorption wavelength and the other is at the reference gas absorption wavelength. The detector receives 100 % signal in the reference chamber since it contains N_2 while the optical filter in front of the detector will eliminate all lights except for the wavelength that the selected gas, i.e. CO_2 can adsorb. The signals will be measured by the detector by deriving the difference between these two signals which is proportional to the amount of the adsorbed gas in the sample chamber. Only then, the gas concentration of the sample gas is measured in unit of parts per million (ppm).

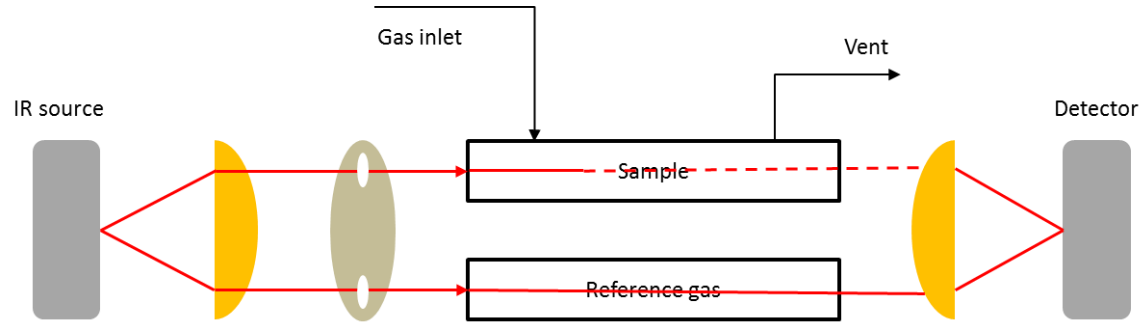

Figure 3-10 Schematic of typical infrared analyser in operation

3.5 Catalytic experimental operation

The section below presents the catalytic experiments involved in this dissertation. The catalytic experiments can be divided to two different reactions: CO and NO oxidation, the former being the core reaction of this thesis. For these reactions, the feed streams involved the use of seven different gas cylinders, provided by BOC Ltd. **Table 3-4** listed the gases; gas contents, providers and experimental usage, employed throughout the thesis. The experiments listed in

the table summarised the catalytic experiments involved and will be elaborated in the following sections.

Table 3-4 Gases used, the supplier and the corresponding experiments

Reaction gases	Provider	Experiments involved
20% CO/ He (95 % certification)	BOC	CO chemisorption CO oxidation: Light off CO kinetic experiments Sulphur poisoning Long-term/ stability
20% O_2/ He (95 % certification)	BOC	CO oxidation: Light off CO kinetic experiments Sulphur poisoning Long-term/ stability NO oxidation: Preliminary light-off
1% NO/ He (98 % certification)	BOC	NO oxidation: Preliminary light-off
Zero grade He (N5)	BOC	CO chemisorption CO oxidation: Light off CO kinetic experiments Sulphur poisoning Long-term/ stability NO oxidation: Preliminary light-off
50 ppm SO_2/ Ar (99.5 % certification)	BOC	Sulphur poisoning
1000 ppm CO_2/ He (98 % certification)	BOC	IR analyser calibration gases
1000 ppm NO_2/ He (98 % certification)	BOC	IR analyser calibration gases

3.5.1 Catalytic activity testing

To commence the catalytic testing of these exsolved base metal systems under CO oxidation, blank experiments in the absence of catalyst (quartz tube only) and with Al_2O_3 powder only were performed prior to any catalytic experiments (pellet and powders) in order to eliminate any possible contribution from the presence of oxides or particulates towards catalyst activity and zero conversion at every temperature were reported. Preliminary screening experiments were performed on two previously formulated exsolved systems; lanthanum-doped strontium titanates ($La_{0.5}Sr_{0.4}Fe_{0.1}Ni_{0.1}Ti_{0.6}O_3$) and lanthanum-doped ceria titanates

($La_{0.7}Ce_{0.4}Ni_{0.4}Ti_{0.6}O_3$), having Ni and FeNi as the exsolved metals, respectively. Several preliminary catalytic experiments were performed with these exsolved pellet systems in order to screen their potential under CO oxidation. These experiments were conducted under constant P_{CO} = 0.5 kPa and at three different P_{O2} (0.25, 1.33 and 3 kPa) while the temperature increases from room temperature to 460 °C. Three P_{O2} were chosen in order to investigate the preliminary nature of these base metal catalysts under stoichiometric and oxidising conditions. Hysteresis was also explored and found to be lower than ±10 % between each measured values for all experiments. The stability of these pellet systems was also tested under continuous stoichiometric CO oxidation (P_{CO}=0.5 kPa, P_{O2}=1.0 kPa, T=523 °C) for 165 hours and the results were compared to that of a 1 wt.% Pt loading commercial Pt/ Al_2O_3 pellet. All experiments were repeated at least twice for reproducibility purposes.

For practical applicability, these exsolved metal systems were further prepared in powder form in order to evaluate and compare their activity on a weight-to-weight basis to commercial Pt/ Al_2O_3 powder catalyst. The activity of these catalysts as a function of temperature, reactants concentrations (like CO) and its stability against time and poisons such as sulphur are considered critical towards their performance. Volumetric dilution within catalyst bed is made by mixing the catalyst powder with Al_2O_3 powder (10 wt. % of each catalyst is diluted with Al_2O_3 to get a total weight of 100 mg) since it was found that this amount of catalyst sample mixed with Al_2O_3 resulted in a reasonable pressure drop within the bed in the range of proven by the pressure testing performed using pressure transducers preceding any catalytic experiments.

The activity of a catalyst as a function of temperature (henceforth, referred as light-off) is a critical feature of its performance and this experiment was performed to assess their potential catalytic activities under CO oxidation. The reaction condition for these light-off experiments is chosen based on our previous literature survey performed on the conditions that a Pt catalyst would face in exhaust converter (refer Chapter 2) and a slightly oxidised condition was chosen, with P_{O2}=1.0 kPa and P_{CO}=0.6 kPa (CO/O_2=0.6). In order to study the effect of temperature, the exsolved metal systems were heated in an inlet feed streams (Pco=0.6 kPa, P_{O2}=1.0 kPa) from room temperature up to 520 °C, where the temperature was held constant after each temperature step of 20 °C, to obtain stable reaction rates measurement, i.e. the rates did not vary more than ± 5 % over 60 min. These reaction conditions were chosen based on our previous literature survey (refer **Table 2-3**), as to mimic the reaction conditions in both petrol and diesel engines. Hence, a slightly oxidised CO oxidation and a temperature of 520 °C were chosen as

the base conditions in this research. Plots of the outlet concentrations (in terms of CO_2 production rates, CO conversion and/ or TOFs) versus reaction temperature are produced from this light-off experiment.

The nature of the catalysts under CO-rich atmospheres and upon sulphur poisoning in comparison to the activities of a state-of-the-art Pt/ Al_2O_3 catalyst powder were also evaluated. These experiments were adopted to monitor their stability against poisons like CO and sulphur since these poisons can be detrimental towards the activity of Pt (i.e. CO) and base metals, also since sulphur is present in the exhaust converter, even though only at a trace amount. Concerning the effect of CO concentrations, CO_2 production rates were observed under increasing CO partial pressure, P_{CO} while keeping the O_2 partial pressure, P_{O2} constant at 0.64 kPa. These experiments were conducted while increasing the P_{CO} from 0.5 up to 18.8 kPa. Sulphur poisoning experiments were also performed under CO oxidation to establish its robustness against sulphur. 50 ppm of sulphur dioxide (SO_2) were added to the inlet feed streams (P_{CO} = 0.6 kPa, P_{O2} = 1.0 kPa) at three time intervals (15, 30 and 60 minutes) and the CO_2 production rates recovery following the poisoning were monitored. 50 ppm of SO_2 was used, which reflects the amount of SO_2 concentration present in exhaust converter, both for petrol (10-60 ppm) and diesel engine (10-100 ppm). The initial CO_2 production rates were first measured prior to poisoning and these experiments were carried out at several temperatures; the operating temperatures of said application; 520 °C for TWC and the temperatures at which the reactor was operated under differential conditions (20 % conversion of CO or less) for kinetic evaluations since at high conversions and high temperatures, the reaction was limited by the mass transfer (temperatures, pressures and concentrations are not uniform through the bed).

A major limitation that has been widely documented in developing base metal catalysts that can rival Pt is mostly due to their low tolerance under sintering, particularly in continuous long-term operation, which then raised the need to probe the stability of these systems. The stability of these catalysts was then tested under continuous CO oxidation (P_{CO} = 0.6 kPa, P_{O2} = 1.0 kPa) for one month (~655 hours) and the results were compared to that of state-of-the-art Pt/Al_2O_3 catalysts. In order to be able to measure the rate of CO_2 production during the long-term experiment, the reactor was operated under differential conditions (20 % conversion of CO or less was used) accordingly.

3.5.2 Carbon monoxide, CO oxidation

Catalyst testing was performed under slightly oxidising CO to O_2 ratios and a stoichiometric reaction of CO oxidation is shown as follows:

$$CO + \frac{1}{2}O_2 \rightarrow CO_2 \qquad \text{Equation 3-5}$$

Prior to any catalytic experiment, a blank experiment was performed to ensure that there were no oxides or particulates which can affect the results produced. The IR analyser was also calibrated once every two weeks by using 0.5 and 1 % of CO_2 / He calibration gas to ensure the accuracy of the measured values. The percentage of the tolerance limit of the calibration of IR analyser were reported to be around ± 0.05 % during each calibration test and these tests were performed for three hours to ensure the stability of the results measured over time. The reaction rates in terms of CO_2 production are normalised to the pellet area decorated with exsolved particles, r_{CO_2}, for all pellet samples and calculated as shown in the equation below;

$$r_{CO_2}(mol\ (CO_2)\ s^{-1}\ m^{-2}) = y_{CO_2} \times \dot{n}\ \times {A_{pe}}^{-1} \qquad \text{Equation 3-6}$$

where y_{CO_2} is the CO_2 concentrations (in ppm) measured by the IR analyser at the gas outlet, ṅ is the total molar flow rate of the reaction and A_{pe} represents the pellet area decorated with exsolved particless.

The rates of CO_2 production were also expressed in terms of turnover frequencies (TOFs), which were defined as the number of CO_2 molecules produced per active site per second. The exposed geometrical projected particle area, A is the total surface metal area on the catalyst which is exposed to the gas phase and available for reaction. The exposed particle area in one pellet is obtained by multiplying the pellet area, decorated with exsolved particles (A_{pe}) with the exposed particle per unit surface (A_p), $A_{pe} \times A_p$. A_p was calculated from the SEM micrograph analysis and the corresponding number of active sites will be given by $(A_{pe} \times A_p)/(a^2 \times k)$, where a is the unit cell parameter of the crystal lattice of the particles and k is the average number of metal active sites per unit cell, a. The faces were considered to be in a (100) termination. For the NiO rock-salt structure, k = 1, for mixed $(FeNi)_3O_4$ and the $(CoNi)_3O_4$ spinel structure, k = 2.

Therefore, by assuming that the active sites are the metal ions located at the outer surface of the particles and there is one active site per surface metal atom, the TOFs for CO_2 production were calculated as follows:

$$TOF(s^{-1}) = \left(N_A \times r_{CO_2} \times a^2\right)/\left(A_{pe} \times A_p \times k\right) \qquad \text{Equation 3-7}$$

where N_A is the Avogadro number (mol^{-1})

The reaction rates, $r^*_{CO_2}$, in terms of CO_2 production for the powders were calculated as follows:

$$r^*_{CO_2}(mol\ (CO_2)\ s^{-1}\ g^{-1}) = \frac{y_{CO_2} \times \dot{n}}{w_p} \quad \text{Equation 3-8}$$

where y_{CO_2} is the CO_2 concentrations (in ppm) measured by the IR analyser at the gas outlet, $\dot{n}$ is total molar flow rate of the reaction and w_p is the weight of the active catalysts (w_p = 10 mg). For the determination of kinetic parameters, the reactor needs to be maintained under differential reactor conditions (i.e. isothermal conditions and the percentage of the conversion needs to be kept low) and due to limitations such as mass transfer limitation at high temperature where the percent of conversion is high, the kinetic evaluations were performed with results attained at less than 20 % conversion [152]. This is because the reactor was considered to operate under the integral conditions at higher conversions, in which the reactor conditions (temperature, pressure) are changing across the reactor. These rates are the average rates since the compositions of the reaction mixtures vary along the catalyst bed, although the nominal temperature of the bed and the feed streams composition are known.

3.5.3 Nitric oxides, NOx oxidation

NO_x oxidation is chosen due to its rising importance in tackling NO_x emission from lean diesel engine as mentioned previously in the literature review, which consumed almost one third of the use of Pt as automotive catalyst to operate the SCR and LNT processes. The main aim of this investigation is to explore the feasibility of these exsolved metal systems as an alternative catalyst in NO oxidation. To date, different authors have measured the activity of their prepared catalysts under highly oxidised NO oxidation using a variety of reaction conditions, e.g. different NO and O_2 concentrations though they are still under the reported range for diesel engine as previously stated in the literature survey. The catalytic testing was performed under highly oxidising condition and a stoichiometric reaction of NO oxidation is as follows:

$$NO + \frac{1}{2}O_2 \leftrightarrow NO_2 \quad \text{Equation 3-9}$$

An NO-NO_2 analyser (XTREAM-NO_x X2GP, Rosemount) was used to measure the production of NO_2 and the analyser was also calibrated every once a month by using 1 % of NO_2/ He calibration gas to ensure the accuracy of the measured values. The minimum detectable NO and NO_2 mole fraction for the XTREAM-NO_x analyser were 1 ppm. The absolute reaction rates

(r_{NO_2}) in terms of NO_2 production for all pellet and powder exsolved systems were calculated as shown below;

For pellet systems,

$$r_{NO_2}(mol\ (NO_2)\ s^{-1}\ m^{-2}) = y_{NO_2} \times \dot{n}\ \times {A_{pe}}^{-1} \qquad \text{Equation 3-10}$$

where y_{NO_2} is the measured NO_2 concentrations (in ppm) at the gas outlet, ṅ is total molar flow rate of the reaction and A_{pe} represents the pellet area decorated with exsolved metals. Following similar active sites assumptions as the ones discussed for CO oxidation (subsection **3.5.2**), the TOFs for NO_2 production were calculated as follows:

$$TOF(s^{-1}) = \left(N_A \times r_{NO_2} \times a^2\right)/\left(A_{pe} \times A_p \times k\right) \qquad \text{Equation 3-11}$$

where N_A is the Avogadro number (mol^{-1})

For powder systems,

$$r^*_{NO_2}(mol\ (NO_2)\ s^{-1}\ g^{-1}) = \frac{y_{NO_2} \times \dot{n}}{w_p} \qquad \text{Equation 3-12}$$

where y_{NO_2} is the measured NO_2 concentrations (in ppm) at the gas outlet and ṅ is the molar flow.

Preliminary temperature effect experiments under NO oxidation were performed under highly oxidised condition (P_{NO} = 0.04 kPa, P_{O2} = 8.0 kPa) and by increasing the temperature, steady state measurements of NO_2 production were recorded. These reaction conditions were adopted from the recent work by Kim et al., which demonstrated lanthanum strontium-doped perovskite type catalysts that can rival Pt under highly oxidised NO oxidation and since they have fairly similar perovskites formulation to ours, but with different preparation method; i.e. citrate method, the reaction condition used in that report was adopted to conduct and compare our groundwork study to theirs [14]. The temperatures were increased from 100 °C up to 440 °C where the temperature was held constant after each steps of 20 °C, to get stable reaction rates measurement, i.e. the NO_2 production rates (r_{NO_2} *or* $r^*_{NO_2}$), did not vary more than ± 5 % over 60 to 180 min. These experiments were carried out for the best performed powders only in order to measure any possible catalytic activity under this reaction. The equilibrium line was calculated (refer Appendices, section **A-1.4**) and plotted to better understand the performance of the powders.

4 CHAPTER 4: EXSOLVED METAL SYSTEMS AS CO OXIDATION CATALYST

4.1 Introduction

This chapter of the thesis summarises the progress of finding the active exsolved base metal catalyst systems for CO oxidation. This research was initiated by assessing the potential catalytic activities, expressed in terms of CO_2 production rates, r_{CO_2}, and turnover frequencies (TOFs) under CO oxidation over previously reported A-site deficient exsolved metal systems for fuel cells and hydrocarbon (HC) oxidation. These exsolved metal systems contained nickel (Ni) and iron-nickel (FeNi) as the exsolved metals [23, 153]. These exsolved metal systems have also demonstrated remarkable tolerance against coking, which is attributed to their socketed properties. Since no attempt has been made by other researchers to investigate their activity and stability for CO and/or NO oxidation, this chapter aims to summarise our research progress in identifying the active exsolved metal powder system, in which their activities, expressed in terms of CO_2 production rates per weight of active catalyst, $r^*_{CO_2}$, and CO conversions were first assessed in a typical temperature-effect experiment under CO oxidation. Powder exsolved metal systems were used for practical applicability and their CO_2 production rates, $r^*_{CO_2}$, and CO conversions were compared on a weight-to-weight basis to accommodate the requirement for industrial sectors to those of the state-of-the-art Pt on alumina (Pt/ Al_2O_3) and/or commercial supported Ni catalysts. Their activities in the CO-rich atmospheres and upon sulphur poisoning were also assessed.

4.2 Exsolved metal system as CO oxidation catalyst

Since the initial objective of this chapter was to determine the capability of these A-site deficient exsolved metal systems to catalyse CO oxidation, this research, which involves the catalytic testing of exsolved metal catalyst systems was initiated by testing two previously formulated A-site deficient exsolved metal pellet systems, consisted of lanthanum-doped strontium titanates and lanthanum-doped ceria titanates ($La_{0.5}Sr_{0.4}Fe_{0.1}Ni_{0.1}Ti_{0.8}O_3$ and $La_{0.8}Ce_{0.1}Ni_{0.4}Ti_{0.6}O_3$) as the initial activity assessment [153]. This is because they have proven to be active in the steam reforming reaction and in new technology such as fuel cells [2]. CO oxidation was chosen as the key reaction in this thesis not only because it is one of the reactions used in the exhaust converter, but also because CO oxidation has been used as a model reaction for assessing catalytic activities of a newly developed catalysts since it can provide preliminary knowledge into more complicated reactions such as water gas shift (WGS) or steam reforming

[154]. The benefit of using these lanthanum-doped strontium titanates perovskites formulations is that they have previously revealed to have favourable chemical, redox and thermal stability. However, due to the nature of strontium (Sr) which favours the formation of the detrimental Ruddlesden–Popper phases [143] towards particle nucleation, a representative sample with ceria (Ce) substitution was also employed to exsolve Ni. Even though Ni and Fe are known as common catalysts in hydrogenation [155], they were chosen as the starting exsolved metals in this preliminary investigation because both metals have been reported to produce significant, but a rather lower activity than that of Pt under CO oxidation, owing to their excellent redox ability. With regards to cobalt (Co), Ni and Fe were chosen as the starting metals because they were much cheaper than Co, even though Co is known to be more active under CO oxidation than the two metals. Nonetheless, systems with Co exsolution are also be included in this chapter and will be further experimented in the following chapter as well. All A-site deficient exsolved metal systems were prepared by our colleague, Dr Dragos Naegu from Prof John T.S. Irvine's research group in St Andrews University. All catalytic experiments were performed at Newcastle University.

4.2.1 Preliminary screening of pellet systems

To first screen the potential activity, in terms of CO_2 production rates, r_{CO_2}, and TOFs, two A-site deficient exsolved metal systems, consisting of lanthanum-doped ceria titanates to exsolve Ni metal ($La_{0.8}Ce_{0.1}Ni_{0.4}Ti_{0.8}O_3$) and lanthanum-doped strontium titanates to exsolve FeNi alloy ($La_{0.5}Sr_{0.4}Fe_{0.1}Ni_{0.1}Ti_{0.6}O_3$) were prepared in the pellet form. The pellet systems were first prepared since they are generally easier to characterise on a microscopic level, for instance, via SEM. The metal particles were only exsolved on one side of the pellet; i.e. top side. These two pellet systems were labelled and henceforth referred to, according to their respective exsolved metal particle composition and the nature of this study; e.g. "Ni-s" and "FeNi-s" for exsolved Ni or FeNi pellet systems used in this screening experiment (s for screening).

The temperature-effect experiment was then performed under CO oxidation over both Ni-s and FeNi-s pellet systems, and for easier future referral, these temperature-effect experiments will be referred to as light-off. This light-off involved a total flowrate, F_t, of 150 ml min^{-1} given at normal temperatures and pressures (NTP) with inlet feed gas mixtures of constant CO partial pressures (P_{CO}) of 0.5 kPa. Three different O_2 partial pressures (P_{O2}) of 0.25, 1.33 and 3.0 kPa were used and the temperature was increased from room temperature to 520 °C. For this light-off, the temperature was held constant during heat-up at each step of 20 °C and the steady states rates measurement was recorded, in which the rates did not vary more than ± 5 % over 60 to

180 min, depending on the time the CO_2 production rates needed to become steady. For pellet systems, the CO_2 production rates, r_{CO_2}, are normalised to the area of the pellet surface decorated with exsolved particles (the top side of the pellet), A_{pe}. The activities were also expressed in terms of the turnover frequencies (TOFs), defined as the number of CO_2 molecules produced per active site per second. Since the exact active sites are not strictly known, it is assumed that the active sites are the metal ions or molecules located at the outer surface of the particles and the number of these metal actives site, denoted as k, are calucalted per unit cell length, a, per surface metal atom. These assumptions were followed for all pellet systems throughout the thesis unless stated otherwise. A detailed calculation of these k and TOF values are shown in Chapter 3 and **A1.3**.

The pellet systems were produced via the modified solid-state synthesis as described in subection **3.2.1** and by Naegu et al. in two of their papers [138, 156]. After the pelletisation process, the pellets were polished on one side (top) and the metals were exsolved only on the polished surface. This polishing step is required in order to produce cleaved surfaces; that is surfaces without the presence of surface defects such as terraces and edge structures due to their limitation that can suppress the surface metal exsolution as explained in the literature review. **Figure 4-1** shows the SEM micrographs and their respective average particle size histograms of the fresh pellet surfaces for: (A) FeNi-s; and (B) Ni-s pellet systems. The fresh surfaces revealed to have rounded exsolved metal particles, and the exsolved metal particles were uniformly distributed across the pellet surface, which is consistent with the materials produced by the exsolution method [153]. The particle size and distributions of all samples were analysed using the ImageJ software. The SEM images were converted to binary images where particles were outlined based on pixel contrast. From this, the number of particles as well as individual particle diameter can be calculated and therefore particles size distribution. Based on this, the exposed area and interface length of the particles are calculated as square microns per square microns of pellet area and microns per square microns of pellet area, respectively. The calculations were carried out assuming the particles have hemispheric geometry.

The particles distributions show that the average particle size lies within the range of 30 to 40 nm for both pellet systems. The average sizes of 38 ± 4 nm and 34.7 ± 5 nm were found for Ni-s and FeNi-s pellets respectively, with considerably narrow particles distribution in the range of 10 to 50 nm. The scope of this screening investigation was, however, limited in terms of particle size (in this case of around 30 nm) due to the potential methodological weakness, in particular, due to the restricted accuracy of the high resolution SEM instrument up to around

20 nm in order to produce higher quality images. The difference in brightness between these two SEM images can be explained by the manipulation of the natural contrast of the SEM, which is required in order to capture all the details of the particles when the tested samples are charging during the scanning to enable easier particle analysis.

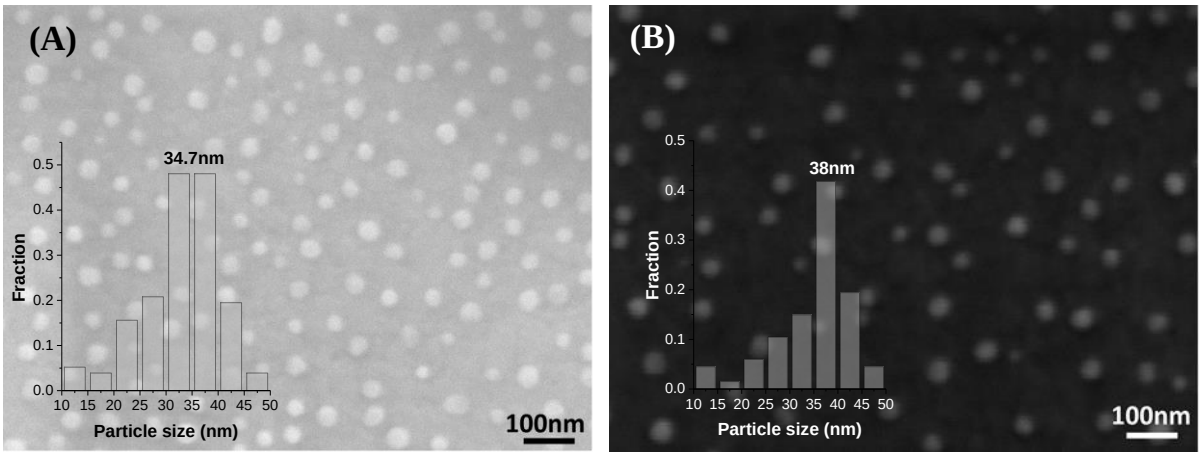

Figure 4-1 SEM micrographs of the surface microstructures of fresh (A) FeNi-s and (B) Ni-s pellet systems with their corresponding particle size histograms with error of around ± 5 nm.

Table 4-1 displays several important particle characteristics used to calculate the TOFs including surface metal area per pellet, for Ni-s and FeNi-s pellet systems. From the table, it can be seen that Ni-s illustrates a slightly higher particles population (77 particles μm^{-2}) compared to FeNi-s (67 particles μm^{-2}) as a result of substituting Ce, instead of Sr on the A-site. The difference in particles population on the pellet surfaces of these Ni-s and FeNi-s pellet systems, is possibly due to the different mobility of the A-site cations during the reduction process. In this case, lanthanum-ceria (La, Ce) and lanthanum-strontium (La, Sr) respectively, which can directly influence the exsolution of the B-site cations on the surface with La known to promote the exsolution. The fact that Sr cation tends to promote the formation of Ruddlesden-popper phases also causes lower particle nucleation thus producing fewer exsolved particles on the surface of FeNi-s pellet system.

Table 4-1 Particle characteristics of average particle size and population and surface metal area per pellet used for TOFs calculations. The calculation for the metal surface area is shown in the Appendices: **A1.3.**

Pellet	Metal loading (%)	Average size (nm)	Particle population (particles μm^{-2})	Pellet area, A_{pe} (cm^2)	Metal surface area (m^2 metal)
Ni-s	Ni: 0.4	34.7 ± 3	77	2.05	5.45×10^{-5}
FeNi-s	Fe: 0.1, Ni: 0.1	38.0 ± 5	67	2.14	3.83×10^{-5}

In order to assess their potential CO oxidation activities expressed in terms of r_{CO_2} and TOFs, the light-off experiments at three different inlet feed gas mixtures were performed over the two pellet systems. Prior to commencing the experiments, a blank experiment with no catalyst was performed under the stoichiometric condition in order to eliminate any possible contribution from the homogeneous reaction. The CO_2 production rate, r_{CO_2}, was below the IR analyser's measurable limit of 0.027 mmol s^{-1} m^{-2} (equivalent to 1 ppm of CO_2) at each temperature at this condition.

Figure 4-2 compares the CO_2 production rates, r_{CO_2}, and the TOFs for FeNi-s and Ni-s pellet systems. It can be seen that the minimum temperature for a measurable CO_2 production rate, r_{CO_2}, and TOF was similar in both systems at all three inlet feed mixture conditions, with both systems initiating the CO_2 production at 260 °C, and below this temperature, the CO_2 production rates, r_{CO_2}, were below the minimum measurable limit of 0.027 mmol s^{-1} m^{-2} (equivalent to 1 ppm of CO_2). To measure reliable kinetic data under the differential conditions, in which the reactor conditions (temperature, pressure) are considered uniform or "gradientless" across the reactor at low conversions, we only used the kinetic data below 0.54 mmol s^{-1} m^{-2}, which corresponds to 20 % CO conversion for all three reaction conditions. Under the stoichiometric condition of the inlet feed gas mixtures (0.5 kPa of CO and 0.25 kPa of O_2), and below the kinetic limit, FeNi-s shows higher TOF values at all temperatures, with measured TOFs of around 45 to 480 s^{-1}. Whereas, the TOFs for Ni-s were around 38 to 152 s^{-1} at a temperature range between 300 and 400 °C. Upon increasing the P_{O2} from 0.25 to 3.0 kPa, Ni-s pellet system did not show any changes in their CO_2 production rates, r_{CO_2}, and TOFs at all temperatures. However, at 460 °C, which is above the kinetic limit of 20 % CO conversion, FeNi-s revealed a jump in TOF values for inlet P_{O2}/ P_{CO} of 2.66 (0.5 kPa of CO and 1.33 kPa of O_2), marked by the unusual TOF of almost 1000 s^{-1}, although at higher P_{O2}/ P_{CO} of 6 (0.5 kPa of CO and 3.0 kPa of O_2), very similar TOFs as those in stoichiometric condition were measured.

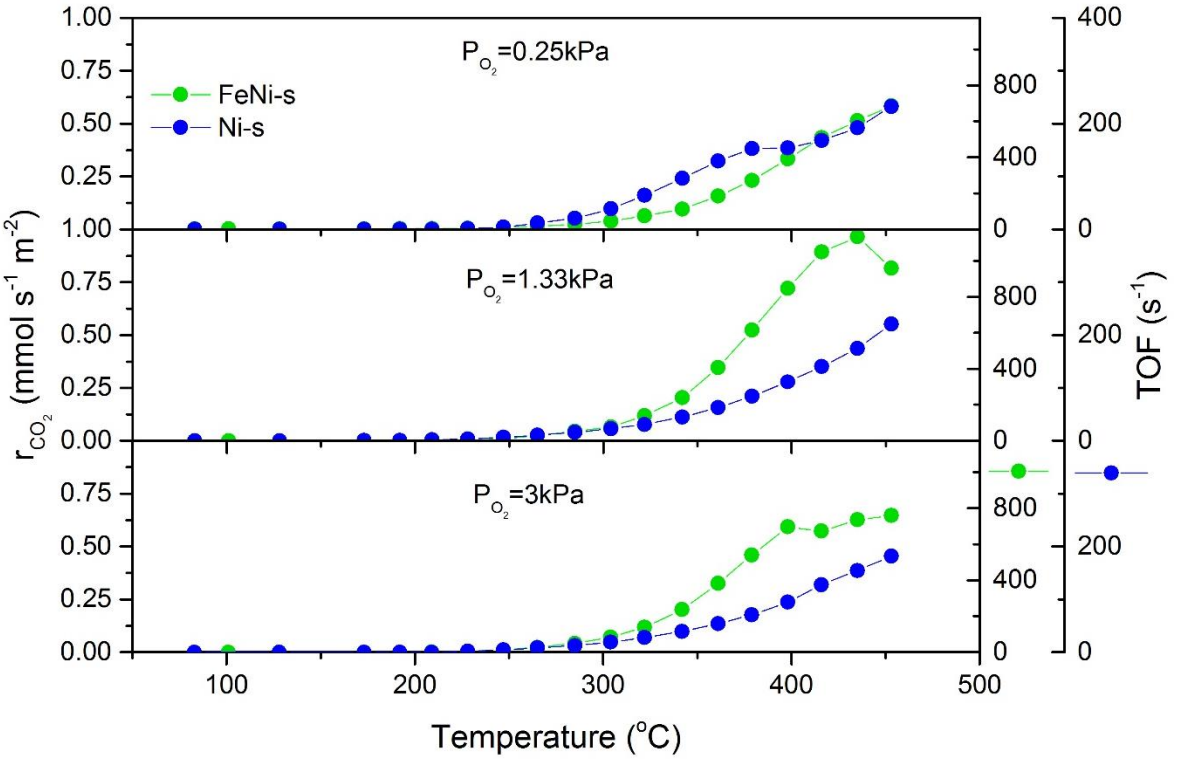

Figure 4-2 CO_2 production rates normalised to pellet area, r_{CO_2}, and TOF values as a function of temperature (light-off) over FeNi-s and Ni-s pellet systems for CO oxidation with inlet feed gas mixtures of P_{CO} = 0.5 kPa, P_{O2} = 0.25, 1.33 and 3.0 kPa and Ft = 150 ml min^{-1}. The rate is normalised with respect to the pellet area decorated with particles (top side only). The colour-coded plots highlight the different TOF axes, shown on the right of the graphs with inner axis representing the TOFs for FeNi-s while the outer axis representing the TOFs for Ni-s pellet systems respectively. Both plots also represent the r_{CO_2} values on the left axis. Error of around ± 5-10 % were found during reproducibility test at each measured point.

The decrease in CO_2 production rates, r_{CO_2}, and TOFs exhibited by FeNi-s pellet system were also seen during repeated experiments as shown in **Figure 4-3**, with error of around 9 % at high temperatures from 400 to 460 °C. Such effect might be connected with the occurrence of surface morphology changes of the active metal at higher temperatures, possibly due to the different metal oxidation between Fe and Ni. In this case, the structural changes deactivate the catalysts at higher temperatures. Since this is only a speculation, further investigations are required and this will be addressed in the latter section, involving FeNi powder systems.

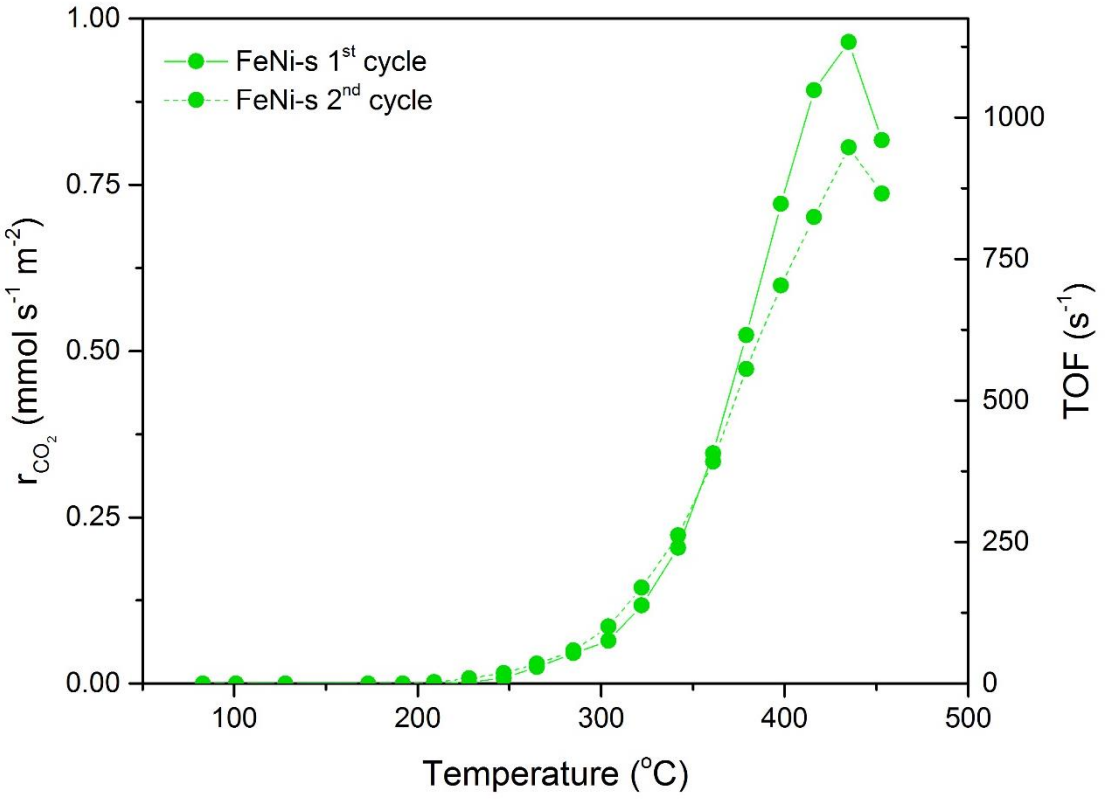

Figure 4-3 Reproducibility of CO_2 production rates, r_{CO_2}, and TOFs under light-off experiments, with an inlet feed gas mixture of P_{CO} = 0.5 kPa, P_{O2} = 1.33 kPa, F_t = 150 ml min^{-1}. The rate is normalised with respect to the pellet area decorated with particles (top side only). The right axis representing the TOFs for FeNi-s.

For comparison, several reported Pt and base metal catalysts were reviewed. Most of the reported base metal catalysts showed low TOFs at the conditions mentioned, though most studies failed to give clear information on the catalysts parameters such as the catalyst weight, which raises uncertainty concerning their actual activities. The nearest conditions were chosen in order to provide an appropriate comparison, although exact comparison was impossible due to the differences in reaction conditions and/or the structure of the catalyst itself. Haneda et al. reported TOFs of around 2 s^{-1} for their alumina-supported Pt catalyst at 160 °C at P_{O2}/ P_{CO} = 2 [157]. Naik et al. reported TOFs of around 1.5 s^{-1} for their titania-encapsulated Pt catalyst under P_{O2}/ P_{CO} = 2.5 at 190 °C [158] with increased thermal stability against sintering. Papaioannou et al. reported TOFs of around 0.35 to 2.72 s^{-1} for several YSZ-supported Pt catalysts with various three-phase-boundary (tpb) lengths at 250 °C at P_{O2}/ P_{CO} = 2.6 [159]. An et al. reported TOFs of around 0.015 and 0.02 s^{-1} for pure mesoporous Co_3O_4 and NiO at 200 °C at P_{O2}/ P_{CO} = 0.4 [160]. It is clear that our exsolved metal systems were more active, having one to two orders of magnitude higher TOFs, in the range of 10^3 s^{-1} than the rest of the catalysts mentioned, especially in comparison to those of Pt.

A major limitation that has been widely documented in developing base metal catalysts that can compete with Pt is mostly due to their high susceptibility to sintering, in particular, during continuous long-term operation. Hence, the long-term stability of these exsolved metal pellet systems was probed at 523 °C and compared to the state-of-the-art commercial Pt on alumina (Pt/ Al_2O_3) pellet catalyst. The commercial Pt/ Al_2O_3 pellet catalyst was chosen for comparison, as opposed to preparing a similar exsolved Pt structure is due to the nature of the study, aiming to only develop potential catalysts that can rival Pt and not involve any mechanistic study of this structure. The long-term stability experiment involves a total flowrate, F_t, of 450 ml min^{-1} given at normal temperatures and pressures (NTP) with an inlet feed gas mixture of 0.5 kPa of CO and 1.0 kPa of O_2. This experiment was conducted at 523 °C for approximately 170 hours (one week) and the TOFs were compared between the three pellet systems. A temperature of 523 °C was used in this experiment only to qualitatively investigate the stability of these exsolved pellet systems at higher temperatures and these values did not represent the true values at this temperature and that the reactor was considered to operate under integral conditions at this temperature (higher CO conversions), which the reactor conditions (temperature, pressure) are changing across the reactor.

Figure 4-4 compares the long-term stability at 523 °C of these FeNi-s and Ni-s pellet systems to those of Pt/ Al_2O_3 pellet catalyst expressed in terms of TOFs. The CO conversions after the initial 15 hours at this temperature were around 48, 5 and 6 % for Pt, FeNi-s and Ni-s pellet systems, respectively at which the measured TOFs were above the kinetic limit of 20 % CO conversion, especially for Pt. FeNi-s pellet system shows relatively stable and higher TOFs than those of Pt, of around ~700 to 1000 s^{-1} at this temperature, whereas Pt only recorded around 0.8 s^{-1} across the time span with observed severe oscillations (~6 %) due to the temperature variation in the lab. These oscillations might also reflect the use of only one flowrate value (450 ml min^{-1}) in the TOFs calculation, which was measured only at one specified time. Similar oscillations were also observed for Ni-s. Conversely, Ni-s shows declining TOFs over time from the initial value of around 200 s^{-1} to 80 s^{-1} after 170 hours of operation. These TOFs are still higher than those of Pt even though the TOFs deteriorate over time. For Ni-based catalysts, Jiang et al. demonstrated extremely stable Ni-based nanowires with no degradation at 440 °C, but the study suffered from inadequate exposure time of only 20 hours. This study, however, offered significant insights on the importance of the size of Ni particles in achieving higher CO oxidation activities and stability for Ni-based catalysts [161], which can be manipulated in our research as well. Not only that, the effect of alloying in enhancing the thermal stability of Ni-based catalysts has also been previously reported by Nikolla et al. in two of their papers. They

have found that these alloys prefer to oxidise carbon (C) atoms rather than forming the C-C bonds, hence improving their carbon chemistry and stability at high temperature of 800 °C. However, their studies were again limited to only at most around 15 hours of continuous operation [113, 162]. This might have explained the prolonged stability of the alloyed FeNi particles on FeNi-s surface, having stable high TOFs across the 170 hours of continuous testing.

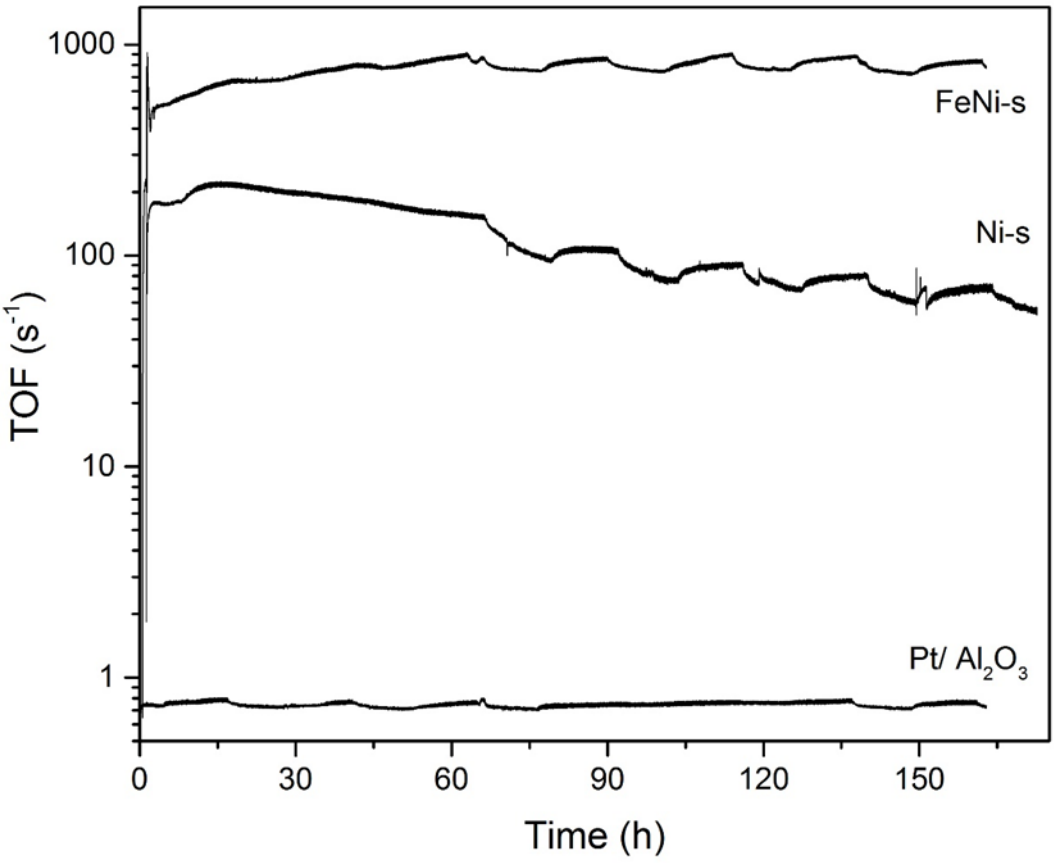

Figure 4-4 TOFs over state-of-the-art Pt/Al_2O_3, FeNi-s and Ni-s pellet systems in the long-term CO oxidation experiment with an inlet feed gas mixture of P_{CO} = 0.5 kPa, P_{O2} = 0.25 kPa, F_t = 450 ml min^{-1} and at 523 °C for 170 hours (one week).

The surface morphologies of these exsolved pellet systems prior to and following experiments were scanned under SEM. Since both FeNi-s and Ni-s pellet systems display similar faceted and enlarged particles after subjected to catalytic experiments, only the surface morphologies of the FeNi-s pellet system were shown to avoid redundancy. **Figure 4-5** compares the surface morphologies of the (A) fresh and (B) post-experimental pellet surfaces of FeNi-s pellet system with their respective particle size histograms. The inset particle size histograms present the particle size analyses for both surfaces, which reveal that the size of the exsolved metal particles expanded following catalytic experiments, from an initial average particle size of 38 nm (refer **Figure 4-1**) to 54 nm. This might suggest that these exsolved particles were oxidised during

the experiments. Particles on the post-experimental surface also exhibited wider particle distribution in the range of 10 to 90 nm, as opposed to 10 to 50 nm on the fresh pellet surface. The exsolved metal particle size ratio between the fresh and post-experimental pellet surfaces was found to be around 1.42. This value is in agreement with the reported lattice expansion from metallic Fe (lattice parameter, a = 0.285 nm) or FeNi (a > 0.357 nm) to mixed Fe oxides (a > 0.835 nm), associating to oxides to metallic particle size ratio of ~2.93 [163]. This finding broadly supports the works of other studies that link the surface oxidation of the particles to the increase of the L_3/L_2 ratio of Fe upon oxidation, although the value was smaller than the oxidation of Fe as it is believed to be the effect of alloying Ni to Fe [164, 165]. By comparing the particles population between the fresh surface (67 particles μm^{-2}) and the experimented surface (75 particles μm^{-2}), no significance changes were observed, which suggests that no agglomeration occurred. This also confirmed the stability of these pinned particles upon subjected to oxidising conditions and long-term continuous operation, which is ascribed to their strong metal-support interaction in which was found to be detrimental to base metals.

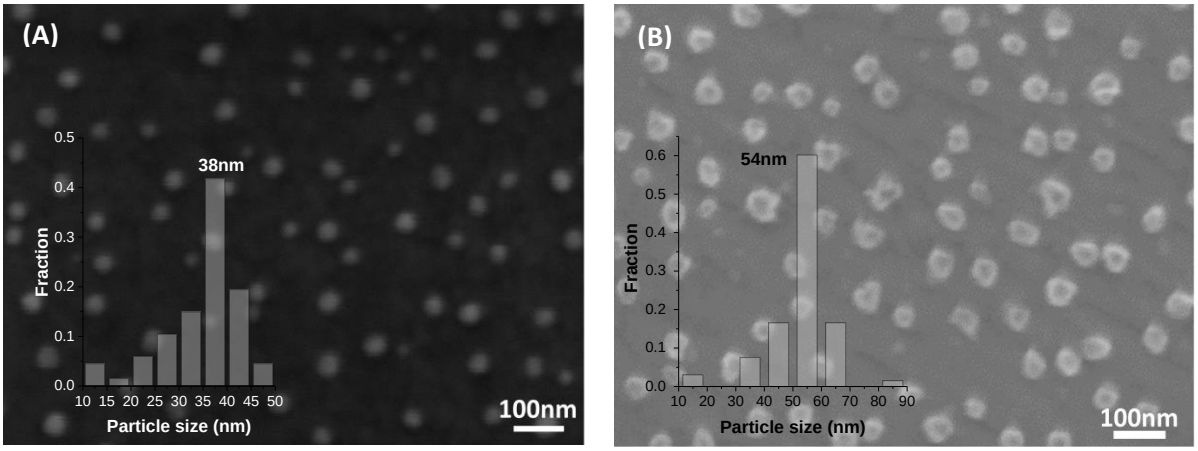

Figure 4-5 Comparison of surface morphology of FeNi-s pellet system (A) prior to and (B) following exposure to catalytic experiments with their corresponding particle size histograms with error of around ± 7 nm.

These preliminary screening catalytic investigations were performed to evaluate the catalytic activities and their continuous long-term stability of exsolved FeNi-s and Ni-s pellet systems, especially in terms of TOFs for CO oxidation. These promising findings clearly indicate that these exsolved metal systems are active in the CO oxidation reaction, in particular, FeNi-s pellet system, which shows high TOFs in the order of 10^3 s^{-1}. Their long-term stability was also confirmed at a relatively high temperature of 523 °C, which imply a huge potential to be employed as catalysts for CO oxidation. The next section moves on to further prepared these exsolved metal systems in powder form in order to evaluate and compare their activity on a

weight-to-weight basis to that of Pt, which is a key requirement for practical applicability. The progress in finding the active exsolved metals, in which their activities are first assessed in a typical light-off experiment in CO oxidation are summarised in the following subsection (**4.2.2)**.

4.2.2 Exsolved metal powder systems

Being the core of this chapter, this subsection traces our research progress in finding the most active exsolved metal powder systems for CO oxidation. This chapter reviews the prepared powder batches chronologically, in which their CO oxidation activities in terms of CO_2 production rates, $r^*_{CO_2}$, were assessed in the typical light-off experiment. Following these, only the most active exsolved metal powder systems are further experimented to explore the nature of the catalysts in the CO-rich atmospheres and upon sulphur poisoning in comparison to those of the state-of-the-art Pt/ Al_2O_3 catalyst powder. These experiments are adopted to monitor their stability against CO and poisons such as sulphur since these components can be detrimental towards the activity of Pt (i.e. CO) and base metals, and also since sulphur is present in the exhaust converter, even though only at a trace amount. Still, since the aim of this investigation is not to fully simulate the exhaust reactions, but only to study one reaction as a base reaction such as in CO oxidation, investigations on the effect of water or hydrocarbons (HC) oxidation, which is also presents in the exhaust converter were not performed. Although, past investigations have revealed that these exsolved metal systems have good activity under HC oxidation with high tolerance against coking [23]. Hence, these investigations are recommended for future work.

For powder systems, the light-off employed a total flowrate, F_t, of 450 ml min^{-1} given at normal temperatures and pressures (NTP) with an inlet feed gas mixture of P_{CO} of 0.6 kPa and P_{O2} of 1.0 kPa. For the light-off, the temperature was increased from RT to 520 °C, in which the temperature was held constant during heat-up at each step of 20 °C and the steady states rates measurement was recorded. Such as the rates did not vary more than ± 5 % over 60 to 180 min, depending on the time the CO_2 production rates, $r^*_{CO_2}$, needed to become steady. The CO_2 production rates, $r^*_{CO_2}$, represent the activities per weight of active metal catalyst powder, w_p, and the activities were also expressed in terms of CO conversions. Ten mg (w_p) of each powder system was diluted in 90 mg of alumina (Al_2O_3) and was loaded into the powder reactor, to give a total weight, W_t, of 100 mg of the powder bed. To enable reliable kinetics data under the differential conditions, in which the reactor conditions (temperature, pressure) are considered uniform or "gradientless" across the reactor at low conversions, only the data under 20 % CO

conversion were used (dashed line, labelled as X_{20}), which corresponds to 0.40 x 10^{-4} mol s^{-1} g^{-1}. Also, comparisons at considerably higher temperatures are sometimes made to qualitatively compare the activities, even though these values did not represent the true values at this temperature since the reactor was considered to operate under the integral conditions at higher CO conversions, in which the reactor conditions (temperature, pressure) are changing across the reactor. The improvements in CO_2 production rates, $r^*_{CO_2}$, of the prepared exsolved powder systems from batch to batch were accomplished by manipulating the preparation parameters especially in terms of grinding method and/or reduction atmospheres and/or the elemental formulation of the exsolved metal systems. For example, in order to increase the particles population, the A-site cation was changed from Sr to Ce.

Figure 4-6 shows the chronological progress of the development of exsolved metal catalyst systems (pellet and powder) in order to find the active formulation and metals under light-off experiment. To date, 67 exsolved metal systems (pellets and powders) were prepared by varying the intrinsic parameters such as the exsolved metals (B-site cations substitutions) and/or the partial substitution of different A-site cations and/or the extrinsic parameters in particular, the reduction atmospheres and/or milling processes. This is because these parameters have been previously reviewed to influence the nature of the exsolved metal particles and distribution. Since this was our first attempt in formulating these exsolved metal systems in powder form, preparation parameters were varied; e.g. the milling methods and reduction parameters used, which then resulted in exsolved metal powder systems with various particle characteristics. Due to the fact that most of these exsolved metal systems were inactive (pink areas in **Figure 4-6**), a detailed description are made only for the most active ones and the light-off plots for the inactive exsolved metal systems are included in the Appendices; **A1.1.1**.

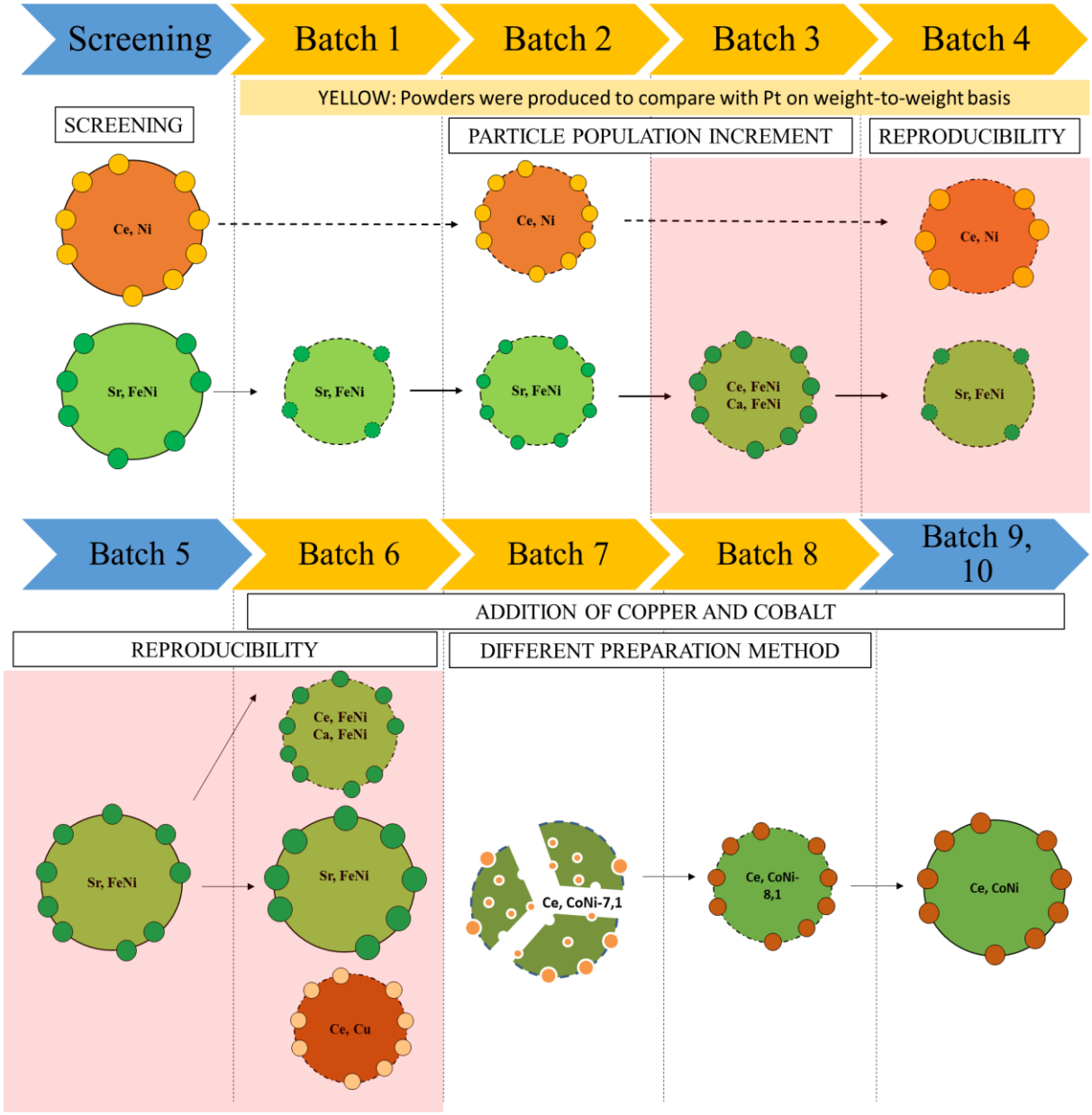

Figure 4-6 Chronological progress of the development of exsolved metal catalyst systems for CO oxidation, starting from the previously discussed preliminary screening experiments (on the far up, left). The blue labels refer to the pellet systems (bigger circles with solid line) whilst the yellow labels refer to the powder systems (small circles with dashed line). The pink areas (Batch 3, 4 and Batch 5, 6) represent the inactive exsolved metal systems and their results are presented in **A1.1.1**. In Batches 1 and 2, powder systems were prepared using similar material formulation as the screening pellet (FeNi-s and Ni-s), intended to increase the exsolved particle population on the powder surface. In Batch 3, exsolved FeNi powder systems with increased particles population were prepared by replacing the A-site cation from Sr to Ce and calcium (Ca). In the following three batches (Batches 4, 5 and 6), the reproducibility of the previous active pellet and powder systems from the screening experiment (FeNi-s) and from Batch 1 (Sr, FeNi-1,2) were tested. In Batches 6, 7 and 8, Cu and Co were added into the formulation of Ce, Ni-2,19 powder system and the effect of altered preparation route was also investigated. This was performed to produce two average particle sizes of 10 and 30 nm in the same powder.

Following the previous preliminary screening experiments, since FeNi-s pellet system showed superior TOFs in both the light-off and long-term stability in comparison to Ni-s, this exsolved metal system, having similar formulation ($La_{0.5}Sr_{0.4}Fe_{0.1}Ni_{0.1}Ti_{0.8}O_3$) was further prepared in powder form (Batch 1). These exsolved metal powder systems were labelled and henceforth referred to, according to their respective A-site cations, exsolved metal composition, their corresponding batch number and the order of testing. For example, "Sr, FeNi-1, 2" represents the second tested exsolved Sr, FeNi powder system from Batch 1. Six exsolved Sr, FeNi powder systems were prepared and tested under the typical light-off experiments, with almost all powder systems showing measurable CO_2 production rates, $r^*_{CO_2}$, at around 320 °C. Below 320 °C, the CO_2 production rates, $r^*_{CO_2}$, were below the minimum measurable limit of 0.007 x 10^{-4} mol s^{-1} g^{-1} (Appendices: **Figure A-2**). Below the kinetic limit, Sr, FeNi-1, 2 shows the smallest temperature gap of 140 °C to that of Pt, although several other exsolved Sr, FeNi powder systems (Sr, FeNi-1,1 and Sr, FeNi-1,3) were also considered active within the kinetic limit and at high temperatures. This was shown by the very similar temperatures upon achieving 20 % CO conversion over the previously mentioned active Sr, FeNi powder systems, Sr, FeNi-1,1, Sr, FeNi-1,2 and Sr, FeNi-1,3 of around 420, 410 and 430 °C respectively. In terms of the exsolved metal particles characteristics, the overall metal exsolution was compromised to only around 10 particles μm^{-2} for all Sr, FeNi powder systems in comparison to around 67 particles μm^{-2} on the previous FeNi-s pellet system. In addition, larger particles of around 40 to 60 nm were also produced, in comparison to the average particle size of around 35 nm on the FeNi-s pellet system. Aside from the fact that Sr cation tends to suppress metal exsolution, this might also be due to the limited control of the particles population in powder form because of the existence of different types of native surfaces such as kinks or edges, which can suppress the exsolution. These surfaces are not easily polished or cleaved in powder sample which makes it more difficult to control the extent of the exsolution.

Following the results achieved from the previous batch, the exsolved particles population in Sr, FeNi powder systems were further increased in Batch 2 in order to enhance their CO_2 production rates, $r^*_{CO_2}$, even though the exsolved particles population were then limited to the non-stoichiometry of the Sr, FeNi powder systems. In Batch 2, several exsolved metal powder systems, having similar formulation as the previously tested Ni-s pellet system ($La_{0.8}Ce_{0.1}Ni_{0.4}Ti_{0.6}O_3$) were also prepared in powder form. Eleven exsolved powder systems, consisting of five Sr, FeNi and six Ce, Ni powder systems were prepared and tested under the typical light-off experiments, with almost all powder systems showing measurable CO_2

production rates, $r^*_{CO_2}$, at a lower temperature of 300 °C (Appendices: **Figure A-3**). In particular, one exsolved Ce, Ni powder system, Ce, Ni-2,19 showed higher CO_2 production rates, $r^*_{CO_2}$, under the kinetic limit, narrowing the temperature gap to 100 °C, which is 40 °C lower than Sr, FeNi-1,2 to that of Pt. Across the exsolved Ce, Ni powder systems, it was found that powder systems with smaller particles with sizes below 30 nm, provided they have similar particles populations revealed to have lower CO_2 production rates, $r^*_{CO_2}$. For Sr, FeNi powder systems, the overall metal exsolution could only be increased to around 20 to 30 particles μm^{-2} for all Sr, FeNi powder systems before it is limited by the non-stoichiometry that restricts further metal exsolution.

Figure 4-7 shows the difference in surface metal particles population between the most active powder systems from Batches 1 and 2; (A) Sr, FeNi-1,2 and (B) Ce, Ni-2,19. Similar to what we have previously observed in the pellet systems, the particles displayed rounded features, even though the particles size and population vary between both powder systems. Sr, FeNi-1,2 powder system is shown to have a bigger average particles size of around 43 nm in comparison to 31 nm particles in Ce, Ni-2,19 powder system. It is also evident from the images that the particles population in Ce, Ni-2,19 is higher compared to the one in Sr, FeNi-1,2, having around 66 particles μm^{-2} in Ce, Ni-2,19 to only 10 particles μm^{-2} in Sr, FeNi-1,2. However, Ce, Ni-2,19 powder system suffers from wider particles distribution ranging from 10 to 50 nm in comparison to Sr, FeNi-1,2, suggestive of more uniform particle distribution in the range of 38 to 55 nm in Sr, FeNi-1,2. This is further confirmed by the inset particle size histograms. From our previous discussion, Ce, Ni-2,19 powder system is shown to be more active than Sr, FeNi-1,2, indicative of the need to improve the particle population of the exsolved FeNi in Sr, FeNi-1,2 formulation. This is performed to enhance their CO_2 production rates, $r^*_{CO_2}$. The surface microstructure of the most active powder systems from each batch is shown in Appendices: **Figure A-1**.

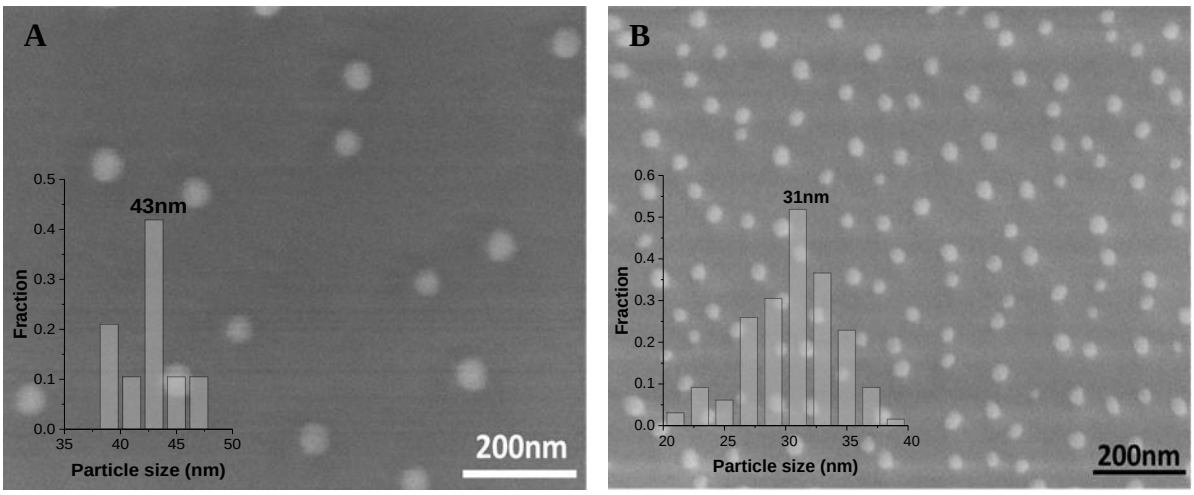

Figure 4-7 The difference in the surface metal particles population for the most active exsolved powder systems, with inserted particle size histograms for (A) Sr, FeNi-1, 2 and (B) Ce, Ni-2, 19 with error of around ± 5 nm.

Since the aim of Batch 3 was to increase the particles population of the exsolved FeNi powder systems, this was successfully achieved by replacing the detrimental Sr with different A-site cations such as calcium, Ca and Ce. By increasing the substitutions amount, the particles population were increased by five to ten times, from 10 to 80 particles μm^{-2} compared to the active Sr, FeNi-1, 2 powder system from Batch 1 (Appendices: Compare **Figure A-1A** with **C**). However, their CO_2 production rates, $r^*_{CO_2}$, were much lower, with the most active one, labelled as Ca, FeNi-3, 5 powder system only managed to achieve 0.16 x 10^{-4} mol s^{-1} g^{-1}, which only corresponds to 8 % of CO conversions at 520 °C (Appendices: **Figure A-4**). Since most Sr, FeNi powder systems demonstrate low activity except the ones from the first batch, for example Sr, FeNi-1, 2, Batch 4 was intended to test the reproducibility of the CO_2 production rates, $r^*_{CO_2}$, of the previous Sr, FeNi powder system. Several Ce, Ni powder systems were also prepared and the average particles size were purposely increased in order to avoid the severe oxidation of the smaller particles. However, all exsolved metal powder systems from Batch 4 were inactive, showing CO_2 production rates, $r^*_{CO_2}$, of around 0.02 x 10^{-4} mol s^{-1} g^{-1}, which only correspond to 1 % of CO conversions at 520 °C (Appendices: **Figure A-5**). This then raised the reproducibility problem of the exsolved metal powder systems even though no microstructural changes were found in either as-prepared or stored exsolved powder systems which can alter their CO_2 production rates, $r^*_{CO_2}$.

The reproducibility issue has again arisen when using pellet (Batch 5), which similar exsolved FeNi pellet system to that of FeNi-s that was prepared and labelled as Sr, FeNi-5, 1. The pellet was again inactive at all temperatures, even though the pellet contained slightly higher particles

population of ~ 100 particles μm^{-2}, compared to 67 particles μm^{-2} on FeNi-s surface. This has also been observed for several other exsolved FeNi powder and pellet systems from Batch 6, which further implies that these exsolved systems were probably susceptible to severe oxidation even during storage. No clear evidence was found to support this assumption since no microstructural changes were found over these exsolved powder systems under SEM. The addition of copper (Cu) and cobalt (Co) into the previously tailored exsolve Ni system to exsolve Cu and CoNi alloys was also tested since both metals are known to show considerably high activities for CO oxidation, as previously discussed in the literature survey. As for exsolved Cu powder system, labelled as Ce, CuNi-6, 4, it shows slightly higher CO_2 production rates, $r^*_{CO_2}$, even though the rates are still very low in comparison to other exsolved powder systems in Batch 6, of around 0.092 x 10^{-4} mol s^{-1} g^{-1}. This only corresponds to around 4.5 % of CO conversions at 520 °C (Appendices: **Figure A-6**).

In Batch 7, besides the addition of Co in the exsolved Ni powder system formulation, the preparation was slightly altered in order to produce two average particle sizes of 10 and 30 nm in the same powder. Since previous study has shown that the metal exsolution within the bulk enables the production of smaller nanoparticles [153], the preparation route was altered by exposing the exsolved metal system to reduction atmospheres in pellet form to exsolved metal onto the polished surface of the pellet prior to the grinding process into powder form (Ce, CoNi-7, 1). This then resulted in different surface morphologies in comparison to a similar exsolved CoNi powder system, Ce, CoNi-8, 1 produced in Batch 8, which follows the normal preparation route (Appendices: **Figure A-7**). In the normal preparation route, the pellet was first ground into a powder prior to exposure it to reduced atmospheres to promote the metal exsolution. The different surface morphologies are illustrated by the schematic diagrams in **Figure 4-6** for Batches 7 and 8. Ce, CoNi-7,1 powder system displays the appearance of empty sockets, which are caused by the grinding process following reduction, leaving the smaller bulk particles on one part of the breakage and empty sockets on the other part. This also resulted in having two ranges of average particle sizes of 10 and 30 nm particles as previously intended, while Ce, CoNi-8, 1 powder system only contains the 30 nm particles and with no empty sockets. Albeit the difference in surface morphologies between both exsolved CoNi powder systems, both powder systems exhibit high CO_2 production rates, $r^*_{CO_2}$, of around 0.8 x 10^{-4} mol s^{-1} g^{-1}, which corresponds to around 40 % of CO conversions at 520 °C (Appendices: **Figure A-8**). Below the kinetic limit, larger temperature gaps of 160 and 210 °C for Ce, CoNi-7,1 and Ce, CoNi-8,1 powder systems to that of Pt were observed. This is evident by the higher temperatures observed

upon achieving 20 % CO conversion for these powder systems of around 430 and 480 °C, for Ce, CoNi-7,1 and Ce, CoNi-8,1 respectively.

Figure 4-8 compares the CO_2 production rates, $r^*_{CO_2}$, and CO conversions for the most active powder systems across all batches to those of commercial Pt and supported Ni catalyst powders. These include one exsolved FeNi powder system from Batch 1 (Sr, FeNi-1, 2), one exsolved Ni from Batch 2 (Ce, Ni-2, 19) and one exsolved CoNi (Ce, CoNi-7,1) from Batch 7. Among the 60 exsolved metal powder systems tested under the typical light-off experiments, only three of these powder systems show significantly higher CO_2 production rates, $r^*_{CO_2}$, than the rest of the systems, although we still have a minimum temperature gap of 100 °C to that of Pt on a weight-to-weight basis. The CO_2 production rates, $r^*_{CO_2}$, presented in **Figure 4-8** also represent the CO_2 production rates, $r^*_{CO_2}$, previously stated for each system. By comparing the CO_2 production rates, $r^*_{CO_2}$, between the exsolved Ni (Ce, Ni-2,19) and the commercial supported Ni powder systems below the kinetic limit, both systems initiated the CO_2 production at a similar temperature of around 300 °C, although significant difference was observed at higher temperatures. 20 % of CO conversion at around 0.4 x 10^{-4} mol s^{-1} g^{-1} was achieved at a lower temperature of 380 °C over the Ce, Ni-2, 19 powder system compared to 400 °C for the commercial Ni catalyst powder.

This suggests that a stronger metal-interface interaction comes into play, which can alter the chemisorption and enhance the CO_2 production rates, $r^*_{CO_2}$, of the embedded Ni particles as opposed to the commercial Ni catalyst [166-168]. Singha et al. reported the CO_2 production rates, $r^*_{CO_2}$, of around 0.15-0.74 µmol s^{-1} g^{-1} at 55 °C, at which the CO oxidation reaction was initiated by their Co_3O_4 powder catalysts prepared by combustion route at $P_{O2}/ P_{CO} = 1$. Upon achieving 100 % CO conversions at 175 °C, the CO_2 production rate, $r^*_{CO_2}$, was around 21.7 µmol s^{-1} g^{-1} [86]. Even though the temperatures at which our exsolved powder systems initiated the CO_2 production and achieved full CO conversions was much higher at around 260 and 480 °C for Sr, FeNi-1,2 powder system, higher CO_2 production rates, $r^*_{CO_2}$, were measured at around 0.002 x 10^{-4} and 2.1 x 10^{-4} mol s^{-1} g^{-1} respectively. Direct comparison at the temperatures used in this study with other studies is, however, impossible since most base metal catalysts suffer from agglomeration at high temperatures, which then demands for the catalytic investigations to be performed at much lower temperatures. For Ce, CoNi-7, 1 powder system, the light-off curve seems to deactivate and level off at around 40 % of CO conversion. This is due to several factors that can possibly contributed to this trend since it is well known than the

catalytic activity of Co catalysts are heavily dependent on the size, geometry and the projected active planes. At this point, we infer that this might due to the use of one particle size and the hemispherical particles did not reveal the active planes of Co for CO oxidation, hence limiting the activities of these particles. However, this is only a speculation of what happened at this point since we do not have any evidence to verify this. Hence, these results need to be interpreted with caution, which merit for future in-depth analysis.

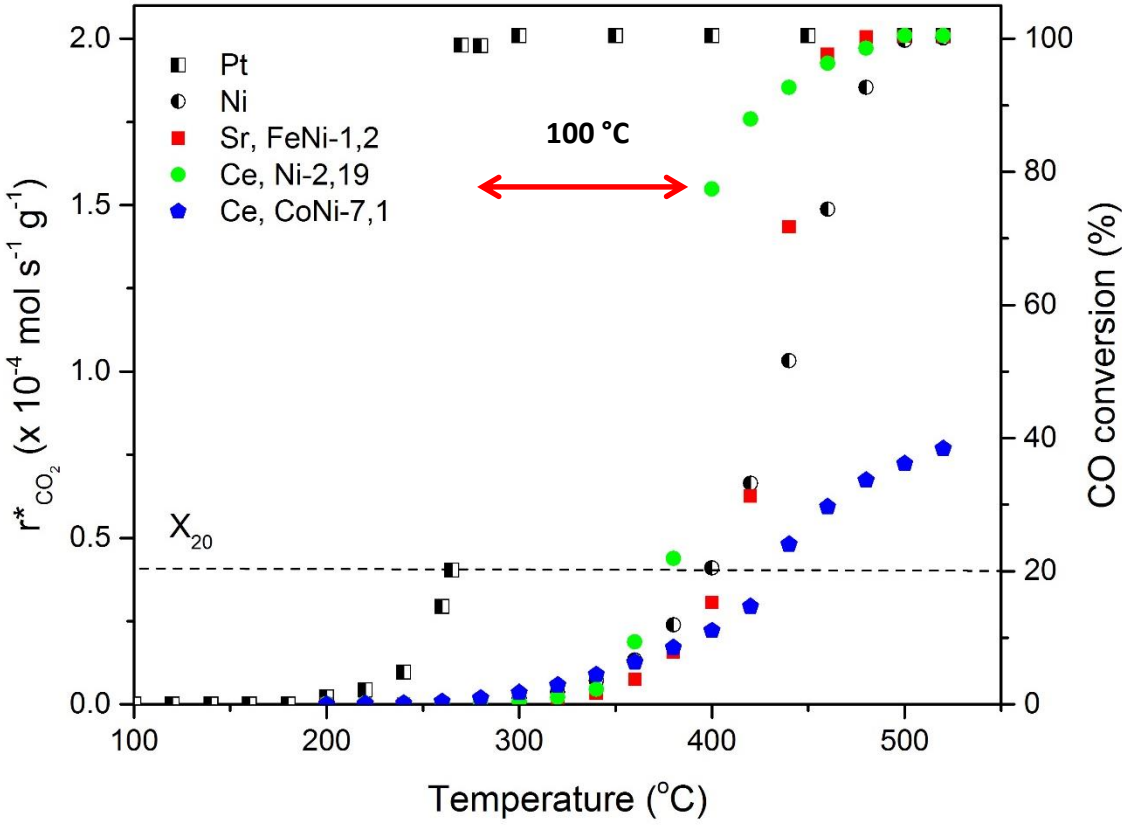

Figure 4-8 CO_2 production rates, $r^*_{CO_2}$, and CO conversions as a function of temperature (light-off) over state-of-the-art Pt/Al_2O_3, commercial Ni/Al_2O_3 SiO_2 and three most active exsolved metal powder systems under CO oxidation reaction with an inlet feed gas mixture of P_{CO} = 0.6 kPa, P_{O2} = 1.0 kPa, F_t = 450 ml min^{-1} and GHSV=26 000 h^{-1}. 10 mg of each catalyst powder (weight of powder, w_p = 10 mg), was diluted in alumina to obtain a total weight of the powder bed, W_t of 100 mg. Error of around ±5 % were found during reproducibility test at each measured point for Pt and Ce, CoNi-7,1.

4.3 CO kinetics and activation

The following section describes the effect of CO partial pressures (henceforth, referred as CO kinetics) on CO_2 production rates, $r^*_{CO_2}$, for the commercial Pt, Ni, Sr, FeNi-1,2 and Ce, CoNi-7,1 powder systems. In this CO kinetics experiment, the P_{O2} was held constant while increasing the P_{CO}, at 520 °C. The CO kinetics experiment involves a total flowrate, F_t, of 450 ml min^{-1}

given at normal temperatures and pressures (NTP) with inlet feed gas mixtures of constant P_{O2} of 0.64 kPa while P_{CO} was varied stepwise between 0.5 to 18.87 kPa, with varying step sizes of 0.6 to 4 kPa. The steady states rates measurement was then recorded. **Figure 4-9** compares the CO_2 production rates, $r^*_{CO_2}$, of the commercial Pt, Ni, Sr, FeNi-1,2 and Ce, CoNi-7,1 powder systems. To enable reliable kinetics data under the differential conditions, only the data under 20 % of O_2 conversion were used, which corresponds to $r^*_{CO_2}$ of 0.85 x 10^{-4} mol s^{-1} g^{-1}.

For Sr, FeNi-1,2 powder system, below the kinetic limit, the CO_2 production rate, $r^*_{CO_2}$, increases with the increase of P_{CO}, and the increase were observed at all P_{CO} up to P_{CO} = 18.87 kPa and this represents the behaviour of most exsolved powder systems tested in similar CO kinetic experiment. However, Ce, CoNi-7,1 powder system shows one order of magnitude rate jump after the stoichiometric condition (P_{CO} = 1.28 kPa) from 0.9 to 2.7 x 10^{-4} mol s^{-1} g^{-1}. Beyond this, the increases in $r^*_{CO_2}$ are minimal until P_{CO} = 18.87 kPa. For the commercial Pt and Ni catalyst powders, the CO_2 production rates, $r^*_{CO_2}$, were above the kinetic limit after the stoichiometric conditions at this temperature. Therefore, these values were not a true representative of the exact values at these reaction conditions. Pt showed no change in the CO_2 production rates, $r^*_{CO_2}$, above the stoichiometric condition (P_{CO} = 1.28 kPa and P_{O2} = 0.64 kPa). Whereas, for Ni, the CO_2 production rate, $r^*_{CO_2}$, increases with P_{CO} until P_{CO} = 5 kPa. However, the experiment was stopped as a result of the reactor flow being blocked, which was triggered by the possible severe accumulation of carbon or coking when P_{CO} reached 7.5 kPa. This was confirmed by SEM, shown in Appendices, **Figure A-10** in which the particles were agglomerated and possible formation of carbon whiskers was found to be severe following this experiment.

The CO oxidation over Pt has been well studied with surface science techniques revealing that at higher temperatures, the Pt surface is covered by adsorbed oxygen, hindering the adsorption of CO on the Pt active sites, hence limiting the rate of CO_2 production, which led to a first-order dependence in P_{CO} at higher temperatures [169, 170]. Even though the $r^*_{CO_2}$ were lower than those of the commercial Pt and Ni powder systems, no coking was observed in this CO-rich environment for both Sr, FeNi-1,2 and Ce, CoNi-7,1 powder systems, albeit both contained Ni particles, which are known to coke severely in these conditions. These results further support the idea of by having pinned Ni particles, which was the novel characteristics of these exsolved systems, it can then delay any agglomeration during operation, preventing them from being dislocated from their sockets in the surface of the parent perovskites. This then resulted in high

resistant towards coking. This was reported earlier by Naegu et al. in their recent study concerning the anti-coking properties of these exsolved systems, attributing to their strong metal–support interaction against agglomeration [23].

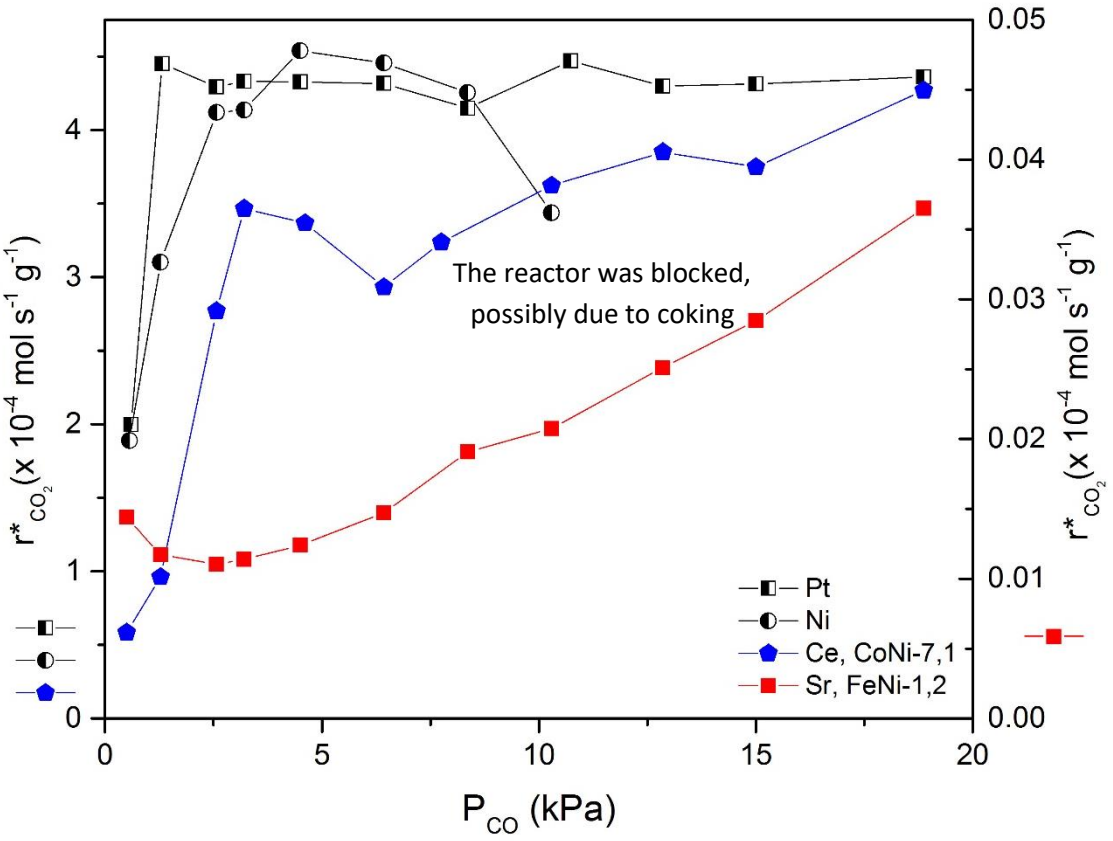

Figure 4-9 CO_2 production rates, $r^*_{CO_2}$, as a function of CO partial pressures (CO kinetics) over two commercial Pt/Al_2O_3 and Ni/ Al_2O_3 SiO_2 catalyst powders and two of the most active exsolved metal powder systems (Sr, FeNi-1 ,2 and Ce, CoNi-7,1) under CO oxidation reaction with inlet feed gas mixture of P_{CO} = 0.5-18.87 kPa, P_{O2} = 0.64 kPa, F_t = 450 ml min^{-1}, GHSV=26 000 h^{-1} and at 520 °C. 10 mg of each catalyst powder (weight of powder, w_p = 10 mg), was diluted in alumina to obtain a total weight of the powder bed, W_t of 100 mg. In order to operate under the differential conditions, the data under 20 % of O_2 conversion were used, which corresponds to $r^*_{CO_2}$ of 0.85 x 10^{-4} mol s^{-1} g^{-1}. Error of around ±5 % were found during reproducibility test at each measured point for Pt and Ce, CoNi-7,1.

Figure 4-10 shows the enhancement of the CO_2 production rates, $r^*_{CO_2}$, of the Ce, CoNi-7,1 powder system, in comparison to other active exsolved metal powder systems after undergoing the CO kinetic experiment. Significant increase in CO_2 production rates, $r^*_{CO_2}$, was observed in both kinetic regions, below the kinetic limit of 20 % CO conversion, X_{20} (differential reactor conditions) and at higher CO conversions (520 °C), which were not observed for other exsolved metal powder systems. The CO_2 production rates, $r^*_{CO_2}$, presented in **Figure 4-9** also represent

the CO_2 production rates, $r^*_{CO_2}$, previously stated for each system in **Figure 4-8** since no activation were observed for the rest of the exsolved meta powder systems. The Ce, CoNi-7,1 powder system with enhanced CO_2 production rates, $r^*_{CO_2}$ and CO conversions will henceforth be referred to as the activated Ce, CoNi-7,1. The activated Ce, CoNi-7,1 shows a CO_2 production rate, $r^*_{CO_2}$, after reaching 5 % of CO conversion at around 200 °C, in comparison to its initial temperature of 350 °C and at 240 °C for Pt. Below these temperatures, the CO_2 production rates, $r^*_{CO_2}$, were below the minimum measurable limit of 0.007 x10^{-4} mol s^{-1} g^{-1}. Below the kinetic limit, the CO_2 production rates, $r^*_{CO_2}$, for the activated Ce, CoNi-7,1 surpassed that of Pt at a low temperature region between 160 to 260 °C,. At 240 °C. the CO_2 production rates, $r^*_{CO_2}$, were around 0.37 and 0.13 x10^{-4} mol s^{-1} g^{-1} for the activated Ce, CoNi-7,1 and Pt respectively. Conversely, at higher temperatures, the activated Ce, CoNi-7,1 only managed to achieve around 1.4 x10^{-4} mol s^{-1} g^{-1} (~ 76 % CO conversion), in comparison to Pt, which transited to the light-off region and achieved 100 % CO conversion (~ 2.1 x10^{-4} mol s^{-1} g^{-1}) at 270 °C. This shows that CO might acts as an activity promoter at these CO-rich conditions for CoNi, although this trend is only applicable to specific exsolved metal formulations such as the exsolved CoNi systems. This is evident by the similar enhanced CO_2 production rates, $r^*_{CO_2}$, observed for the Ce, CoNi-8,1 powder system which has been subjected to similar activation in the CO-rich atmosphere (Appendices: **Figure A-8**). Such effect might be connected with the occurrence of surface morphology changes of the active metal, which often referred to as structural promoter. This kind of behaviour has been reported previously for sulphur for reactions such as preferential CO oxidation (PROX), which resulted in high CO selectivity upon poisoning [171]. This activation of exsolved CoNi powder system would require in-depth investigations in order to pinpoint the origin of the enhanced CO_2 production rates, $r^*_{CO_2}$, therefore, this activation is discussed in detail in the following chapter.

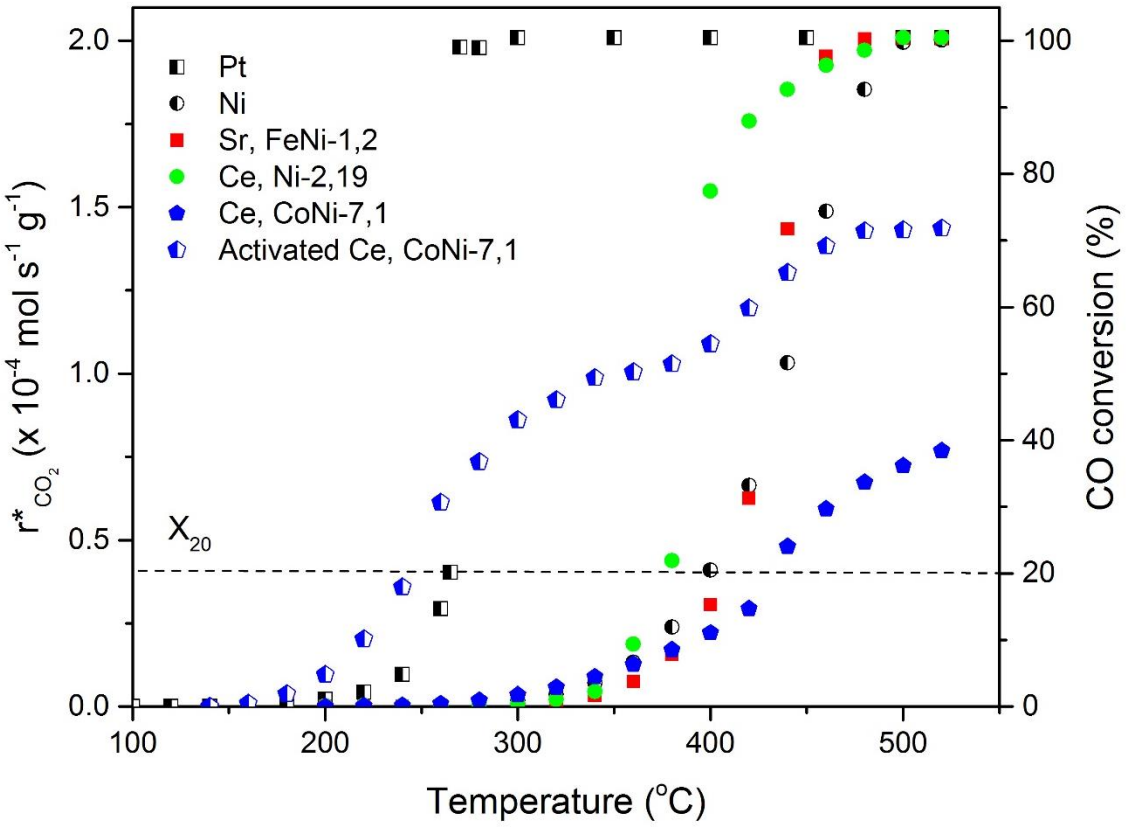

Figure 4-10 Comparison of the CO_2 production rates, $r^*_{CO_2}$, and the conversion of CO as a function of operating temperature (100-520 °C) in CO oxidation with an inlet feed gas mixture of P_{CO} = 0.6 kPa, P_{O2} = 1.0 kPa, F_t = 450 ml min^{-1} and GHSV=26 000 h^{-1} of the most active powder systems to state-of-the-art Pt/ Al_2O_3 and commercial Ni/ Al_2O_3 SiO_2 catalyst powders. 10 mg of each catalyst powder (weight of powder, w_p = 10 mg), was diluted in alumina to obtain a total weight of the powder bed, W_t of 100 mg. Error of around ±5 % were found during the reproducibility test at each measured point for Pt and Ce, CoNi-7,1.

4.4 Sulphur poisoning

One of the greatest challenges in developing the alternative catalyst to Pt, especially from base metals is that they are highly susceptible to sulphur. This often involves the irreversible poisoning of base metals and because of this, the last decades have seen growing research in order to tackle this problem [172]. Hence, this part of the chapter evaluates the effectiveness of these active exsolved metal powder systems during sulphur poisoning and the recovery of their CO_2 production rates, $r^*_{CO_2}$, are compared to those of the commercial Pt and Ni catalyst powders. As mentioned previously, 50 ppm of SO_2 was co-fed with the inlet feed gas mixture, containing 0.6 kPa of CO and 1.0 kPa of O_2 at three different time intervals of 15, 30 and 60 minutes (henceforth referred to as Zone B, D and F) and the poisoning effect and its reversibility upon removal of the sulphur source on the CO_2 production rates, $r^*_{CO_2}$, were monitored. To enable reliable kinetics data under the differential conditions, we limit our data to 20 % of CO

conversion, which corresponds to 0.4 x 10^{-4} mol s^{-1} g^{-1}, which then resulted in the different poisoning temperatures used between the powder systems.

Figure 4-11 presents the results from the poisoning-recovery experiments for three powder systems. The figure shows the effect of poisoning for (1) Pt and (2) Ni at 240, respectively. **Figure 4-11-3** presents the poisoning-recovery results for Ce, Ni-2, 19 powder system at 400 °C. The poisoning for Ce, CoNi-7,1 powder system is included and discussed in the following chapter. At 200 °C, Pt shows an initial rate of around 0.078 x 10^{-4} mol s^{-1} g^{-1}, whereas at 400 °C, commercial Ni system shows an initial rate of around 0.55 x 10^{-4} mol s^{-1} g^{-1}. These represent around 4 and 25 % conversion of CO respectively. During the first poisoning in Zone B, the CO_2 production rates, $r^*_{CO_2}$, were decreasing to around 0.02 x 10^{-4} and 0.025 x 10^{-4} mol s^{-1} g^{-1} for Pt and Ni systems respectively. After the first 15 minutes of SO_2 poisoning, almost 76 % of the CO_2 production rates, $r^*_{CO_2}$, were recovered upon the removal of the sulphur source from the inlet feed gas mixtures for Pt in approximately three hours. However, no increase in CO_2 production rates, $r^*_{CO_2}$, was observed for commercial Ni after two hours. Further poisoning in Zone D and F shows similar recovery trends with Pt, showing slightly reduced activities after each poisoning, whereas Ni shows severe deactivation after each poisoning interval. On the other hand, closer inspection of the figure for Ce, Ni-2,19 shows significant CO_2 production rates, $r^*_{CO_2}$, recovery of around 65 % of the initial rates (0.39 x 10^{-4} mol s^{-1} g^{-1}), albeit containing Ni, the outcomes are conflicting to those obtained for the commercial Ni catalyst at a rather similar temperature of around 400 °C.

For Pt, a possible explanation for this might be that the adsorption of the sulphur component on the surface inhibited the associative chemisorption of CO and O_2 on Pt, causing the reduced activity during poisoning [173]. Since temperatures can influence the degree of the sulphur poisoning, even a low concentration of sulphur can lead to a huge performance loss at low temperatures. This supports our findings for Pt, at relatively low temperature of ~240 °C, poisoning can be reversed, but at the expense of reduced activity after each poisoning which reflects the lower degree of sulphur desorption at low temperatures [114]. On the other hand, the majority studies on sulphur poisoning involving Ni-based catalysts have reported on the irreversible sulphur poisoning of these catalysts, similar to what we have observed for the commercial Ni catalyst, as shown in **Figure 4-11-B**. This is believed to be because of the weakened chemisorption of CO after sulphur poisoning [174, 175]. The reversibility observed in **Figure 4-11-C** by these exsolved systems follows a rather similar trend as those observed for Pt. During the poisoning, sulphur was believed to chemisorb on the Ni active sites and

following the removal of the sulphur source, CO was believed to only chemisorb on the free nickel active surfaces, resulting in the decrease of activity. Then again, due to the sulphur that predominantly adsorb on the outer shell of the particles [176], it seems that the potential active sites of these exsolved systems are believed to be on the metal-support interface, thus preventing the sulphur from blocking the inaccessible active sites, making them still available for reaction during the poisoning and the recovery. This is evident from the plateau CO_2 production rates, $r^*_{CO_2}$, in Zone D and F. Although we could not eliminate the metal surfaces as the active sites since if the metal surfaces are also the active sites, we would expect that the adsorption of sulphur on the outer shell of the particles would to cause the reduced recovered CO_2 production rates, $r^*_{CO_2}$, in comparison to its initial rates. Not only that, TiO_2 was previously reported to have weaker interaction with SO_2, in comparison to that of Al_2O_3 due to the stronger metal-support interaction in TiO_2-supported catalysts, which then promotes the desorption of SO2 on the surface, improving the availability of the active sites for reaction [177]. However, this is merely a speculation of what happened during the poisoning of our exsolved systems since we do not have any evidence to verify this. Hence, these results need to be interpreted with caution, which merit for future in-depth analysis.

1

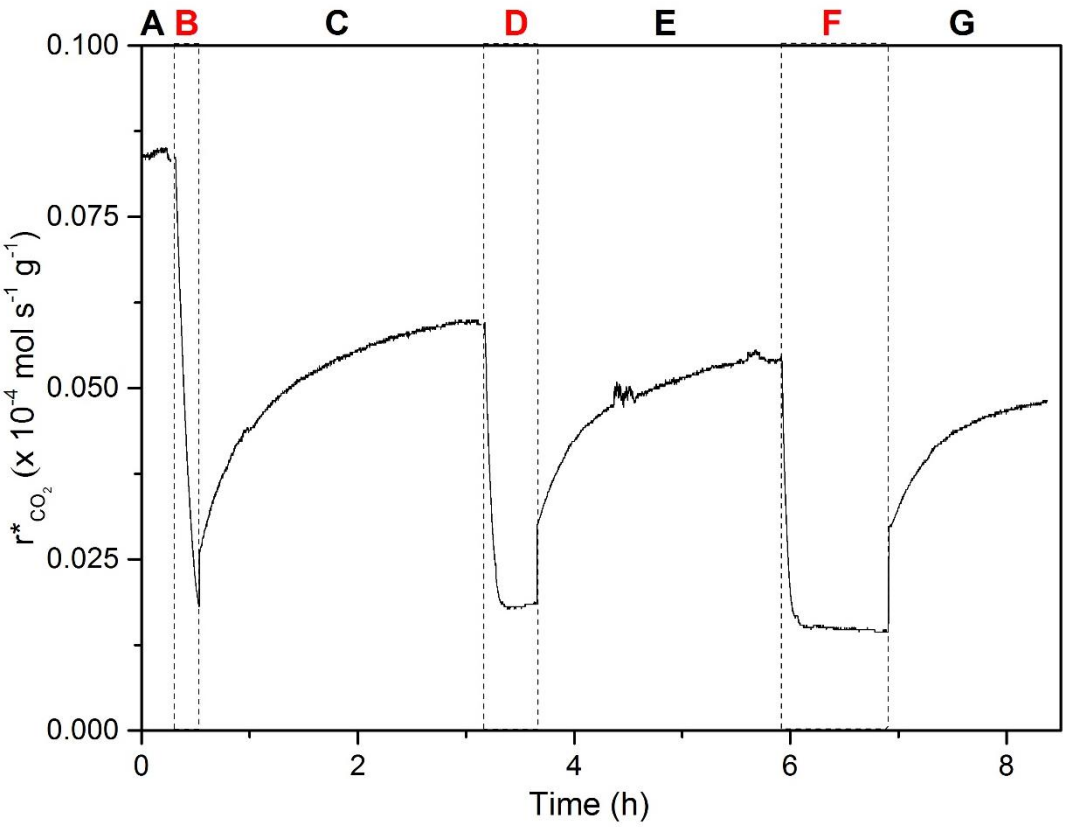
A B C D E F G
0.100
0.075
0.050
0.025
0.000
r*CO2 (x 10-4 mol s-1 g-1)
0
2
4
6
8
Time (h)

2

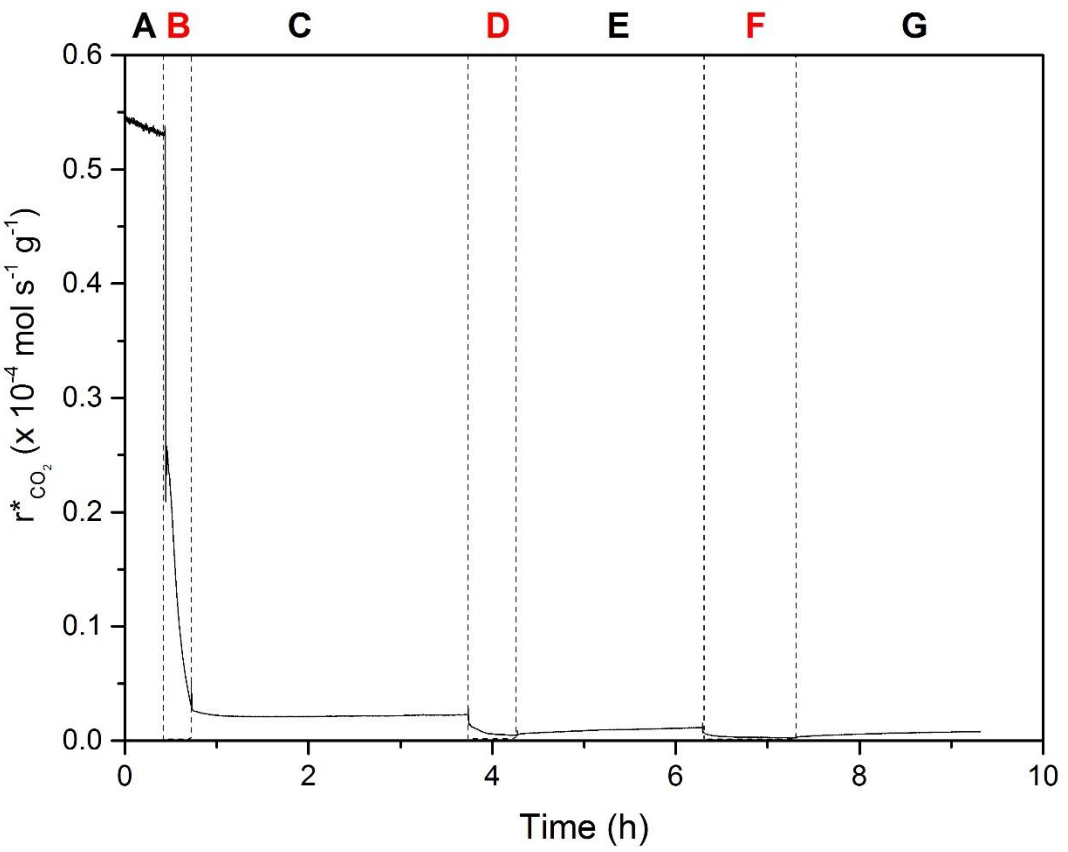
A B C D E F G
0.6
0.5
0.4
0.3
0.2
0.1
0.0
r*CO2 (x 10-4 mol s-1 g-1)
0
2
4
6
8
10
Time (h)

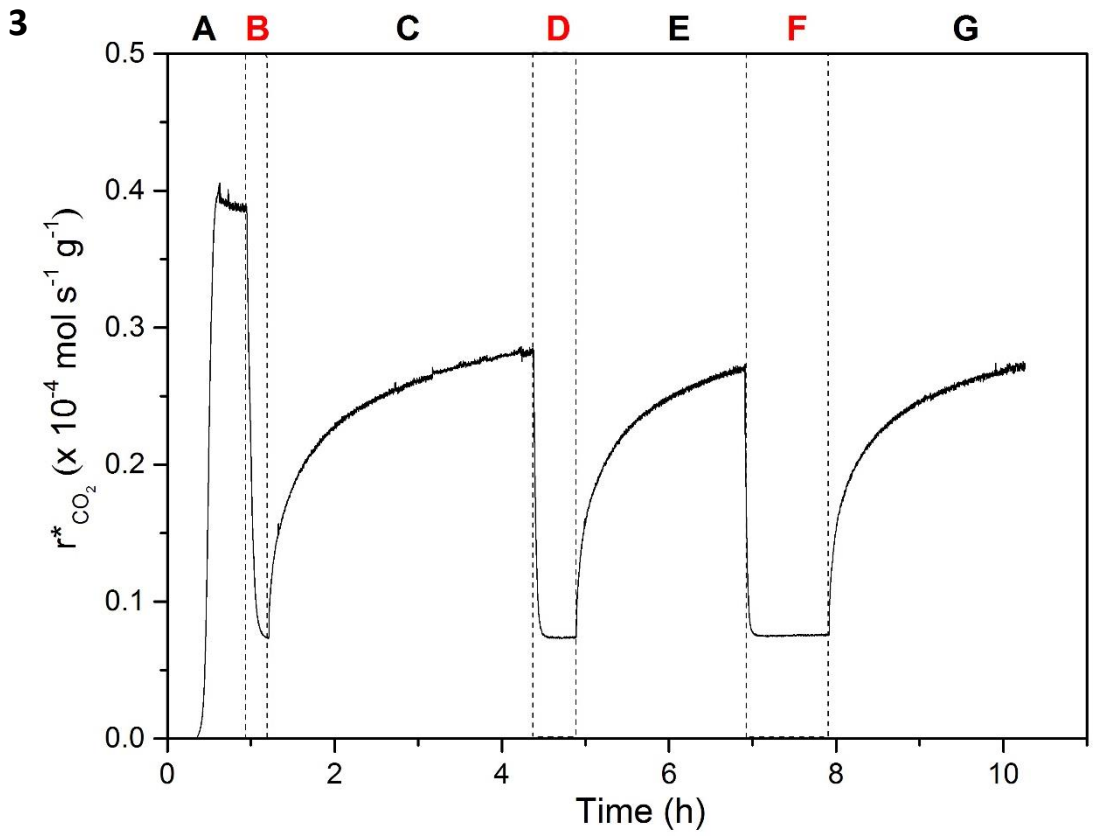

Figure 4-11 CO_2 production rates, $r^*_{CO_2}$, and rates recovery during sulphur poisoning (50 ppm SO_2) under the differential CO oxidation reaction with an inlet feed gas mixture of P_{CO} = 0.6 kPa, P_{O2} = 1.0 kPa, F_t = 450 ml min^{-1} for (1) Pt at T = 240 °C, (2) Ni at T = 400 °C and (3) Ce, Ni-2,19 powder system at T= 400 °C, respectively. The temperatures were chosen in order to operate under differential conditions (20 % of CO conversion or less) for reliable kinetic investigations.

4.5 Post-experiment particle characterisation

The surface morphologies of the exsolved powder system prior and post-experimental were viewed under SEM. **Figure 4-12** presents the surface morphologies of the Ce, Ni-2,19 (A) prior to and (B) following catalytic experiments, where the exsolved powder systems were exposed to several catalytic experiments (light-off, CO kinetics), with inset histograms depicting the particle size analyses for both surfaces. Similar surface morphology changes to those observed on their pellet counterparts (Ni-s and FeNi-s) were also observed for Sr, FeNi-1,2 powder system, revealing faceted and enlarged particles following the catalytic experiment. Particle size increment was also observed with the average particle size of the fresh and experimented systems to be around 31 and 50 nm respectively, which corresponds to an oxidised to fresh particles size ratio of around 1.61. This value again mirrored the expansion of Ni lattice from pure Ni^0 (a = 0.3524 nm) to $Ni^{2+}O^{2-}$ (a = 0.4207 nm) with the particle size ratio between oxidised and pure Ni metal being 1.2, suggesting that the particles were fully oxidised in these reaction

conditions [178]. However, no formation of carbon whiskers or particles uplifting were observed, leaving the particles still fixed at their pinned position thus maintaining their high activities. This then highlights the strong metal-support interaction between the metal particles and the perovskites support, which preserved the particles during catalysis while preventing any particles agglomeration or coking. Uniform Ni particles morphology and sizes of 10–40 nm with strong metal support interaction were also found by Singa et al., which attributed these characteristics to their higher resistance towards coke formation, inhibiting the particle agglomeration during the catalytic process, although their study involved the syngas reaction [179]. The particle characteristics of Ce, CoNi-7,1 powder system are not included since it is discussed in detail in the following chapter.

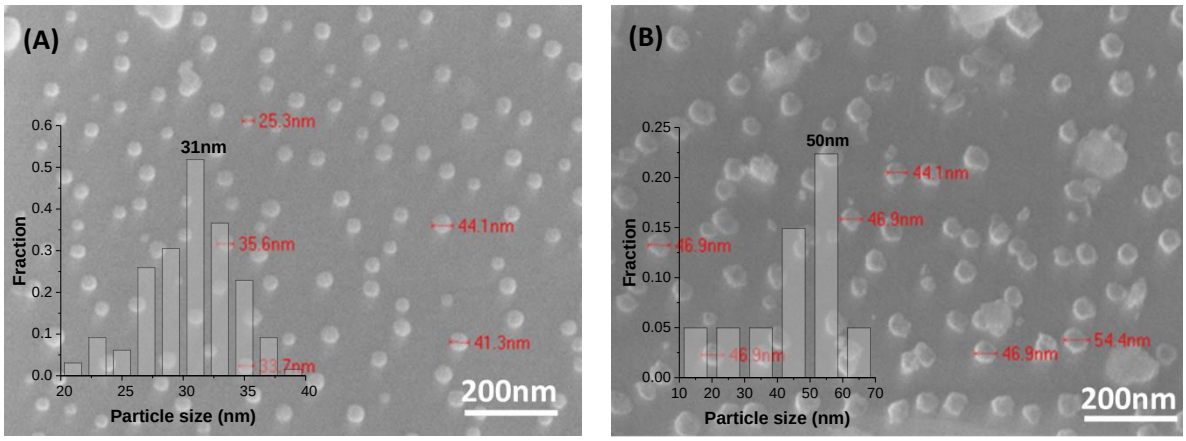

Figure 4-12 Comparison of surface morphologies of Ce, Ni-2,19 (A) prior to and (B) following exposure to catalytic experiments with their respected particle size histograms with error of around ± 5 nm for each histogram.

4.6 Summary

The purpose of the current investigations was to summarise the activity assessment in terms of their CO_2 production rates, $r^*_{CO_2}$, and CO conversions of the exsolved metal powder systems for CO oxidation, as an alternative to the state-of-the-art Pt/ Al_2O_3 catalyst powder. This particular study has examined 60 exsolved metal powder systems with different exsolved metals, and various particle characteristics and the results of the most active powder systems are reported in this chapter. Their CO oxidation activities were also assessed in the CO-rich atmospheres and sulphur poisoning.

Several key characteristics of these exsolved metal powder systems were established from this chapter:

1. Exsolved metal pellet systems were significantly active and robust in CO oxidation reaction, proven by the high and stable TOFs, as shown in the preliminary screening

catalytic testing with significantly high and stable TOF values in the range of 1000 s^{-1} for 170 hours.

2. Exsolved FeNi and Ni powder systems seemed to have high CO_2 production rates, $r^*_{CO_2}$, although they are still inferior to Pt on a weight-to-weight basis with 100 °C temperature gap, and the CO_2 production rates, $r^*_{CO_2}$, of the active powders were unable to reproduce.
3. Increasing CO_2 production rates, $r^*_{CO_2}$, in the CO-rich atmospheres suggested that these materials were not easily poisoned by CO at 520 °C
4. The recovery of the CO_2 production rates, $r^*_{CO_2}$, are possible after sulphur poisoning although the rates were lower than the initial rates prior to poisoning which are similar to those of Pt
5. CO-rich atmosphere enabled the "activation" of specific exsolved metal powder systems which then resulted in permanent increase in CO_2 production rates, $r^*_{CO_2}$.

Thus far, this chapter has reviewed the activities of 67 different exsolved metal systems (pellet and powder systems) for CO oxidation. The following chapter will focus on one considerably active exsolved CoNi system for CO oxidation. This was performed since we have observed previously that its CO_2 production rates, $r^*_{CO_2}$, can be further enhanced especially at the low-temperature region by means of exposure to CO-rich environment. Comprehensive catalytic investigations on exsolved CoNi systems in the light-off, CO kinetics, sulphur poisoning experiments and their long term stability are explored. The so-called "activation" and the logic behind this phenomenon are also investigated in detail using surface microstructure tracking.

5 CHAPTER 5: EXSOLVED CoNi SYSTEM AS CO AND NO OXIDATION CATALYSTS

5.1 Introduction

The central aim of this chapter is to critically examine the role of Co partial substitution in the exsolve metal system formulation, previously tailored to exsolve Ni ($La_{0.7}Ce_{0.1}Ni_{0.4}Ti_{0.6}O_3$) for CO oxidation [153]. This study sets out to first investigate the link between the particle characteristics and the catalytic and kinetic behaviour of this exsolved CoNi system ($La_{0.7}Ce_{0.1}Co_{0.3}Ni_{0.1}Ti_{0.6}O_3$) for CO oxidation, since this exsolved powder system (Ce, CoNi-7,1) has previously revealed enhanced CO_2 production rates, $r^*_{CO_2}$, following exposure to CO-rich atmospheres, which was not observed for other exsolved systems. Pellet systems were utilised in this study, called the particle tracking, intending to closely monitor the microstructures of these CoNi particles at key stages of catalytic experiments. In-depth characterisations and analyses were performed on the active structures to establish the origin of the enhanced CO_2 production rates, $r^*_{CO_2}$, previously observed for the Ce, CoNi-7,1 powder system. The significant role of the interface length was also addressed. In order to assess its activities in comparison to Pt on a weight-to-weight basis, the catalytic activities, expressed as CO_2 production rates, $r^*_{CO_2}$, and CO conversions of the exsolved CoNi powder system, which is the Ce, CoNi-7,1 were explored in detail, aiming to rival Pt for CO oxidation. Its activities concerning the CO kinetics, sulphur poisoning and long-term stability experiments were also addressed.

5.2 Experimental design

The catalytic investigations described in this chapter can be divided into two main parts:

a) To investigate the link between the kinetic behaviour and particle characteristics of the exsolved CoNi systems and to investigate the origin of the observed enhancement of CO_2 production rates, $r^*_{CO_2}$, in the Ce, CoNi-7,1 powder system. These investigations involve the exsolved CoNi and Ni pellet systems and are discussed in section **5.3**.

b) To explore the effect of temperature and poisons such as CO and sulphur on the CO_2 production rates, $r^*_{CO_2}$, of the exsolved CoNi powder system (Ce, CoNi-7,1 from Batch 7) and its long-term stability in detail since only the important results have been introduced in the previous chapter. This is discussed in section **5.4**.

For the pellet system experiment, three pellet systems were used, consisting of two exsolved CoNi pellet systems with different average particle sizes (30 and 10 nm) and one exsolved Ni pellet system (30 nm particles). These three systems were labelled and are henceforth referred to according to their respective exsolved particle composition and particle size. Therefore, "CoNi-30nm" represents the exsolved CoNi pellet system with 30 nm particles, "CoNi-10nm" is for the exsolved CoNi pellet system with 10 nm particles, and "Ni-30nm" denotes the exsolved Ni pellet system with 30 nm particles. The exsolved Ni pellet system has similar particle characteristics to those of one of the exsolved CoNi pellet systems (CoNi-30nm) and was also investigated in order to compare the kinetic behaviour of exsolved CoNi and Ni particles. Detailed descriptions of these pellet systems are provided in the following subsection. However, due to the drawbacks associated with the use of Co as oxidation catalyst, and particularly because they suffer from microstructural changes during oxidation which might affect their activity over time [15], the particle tracking experiment was also performed. Since these exsolved particles were stable during operations due to the socketed property, as previously reported [23], and thus it is possible to closely monitor the evolution of particles at nanoscale at key stages of the catalytic experiment in order to address the possibility of microstructural changes in Co during the experiments.

The reaction conditions such as the inlet feed gas mixtures and operating temperatures employed in these catalytic investigations involving the pellet systems; in light-off (CO and NO oxidation) and CO kinetics experiments are listed in the following subsection (**5.3.2)**. The catalytic activities (CO_2 production rates, $r^*_{CO_2}$, and CO conversions) of the exsolved CoNi powder system (Ce, CoNi-7,1) were investigated in terms of temperature, the effect of CO and sulphur and its long-term stability in comparison to that of a commercial Pt powder catalyst for CO oxidation. The detailed experimental reaction conditions and results are presented and discussed in section **5.4**. The experimental setup for the pellet and powder systems and the calculations concerning their activities have been discussed in detail in Chapter Three.

5.3 Exsolved CoNi pellet systems

This section discusses the results obtained from the particle tracking and catalytic experiments performed on the CoNi-30nm and Ni-30nm exsolved pellet systems. These investigations involved the light-off and CO kinetics experiments. The effect of interface length in the light-off experiment is considered in section **5.3.8**. The preliminary NO oxidation experiment employing two exsolved CoNi pellet systems, CoNi-30nm and CoNi-10nm, is then explored and presented in subsection **5.3.9**.

5.3.1 Description of pellet systems

The A-site deficient perovskite system, previously tailored to exsolve Ni ($La_{0.8}Ce_{0.1}Ni_{0.4}Ti_{0.6}O_3$), was utilised to further substitute cobalt (Co) to enable the exsolution of CoNi alloy particles ($La_{0.8}Ce_{0.1}Co_{0.3}Ni_{0.1}Ti_{0.6}O_3$), since it is well known that Co offers remarkable low-temperature activity under CO oxidation. This key advantage of Co over other base metals has been demonstrated in several studies [9, 10, 180]. Pellet systems were prepared since they are generally easier to characterise at the microscopic level, and the particles were exsolved only on one side of the pellet. These pellet systems functioned as well-defined model systems to relate their particle characteristics, including particle size, shape, population, spatial arrangement and chemistry, to their catalytic and kinetic behaviour. Two exsolved pellet systems were prepared, CoNi-30nm and Ni-30nm, having similar average particle sizes of around 30 nm with particle populations of around 137-140 particles μm^{-2} in order to rule out any effect of particle size in both exsolved metal pellet systems. Another exsolved CoNi pellet system having smaller particles of 10 nm (CoNi-10nm) was also prepared, aiming to study the effect of interface length on their activities, expressed in terms of CO_2 production rates, r_{CO_2}, and TOFs. Therefore, the CoNi-10nm pellet system was prepared to have almost twice the metal-support interface length of the ones in CoNi-30nm pellet. This results are presented in subsection **5.3.8**.

5.3.2 Description of particle tracking experiment

In order to address the potential of microstructural changes of Co during operations and to better understand how they occur, particle tracking experiments on both CoNi-30nm and Ni-30nm pellet systems were performed. These were performed to monitor the particles at several key stages of catalytic experiments, mostly via SEM and XPS, by tracking specific particles (or areas of particles), as shown in **Figure 5-1** below. The first step in this experiment was to first scan and analyse the fresh pellet surfaces under SEM and XPS to distinguish the fresh morphologies of the surface particles and also to mark specific areas of particles for further tracking. Several representative areas were identified and the particles were numbered based on geometrical distances to the pellet edge and according to the proximity to surface features such as pores or 'terraces'. Then, the pellets were tested in specific catalytic experiments (following the experimental sequence listed in **Table 5-1**), followed by another surface and elemental characterisations (SEM and XPS) at each key stage of the experiments. Each marked area was again located and inspected so as to monitor the particles' evolution at the individual and collective levels and to link this to its catalytic behaviour. These steps were repeated at each key stage.

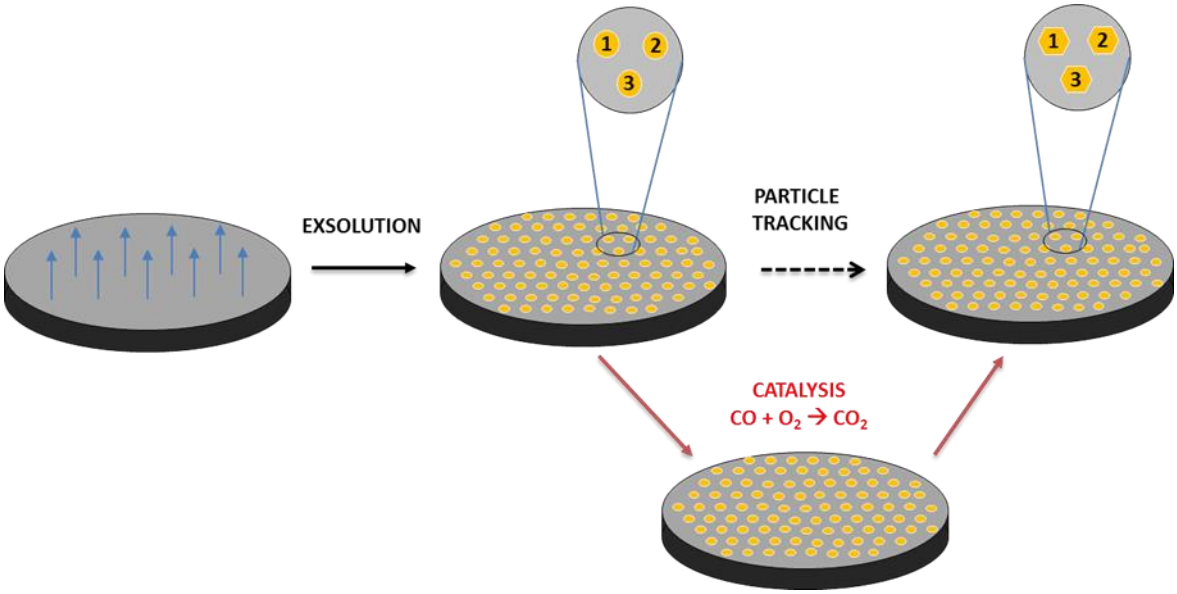

Figure 5-1 Schematic diagram of the particle tracking experiments

Table 5-1 below illustrates the six key experimental stages at which the pellets were subjected to particle tracking via SEM and XPS. These catalytic stages are referred to throughout this section (**5.3**), and therefore, in some parts of the thesis, readers will need to refer to this table which describes the key stages involved. The material characterisations were performed by our collaborators as follows: SEM and particle analysis by Dr Dragos Naegu (St Andrews University), HIM and XPS by Dr Andrew Barlows and Dr Billy Murdoch (NEXUS, Newcastle University), and TEM-EDX analysis by Dr David Miller (St Andrews University). EELS was performed by our colleague, Hervé Ménard, in Sasol (UK) Ltd, St Andrews. Meanwhile all the catalytic experiments were performed here at Newcastle University.

Table 5-1 Inlet reaction conditions, and surface and elemental characterisations involved at each key stage of the catalytic experiments under CO oxidation for CoNi-30nm and Ni-30nm pellet systems. Stages 1 to 5 are under CO oxidation whilst Stage 6 is under NO oxidation.

Stages No.	Catalytic stages	Inlet conditions of the feed gases	Analysis
1	Fresh	After particle exsolution	SEM, XPS
2	Light-off	Light-off P_{CO} = 0.6 kPa, P_{O2} = 1.0 kPa, T = 100-520 °C	SEM, XPS
3	CO kinetics	CO kinetics P_{CO} = 0.5-6.5 kPa, P_{O2} = 0.64 kPa, T = 520 °C	SEM

4	CO kinetics	CO kinetics P_{CO} = 8-18.87 kPa, P_{O2} = 0.64 kPa, T = 520 °C	SEM, XPS
5	Light-off	Light-off P_{CO} = 0.6 kPa, P_{O2} = 1.0 kPa, T = 520-280 °C	SEM, XPS, EELS, XRD, TEM-EDX
6	Preliminary NO oxidation light-off	Light-off P_{NO} = 0.04 kPa, P_{O2} = 8.0 kPa, T = 100-440 °C	SEM

5.3.3 Particle characterisations

In this particle tracking experiment, two exsolved pellet systems were used, CoNi-30nm and Ni-30nm. The pellets were prepared by our colleague, Dr Dragos Naegu, from St Andrews University via the exsolution method and the as-prepared pellet surfaces were characterised under SEM (Stage 1) to establish the fresh morphologies of the surface particles prior to any catalytic experiments. **Figure 5-2** shows the SEM micrographs and their respective particle size histograms for the fresh pellet surfaces for both (A) CoNi-30nm and (B) Ni-30nm pellet systems. The fresh metal particles are shown to have similar rounded shape and strong evidence of uniform particle size and distribution across the pellet surface was found on both pellet surfaces. This is consistent with materials produced by the exsolution method [128]. The inserted particle histograms show an average particle size of around 30 ± 3 nm for both exsolved metal pellet systems, with similar particle populations of around 144 and 137 particles μm^{-2} for CoNi-30nm and Ni-30nm respectively.

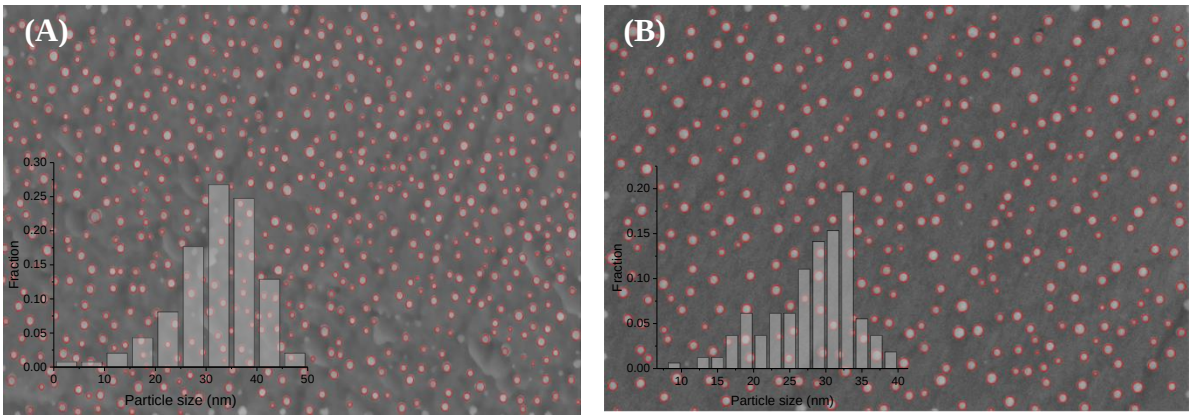

Figure 5-2 SEM micrographs of the surface microstructures of fresh (A) CoNi-30nm and (B) Ni-30nm pellet systems with their corresponding particle size histograms with error of around ± 5 nm for each histogram.

Table 5-2 below displays several important particle characteristics including the surface metal area and interface length per pellet, for the three pellet systems CoNi-30nm, CoNi-10nm and

Ni-30nm. For the CoNi-10nm pellet system, this data, along with its respective fresh surface SEM micrographs is considered below in subsection **5.3.8**. Note that the particle characteristics for the CoNi-30nm and Ni-30nm pellet systems are very similar in terms of their average particle sizes, particle populations, surface metal areas and interface lengths. Whereas, for the CoNi-10nm pellet system, the interface length is 23.36 µm metal μm^{-2}, which is almost twice the value for the CoNi-30nm pellet system at 13.27 µm metal μm^{-2}.

Table 5-2 Particle characteristics of average particle size and population, surface metal area and interface length used for TOFs calculations, with k as the average number of metal active sites per metal unit cell length, a

System	Average size (nm)	Particle population (particles μm^{-2})	Pellet area, A_{pe} (cm^2)	Metals area (μm^2 metal μm^{-2})	Interface length (µm metal μm^{-2})	Metal unit cell, a (nm)	k value for metal
CoNi-30nm	30 ± 2	144	1.86	0.25	13.27	0.80	2
CoNi-10nm	10 ± 2	721	1.86	0.17	23.36	0.81	2
Ni-30nm	30 ± 4	137	1.82	0.22	12.20	0.43	1

5.3.4 Light-off

In this section, the microstructural evolution of the exsolved metal pellet systems was followed at nanoscale at relevant inlet reaction conditions in CO oxidation. Here, the link between the physical and chemical properties of the pellet systems and their kinetic behaviour was evaluated. The light-off experiment involved a total flowrate, F_t, of 150 ml min^{-1} given at normal temperatures and pressures (NTP) with an inlet feed gas mixture of P_{CO} of 0.6 kPa and P_{O2} of 1.0 kPa. The temperature was increased from room temperature to 520 °C and the temperature was held constant during heat-up at each step of 20 °C. The steady states rates measurements were then recorded. Aside from the CO_2 production rates, r_{CO_2}, the activities were also expressed in terms of TOFs. The assumptions for the active sites were followed as stated in subsection **4.2.1**. A detailed equation and calculation of these TOFs is shown in Chapter Three and Appendices (**A1.3)**.

Figure 5-3 compares the rates of CO_2 production, r_{CO_2}, and the TOFs between CoNi-30nm and Ni-30nm pellet systems. Since most of the CO_2 production rates, r_{CO_2}, and TOFs were within

the kinetic limit of 20 % CO conversion (0.72 mmol s^{-1} m^{-2}), we can assume that these results were obtained under the differential reactor conditions at all temperatures. It can be seen that the minimum temperature for a measurable CO_2 production rate, r_{CO_2}, and TOF varies between the pellet systems with the CoNi-30nm pellet system initiating the CO_2 production at a lower temperature of 180 °C compared to 300 °C for Ni-30nm pellet system. Below these temperatures, the CO_2 production rates, r_{CO_2}, were below the minimum measurable limit of 0.037 mmol s^{-1} m^{-2}. The CoNi-30nm pellet system was able to convert 5 % of CO into CO_2 at around 250 °C with recorded CO_2 production rate, r_{CO_2}, and TOF of around 0.18 mmol s^{-1} m^{-2} and 65 s^{-1} respectively. At the same temperature, the CO_2 production rate, r_{CO_2}, for the Ni-30nm pellet system was still below the measurable limit. At 460 °C, the CO_2 production rate, r_{CO_2}, and TOF for the CoNi-30nm pellet system were around 0.72 mmol s^{-1} m^{-2} and 250 s^{-1} (20 % CO conversion), while the CO_2 production rate, r_{CO_2} and TOF for Ni-30nm at the same temperature were only able to achieve around half of the measured values of r_{CO_2} and TOF for CoNi-30nm, which correspond to around 0.38 mmol s^{-1} m^{-2} and 133 s^{-1}. The light-off curve for both r_{CO_2} and TOFs seems to deactivate and level off below 0.75 mmol s^{-1} m^{-2} and 250 s^{-1} which is similar to what we have observed previously for Ce, CoNi-7, 1 powder system. Our previous speculation on the logic behind this will be explained following the SEM and XPS results later on.

The activity of these exsolved pellet systems appears to depend strongly on the type of exsolved metals on the surface, especially in the low temperature region. This is consistent with the key advantage of Co, which offers remarkable low-temperature CO oxidation activities over other base metals, and this has been demonstrated by several research groups [107, 181, 182]. These TOFs of around 65 to 280 s^{-1} at a temperature range between 260 and 520 °C for the CoNi-30nm pellet system compare favourably with the TOF values reported for noble metals, especially Pt. McClure et al. reported similar TOFs of around 20 to 300 s^{-1} for their silica-supported Pt catalysts at higher temperatures of 290-380 °C at P_{CO}/ P_{O2} = 0.5-2 [170]. McRea et al. also reported TOF value of 20 s^{-1} at 350 °C over unsupported Pt (557) single crystals at P_{CO}/ P_{O2} = 0.4 [183]. At a higher temperature of 520 °C, CoNi-30nm and Ni-30nm pellet systems showed high TOFs of around 213 and 280 s^{-1} respectively, which correspond to around 0.675 mmol s^{-1} m^{-2} and 0.82 mmol s^{-1} m^{-2} (16 and 23 % CO conversion) respectively.

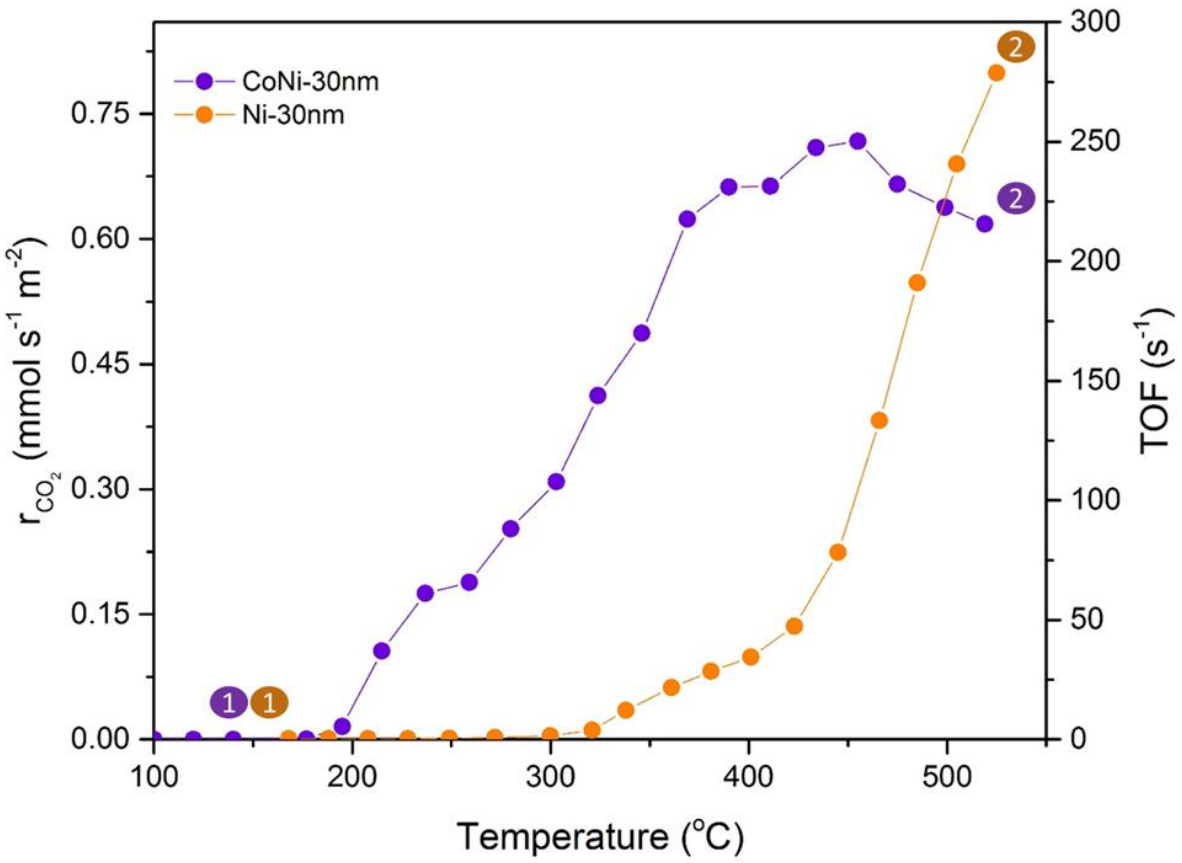

Figure 5-3 CO_2 production rates, r_{CO_2}, and TOF values as a function of temperature (light-off) over Ni-30nm and CoNi-30nm pellet systems under CO oxidation reaction with an inlet feed gas mixture of P_{CO} = 0.6 kPa, P_{O2} = 1.0 kPa, F_t = 150 ml min^{-1}. The rate is normalised with respect to the pellet area decorated with particles (top side in **Figure 5-1**). The numbers are colour-coded to highlight the catalytic key stages at which particle tracking or other analyses were conducted and the start and end points of the catalytic experiment, following the numbered key stages and catalytic experiment listed in **Table 5-1**. Corresponding TOF values are shown on the right axis and error of around ±5 % were found during repeated experiments at each measured point.

The correlation between their catalytic activities and particle characteristics was then assessed via the particle tracking experiment by monitoring the surface morphologies under SEM at Stage two (after light-off). **Figure 5-4** compares the SEM micrographs of (A, B) CoNi-30nm and (C, D) Ni-30nm pellet systems at two different experimental stages: (1) fresh and (2) after the light-off experiment. As previously observed, the fresh surfaces exhibit rounded exsolved particles (**Figure 5-4A, C**), however, following light-off experiments, the surface particles display expanded and faceted features on both pellet surfaces (**Figure 5-4B, D**). It is believed that the expanded particles are due to the differences in oxidation mechanisms and the different degree of metal particle oxidation between Co and Ni. This will be explained later on in this chapter.

For the Ni-30nm pellet system, the increased size of Ni particles exhibited somewhat similar or slightly larger values of oxidised-to-fresh size ratio than the expected lattice expansion from metallic Ni (Ni°) to rocksalt nickel (II) oxides (NiO), while still retaining the metal core due to the slower O_2 inward diffusion of Ni. However, for the CoNi-30nm pellet system, the appearance of edge structures and distinct dark spots on the tops of the particles, which are not observed on the Ni-30nm surface, are believed to be due to the formation of hollow cores. This is caused by a much faster Co outward diffusion compared to the inward O_2 diffusion once cobalt (II) oxide (CoO) is formed. This then resulted in the hollowing of the metal cores, expanding the particles laterally. The metal particles were also subjected to additional compressive strain when they expanded during light-off as a result of them being pinned to the support to begin with. Although the lattice expansion from metal to oxide phases was considerably larger than the metal-support expansion experienced by the support lattice, due to the lower O_2 diffusion rates, these strain-induced sites which are normally present at the metal oxide-support interface have been associated to provoke changes on the catalytic activities of supported metal catalysts [184]. It has been reported that this can affect the catalytic activities of metal catalysts, due to the modified electronic structure at the metal-support interface which then causes a perturbation in the shape formed by the expanding metal particles. This has been previously reported for other metals; for example, Commoti et al. reported the creation of facets and defect sites for gold (Au) supported on various reactive supports which then influenced the activity of the catalysts for CO oxidation, demonstrating the strong effect of metal-support interaction [185].

The detailed oxidation mechanisms of both exsolved metal systems are described and discussed in subsection **5.3.6**, which also includes an explanation supported by XPS results.

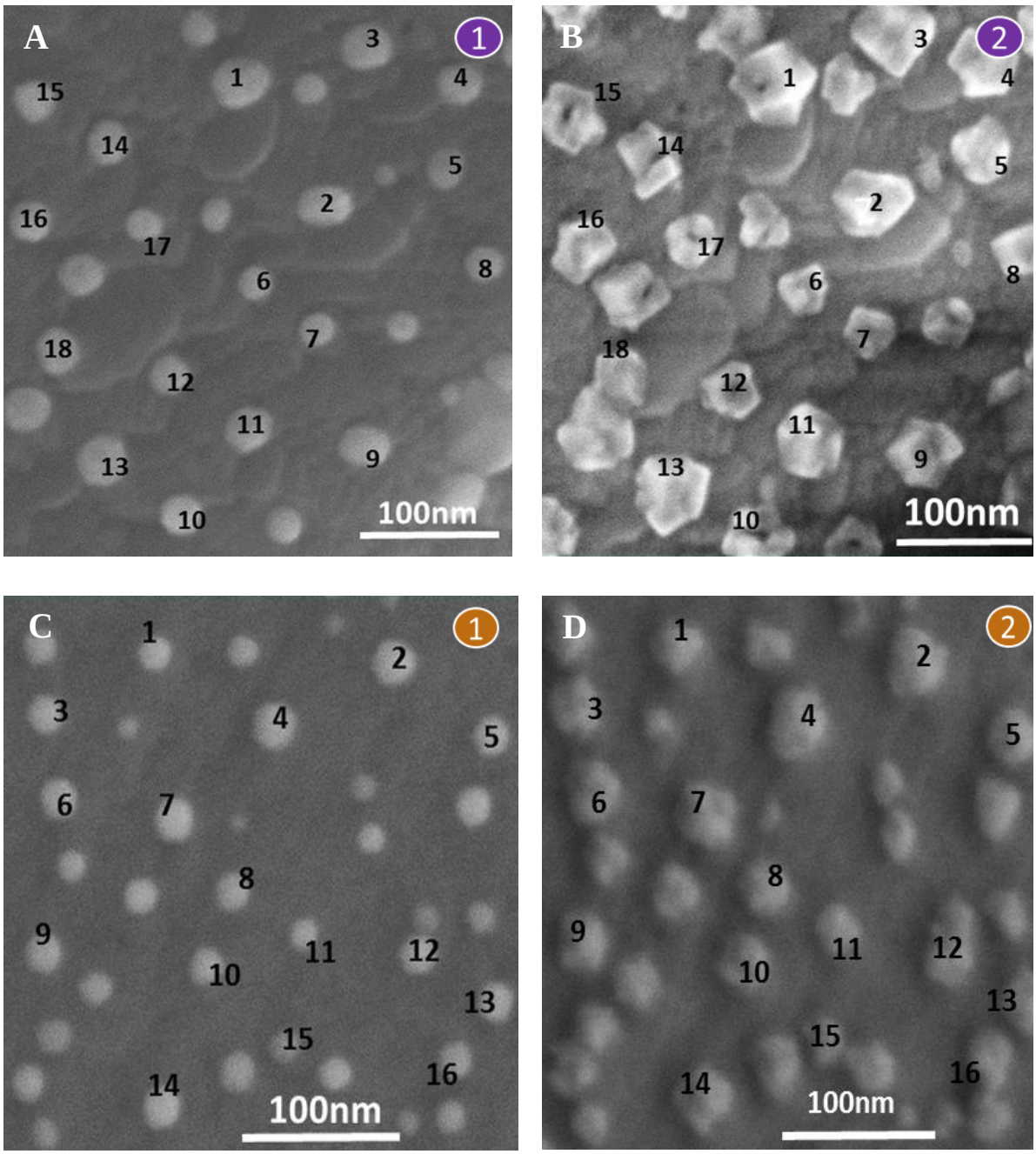

Figure 5-4 SEM micrographs of tracked areas for (A, B) CoNi-30nm and (C, D) Ni-30nm pellet systems collected at room temperature at the highlighted stages of catalytic testing with the colour-coded numbers as indicators of the sequence in which the experiments were carried out and also of the stages at which particle tracking or other analyses were conducted: with (1) fresh metal particles; and (2) particles after light-off.

5.3.5 CO kinetics and activation

This section describes the effect of CO partial pressures (CO kinetics) on the CO_2 production rates, r_{CO_2}, of the exsolved CoNi-30nm and Ni-30nm pellet systems. The CO kinetics experiment was performed in CO oxidation following the inlet feed gas mixtures listed in **Table 5-1** for Stage 3 and 4. In this experiment, P_{O2} was held constant while P_{CO} was allowed to vary

at 520 °C. The CO kinetics experiment involves a total flowrate, F_t, of 150 ml min^{-1} given at normal temperatures and pressures (NTP) with inlet feed gas mixtures containing constant P_{O2} of 0.64 kPa and with P_{CO} was varied stepwise between 0.5 to 18.87 kPa, with varying step sizes of 0.6 to 4 kPa. The steady state rates measurement was then recorded. **Figure 5-5** compares the CO_2 production rates, r_{CO_2}, of both CoNi-30nm and Ni-30nm pellet systems in the CO kinetics experiment. The dashed line, labelled as X_{20} in the figure, shows the limits at which 20 % of O_2 conversion is achieved by both pellet systems, corresponding to a CO_2 production rate, r_{CO_2}, of 1.54 mmol s^{-1} m^{-2}. To enable reliable kinetic data under differential conditions, we limit our data below this kinetic limit (dashed line).

For the Ni-30nm pellet system, the CO_2 production rates, r_{CO_2}, below the kinetic limit increase with increasing P_{CO} from 0.5 to 3.21 kPa with rate increments from 0.5 to 1.53 mmol s^{-1} m^{-2}. The CO_2 production rates, r_{CO_2} , continue to increase until P_{CO} = 18.87 kPa (Stage 4). The CO_2 production rate, r_{CO_2}, at this P_{CO} was around 4.5 mmol s^{-1} m^{-2} (~ 57 % of O_2 conversion). The CO_2 production rates, r_{CO_2}, of CoNi-30nm also increase with increasing P_{CO} (0.5-3.21 kPa), from 0.2 to 0.9 mmol s^{-1} m^{-2} below the kinetic limit. The CO_2 production rates, r_{CO_2}, of CoNi-30nm, however, peaked at between 3.21 to 4.5 kPa of CO (Stage 3), revealing a jump in rates of around one order of magnitude from 0.9 mmol s^{-1} m^{-2} (P_{CO} = 3.21 kPa) to 5.2 mmol s^{-1} m^{-2} (P_{CO} = 4.5 kPa), suggesting a possible occurrence of microstructural changes in the particles at this reaction condition. This also mirrored the results gained for the previous Ce, CoNi-7,1 powder system in the CO kinetics experiment (**Figure 4-9**), with a similar jump in rates ($r^*_{CO_2}$) although at slightly lower values of P_{CO} between 1.28 and 2.57 kPa. A further increment of P_{CO} up to 18.87 kPa (Stage 4) resulted in a marginal increase in CO_2 production rates, r_{CO_2}, from 5.2 to 7.1 mmol s^{-1} m^{-2}, signifying the completion of the reorganisations of the particles into stable structures. **Figure 5-5** also reveals that the CO_2 production rates, r_{CO_2}, appear to increase with increasing P_{CO}, although at this temperature (520 °C), the rates were limited by the integral condition of the reactor, operating at the high conversion of O_2, hence the reaction was mass transfer limited. The full O_2 conversion, which corresponds to around 7.8 mmol s^{-1} m^{-2}, was exhibited by the CoNi-30nm pellet systems at 18.87 kPa of CO (Stage 4).

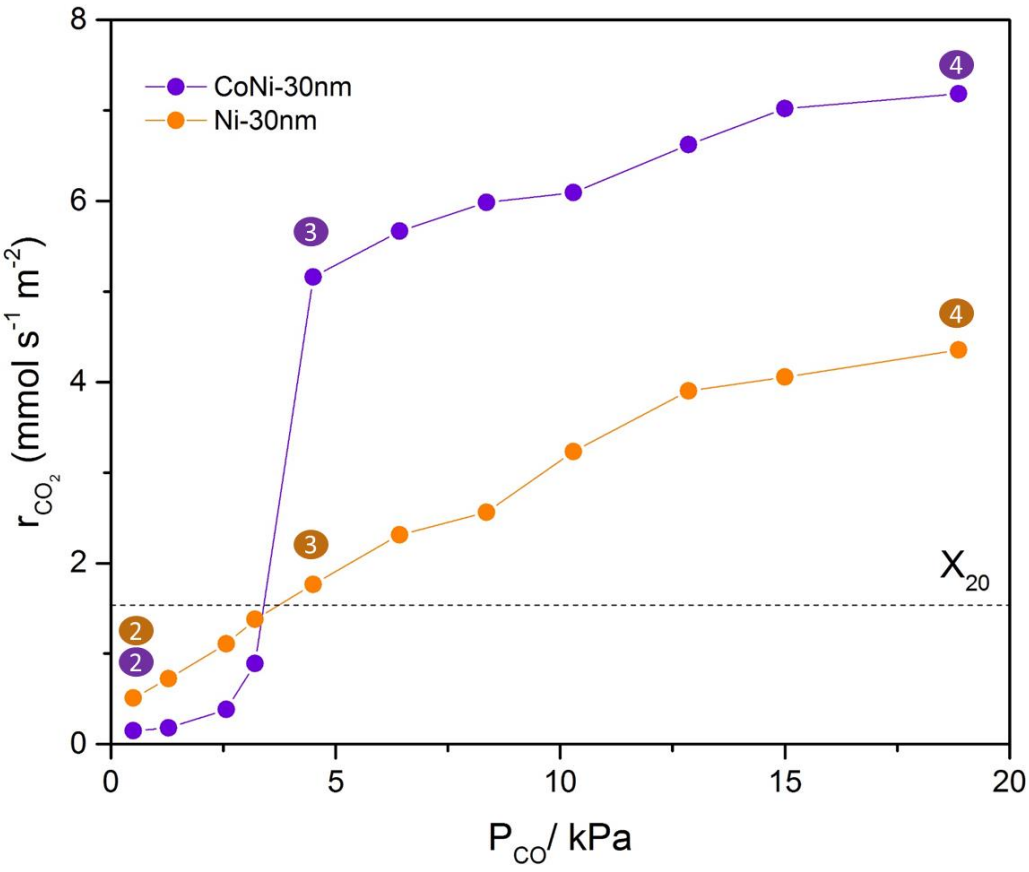

Figure 5-5 CO_2 production rates, r_{CO_2}, as a function of CO partial pressures (CO kinetics) over Ni-30nm and CoNi-30nm pellet systems in CO oxidation reaction with an inlet feed gas mixture of P_{CO} = 0.5-18.87 kPa, P_{O2} = 0.64 kPa, F_t = 150 ml min^{-1}. The rate is normalised with respect to the pellet area decorated with particles (the top side in **Figure 5-1**). The numbers are colour-coded to highlight the catalytic key stages at which the particle tracking or other analyses were conducted and the start and end points of the catalytic experiment, following the numbered key stages and catalytic experiments listed in **Table 5-1**. Error of around ±5 % were found during repeated experiments at each measured point.

In order to confirm our previous hypothesis regarding the rates jump exhibited by the CoNi-30nm pellet system, the microstructural changes at the CoNi-30nm pellet surface were examined under SEM at Stage 3 and 4. **Figure 5-6** shows the SEM micrographs of the CoNi-30nm pellet system at three experimental stages: (A) Stage 2, after the light-off experiment; (B) Stage 3, after the rate jump in the CO kinetics experiment; and (C) Stage 4, after the completion of the CO kinetics. After the rates jump (Stage 3), it seems that the expanded exsolved metal particles on the surface of the CoNi-30nm pellet system at Stage 2 were altered to become cube-like structures, although closer inspection of **Figure 5-6** shows the appearance of additional features which are believed to be empty sockets, especially at particle numbers 4, 5, 6, 7 and 17. This supports our previous hypothesis concerning the rates jump, which coincides with the microstructural changes in the metal particles, from expanded, faceted particles in Stage 2, into

cubic-like structures with several empty sockets in Stage 3. The formation of these empty sockets is caused by the dominant effect of hollowing which causes the particles to become dislocated from their sockets. Not only that, but several particles (1, 2, 3 and 14) were restructured into cubic structures and they also appear to relocate at the edge of their sockets, and at a particular angle, revealing perhaps a specific active geometric plane. These empty sockets, however, effectively reduce the population of the active structures to almost half of the initial particle population, equating to around 44 cubes μm^{-2}, from an initial population of 144 particles μm^{-2}. Further increments of P_{CO} up to 18.87 kPa of CO (Stage 4) which show minimal increases in CO_2 production rates, r_{CO_2}, matching the minimal microstructural changes between Stage 3 and 4 (compare **Figure 5-6B** and **C**), signifying the completion of the formation of stable nanocubic structures. On the other hand, the Ni-30nm pellet system shows surface structures similar to the one in Stage 2 (**Figure 5-4D**) and this was preserved throughout the experiment. Further analysis is required to fully investigate the reasoning behind the decreased metal population and since Ni was present, the possibility of producing the toxic and volatile Ni carbonyls (e.g. $Ni(Co)_4$) [186] needs to be investigated via EDX, for example. This will be included for future recommended work.

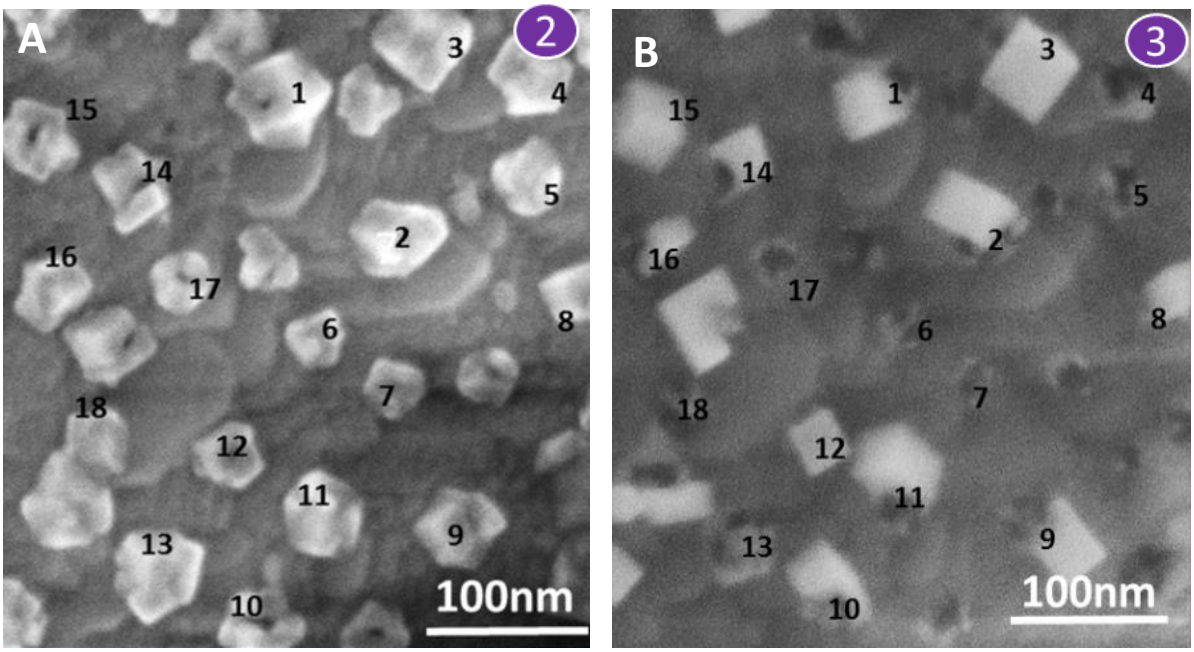

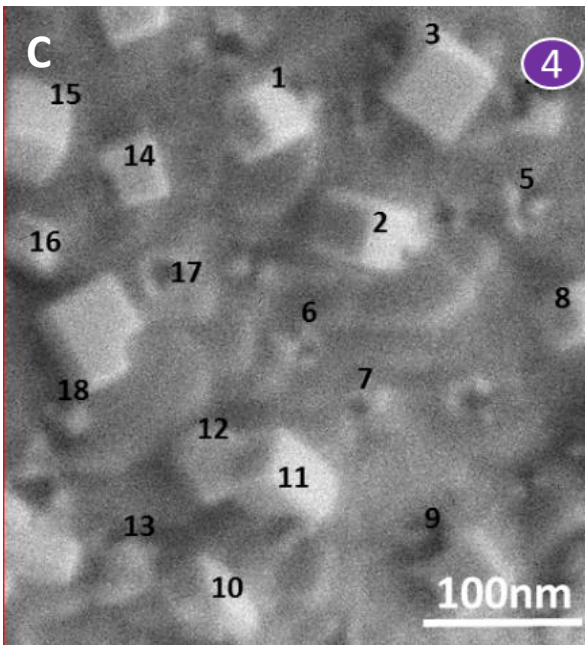

Figure 5-6 SEM micrographs of tracked areas for CoNi-30nm pellet system collected at room temperature at the highlighted stages of catalytic testing with the colour-coded numbers as indicators of the sequence in which the experiments were carried out and also the stages at which particle tracking or other analyses were conducted: (2) faceted metal particles after light off; (3) cubic-like structures formed during the partial CO kinetic experiment; and (4) final 'cube' microstructure after completion of the CO kinetic.

Both pellet systems were then subjected to another light-off experiment (Stage 5), following the CO kinetics (Stage 4) as listed in **Table 5-1**. This was performed in order to assess how the CO_2 production rates, r_{CO_2}, and TOFs were affected due to the change in the surface structures of the CoNi-30nm pellet system. The experimental conditions employed here are similar to those reported for the previous light-off, as described in section **5.3.4.** In order to minimise redundancy, experimental descriptions will only be given for experiments that have not been previously explained. Thus, in some part of the thesis, readers will need to refer to specific sections, figures or tables describing the relevant material. **Figure 5-7** shows the rates of CO_2 production, r_{CO_2}, and TOFs of the CoNi-30nm and Ni-30nm pellet systems in the light-off following the microstructural surface changes of the CoNi-30nm. The dashed horizontal line, labelled as X_{20} in the figure, shows the limit at which 20 % of CO conversion is achieved by both pellet systems in order to measure reliable kinetic data under differential conditions. The CO_2 production rates, r_{CO_2}, and TOFs of the restructured pellet (henceforth referred to as the activated CoNi-30nm pellet system) are represented by the dashed purple plot (from Stage 4 to Stage 5).

For the Ni-30nm pellet system, no significant activations of the CO_2 production rates, r_{CO_2}, and TOFs were observed from 300 to 500 °C, although slight increases in CO_2 production rates, r_{CO_2} , and TOFs were observed at 520 °C, from 0.799 mmol s^{-1} m^{-2} (277.75 s^{-1}) to 0.957 mmol s^{-1} m^{-2} (332.75 s^{-1}). The CO_2 production rates, r_{CO_2}, did not changed with temperature, even though the particles were shown to grow from 30 nm to around 39 nm and the microstructure and TOFs were preserved , revealing the high stability of these exsolved Ni system. This is not often observed with most supported metal catalysts due to the size-dependency of the activities, which would result in activity loss in metal-based catalysts. Comotti et al. observed an activity loss displayed by their supported gold catalysts due to the growth of the gold particles from 3 nm to 4.9 nm following calcination at higher temperatures [185]. At such, it was believed that the NiO component at the metal-support interface, with strong interaction with the perovskite support, as is evident from the lack of sintering (e.g. microstructural change), was the potential active site for this exsolved Ni system. This has also been observed by Tang et al. in their study of the effect of Ni contents on the CO oxidation activities of NiO-CeO_2 catalysts, and they attributed the high CO conversion of ~70 % at 225 °C to the interfacial NiO component along with the stronger NiO-support interaction. They also ruled out the effect of the change in particle size as the dominant factor influencing the activities [187].

On the other hand, for the CoNi-30nm system, it can be seen that the minimum temperature for measurable CO_2 production rate, r_{CO_2}, and TOF has been compromised, with the activated CoNi-30nm pellet system reaching 5 % of CO conversion at a higher temperature of 330 °C, which is 80 °C higher than what was observed previously with its fresh counterpart at 250 °C. Below the previously mentioned temperatures, the CO_2 production rates, r_{CO_2}, were below the minimum measurable limit of the IR analyser (0.037 mmol s^{-1} m^{-2}). Below the kinetic limit, for instance, at around 300 to 310 °C, the TOF values differ quite significantly between both exsolved CoNi pellet systems. The activated CoNi-30nm pellet system recorded a value of TOF of around 200 s^{-1} while its fresh counterpart only managed to achieved around 100 s^{-1}. This corresponds to around 10 % of CO conversion by both pellet systems. At 520 °C, an enhanced CO_2 production rate, r_{CO_2}, was observed for the activated CoNi-30nm pellet system, showing more than twice the initial CO_2 production rates, r_{CO_2}, from 0.62 mmol s^{-1} m^{-2} for fresh CoNi-30nm to around 1.58 mmol s^{-1} m^{-2}. A TOF value of around 1155 s^{-1} was recorded for the activated CoNi-30nm pellet system, which was five times higher than the fresh pellet system, with a value of around 215 s^{-1}. Furthermore, at higher temperatures between 320 to 520 °C, the activated CoNi-30nm showed superior TOFs ranging from 187-1155 s^{-1} in comparison to the

initial TOFs of the CoNi-30nm and Ni-30nm pellet systems (125-225 s^{-1}). Surprisingly, these enhanced CO_2 production rates, r_{CO_2}, and TOFs were achieved by an essentially less active area, as is evident from the particle populations given in the table inset in the figure. The enhanced CO_2 production rates, r_{CO_2}, and TOFs observed for the activated CoNi-30nm pellet system corroborate most studies showing that the activities of Co-based catalysts are known to be strongly dependent upon the microstructure, including the particle shapes, sizes and exposed planes, as is evident from the massive investigations performed recently in manipulating the Co microstructure through pre-treatment in order to form specific active structures to suit specific reactions such as CO oxidation [15, 188].

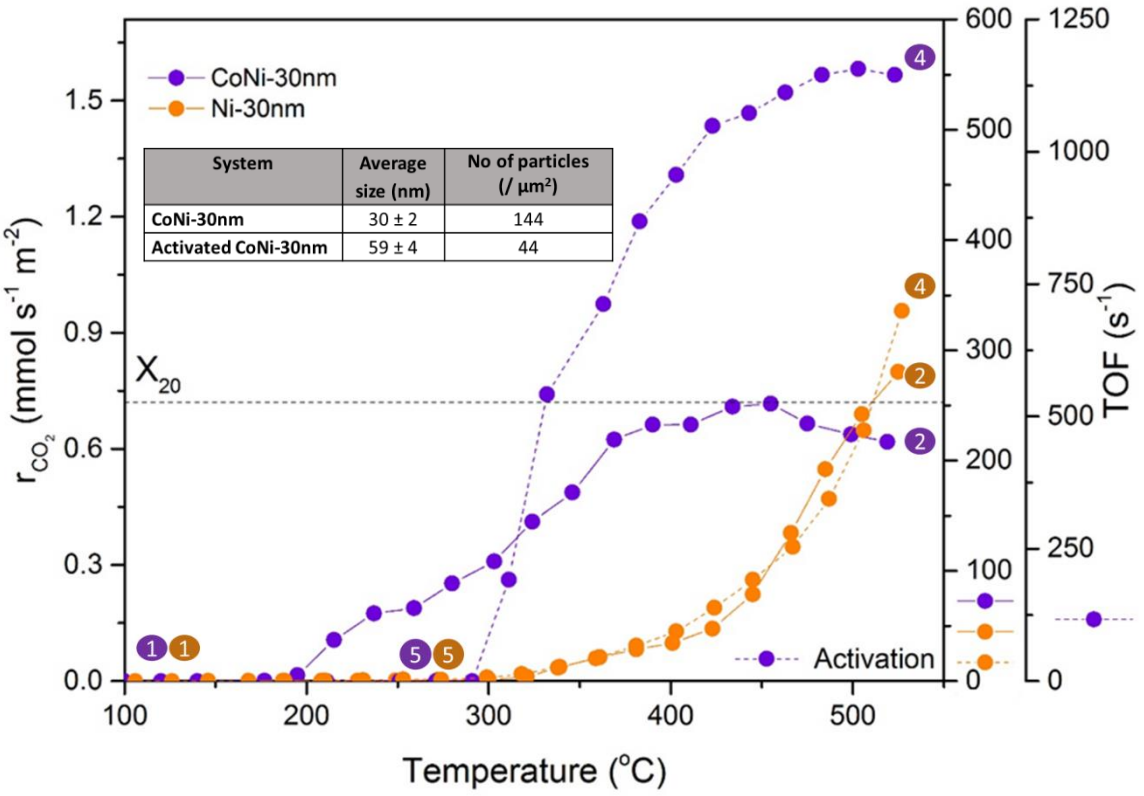

Figure 5-7 CO_2 production rates, r_{CO_2}, and TOF values as a function of temperature (light-off) over Ni-30nm and CoNi-30nm pellet systems in the CO oxidation reaction with an inlet feed gas mixture of P_{CO} = 0.6 kPa, P_{O2} = 1.0 kPa, F_t = 150 ml min^{-1}. The rate is normalised with respect to the pellet area decorated with particles (top side in **Figure 5-1**). The numbers are colour-coded to highlight the start and end points of each catalytic experiment and also the stages at which particle tracking or other measurements were conducted, following the key stages and catalytic experiments listed in **Table 5-1**. Corresponding TOF values are shown on the right axes; with the outer axis corresponding to the TOFs of the activated CoNi-30nm pellet system, while the inner axis representing the TOFs for fresh CoNi-30nm and Ni-30nm. The inset table shows the difference in the number of particles between the fresh and activated

CoNi-30nm pellet systems. Error of around ±5 % were found during repeated experiments at each measured point.

Another light-off was performed using a similar activated CoNi-30nm pellet system but with the particles being removed mechanically, aiming to quickly test the role of the cubic structures and/or their interactions with the support. Significant drops in CO_2 production rates, r_{CO_2}, were observed at all temperatures which further indicates the critical role of these two key structures; nanocubes and cube-perovskite interface, which reinforce the enhanced activities of the exsolved CoNi pellet system (Appendices: **Figure A-12**). This suggests that the potential active sites may lie on the cubic structure itself and/or its metal-support interface, although we cannot pinpoint the exact origin of the enhanced activities at this point, which in itself merits in-depth future investigation.

The TOF values of these exsolved Ni and CoNi metal systems investigated in this work were compared to some of the reported active catalysts in CO oxidation, as listed in **Table 5-3** below. Again, most of the reported base metal catalysts show low TOFs at the reaction conditions mentioned, although most of the studies did not give clear information on the catalyst parameters, such as the catalyst weight, which then lead to uncertainty concerning their actual activities. The TOFs of several metal catalysts using the nearest conditions as ours were chosen in order to provide an appropriate comparison, although direct comparison was impossible due to the differences in reaction conditions and/or the structure of the catalyst itself. The TOFs of these exsolved systems were higher than those reported in the table, although at much higher temperatures than the ones reported for base metals. For instance, at 520 °C, TOFs in the range of 1000 s^{-1} were measured, indicating the higher stability of these systems against sintering at high temperatures and hence preserving the activities at such temperatures. This is, however, not the case in most studies, which demonstrates the benefits of Co in low-temperature CO oxidation, but they also show a loss in activity at higher temperatures such as RT [189]. At a lower temperature of 200 °C, An et al. reported TOFs of around 0.015 s^{-1} for their pure mesoporous Co_3O_4 and NiO at P_{CO}/ P_{O2}= 0.4 [160].

Table 5-3 Previously reported studies of Pt-, Co- and Ni-based catalysts, comparing the inlet feed gas mixture conditions and TOF values to those of the work reported in this chapter

Catalyst	Type of Co catalysts	Catalysts weight (g)	Reaction conditions	TOF	Ref.
Ni-30nm	Exsolved	Pellet	CO/ O_2=0.6	At 200 °C TOF_{fresh} = 0 s^{-1} At 520 °C	This work

				TOF $_{fresh}$ = 280-300 s^{-1}	
CoNi-30nm	Exsolved	Pellet	CO/ O_2=0.6	At 200°C TOF $_{fresh}$ = 40 s^{-1} At 520°C TOF $_{fresh}$ = 400 s^{-1}	This work
Activated CoNi-30nm	Exsolved	Pellet	CO/ O_2=0.6	At 200°C TOF $_{fresh}$ = 0 s^{-1} At 520°C TOF $_{fresh}$ = 1125 s^{-1}	This work
Pt	Pt (1wt.) on Al_2O_3	0.03	CO/ O_2=0.5	At 160°C TOF=2 s^{-1}	[157]
Encapsulated Pt/ Si TiO_2	Polymer citrate	0.1	CO/ O_2= 0.4	T_{100}=195°C TOF at T_{100}=3.92 s^{-1}	[158]
Encapsulated Rh/ Si TiO_2	Polymer citrate	0.1	CO/ O_2= 0.4	T_{100}=140°C TOF at T_{100}=5.09 s^{-1}	[158]
Encapsulated Ru/ Si TiO_2	Polymer citrate	0.1	CO/ O_2= 0.4	T_{100}=165°C TOF at T_{100}=3.8 s^{-1}	[158]
Co_3O_4	Nano belts Nano cubes		CO/O_2= 0.125	T_{10} = 56°C, TOF $_{NB}$=0.0074s^{-1} TOF $_{NC}$=0.0027s^{-1}	[190]
Co_3O_4	Pure mesoporous oxides	0.01-0.1	CO/ O_2= 0.4	At 200°C TOF=0.015 s^{-1}	[160]
Co_3O_4	Nanocubes and Co_3O_4/ $Co(OH)_2$	0.1	CO/ O_2=0.06	At 100°C TOF_{NC}=0.024 s^{-1} $TOF_{Co(OH)2}$=1.23 s^{-1}	[182]
NiO	Pure mesoporous oxides	0.01-0.1	CO/ O_2= 0.4	At 200°C TOF=0.02 s^{-1}	[160]

* T_{100} represents the temperature at which full CO conversion was achieved while T_{10} represents the temperature at which 10 % of CO was converted into CO_2 for the catalysts mentioned.

The microstructure of the pellet surface was again viewed under SEM following the previous light-off. **Figure 5-8** presents the SEM micrographs of the CoNi-30nm pellet system at two experimental stages: (A) Stage 4, after completion of the CO kinetics; (B) Stage 5, after the light-off experiment. There are no significant changes in microstructure observed between Stage 4 and 5, and the fact that these structures were preserved after the experiments signify the

high stability of these nanocubic structures againts sintering during the experiment. It is also worth noting that the enhanced TOFs at high temperatures were measured using these rather intricate particle structures, which suggests that particular active structures were formed during the activation process.

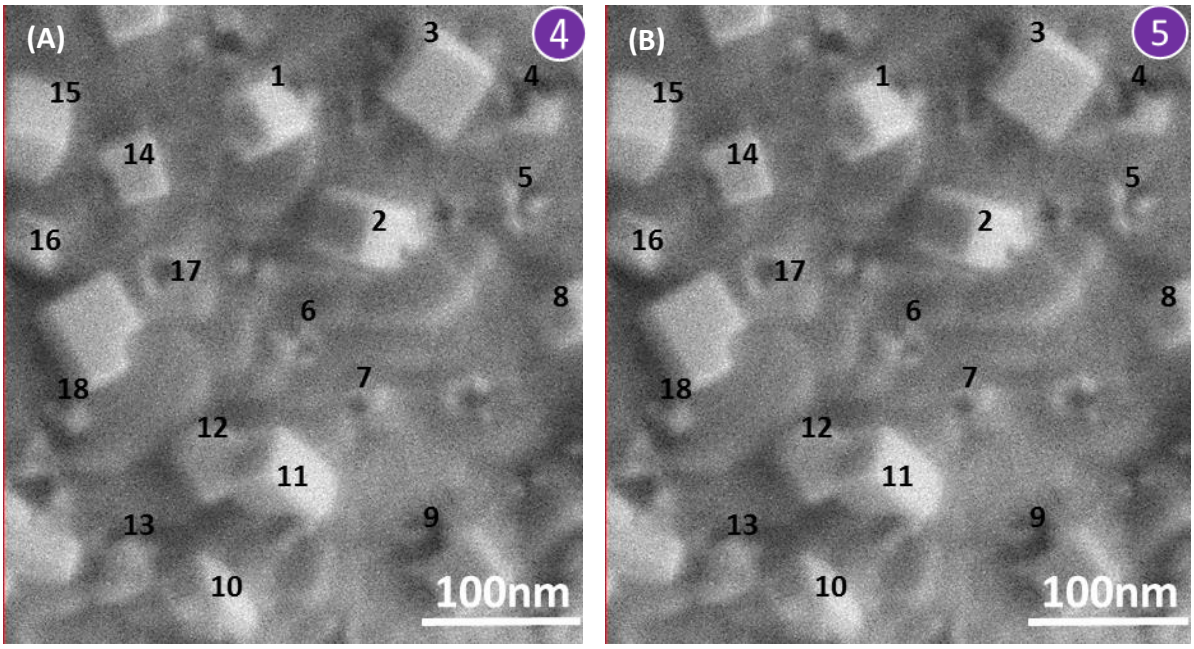

Figure 5-8 SEM micrographs of tracked areas for CoNi-30nm pellet system collected at room temperature at the highlighted stages of catalytic testing with the colour-coded numbers as indicators of the sequence in which the experiments were carried out and also the stages at which particle tracking or other analyses were conducted: (4) final 'cube' microstructure after completion of the CO kinetic; and (5) preserved cube structure after another light-off.

5.3.6 XPS characterisations

The surface chemistry of the CoNi-30nm pellet system was probed using XPS, aiming to investigate the change in metal oxidation states and binding energies of the CoNi particles during the occurrence of the microstructural changes. The XPS analyses were performed at three stages (Stage 1, 2 and 4) to illustrate the surface chemistry at three different microstructures: the initial rounded particles, edge structure with hollow cores, and cubic structures. **Figure 5-9** shows the results obtained from the XPS analyses, including: (A) the full XPS spectra, consisting of all the surface components at all three stages; (B) Co 2p; and (C) O 1s spectra. The full XPS spectra for all three stages were very similar, with all six components present at all three stages but at slightly different shifts and intensities.

For Co, two pairs of sharp characteristic peaks between ~781 and 806 eV were found in all three stages, indicating the presence of oxide species, consisted of Co^{2+} and Co^{3+}. These peaks combine with the pair spin-orbit splitting between the two peaks of around 16 eV, in agreement

with Wang et al. who also observed this as a key characteristic for a spinel structure, confirming the formation of the spinel Co_3O_4 structure [191, 192]. Initially, the Co 2p spectra showed broad mixed oxidation (782, 798 eV for Co^{3+} and 787, 804 eV for Co^{2+}) and metallic Co (781 eV) peaks at around ~780-790 eV, associated with a CoO-like peaks [193], with a narrow Co_3O_4 peak suggesting that the fresh pellet surface was slightly oxidised prior to light-off (Stage 1). Upon oxidation during light-off (Stage 2), the CoO/Co_3O_4 peaks were slightly broadened with reduced satellite peaks. Two widened Co^{2+} peaks were found at 786.5 and 803 eV, suggesting the reduced amount of Co^{2+} ions after the lightoff (oxidation to Co^{3+}) whilst two sharp peaks at 781 and 796.5 eV were attributed to Co^{3+}. The satellite peaks were increased upon exposure under CO-rich conditions (Stage 4) and the CoO/Co_3O_4 peak shifted towards the spinel Co_3O_4 structure, indicated by the increase in Co^{2+} and Co^{3+} intensities as the spinel structure appears, which coincides with the formation of the cubic structures. At this stage, the increases were more apparent for Co^{2+}, as is evident from the high binding energy shoulders at 786 and 803 eV. This is indicative of the incomplete conversion of Co_3O_4 to CoO during the reduction under CO-rich conditions. This is probably due to the partial formation of metal-support components, which are less oxidisable, and is indicative of a higher metal-support interaction between the cubes and the perovskite support. This has also been observed by Riva et al., who investiaged the effect of metal-support interaction for their titania-supported Co catalyst, and they found that the formation of Co-support components resulted in less reducible Co at the employed reduction conditions, and this was attributed to the higher metal-support interactions of these phases [194].

The three O 1s spectra in **Figure 5-9 C** can be deconvoluted into two main peaks (529.2 and 533 eV) between 528 and 533 eV, confirming the presence of both surface lattice oxygen (O_{latt}) and surface adsorbed oxygen (O_{ads}) [195] on the surface of the CoNi-30nm pellet system. These oxygen species are known to be strong electrophilic reactants which are generally responsible for the total oxidation of CO on oxide materials [188]. A more prominent lattice O_2 peak was observed after light off (Stage 2) and another even more so after activation (Stage 4) compared to its fresh surface, indicating the increase in oxygen species which is beneficial for the oxidation of CO. The O 1s peaks were also shifted towards the lower binding energies, which has also been observed previously by Kim et al. for a spinel $NiCo_2O_4$ and Co_3O_4 [196].

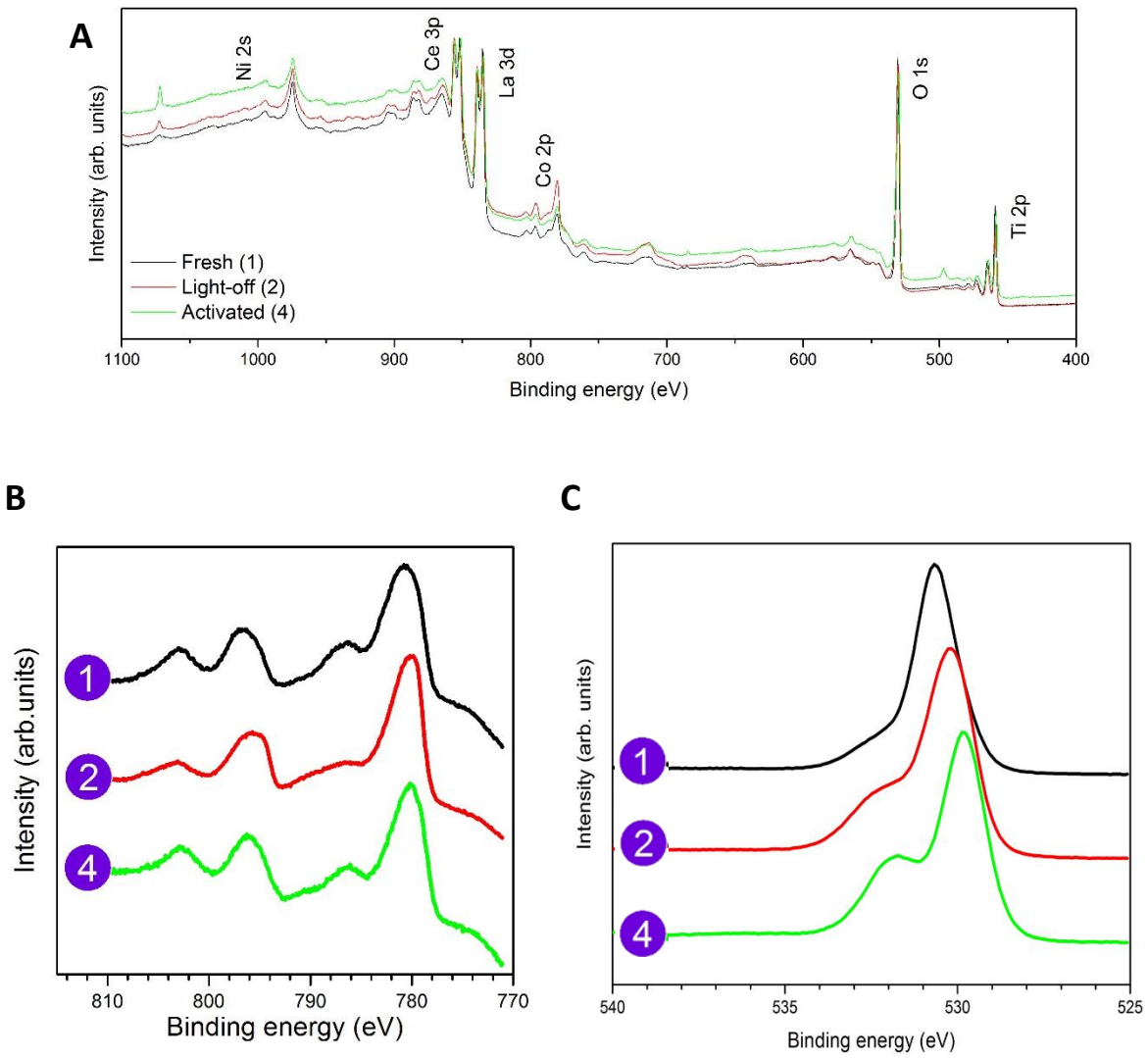

Figure 5-9 XPS details for the CoNi-30nm pellet system at three key stages (1, 2 and 4): (A) Full XPS survey; (B) Co 2p XPS spectra collected at room temperature; and (C) O 1s spectra bands at the highlighted stages.

To sum up, the exsolved metal particles on the surface of the fresh CoNi-30nm pellet system initially exhibited a rounded shape with a slight observed surface oxidation and, following the light-off experiment, the particles were faceted and expanded due to the oxidation of the Co particles, as confirmed by the increase in Co^{2+} and Co^{3+} in the XPS spectra. Exposure to CO-rich atmospheres increased the amount of Co^{2+}, indicating the possibility of an incomplete transition from CoO into Co_3O_4 spinel structures as the cubic structures were formed. An increment in oxygen species was also observed, which might also contribute to the observed enhanced CO oxidation activities after the formation of cubic structures.

In the light of the surface microstructural changes viewed under SEM and the XPS analyses of each microstructure namely the initial rounded particles, edge structure with hollow cores, and

the cubic structures, a possible oxidation mechanism can be proposed which we believe occurred during the light-off and CO kinetic experiments. **Figure 5-10** shows a schematic diagram of the possible oxidation mechanisms of the Ni and CoNi particles on the surface the Ni-30nm and CoNi-30nm pellet systems. The significant differences in behaviour between the Ni and CoNi particles, especially during light-off, could be associated with the different nature of the metal oxidation mechanisms which come into play particularly during the light-off. This appears to have altered the socketed characteristics of the CoNi particles, assisting the displacement of the CoNi particles from their sockets in the following CO kinetics experiment. These findings may have important implications for designing Co-based catalysts that can rival Pt in the future, which can be tuned to give the desired activities for specific reactions.

The Ni particles on the Ni-30nm pellet surface followed a typical oxidation behaviour from metallic Ni to rocksalt NiO structure, exhibiting asymmetrical particles with non-smooth shells as they crystallise to NiO due to the high temperature oxidation, which is believed to occur during the light-off experiment (see **Figure 5-10-2**). The formation of voids or hollow cores was prevented due to the minimal inward diffusion of O and the growth of the core Ni atoms by diffusion solely through the existing Ni/ NiO layer. These results match those observed by Railsback et al., who reported similar observations with a similar particle size (~26 nm) and oxidation temperature [197]. These NiO structures aided the total oxidation of CO, as is evident from the high TOFs reported under light-off, owing to the strong CO removal activity by acting as a promoter to remove CO by weakening the C-O bond for easier dissociation to CO_2 [178].

Conversely, the chemical transformation of Co particles on the CoNi-30nm surface via oxidation involved a phase transformation from metallic Co into the predominant Co_3O_4 spinel structures with an oxide intermediate phase of the rocksalt CoO structure, following a rather complicated diffusion mechanism known as the Kirkendall Effect. The difference in diffusion rates between Co and O resulted in the observed hollow structures as shown in **Figure 5-10B**. In order to explain what happened during this nanoscale restructuring of Co, a schematic interpretation is presented in **Figure 5-10(4-9)**. Upon experiencing oxidation in the light-off experiment, a thin oxide layer (CoO) was formed on the surface of the metallic Co particles. In the metallic Co, O diffuses outward faster than Co, allowing it to enter Co° particles, and once the level of O was adequate, CoO was formed (see **Figure 5-10-5**). The fast diffusing species then changed to Co, allowing Co to diffuse outward faster in the CoO phase than the inward diffusion of O, hollowing the core and expanding the oxide shell laterally (see **Figure 5-10-6** and **B**). Further oxidation at high temperatures resulted in continuous rapid lateral expansion of

the confined core to complete the conversion, causing an extensive strain force due to its being initially pinned to the support, inducing the oxide layer to rupture and exposing the inner core of the particles (see **Figure 5-10-7** and **B**) [198]. The formation of these hollow cores is believed to have weakened the socketed characteristics of the particles in the support, conceding the restructuring into cubes quite effortlessly upon exposure to CO-rich atmospheres (see **Figure 5-10-9** and **A**). Sadasivan et al. also observed the breaking of the large hollow Co particles formed by the 29 nm Co particles during a preceding oxidation to form smaller particles during subsequent reduction [199]. This outward expansion also brought the particles closer to each other, connecting certain particles which may then have further facilitated the restructuring into cubes. As the transformation from CoO to Co_3O_4 approached completion, with Co atoms as the mobile species and the O anion expected to be rigid due to the low diffusion activation energy of Co atoms in the CoO phase, no further hollowing process was observed during the complete transition to Co_3O_4. Instead, the 'cubes' were rearranged to sit next to the empty sockets, partially exposing them in the process [200, 201]. This resulted in a greater and more anisotropic expansion upon oxidation as compared to Ni particles.

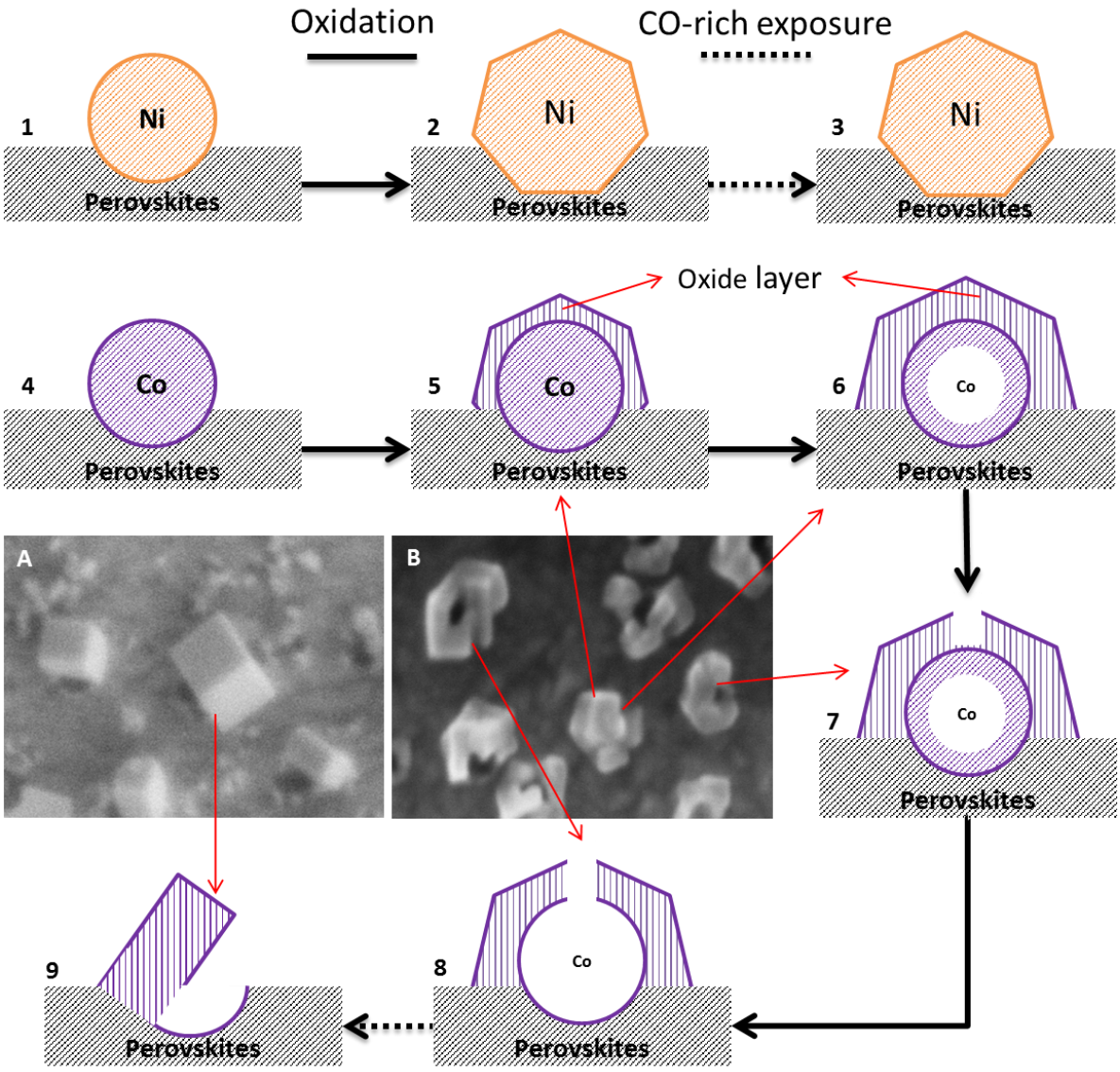

Figure 5-10 Schematic mechanism for the oxidation of Ni and Co particles via the Kirkendall effect: (1-9) represent a schematic diagram of the restructuring, where (A) shows the particle details from the CoNi-30nm system after activation in a CO-rich environment and (B) provides particle details from the CoNi-30nm system after the light off.

5.3.7 Characterisations of active cubic structures

A more detailed account of the activated slanted nanocube structures is presented in this subsection in order to understand the nature of these active structures, and particularly the origin of their enhanced activity after activation. Various surface chemical analyses were performed on the activated CoNi-30nm pellet system, including XRD, STEM-EDX and XPS. The XRD of the cube structures was performed primarily to determine the crystal structure and the lattice parameter of Co. **Figure 5-11** below highlights the perovskite peaks, which include a set of broad peaks (*) indicative of the presence of the spinel-type structure. These diffraction patterns evidently indicate the presence of Co spinel peaks. These results seem to be consistent with

other studies which also reported the formation of the Co spinel based on the presence of these modest intensity lines found at 2θ = 31.3, 36.9, 38.9 and 44.9 °, which correspond to the (220), (311), (222) and (400) reflection planes of Co_3O_4 (space group: Fd3m, ICSD − 69378) [202, 203]. These XRD results were then used to calculate the lattice spacing, d, and the lattice parameter, a, via Braggs Law. The diffraction peak at 36.9 °, correspoding to the (311) reflection was chosen instead of the lower 31.3 ° (220) reflection due to a possible overlap between the peak at 31.3 ° and the perovskite peak. The lattice parameter, a, was found to be around 0.81 nm, which is in agreement with the large spinel lattice parameters of around 0.8-0.9 nm reported by Sickafus et. al [204]. Lv et al. also found similar diffraction peaks (220, 311 and 400) attributed to the Co_3O_4 phase in spinel structures, confirming the presence of single crystal Co_3O_4 nanocubes on the surface [182].

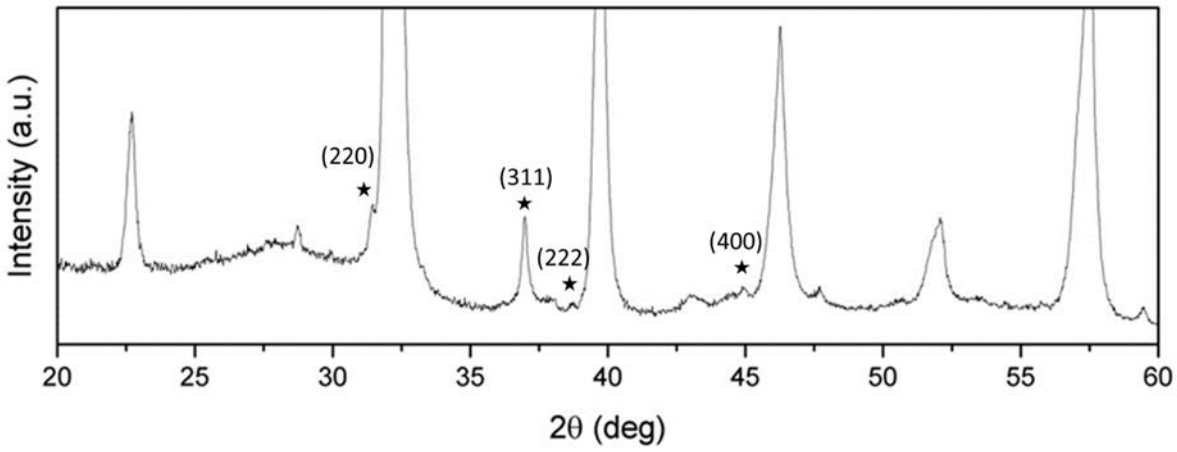

Figure 5-11 XRD pattern of the cube structure corresponding to the structure in **Figure 5-10**A, with the asterisk symbols indicating the peaks originating from the spinel structure ascribed to the 'cubes', while the rest of the major reflections originate from the underlying perovskite.

The cubic nanostructures were further analysed in detail via TEM-EDX, aiming to characterise the morphology and to obtain an elemental map across the nanocubes. **Figure 5-12** presents the results obtained from the STEM-EDX analysis. The top half of the figure shows (A) the cross-sectional TEM of the cube structure, extracted by the FIB; and (B) the TEM-EDX elemental line scan (red dashed line in (A)) across the perovskite interface. It is apparent from the cross-sectional image that the cube was relocated at the edge of a possibly empty socket (see white spot at Zone 2 in **Figure 5-12A**). Also, it is clearly shown in **Figure 5-12B** that the cubic spinel crystals were rich in Co, although also containing some Ni and oxygen. However, the concentrations of Co and Ni were gradually depleted as the metal-perovskites interface was approached (depth of ~100 nm, Zone 2) and this is likely to be due to the fact that this might be

the region where the exsolution occurred prior to dislocation. This further supports the presence of the empty sockets at which the cubes were purportedly fixed, as is apparent from the negligible amount of Co at this region. Further down the perovskite lattice (Zone 3), negligible amounts of Co and Ni were observed, which confirmed the occurrence of exsolution from this region with the perovskite lattice containing only La and Ti.

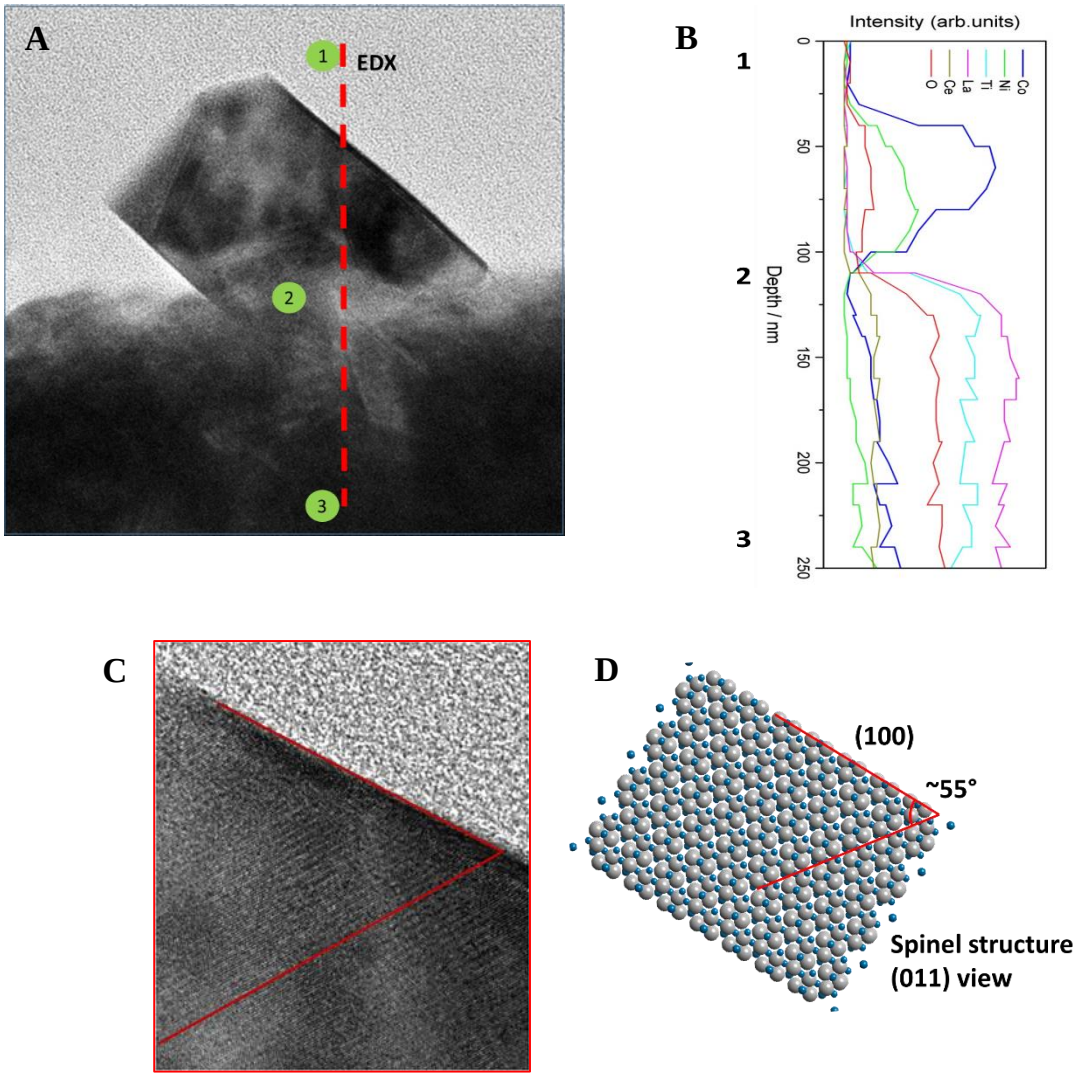

Figure 5-12 TEM-EDX scan and the crystal structures of the cube: (A) cross-sectional TEM micrograph extracted from **Figure 5-10A** by FIB; (B) TEM-EDX analysis across the dotted line shown in (A); (C) details from (A) highlighting the angle between the surface of the 'cube' and the observed atomic planes; and (D) spinel crystal structure and orientation corresponding to (C).

The bottom half of the figure reveals the angle of which the cube was planted at the edge of the empty sockets and also the possible exposed active atomic plane, which might explain the enhanced activity of this exsolved CoNi system. By comparing a spinel crystal structure schematic with the image in (Figure 5 12C), it is revealed that the cubes were planted at an angle of ~55 ° with an exposed (100) atomic plane, at the edge of their empty sockets on a

perovskite oxide surface mainly composed of La and Ti. This is a rather interesting outcome if we relate this to their enhanced TOFs since it has been widely reported that the (100) plane is considered inactive under CO oxidation, compared to other higher index planes [205].

In order to understand the phase transitions of these cube structures, the mapping of the Co-valence state with a high spatial resolution on the nanoscale is required. XPS was used to determine the atomic composition and elemental chemical state of the restructured CoNi-30nm pellet. **Figure 5-13A** and **B** show the XPS results obtained, where (A) reveals the full XPS spectra and the elemental quantification in the inserted pie chart achieved via XPS. Since the XPS spectra was known to primarily mirror the composition on the surface region, a small amount of Co (refer pie chart, blue for Co) of around 6 % were present on the surface, suggesting the lack of Co in the near surface region, similar to the results reported for the EDX spectrum earlier. The higher atomic percentage of oxygen (red, 65 %) suggests that the perovskite surface was covered with oxides, with La and Ti as the main bulk components. On the other hand, **Figure 5-13B** presents the best fitting for Co 2p 3/2 and Co 2p 1/2 spectra of the cube structure and the deconvolution of both spectra was made using reference peaks for various oxidations of Co adopted from previous researches [206, 207], with 780.4, 795.8 eV for Co^{2+} and 778.5, 794.2 eV for Co^{3+}. Furthermore, the reference values of 784.2, 787.9 and 802.8 eV for the Co^{2+}, Co^{3+} satellite shake-up peaks were also included in the deconvolution. The spectra were deconvoluted into ten separate peaks, corresponding to Co^{2+} and Co^{3+}. These spectra confirm the existence of both oxidation states, which present in a spinel Co_3O_4 structures. This is again consistent with the results obtained from XRD. However, the difference in peaks intensity between oxidation states clearly revealed that Co ions were mainly present as Co^{2+} in these cube structures. The cubes were also briefly analysed by Electron Energy Loss Spectroscopy (EELS). The EELS analysis of valence state was carried out since the intensity ratio of L_3/L_2 for Co is very sensitive to the valence state of Co, which then simplifies interpretation of the spectra (**Figure A-13**). The L_3/L_2 ratio of Co ions in this structure was measured at ~3.88, thus confirming the average valence state of Co to be between +2 and +3 [208, 209].

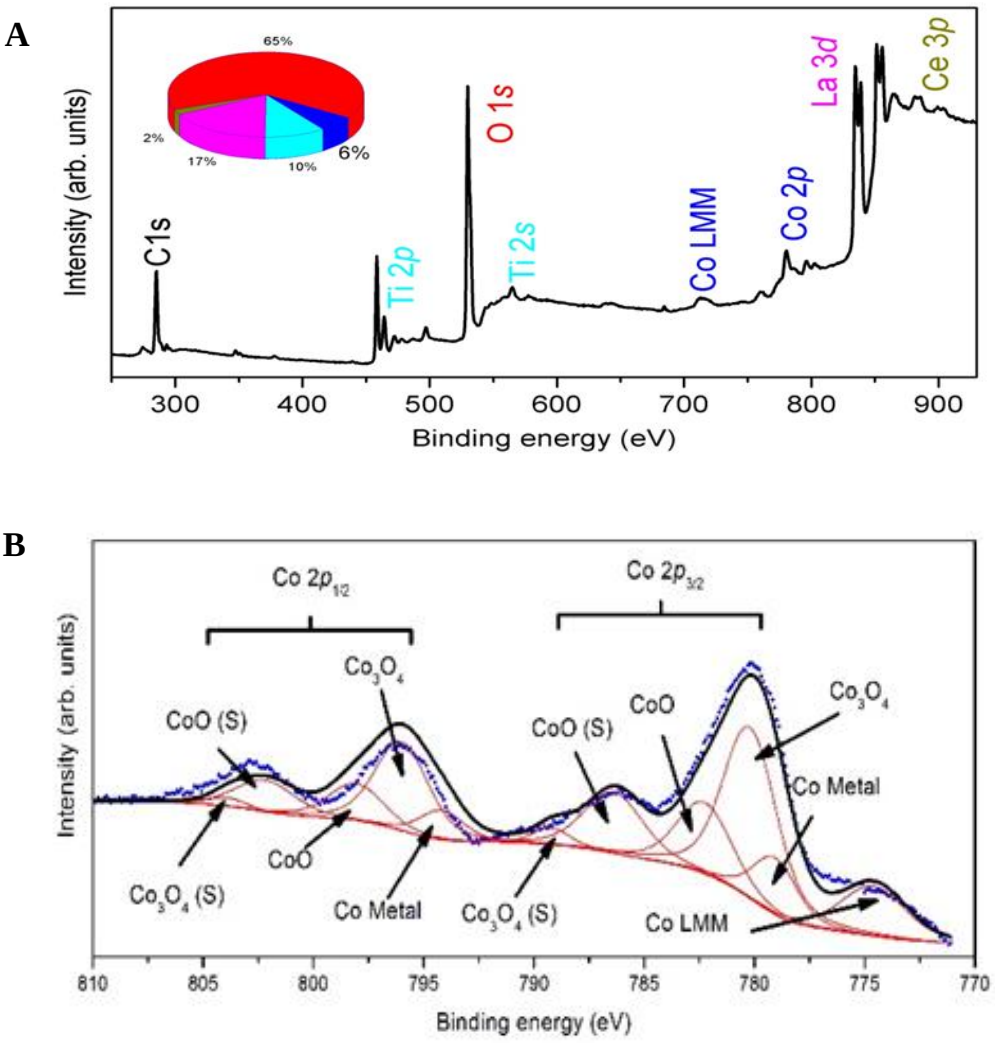

Figure 5-13 XPS spectra of the cube structure in **Figure 5-12A**: (A) surface analysis and quantification pie chart from XPS corresponding to **Figure 5-10A**, with the colour-coded elements and (B) Co 2p XPS spectra collected at room temperature.

These in-depth analyses revealed two key characteristics of the nanocubes present on the activated CoNi-30nm pellet system which were found to be adverse towards CO oxidation. These characteristics include the pronounced amount of the less active Co^{2+} on the surface of the cubes [210] as opposed to the active Co^{3+} in CO oxidation. Not only that, but the exposed (100) planes on the surfaces of these Co_3O_4 cubes have been proven to be less active than crystals with geometries that expose higher index planes which are richer in Co^{3+} [205]. These findings contradict most previously reported studies, in which their high low-temperature CO oxidation activity was attributed to the existence of higher geometric planes in conjunction with the presence of Co^{3+} cations. Xie et al. investigated the oxidation of CO at low temperature using Co_3O_4 nanorods, achieving full CO conversion at a rather low temperature of -77 °C, which was attributed to the preferential exposed (110) plane which only consists of Co^{3+} [9].

They also proved that planes with Co^{2+} are inactive under CO oxidation. Teng et al. found that plate-like Co_3O_4 nanocrystals with the predominantly exposed plane of (111) showed the highest CO oxidation activities, expressed in terms of the lowest temperature at 50 % CO conversion of 190 °C [205]. Sun et al. also discovered a similar predominant exposed (111) plane on their ultrathin Co_3O_4 nanowires, producing the highest CO oxidation activity, and this was attributed to the larger surface area and the abundance of Co^{3+} on the surface [211]. The position of Co^{3+} cations also plays a role in the CO oxidation activities of Co-base nanocrystals. Hu et al. revealed that the Co^{3+} ions on the surface layer of the (011) planes were more reactive than those on the first sub-layer of the (001) planes, which then resulted in differing activities in the two planes [190].

In the previously reported literature, most studies ascribed the high activities to the existence of Co^{3+}, and none of them revealed the (100) plane as the active planes for CO oxidation. This raises some important questions regarding the origin of the enhanced activities of these cubes. From this, it is possible to infer that the activities were likely to originate at the cube-perovskite interface, and this has been observed by Cargnello et al. especially for CO oxidation [212]. In their study, it was revealed that not only are they size-dependent, but the interaction between the metals and the CeO_2 support also contributed to the enhanced CO oxidation activities by CeO_2-supported Ni, which exhibits rates similar to that of Pt and Pd.

5.3.8 Effect of interface length

As previously stated, due to the nature of the active cubic structures having pronounced amounts of inactive Co^{2+} and exposed (100) plane surfaces, it is possible that the active site lies within the interface between the cube and the perovskite surface. To test this hypothesis, an equivalent system but with 10 nm particles (CoNi-10nm) was prepared, having almost half of the area of exposed particles, but with twice the particle-perovskite interface length compared to equivalent CoNi-30nm particles (**Table 5-2**). The CoNi-10nm pellet system was then activated in a similar manner as that used for CoNi-30nm in order to produce similar cubic microstructures as in the activated CoNi-30nm. The initial state and the transformation of 10 nm CoNi particles on the CoNi-10nm pellet surface after the activation were viewed under HIM. Its activated catalytic rates in terms of CO_2 production rates, r_{CO_2}, and TOFs were investigated and compared to those of CoNi-30nm. HIM was used due to the low resolution of the current high resolution SEM, which limits its usage down to ~20 nm to produce higher quality images.

Figure 5-14 compares the HIM images of (A) fresh and (B) activated CoNi-10nm pellet surfaces. The initial particles revealed a similar rounded shape as those on the CoNi-30nm pellet surface but with lower average particle size of 10 nm and higher particle population (721 particles μm^{-2}). For the activated surface, a comparison was made between the SEM images (Refer Appendices: **Figure A-14**) in order to compare the microstructures. CoNi-10nm shows fewer cubic structures and less hollow cores, compared to the relatively more cubic structures with ruptured metal particles observed on the CoNi-30nm surface after undergoing CO kinetics at 520 °C, suggesting a difference in the oxidation mechanisms which is believed to be size-dependent. Unruptured metal particles on CoNi-10nm surface might be due to the easier oxidation of Co and Ni through the thin oxide layer, normally formed with smaller metal particles below 10 nm [197]. This is in agreement with the report from Sadasivan et al., which concluded that the smaller Co particles of around 6 to 10 nm in size are easily oxidised and did not form hollow core structures. The initial fast oxidation would formed a thin oxide layer and was not size-dependent, but further oxidation is highly dependent on particle size [199]. This has also been observed by Varon et al. with unsupported Co particle catalysts, who also observed the formation of oxide particles with 6 nm particles, rather than the formation of hollow core structures [213]. The degree of formation of cubic structures might also be related to its dependency on the reduction parameters. In this case, the temperature of the CO kinetics experiment is salient. For example, for smaller particles, higher reduction temperature and a longer reduction time might have resulted in greater cubic formation in comparison to the reduction conditions used for larger Co particles.

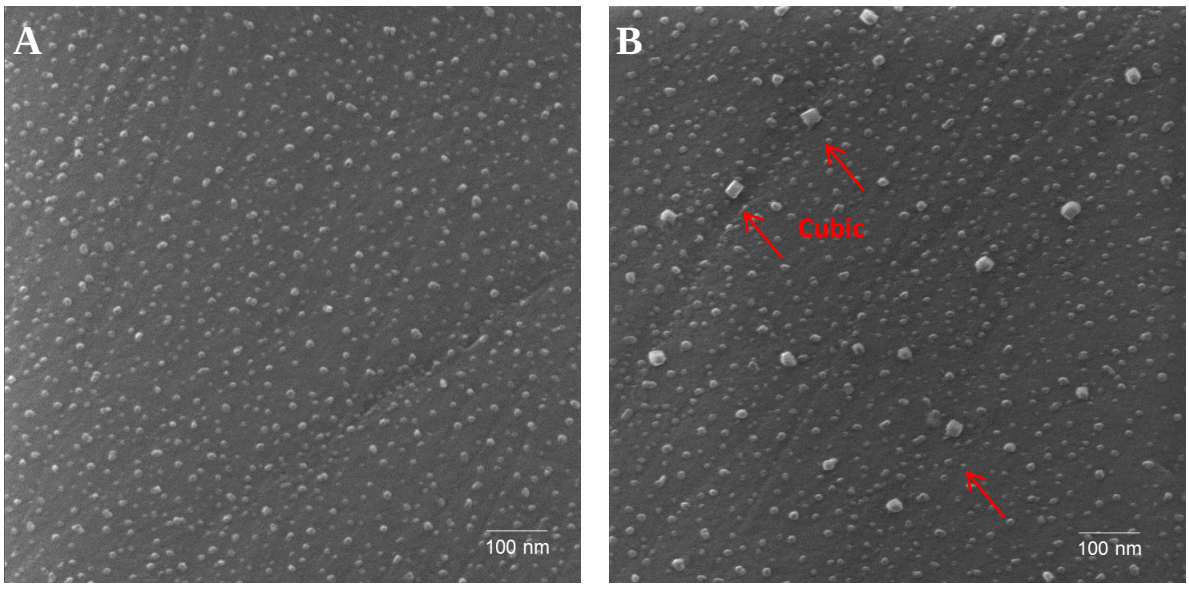

Figure 5-14 Microstructure of CoNi-10nm after activation treatment, extracted using HIM: (A) fresh and (B) after activation.

The activated CoNi-10nm system was then subjected to light-off and the activated activities in terms of CO_2 production rates, r_{CO_2}, and TOFs were evaluated. The experimental conditions employed here is similar to those reported for the previous light-off, as described in section **5.3.4. Figure 5-15** compares the CO_2 production rates, r_{CO_2}, and TOFs of the activated CoNi-30nm and CoNi-10nm pellet systems. The dashed line, labelled as X_{20} in the figure, shows the limit at which 20 % of CO conversion is achieved by both pellet systems, corresponding to a CO_2 production rate, r_{CO_2}, of 0.72 mmol s^{-1} m^{-2}. It can be seen that the temperatures for converting 5 % of CO into CO_2 (CO_2 production rate, r_{CO_2}, of 0.18 mmol s^{-1} m^{-2}) are different between both pellets with different interface lengths, where pellet with larger interface length (CoNi-10nm) converted 5 % of CO_2 at a much higher temperature of around 430 °C, compared to around 260 °C for the pellet with smaller interface length (CoNi-30nm). Below the kinetic limit and in the low temperature region, it is believed that other parameters such as particle size, and/or structure also contributed to the high CO_2 production rates, r_{CO_2}, and TOFs, which is evident from the massive difference between the r_{CO_2}values of CoNi-30nm with half the interface length in comparison to that of CoNi-10nm.

At 520 °C, the CO_2 production rate, r_{CO_2}, and TOF at 520 °C for the activated CoNi-10nm pellet system were above 2.15 mmol s^{-1} m^{-2} and 2500 $s^{-}1$ respectively, which corresponds to 60 % CO conversion. These values were two times higher than that reported for the CoNi-30nm pellet system of around 1.58 mmol s^{-1} m^{-2} and 1156 s^{-1}. This indicates that the main active sites which contributed to the doubled CO_2 production rates, r_{CO_2}, and TOFs above 450 °C are close to or at the metal-support interface as a result of the doubled interface length. Papaioannou et al. observed an increased in CO_2 production rates with increasing temperature from 250 to 290 °C for the patterned YSZ-supported Pt catalysts with increasing interface length or three-phase-boundary (tpb), which was attributed to the modified Pt active sites close to or at the tpb due to the presence of the YSZ support [159].

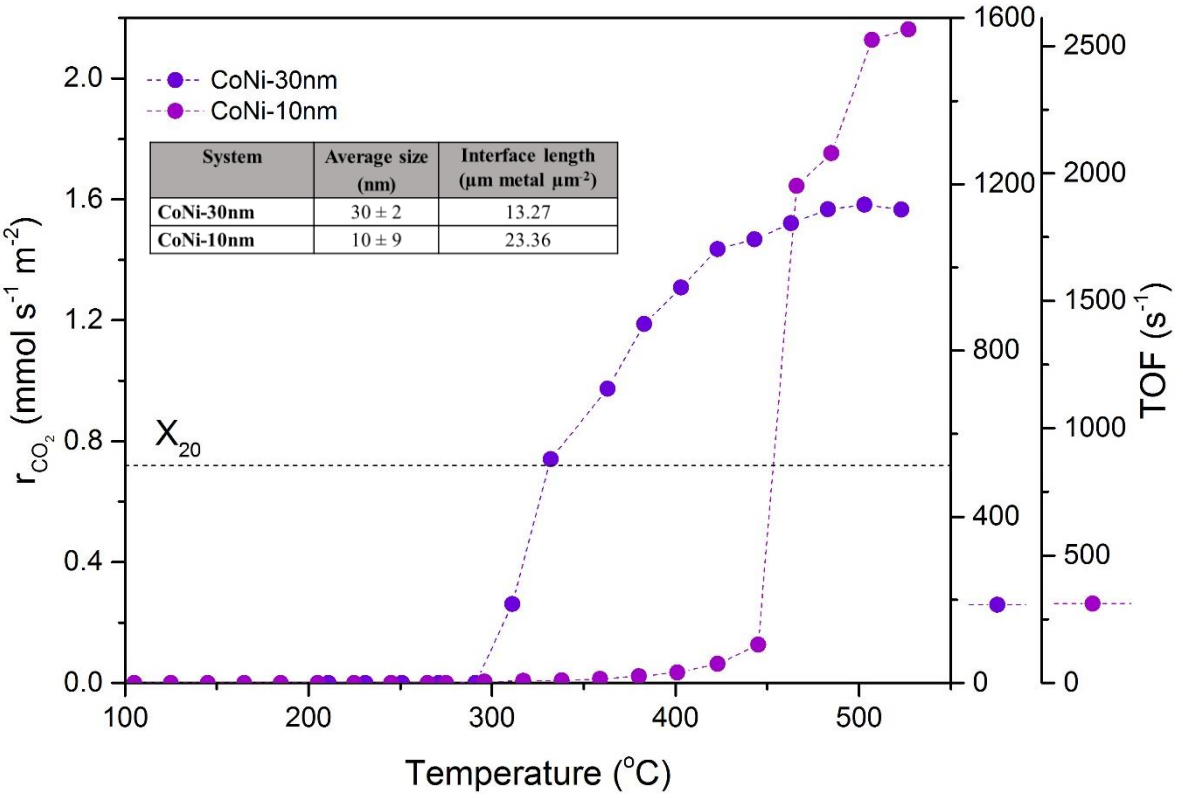

System	Average size (nm)	Interface length (µm metal µm^{-2})
CoNi-30nm	30 ± 2	13.27
CoNi-10nm	10 ± 9	23.36

Figure 5-15 CO_2 production rates, r_{CO_2}, and TOF values as a function of temperature (light-off) over two activated CoNi pellet systems: CoNi-10nm and CoNi-30nm in CO oxidation reaction with an inlet feed gas mixture of P_{CO} = 0.6 kPa, P_{O2} = 1.0 kPa, F_t = 150 ml min^{-1}. The rate is normalised with respect to the pellet area decorated with particles (top side in **Figure 5-1**). Corresponding TOF values are shown on the right axes; with inner axis represents the TOFs for activated CoNi-30nm, while the outer axis represents the TOFs for activated CoNi-10nm. These results were repeatable (two trials) with an error of less than ± 5 % between the trial measured at each point.

5.3.9 Preliminary NO oxidation

The main aim of this investigation was to explore the feasibility of these exsolved CoNi systems as alternative catalysts for NO oxidation. The activated exsolved CoNi-30nm and CoNi-10nm pellet systems were used and their activities expressed in terms of NO_2 production rates, r_{NO_2}, and TOFs were measured under a typical temperature experiment. The activity of several reported catalysts under highly oxidised NO oxidation has been measured in different studies using a variety of reaction conditions, such as different NO and O_2 concentrations. However, they are still under the reported range for diesel engines, as previously described in the literature review. In a recent article, Kim et. al [14] have demonstrated several lanthanum strontium-doped perovskite-type catalysts that can rival Pt under highly oxidised NO oxidation. Since they have fairly similar perovskite formulations to ours, but with different preparation method; i.e. citrate method, the reaction conditions as used by Kim et al. were adopted to conduct and

compare our groundwork study to theirs. However, their results were limited to only NO oxidation but suffers from inactivity under CO and HC oxidation, whereas, we have proven in the earlier chapter that the TOFs of our exsolved metal systems were comparable or slightly higher to that of Pt in CO oxidation reaction.

The NO oxidation light-off experiment was performed with both activated CoNi-30nm and CoNi-10nm pellet systems. The experiment involves a total flowrate, F_t, of 150 ml min^{-1} given at normal temperatures and pressures (NTP) with an inlet feed gas mixture of 0.04 kPa of NO and 8.0 kPa of O_2. The temperature was increased from RT up to 440 °C, which the temperature was held constant during heat-up at each step of 20 °C and the steady states rates measurements were recorded. Aside from the NO_2 production rates, r_{NO_2}, the activities were also expressed in terms of TOFs. **Figure 5-16** compares the rates of NO_2 production, r_{NO_2}, and the TOFs between the exsolved CoNi-30nm and CoNi-10nm pellet systems,. The dashed line, labelled as X_{20} in the figure, shows the limit at which 20 % of NO conversion was achieved by both pellet systems, which corresponds to an NO_2 production rate, r_{NO_2}, of 0.012 mmol s^{-1} m^{-2}.

It can be seen that the minimum temperatures for measurable NO_2 production rates, r_{NO_2}, are different between both pellets with different interface lengths, where pellet with larger interface length (CoNi-10nm) shows the production of NO_2 at a much lower temperature of around 180 °C, compared to around 300 °C for the CoNi-30nm pellet with smaller interface length. Also, the rates for NO_2 production, r_{NO_2}, and TOFs for the CoNi-10nm pellet with larger interface length are greater at all temperatures. The recorded TOF at 520 °C of around 16 s^{-1} for the CoNi-10nm pellet with larger interface length is two times higher than that for smaller interface length (8 s^{-1}). This indicates that the main active sites lie near to or at the metal-support interface due to the doubled activities as a result of a twofold increase in interface length. This was seen to be valid from 340 to 520 °C, and at lower temperatures, it is believed that other parameters such as particle size can also influence the higher activities of CoNi-10nm. Smaller particles were instead found to be more active under highly oxidised NO oxidation, even at low temperature. This reflects the findings reported by Shao et. al [103] that, by reducing the particle size from around 26 nm to 8 nm, their low-temperature activity in NO oxidation was significantly improved, at around twice of the initial particle size.

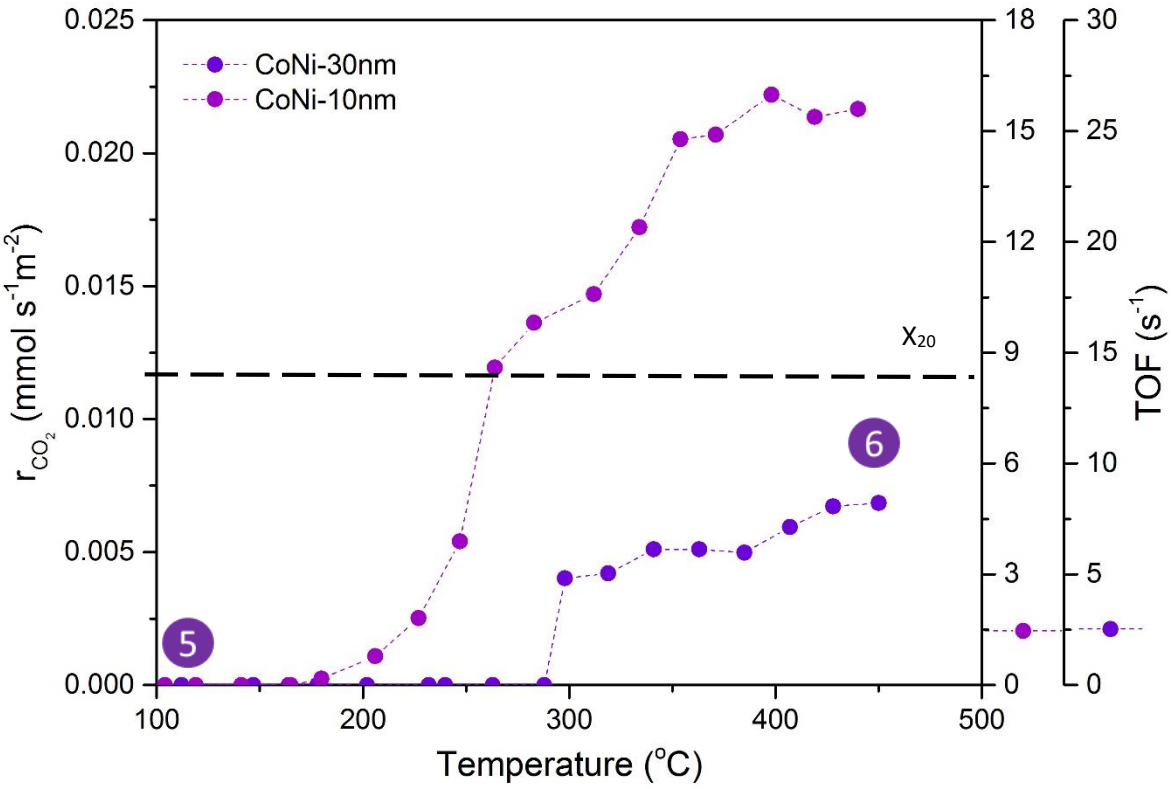

Figure 5-16 NO_2 production rates normalised to pellet area, r_{NO_2}, and TOF values as a function of temperature (light-off) over two activated CoNi pellet systems; CoNi-10nm and CoNi-30nm under highly oxidised NO oxidation reaction with inlet feed gas mixture of P_{NO} = 0.04 kPa, P_{O2} = 8.0 kPa, F_t = 150 ml min^{-1}. The rate is normalised with respect to the pellet area decorated with particles (top side in **Figure 5-1**). The numbers are colour-coded to highlight the starting and end points of each catalytic experiment and also the key stages at which particle tracking or other measurements were conducted following the key stages and catalytic experiments listed in **Table 5-1** for the CoNi-30nm pellet system (purple). Corresponding TOF values are shown on the right axes; with inner axis represents the TOFs for activated CoNi-10nm, while the outer axis represent the TOFs for activated CoNi-30nm. Error of around ±5 % were found during repeated experiments at each measured point.

Having discussed how the active cubic structures assisted the enhanced CO_2 production rates, r_{CO_2}, and TOFs under CO oxidation in the previous subsection, the particles on the CoNi-30nm system were again tracked under NO oxidation (Stage 6: following NO oxidation) and their surface morphology was compared to those in Stage 5 (following the second light-off). This section describes the surface morphologies of the active cubic particles structures following the NO oxidation temperature experiment (Stage 6), which was performed to determine the stability of the active cubic spinel structures under another key reaction such as NO oxidation. **Figure 5-17** compares the morphologies of the tracked particles between Stage 5 and Stage 6. From the images, it is evident that the structures still retained their pinned cubic structures, which is indicative of its stronger metal-support interaction against agglomeration. However, closer

inspection of the figure shows the appearance of additional features, especially at particles numbered 3 and 18 and in between 11 and 12. These features need to be interpreted with caution due to the preliminary nature of this study, which makes it is impossible to draw firm conclusions concerning the origin of these new features. Therefore, more investigation of this reaction is required.

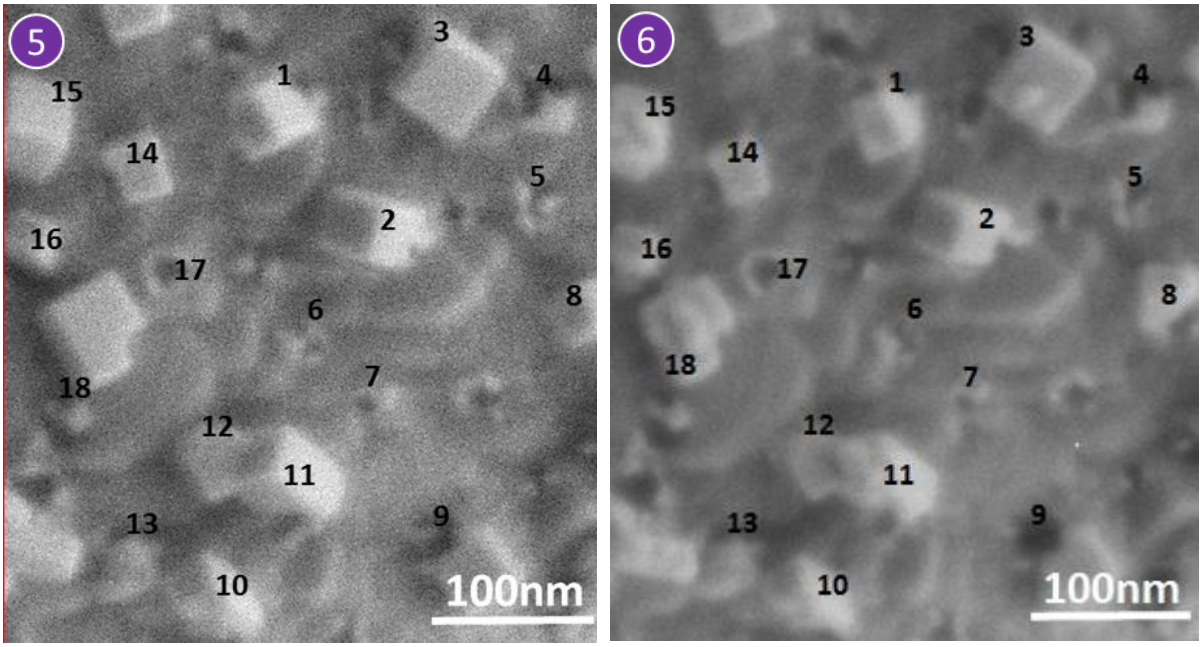

Figure 5-17 SEM micrographs of tracked areas for the CoNi-30nm system collected at room temperature at the highlighted stages of catalytic testing with the colour-coded numbers as indicators of the sequence in which the experiments were carried out and also the stages at which particle tracking or other measurements were conducted: (5) 'cube' microstructure after the second light-off; and (6) after the NO oxidation light-off experiment.

In terms of practical applicability, this was rather beneficial since we need a catalyst which can perform well in two reactions and within both regions of temperature, providing that a reasonable temperature range was used. This is especially true if the aim was to commercialise this as an industrial catalyst. A reasonable active low-temperature oxidation catalysts are certainly crucial, for instance, during the cold start of the exhaust converter, yet as a TWC, the catalysts also need to be active at high temperatures in order to catalyse the conversion of toxic exhaust gases during the application of the exhaust converter, which operates at around 500-1100 °C. This then supports the benefits displayed by these exsolved systems as compared to many other reported Co-based catalysts, which are revealed to be active even under O °C in CO oxidation reaction, despite such traits not being essential in the applications mentioned.

5.4 Exsolved CoNi powder system

This section discusses the results obtained from the catalytic experiments performed on the previously activated Ce, CoNi-7,1 powder system. These investigations involve the evaluation of its activities expressed as CO_2 production rates, $r^*_{CO_2}$, and CO conversions, in terms of temperature, the effect of CO and sulphur, and its long-term stability in comparison to that of commercial Pt powder catalyst for CO oxidation. Preliminary NO oxidation experiment is also evaluated in subsection **5.4.5**.

5.4.1 Light-off

In this section, the CO_2 production rates, $r^*_{CO_2}$, and CO conversions of the activated Ce, CoNi-7,1 powder system from Batch 7 were evaluated under light-off for CO oxidation. The experimental conditions employed here are similar to those reported for the previous light-off, as described in section **4.2.2**. **Figure 5-18** compares the rates of CO_2 production, $r^*_{CO_2}$, and the CO conversions between commercial Pt, Ni and the activated Ce, CoNi-7,1 powder systems. The dashed line, labelled as X_{20} in the figure, highlights the kinetic limit of 20 % of CO conversion was achieved by all powder systems, which corresponds to a CO_2 production rate, $r^*_{CO_2}$, of 0.03 x 10^{-4} mol s^{-1} g^{-1}. This is done to measure reliable kinetic data under differential conditions.

Comparing the figure below with **Figure 4-8**, the production of CO_2 was initiated at a much lower temperature of 160 °C for the activated Ce, CoNi-7,1 powder system, which is 100 °C lower in comparison to its initial activities prior to activation (260 °C). Below this temperature, the CO_2 production rates, $r^*_{CO_2}$, were below the minimum measurable limit of the IR analyser of 0.007 x 10^{-4} mol s^{-1} g^{-1}. Below the kinetic limit, it is apparent that the CO_2 production rates, $r^*_{CO_2}$, of the activated Ce, CoNi-7,1 powder were higher than both commercial Pt and Ni catalysts in the low-temperature region between 160 to 260 °C, which is evident from the lower temperature upon reaching 20 % of CO conversion of 240 °C. At the same temperature, however, Pt only managed to reach around 0.125 x 10^{-4} mol s^{-1} g^{-1} (~5 % of CO conversion), while the CO_2 production rates, $r^*_{CO_2}$, for the Ni catalyst were still below the measurable limit of the IR analyser. This again denotes the importance of the addition of Co in the exsolved Ni formulation, which corroborates the successful investigations of Co-based catalysts for low-temperature CO oxidation. The CO_2 production rates, $r^*_{CO_2}$, for Pt reveal a sharp increase at 280 °C, indicating the transition to the light-off regime, with measured CO_2 production rates, $r^*_{CO_2}$, of around 2.1 x 10^{-4} mol s^{-1} g^{-1} which corresponds to full CO conversion. Meanwhile, the

CO_2 production rates, $r^*_{CO_2}$, for the Ce, CoNi-7,1 powder system increased from 0.01 x 10^{-4} mol s^{-1} g^{-1} at 180 °C up to 1.5 x 10^{-4} mol s^{-1} g^{-1} at 520 °C, which corresponds to only around 72 % of CO conversion.

Alvarez et al. reported CO_2 production rates, $r^*_{CO_2}$, of around 1.76-2.94 µmol s^{-1} g^{-1} upon reaching full CO conversion at sub-ambient temperatures of around -20 to -55 °C, at P_{CO}/ P_{O2} = 0.16 over three mesoporous Co_3O_4 catalysts with different morphologies of wires, rods and mixtures of rods and wires [88]. Teng et al. reported CO_2 production rates, $r^*_{CO_2}$, of around 2.81-4.96 µmol s^{-1} g^{-1} upon reaching full CO conversion at -73 °C, at P_{CO}/ P_{O2} = 0.04 over four Co_3O_4 nanocrystals with different morphologies of plates, rods, cube and sphere [205]. In particular, the cube nanocrystals with a similar predominant exposed plane of (100) recorded around 3.37 µmol s^{-1} g^{-1} upon achieving full conversion at the temperature mentioned, in which the CO_2 production rate, $r^*_{CO_2}$, is lower than those recorded for our nanocubes of around 1.5 x 10^{-4} mol s^{-1} g^{-1} at 80 % CO conversion, although, their temperatures were much lower than ours. Note that the CO_2 production rates, $r^*_{CO_2}$, of all powder systems tested were at similar orders of magnitude (low temperatures: 10^{-5}, high temperatures: 10^{-4} mol s^{-1} g^{-1}). Therefore, since the commercial Pt powder would have a higher metal surface area compared to that of the Ce, CoNi-7,1 powder system, we would expect that the TOFs of the latter system would be higher or at least comparable to that of Pt at all temperatures. However, we were not able to verify this due to the metal particles being damaged by the friction occurring from contact with the bigger Al_2O_3 balls during the removal of the powder systems from the reactor, as seen via SEM (refer Appendices, **Figure A-9**) following the experiments. This made it impossible to estimate the exact surface metal area of these particles.

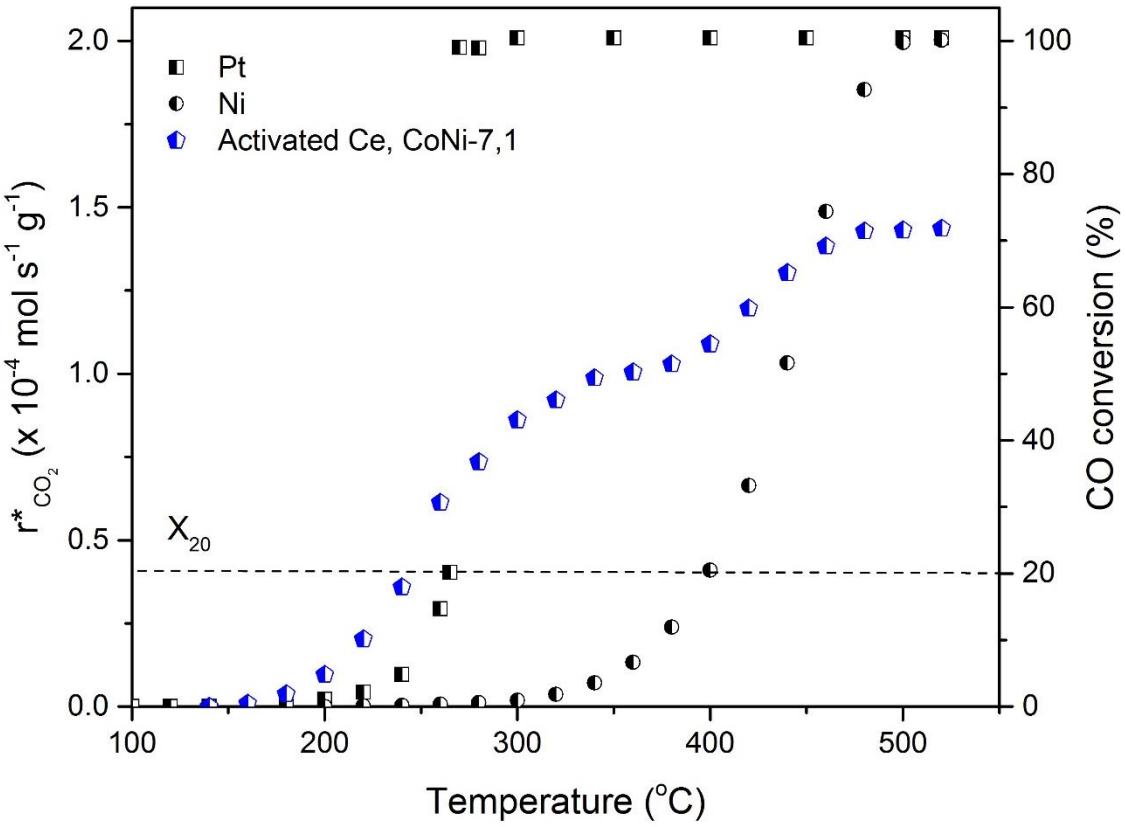

Figure 5-18 CO_2 production rates, $r^*_{CO_2}$, and CO conversion as a function of temperature (light-off) over commercial Pt/Al_2O_3, Ni/SiO_2 Al_2O_3 and activated Ce, CoNi-7,1 powder systems under CO oxidation reaction with an inlet feed gas mixture of P_{CO} = 0.6 kPa, P_{O2} = 1.0 kPa, F_t = 450 ml min^{-1} and GHSV=26 000 h^{-1}. The weights of both powders are similar (weight of powder, W_p = 10 mg), diluted in alumina with a total weight of the powder bed, W_t, of 100 mg. Error of around ±5 % were found during repeated experiments at each measured point.

In an attempt to address the repeatability of producing similar initial CO_2 production rates, $r^*_{CO_2}$, and the formation of these active structures for future use, the light-off experiments were repeated at least three times using fresh and activated Ce, CoNi-7,1 powder systems. These experiments were performed within one month between each powder system. The fresh powders were first tested in the typical light-off experiment prior to activation under CO-rich atmospheres, and their activated CO_2 production rates, $r^*_{CO_2}$, were also assessed. **Figure 5-19** illustrates the repeatability of these fresh and activated exsolved CoNi powder systems. On average, all powder systems tested showed repeatable CO_2 production rates, $r^*_{CO_2}$, and repeated activations were also confirmed for all three powders following activation, with error levels of less than ± 10 % between trials measured at each point. These results also indicate that the CoNi particles were more stable under ambient conditions, and had not been destroyed by prolonged storage and/or by repeated activations. The steady reorganisation of particle structure following

similar activation routes was also confirmed, also indicative of the stable nature of the active cubic structures of the activated systems.

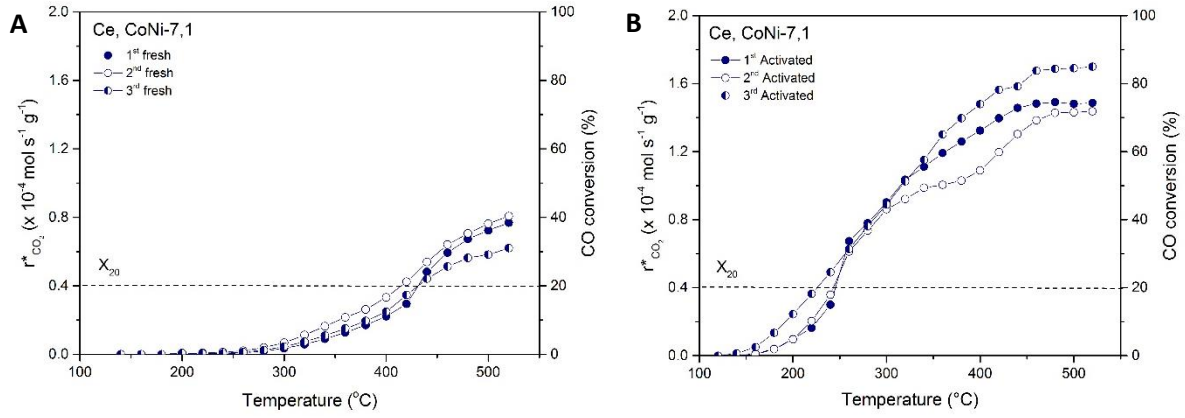

Figure 5-19 Reproducibility of CO_2 production rates, $r^*_{CO_2}$ and CO conversion under light-off experiments, with an inlet feed gas mixture of P_{CO} = 0.6 kPa, P_{O2} = 1.0 kPa, F_t = 450 ml min^{-1} and GHSV=26 000 h^{-1}. The weights of both powders are similar (weight of powder, W_p = 10 mg), diluted in alumina with a total weight of the powder bed, W_t, of 100 mg, with: (A) fresh and (B) activated Ce, CoNi-7,1 powder light-off activities.

5.4.2 CO kinetics

The following section describes the effect of CO partial pressures (CO kinetics) on the CO_2 production rates, $r^*_{CO_2}$,of the Pt and activated Ce, CoNi-7,1 powder systems. The experimental conditions employed here are similar to those reported for previous CO kinetics experiment, as described in section **4.3**. Reliable kinetics data measurements were performed at 180 °C, at which the reactor is assumed to operate under differential conditions (low O_2 conversion of less than 20 %). Several experiments were also performed at higher temperatures of 360, 400 and 440 °C, aiming to study the effect of temperature on the CO_2 production rates, $r^*_{CO_2}$, of Pt and Ce, CoNi-7,1 powder systems. **Figure 5-20** shows the CO_2 production rates, $r^*_{CO_2}$, for the Pt and Ce, CoNi-7,1 powder systems in the CO kinetics experiment at (A) 180 °C and (B) 360, 400 and 440 °C.

For the Ce, CoNi-7,1 system at 180 °C, the rate of CO_2 production, $r^*_{CO_2}$, increases with increasing P_{CO} from 0.5 to 7.5 kPa, before it decreases following further increases of P_{CO} up to 18.87 kPa. At 7.5 kPa of CO, the CO_2 production rate, $r^*_{CO_2}$, measured for Ce, CoNi-7,1 was around 0.87 x 10^{-4} mol s^{-1} g^{-1} (~20 % of O_2 conversion), although, at the same P_{CO}, Pt only managed to achieve around 0.005 x 10^{-4} mol s^{-1} g^{-1} (refer to the graph inset in **Figure 5-20A**). At this temperature, it is well documented that the decrease in the CO_2 production rates, $r^*_{CO_2}$, observed for Pt attributed to the strong adsorption of CO lead to the poisoning of Pt by

CO [160, 214, 215]. For the Ce, CoNi-7,1 powder system, the CO_2 production rate, $r^*_{CO_2}$, increases with increasing P_{CO} at all three temperatures of 360, 400 and 440 °C, while decreasing rates with increasing P_{CO} were observed for Pt at all three temperatures. The differing P_{CO} dependencies in the two powder systems simply reflects the difference in adsorption sites between O_2 and CO during the reaction [216]. This implies that CO and O_2 did not compete for the same adsorption active sites in the exsolved CoNi system, which hence facilitated the reaction even at high CO concentrations. For base metals, the repeated redox mechanism is most often involved, where CO (g) adsorbs on Co oxide (Co^{3+}) and reacts with the lattice oxygen to form CO_2, thus creating an O_2 vacancy and reducing the oxidation state of the Co site (Co^{2+}). Molecular O_2 (g) then fills these O_2 vacancies and oxidises the Co sites to Co^{3+} again [85]. Meanwhile, at low temperatures, the creation of O_2 vacancies at high CO concentrations would then provoke the restructuring of the particles, hence impeding CO adsorption and causing the production of CO_2 to drop [88].

An et al. [160] reported that the increase in TOF from 0.001 to 0.02 s^{-1} with increasing temperature (150-200 °C) for pure mesoporous Co_3O_4 and NiO in reducing conditions (P_{CO}/P_{O2} = 2.5). This accords with the increase in CO_2 production rates, $r^*_{CO_2}$, for the Ce, CoNi-7,1 powder system from 2.3 to 3.4 x 10^{-4} mol s^{-1} g^{-1} at similar inlet reaction conditions (dashed line: P_{CO}/P_{O2} = 2.5), although, at a much higher temperatures of 360 to 440 °C. However, at low CO concentrations, higher CO_2 production rates, $r^*_{CO_2}$, were observed for Pt. This is because at these conditions, O_2 largely covers the Pt surface but as the CO concentration increases, CO then slowly populates the surface, hence hindering the adsorption of O_2 on the surface to complete the reaction [217, 218]. As highlighted in both figures, CO oxidation favours the Ce, CoNi-7,1 system at lower temperatures and/or at higher CO concentrations, while at higher temperatures or low CO, the CO_2 production favours that of Pt.

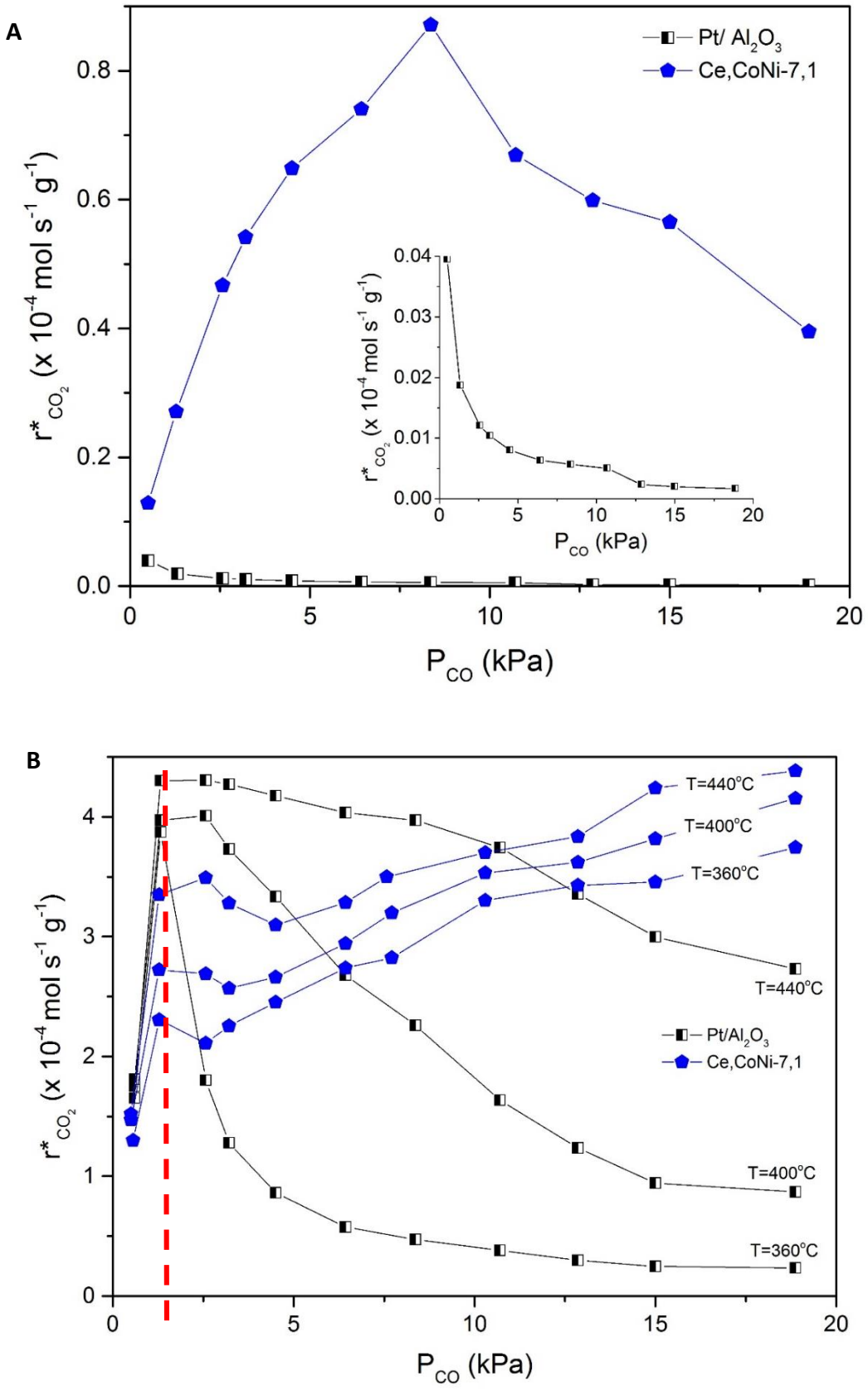

Figure 5-20 CO_2 production rates, $r^*_{CO_2}$, as a function of CO partial pressure (CO kinetics) over Pt and activated Ce, CoNi powder system in the CO oxidation reaction with an inlet feed gas mixture of P_{CO} = 0.5-18.87 kPa, P_{O2} = 0.64 kPa, F_t = 450 ml min^{-1}, GHSV=26 000 h^{-1} and at

temperatures of (A) 180 °C and (B) 360-440 °C. The inset in (A) presents the detail of the Pt plot. The weights of both powders are similar (weight of powder, W_p = 10 mg), diluted in alumina with a total weight of powder bed, W_t, of 100 mg. Error of around ±5 % were found during repeated experiments at each measured point.

5.4.3 Sulphur poisoning

Since the sulphur poisoning investigation of Ce, CoNi-7,1 powder system was not introduced in the previous chapter, this section evaluates the reversible sulphur poisoning of this exsolved CoNi system in comparison to that of the commercial Pt and Ni catalysts (**Figure 4-11-1, 2**). **Figure 5-21** presents the results obtained from the poisoning-recovery experiments for the Ce, CoNi-7,1 powder system at two poisoning temperatures of (1) 240 and (2) 520 °C. A temperature of 240 °C was chosen to enable the measurement of reliable kinetic data, at which the reactor is assumed to operate under differential conditions at this temperature and this would also allow a direct comparison with the results obtained for Pt at a similar temperature. Meanwhile, 520 °C was chosen to qualitatively explore the rates recovery at higher temperatures. The experimental conditions employed here are similar to those reported for the previous sulphur poisoning experiments, as described in section **4.4** except for Zone B*, C* and D*.

At 240 °C, the Ce, CoNi-7,1 powder system shows an initial CO_2 production rate, $r^*_{CO_2}$, of around 0.4 x 10^{-4} mol s^{-1} g^{-1}, which represents approximately 20 % conversion of CO at Zone A. Following the first 15 minutes of sulphur poisoning (Zone B*), the CO_2 production rate, $r^*_{CO_2}$, decreases with time and finally deactivates to below the measurable limit of CO_2 production rates, $r^*_{CO_2}$. Upon the removal of the sulphur source, the CO_2 production rates, $r^*_{CO_2}$, were allowed to recover. However, we were unable to recover the CO_2 production rates, $r^*_{CO_2}$, after two hours (Zone C*). Since sulphur can be decomposed at relatively higher temperatures of around 500-700 °C [219], the temperature was then increased to 520 °C (Zone D*). The CO_2 production rates, $r^*_{CO_2}$, were seen to recover immediately after the temperature increase, although, it took almost 17 hours to stabilise, as shown in Zone D* and A in **Figure 5-21-1** and **B**, respectively. The recovered CO_2 production rate, $r^*_{CO_2}$, of around 1.15 x 10^{-4} mol s^{-1} g^{-1} mirrored the activated CO_2 production rates, $r^*_{CO_2}$, measured under light-off at high temperatures, corresponding to almost 60 % of CO conversion.

Subsequent sulphur poisonings at 520 °C were performed at two time intervals of 15 and 30 minutes (Zone B and D), and it can be seen that the poisoning can be reversed although at the expense of prolonged time and reduced recovered rates. Almost 20 hours were needed to

recover the rates (Zone C and D), however, only 75 % of the $r^*_{CO_2}$, was able to recover in Zone C. This result matches the point made by Yao et al. [152], who claimed that the sulphur induced at low temperatures was harder to remove than that induced at high temperatures, emphasising yet again the strong effect of temperature in sulphur poisoning. Not only that, but Viscoti et al. observed a decrease in CO conversion at low sulphur loadings of below 100 ppm, but with selectivity of higher C-chain processes over Co/ Al_2O_3 catalysts being unaffected. This was ascribed to the preferential adsorption of sulphur on active sites that responsible for CO adsorption, which then decreases the active sites for CO adsorption, hence limiting the CO conversion [220]. This then implies the strong effect of sulphur on the active sites of preferred catalysts, especially for Co in CO oxidation.

The capability of this Ce, CoNi-7,1 powder system to reverse the poisoning by sulphur can be explained partly by the fact that the potential active sites lie near to or on the metal-support interface, especially at higher temperatures as previously discussed. This then prevents the severe blockage of the active sites and hence making them still available for reaction. This phenomenon can be explained by the fast adsorption process, which results in sulphur predominantly adsorb onto the outer shell of the particles, rather than at the interface [176]. This then forms less stable surface sulphates, and hence they are easier to desorb at higher temperatures. However, the prolonged recovery time at 520 °C indicates that the sulphur desorption process is a slow process and thought to involve surface-segregates. The faster recovery from poisoning of the previous Sr, FeNi-1,2 powder system (**Figure 4-9-3**) can also be explained to be due to the stronger pinned particles, preventing the formation of surface sulphates in between loose particles, provoking prolonged recovery time. This might be the case for this exsolved CoNi system. Royer et al. have reported that SO_2 poisoning is to some extent surface-sensitive with $LaCo_{1-X}Fe_XO_3$ catalyst under methane oxidation, and they found that the extent and rate of poisoning-recovery phases are strongly dependent on the morphology of the catalysts, in which prolonged time of around 200 hours was required to totally reverse the poisoning of loose particles, compared to the more compact particles [221].

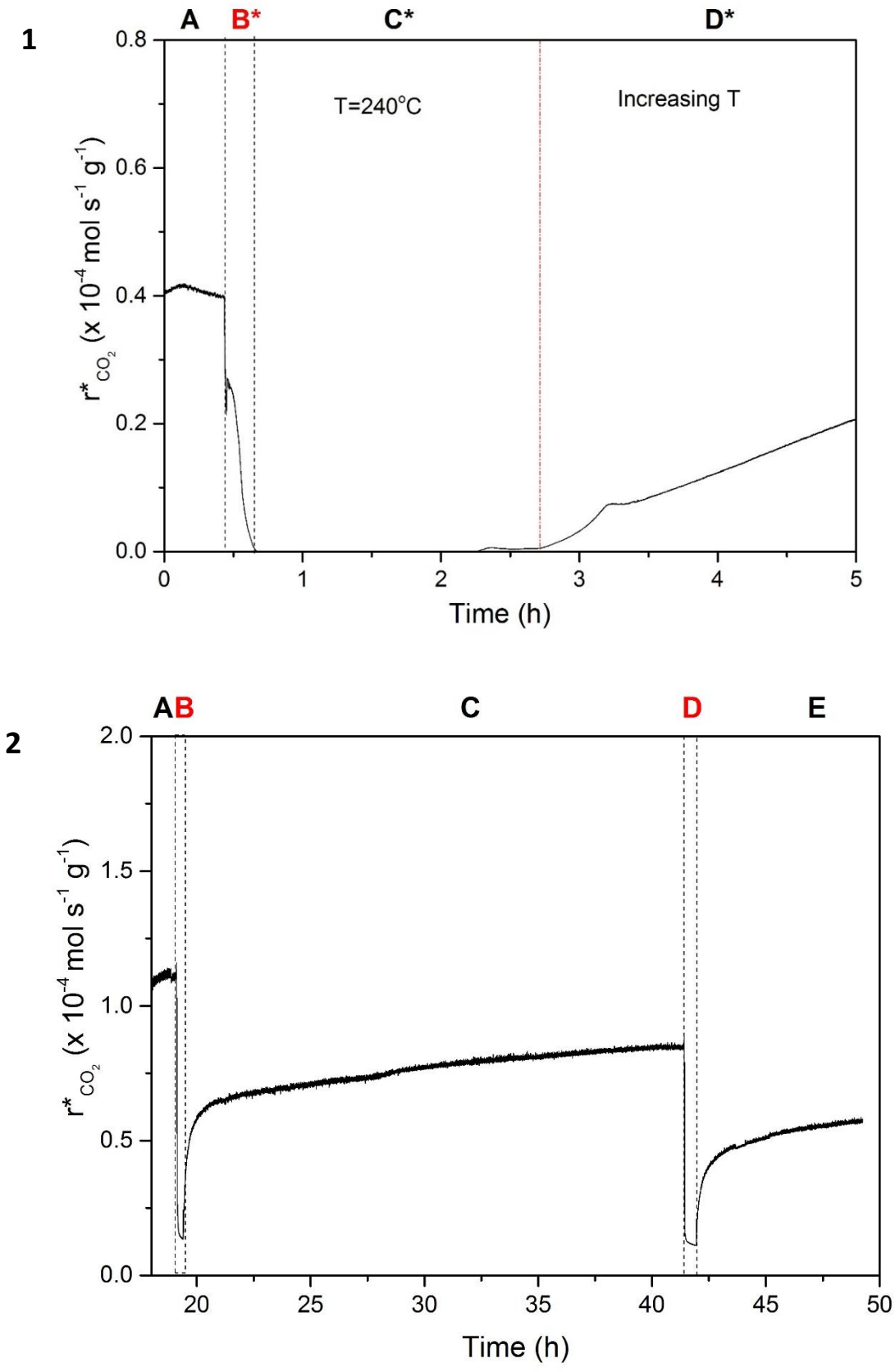

Figure 5-21 CO_2 production rates, $r^*_{CO_2}$, and rate recovery during sulphur poisoning over the activated Ce, CoNi-7,1 powder system in the CO oxidation reaction with an inlet feed gas mixture of P_{CO} = 0.6 kPa, P_{O2} = 1.0 kPa, F_t = 450 ml min^{-1}, GHSV=26 000 h^{-1} and at

temperatures of (1) 240 and (2) 520 °C for Ce, CoNi-7.1 powder systems. The weight of powder, W_p of 10 mg was diluted in alumina to get a total weight of the powder bed, W_t, of 100 mg. 240 °C was chosen for the kinetic investigations in order to operate under differential conditions (<20 % of CO conversion) while 520 °C was chosen as the final temperature since this is consistent with exhaust applications.

5.4.4 Long-term stability

As pointed out in the literature review, the long-term stability during continuous operation is considered as one of the key issues that need to be tackled in order to produce alternative base metal catalysts that can rival Pt not only in activity but also in terms of long-term stability. The aim of the present experiment was to examine the stability of the activated Ce, CoNi-7,1 powder system in comparison to Pt on a weight-to-weight basis. The remarkable stability of these exsolved systems has also been proven in the previous chapter, which recorded stable CO_2 production rates, $r^*_{CO_2}$, for almost 170 hours at 523°C. This corroborates the findings of other studies, in which the idea is that confined particles lead to stronger metal-oxide interface, thus, enhancing their stability and preventing them from agglomeration at high temperatures [23].

This long-term stability experiment involved a total flowrate, F_t, of 450 ml min^{-1}, given at normal temperatures and pressures (NTP) with an inlet feed gas mixture of 0.6 kPa of CO and 1.0 kPa of O_2 at 200 °C for approximately 655 hours (one month). The activities were expressed in terms of CO_2 production rates, $r^*_{CO_2}$, and comparisons were made to those of Pt. 200 °C was used in this experiment to allow for the collection of reliable kinetics data where the reactor is assumed to operate under differential conditions (low CO conversion of less than 20 %) at this temperature for both the activated Ce, CoNi-7,1 and Pt systems. **Figure 5-22** compares the long-term stability of the Pt and Ce, CoNi-7,1 powder systems, at 200 °C for 655 hours. At this temperature, both powder systems show relatively stable CO_2 production rates, $r^*_{CO_2}$, of around 0.43 x 10^{-4} and 0.03 x 10^{-4} mol s^{-1} g^{-1}, for Ce, CoNi-7,1 and Pt respectively, across the time span. Again, the observed severe oscillations (~ 6 %) were due to the temperature variation in the lab. These inconsistencies reflect the use of only one flowrate value (450 ml min^{-1}) in the rates calculation which was only measured at a specified time. No deactivation was observed in either powder system upon reaching 655 hours, and it was quite interesting to note that the Ce, CoNi-7,1 powder system did not suffer from any major deactivation due to the prior sulphur poisoning, even though the same powder system was used for this experiment following the poisoning experiments. This again demonstrates the outstanding stability of the restructured pinned cubic particles over four weeks with preserved activities. Most reports only claim the stability of their base metal catalysts after exposure to reactions for at most ~150 hours, and

most of them did not feature an intricate morphology such as the ones we have in this system [222]. However, in two of their papers, Lv et al. have reported that their ordered nanoarchitectures of Co_3O_4 nanocubes grown on the surface of Co $(OH)_2$ nanosheets are stable for 300 minutes at 110 °C with unchanged surface morphology. This indicates the stability of an interesting morphology of its catalyst [89], like the one described in this work. However, their studies were again limited to only, at most, five hours of continuous operation.

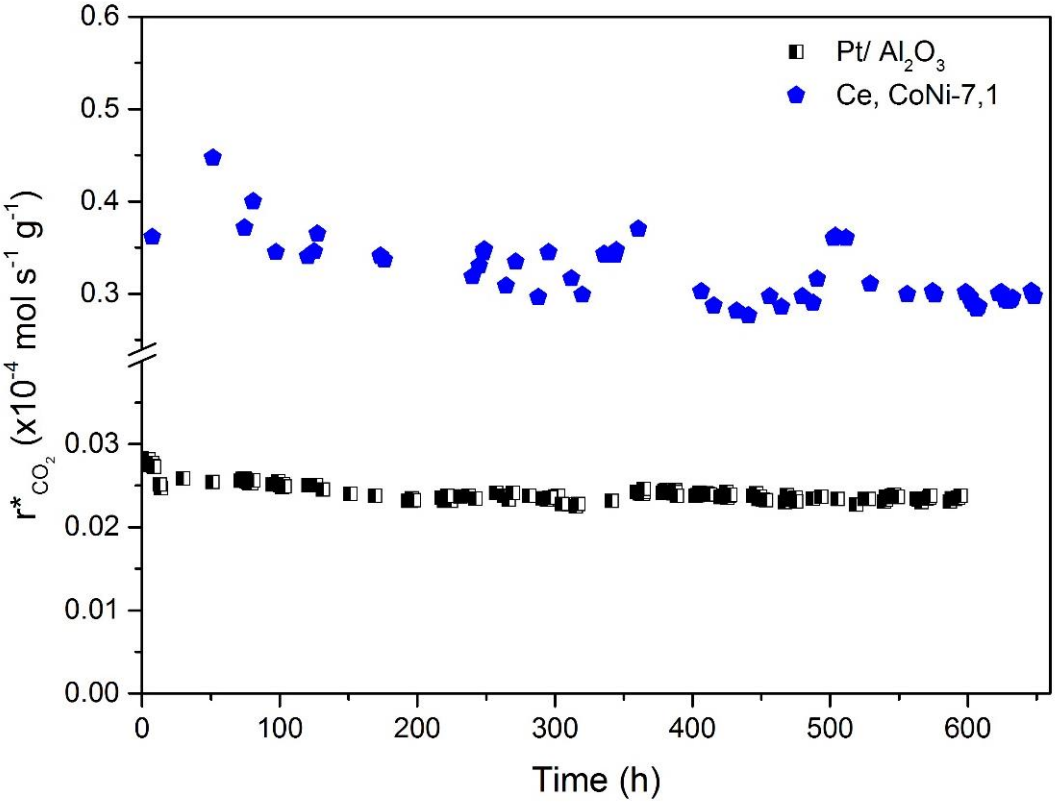

Figure 5-22 CO_2 production rates, $r^*_{CO_2}$, over state-of-the-art Pt/Al_2O_3 and activated Ce, CoNi-7,1 powder systems in a long-term CO oxidation experiment with an inlet feed gas mixture of P_{CO} = 0.6 kPa, P_{O2} = 1.0 kPa, F_t = 450 ml min^{-1}, GHSV=26 000 h^{-1} and at temperatures of 200 °C for 655 hours. The weights of both powders are similar (weight of powder, W_p = 10 mg), diluted in alumina with a total weight of the powder bed, W_t, of 100 mg.

5.4.5 NO oxidation

The final part of this chapter reviews the preliminary experimental findings for the most active exsolved metal powder system (Ce, CoNi-7,1) discussed in the earlier chapter, under another key reaction of NO oxidation. This section assesses the NO_2 production rates, $r^*_{NO_2}$, of the activated Ce, CoNi-7,1 powder system (i.e. the active cubic structures) under highly oxidised NO oxidation, mimicking rather similar reaction condition that would be faced by a Pt catalyst in a diesel exhaust converter. Comparison to Pt on a weight-to-weight basis was also

investigated. This study, however, does not conduct full kinetic investigations under NO oxidation, which is beyond the scope of this thesis and is recommended as future work. The NO oxidation light-off experiment was performed over Pt and activated Ce, CoNi-7,1 powder systems. The light-off involves a total flowrate, F_t, of 450 ml min^{-1} given at normal temperatures and pressures (NTP) with an inlet feed gas mixture of 0.04 kPa of NO and 8.0 kPa of O_2. The temperature was increase from RT up to 440 °C, which the temperature was held constant during heat-up at each step of 20 °C and the steady states rates measurements were recorded. Aside from the rates of NO_2 production, $r^*_{NO_2}$, the activities were also expressed in terms of NO conversion. **Figure 5-23** compares the rates of NO_2 production, $r^*_{NO_2}$, and the NO conversions of the Pt and activated Ce, CoNi-7,1 powder systems. The dashed line, labelled as X_{20} in the figure, shows the kinetic limit at which 20 % of NO conversion is achieved by both powder systems, corresponding to an NO_2 production rate, $r^*_{NO_2}$, of 0.027 x 10^{-4} mol s^{-1} g^{-1}. This is done to measure reliable kinetic data under differential conditions. The dashed line illustrates the equilibrium line for NO oxidation at the inlet reaction conditions and the calculations for this line are shown in Appendices**, A1.4**.

NO_2 production was initiated at 160, 200 and 180 °C for Pt, Ni and Ce, CoNi-7,1 respectively. Below the kinetic limit and at all temperatures (100-440 °C), the NO_2 production rates, $r^*_{NO_2}$, for Pt and Ce, CoNi-7,1 powder systems were comparable with around ± 5 % difference at each measured point. The NO_2 production rate, $r^*_{NO_2}$, increased with increasing temperature and achieved a maximum of 0.043 x 10^{-4} mol s^{-1} g^{-1} (equivalent to around 35 % of NO conversion) at 360 °C for the Pt and Ce, CoNi-7,1 powder systems before the reaction was thermodynamically limited at high temperatures. This plot trend exhibited by Ce, CoNi-7,1 powder system revealed the importance of the small, hemispheric particles in aiding the high activity under highly oxidised NO oxidation, in which has been explained previously in subsection **5.3.9**. Ni reaches a maximum of 0.035 x 10^{-4} mol s^{-1} g^{-1} (equivalent to around 26 % of NO conversion) at a slightly higher temperature of 380 °C.

Prior studies that have noted the importance of Co as alternative catalyst NO oxidation especially in low-temperature region have revealed that the active structure contributing to these activities originates from the spinel structure of the Co, which confirms the association of the active Co spinel cubic structures of our system in this reaction [13]. From the plot, it is obvious that the addition of Co in Ni enhanced the activity in the low-temperature region. Zhong et. al [223] have previously revealed that, by adding Co into Ni-doped perovskites, enhanced NO_2 production rates were observed owing to the superior NO adsorption capability of Co in relation

to Ni. They also revealed that the co-existence of Co and Ni cations on the B-site can tune the NO and O_2 adsorption, given that O_2 has a moderate adsorption strength to further improve the complete oxidation of NO at low temperatures. This also consistent with the results reported by Chen and co-workers, stating that the amounts of O_2 and NO desorption activities is associated with the reducibility of the B-site cations in the low temperature region, because the key factors in achieving high NO oxidation activities are related closely to the ability for NO adsorption and the availability of active O_2 [224].

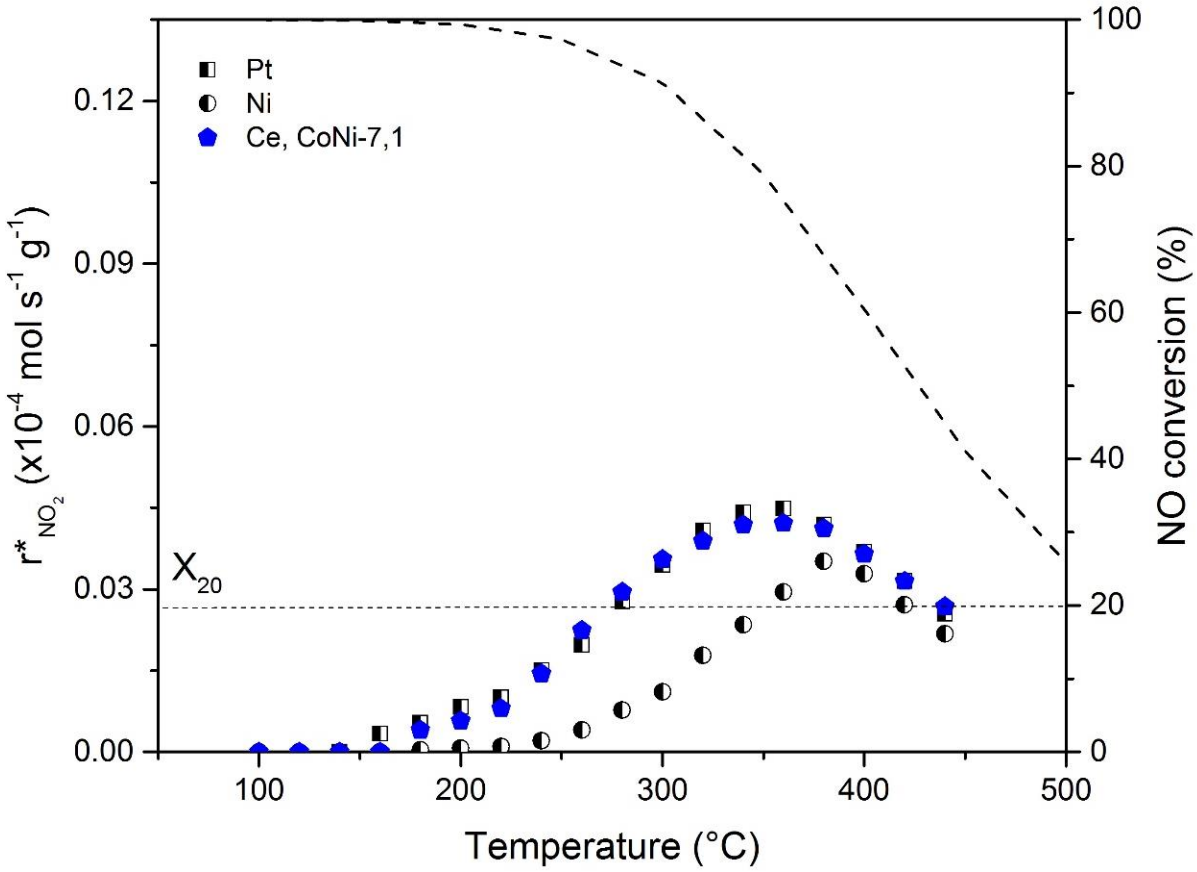

Figure 5-23 NO_2 production rates, $r^*_{NO_2}$, and NO conversion as a function of temperature (light-off) over state-of-the-art Pt Al_2O_3, commercial Ni/ Al_2O_3 SiO_2 and activated Ce, CoNi-7,1 powder systems in the highly oxidised NO oxidation reaction with an inlet feed gas mixture of P_{NO} = 0.04 kPa, P_{O2} = 8.0 kPa, F_t = 450 ml min^{-1} and GHSV= 26 000 h^{-1}. The weights of all powders are similar (weight of powder, w_p = 10 mg), diluted in alumina with a total weight of the powder bed, W_t, of 100 mg. Error of around ±5 % were found during repeated experiments at each measured point. The dashed line represents the equilibrium line for NO oxidation at this reaction condition.

5.5 Summary

The present investigation was designed to assess the feasibility of the exsolved CoNi system as an alternative to Pt under CO oxidation. Further substitution of Co in the previously tailored

exsolved Ni system demonstrated relatively high activities in comparison to those reported in the literature, especially in the low-temperature region, and these findings highlight the role of particle confinement in producing enhanced TOFs during reactions. Not only that, but one of the more significant findings to arise from this study is that these nanostructures can be reorganised or restructured to produce even more intricate structures such as the active cubic structures positioned at an angle of ~55° at the edge of empty sockets. Furthermore, surprisingly, these restructured particles show enhanced activity comparable to or even exceeding the TOF values reported for noble metals. In addition, this nanoscale reorganisation has been followed via what we call a particle tracking experiment, in which specific areas of individual particles were subjected to surface chemistry and elemental analyses at each key stage of the catalytic experiments to link their microstructural evolution to their catalytic and kinetic behaviour. This particle tracking experiment can serves as an effective tool to provide strong additional evidence for particle monitoring at nanoscale. The restructuring of CoNi particles is explained based on the different diffusion capability of Co metals compared to oxygen, following the mechanism called as the Kirkendall effect. The characteristics of the active cube structures were also explored, revealing rather mediocre features under CO oxidation, such as being rich in Co^{2+} with exposed (100) planes rather than the more active CO^{3+} with higher index planes. The active structures also revealed a sparser particle population, suggesting higher activity per active site compared to the initial particles. The augmenting effect of this partially pinned nanocube structural arrangement, in conjunction with the cube-perovskite interaction at the interface resulted in the activated, high TOFsobserved. The effect of interface length was also investigated and we have shown that it has a significant effect on the TOFs, especially at high-temperature CO oxidation.

In terms of practical applicability, the previously tailored exsolved CoNi powder (Ce, CoNi-7,1) with two particle sizes range of 10 and 30 nm were thoroughly explored in catalytic investigations involving CO and NO oxidation reactions. Detailed catalytic testing in CO oxidation was successfully performed, covering several critical aspects including the effect of temperature (light-off), CO concentration (CO kinetics), sulphur poisoning and long-term stability. The powder was also activated in CO-rich atmospheres to produce the active structures and its activities were tested and compared to those of Pt on a weight–to-weight basis. The prolonged stability with preserved CO_2 production rates, $r^*_{CO_2}$, for ~655 hours of this "activated" exsolved CoNi system revealed the strong synergistic effect between the particles and the perovskite lattice, confirming the robustness of the active structures. The reversible recovery tendencies found after sulphur poisoning contradict previously reported results in the

literature for base metal-based catalysts, which exhibit irreversible poisoning by sulphur at higher temperatures.

An initial groundwork with NO oxidation has discussed the potential of the exsolved CoNi system to function effectively not only for CO oxidation but also in highly oxidised NO oxidation. This investigation clearly indicates that the activated particle structures were significantly active in conditions of highly oxidised NO oxidation in comparison to those of Pt. This study also highlighted the role of the smaller particles, which showed higher activities than the larger particles across the temperature range employed, hence strengthening the idea of using a range of particle sizes to enable its dual functionality in the two key reactions of CO and NO oxidation. However, since this is only an initial investigation, it has only examined the effect of temperature on the NO_2 production rates, $r^*_{NO_2}$, which makes it impossible to address the exact origin of the high NO oxidation activities of the active cubic structures. Secondly, the small sample size, using only two particle sizes in these investigations, means that extreme caution must be applied in interpreting the findings, as it might not be possible to generalise them for a wider range of particle sizes. Therefore, further mechanistic investigations and experimentation into the role of the active cubic structures and the location of the active sites under NO oxidation are strongly recommended.

Overall, the exsolved CoNi system has demonstrated superior intrinsic activity (especially in terms of TOFs) due to particle confinement, owing to its strain-induced active sites. It can also reorganise into certain intricate structures, showing enhanced activities, resembling those of noble metals under CO and NO oxidation. These investigations help shed new light in designing the particle structures in forming active structures that can enhance activities per active site at relevant conditions for CO or NO oxidation, and thus rivalling Pt in the near future. However, further experimental work is needed, such as testing a wider range of particle sizes which could be of importance since this work has only been able to examine two particle sizes.

6 CONCLUSION AND FUTURE RECOMMENDED WORK

6.1 Conclusion

In this work, we demonstrate a novel approach for tailoring the catalytic activities of base metal catalyst systems by inducing high, long-lasting activity, to rival Pt for CO and NO oxidation on a weight-to-weight basis by having pinned nanoparticles on the perovskite support. In our preliminary screening study that was performed at the earlier stage of this research, the activities of these exsolved metal pellet systems, expressed in TOFs, are shown to be comparable to that of Pt catalysts reported in the literature, by having TOFs in the range of 1000 s^{-1}. This preliminary study also shows that the pinned characteristics of these exsolved metal pellet systems aid the long-term stability of the systems, inhibiting the agglomeration of particles at high temperatures. This was evident from the stable TOF values of around 1000 s^{-1} observed over exsolved FeNi pellet system at 523 °C for 170 hours under stoichiometric CO oxidation condition.

Since these exsolved metal systems showed remarkable TOFs for CO oxidation and the fact that most literature did not present direct activity comparison, either in the form of activity per active sites, e.g. TOFs or on a weight-to-weight basis to Pt, these exsolved metal systems were further prepared in powder form. The activities of these powders, expressed in terms of CO_2 production rates per weight of active catalyst, $r^*_{CO_2}$, and CO conversions were first assessed and compared on a weight-to-weight basis to the activities of a state-of-the-art Pt/Al_2O_3 catalyst powder in typical light-off experiments. Since this was our first attempt to produce these exsolved metal systems in powder form, various preparation parameters and materials components were varied and 60 exsolved metal powder systems were successfully prepared and their CO_2 production rates, $r^*_{CO_2}$, were tested in the light-off experiments. The enhancements in CO_2 production rates, $r^*_{CO_2}$, of the prepared exsolved powder systems were accomplished by manipulating the preparation parameters; e.g. grinding method and/or reduction atmospheres and/or the elemental formulation of the exsolved metal systems. For example, in order to increase the particles population, the A-site cations are changed to further enhance their activities.

However, only four exsolved metal powder systems exhibit the CO_2 production rates, $r^*_{CO_2}$, near to that of Pt, with exsolved Ce, Ni from Batch 2 (Ce, Ni-2,19), showing the nearest activity under the kinetic limit of 20 % CO conversion with only around 100 °C temperature gap to that

of Pt. This kinetic limit represents the limit where the reactor was considered to operate under the differential conditions; i.e. the reactor conditions (temperature, pressure) are considered uniform or "gradientless" across the reactor at low conversions to enable reliable kinetic data to be measured. Increasing CO_2 production rates, $r^*_{CO_2}$, with increasing P_{CO} under CO kinetics experiment were also observed for most exsolved metal systems, indicating the anti-coking of these systems under CO-rich atmospheres. They also display reversible sulphur poisoning that is not the case for most reported base metal catalysts, which are known to be irreversibly poisoned by sulphur. Among these four powder systems, enhanced CO_2 production rates, $r^*_{CO_2}$, were observed for exsolved CoNi powder system (Ce, CoNi-7,1), containing both 10 and 30 nm size metal particles upon exposure to CO-rich environment, insinuating the fact that CO acts as structure promoter for CoNi particles. These enhanced $r^*_{CO_2}$ were observed especially at low temperature region with higher CO_2 production rates, $r^*_{CO_2}$, of around 0.25 $x10^{-4}$ mol s^{-1} g^{-1} (10 % CO conversions) at 220 °C. At the same temperature, the initial CO_2 production rates, $r^*_{CO_2}$, for the exsolved CoNi before activation and Pt were below the measurable limit and 0.05 $x10^{-4}$ mol s^{-1} g^{-1}, respectively.

Due to the enhanced CO_2 production rates, $r^*_{CO_2}$, observed by the previous exsolved CoNi powder system (Ce, CoNi-7,1) following exposure under CO-rich atmospheres, this system was chosen to be investigated further in order to link its catalytic and kinetic behaviour to their particle characteristics. This was performed to pinpoint the origin of the enhanced activities, which involved the tracking of metal particles at each catalytic key stage to closely monitor the potential microstructural changes that can cause the activation. CoNi particles were seen to restructure into semi-planted Co_3O_4 nanocubes, revealing the inactive (100) geometric planes with the presence of Co^{2+}, following an oxidation mechanism known as the Kirkendall effect. This restructuring matched the rates jump observed during the CO kinetics experiment, signifying the occurrence of this microstructural changes on the exsolved CoNi system during this experiment, which was not observed for exsolved Ni system. The effect of the metal-support interface length was also studied and it was believed that at high temperatures above 450 °C, the cubes-support interface were the active sites, due to the doubled TOFs ascribed to the doubled interface length of the exsolved CoNi systems. TOF of above 2500 s^{-1} was recorded at 520 °C for the exsolved CoNi pellet system with twofold interface length (CoNi-10nm), compared to 1156 s^{-1} for system with smaller interface length (CoNi-30nm). Below 450 °C, it was believed that apart from the metal-interface active sites, the rates were probably also size- and structure-dependent. Comprehensive catalytic investigations were also performed on the

Ce, CoNi-7,1 powder system to determine the extent of sulphur poisoning and the long-term stability of this exsolved CoNi powder system. Reversible sulphur poisoning was observed, especially at high temperatures, although the time it needs to recover was relatively longer (~20 hours) than that of Pt and other exsolved metal systems (at most 5 hours). Stable CO_2 production rates, $r^*_{CO_2}$, of 0.43 x 10^{-4} mol s^{-1} g^{-1} over almost one month (655 hours) at 200 °C were observed over Ce, CoNi-7,1 powder system, revealing the stability of these intricate semi-planted Co_3O_4 nanocube structures yet again.

The initial groundwork under highly oxidised NO oxidation using these activated exsolved CoNi systems were performed to explore the dual functionality of these intricate structures under two oxidation reactions. A rather similar interface length effect was observed as the one for CO oxidation, in which at higher temperatures between 360-520 °C, the active sites lie within the proximity of the cubes-support interface while at low temperatures, other parameters such as particle size seem to influence the higher TOFs of exsolved CoNi system with larger interface length. The highest TOF measured by this system was around 16 s^{-1} at 520 °C. In terms of the NO_2 production rates per weight of active catalyst, $r^*_{NO_2}$, Ce, CoNi-7,1 powder system showed comparable rates to that of Pt with only ± 5 % of difference at each measured point within the temperature range used (100-440 °C), displaying the combined effect of having both 10 and 30 nm particles. The maximum NO_2 production rates, $r^*_{NO_2}$, observed by Pt and exsolved CoNi were around 0.43 and 0.45 x 10^{-4} mol s^{-1} g^{-1} (equivalent to around 35 % of NO conversion) at 360 °C, respectively before the reaction was thermodynamically limited at high temperatures. This then confirms the dual functionality of activated exsolved CoNi system in two oxidation reactions; CO and NO oxidation.

To conclude, we were able to develop a redox tolerant, well-anchored nanoparticles base metal catalysts using A-deficient exsolved system which can rival Pt in CO and NO oxidation and temperature of practical significance. We also demonstrated their ability to restructure into active nanocubes which enhanced the catalytic ability at low temperature region and at high temperatures, serve as platform for further chemical and morphological transformations which can unlock superior functionality in base metal systems. It is also worth noting that aside from enabling the above demonstration, the particle tracking experiments employed here illustrate vividly that the evolution of base metal particles during the CO oxidation reaction and are invaluable for decoding kinetic behaviour and establishing insightful structure-property correlations. Although this research is seen as a new approach to produce active base metal catalysts rivalling those of Pt in these reactions, further vital works are required such as to

optimised the preparation route in terms of time and cost for future commercialisations as industrial catalysts.

6.2 Future recommended work

Since this was our first attempt in investigating the catalytic activities of these exsolved metal systems for CO and NO oxidation, mimicking the reaction conditions employed in the exhaust converters, this research was mainly aimed to assess their activities on a weight-to-weight basis to rival Pt. However, since the primary aim was not to entirely simulate the exhaust reactions, we only focused on two main reactions in this thesis, which then led to several opportunities for furthering the work presented in this thesis. Exhaust reactions such as HC oxidation would then need to be addressed in the near future, hence, this work is recommended as future work. The following are the main recommended future work that need to be addressed in order to complete this research. The work is divided into two essential parts as follow:

1. Optimising the preparation route and material characterisations of exsolved metal systems:

- Appropriate manipulation of the preparation parameters. For example, in order to monitor the effect of the reduction temperatures in provoking the exsolution, other parameters would need to be constant to avoid overlap between other parameters such as reduction time. This was not performed in this research since it needs more time, therefore, it is recommended for future work.
- Characterisations of base metals surface metal area using nitric oxides titration techniques.
- Investigations on the reduced surface metal after each stage of experiments such as activation, sulphur poisoning and long-term experiments to identify the possible formation of toxic Ni carbonyls or the components on the surfaces after poisoning via EDX
- Optimising the formation of the active nanocubes structures by investigating the parameters affecting the oxidation-reduction behaviour of the exsolved CoNi systems, such as the particle size, reduction time and temperatures.
- In-depth characterisations of active nanocubes structures; such as retest under XPS and refitting the peaks to eliminate any overlapping peaks for other materials

2. Fuller catalytic investigations of exsolved CoNi system:

- Full investigation of catalysis of the exhaust reactions using the exsolved CoNi system, which includes catalytic investigations for in system involving all exhaust reactions such

as HC oxidation and NO reduction. Not only that, the effect of water in the reactions also needs to be addressed. Thermal long-term stability test involving start-up and shut down cycles are also required since it mimics the real conditions of exhaust catalysts.

- Investigation on the effect of wider range of interface length and surface metal area in order to pinpoint the exact active sites of the exsolved CoNi systems. This is due to the utilisation of only two ranges of interface length in this research with no investigations performed in terms of varying the surface metal area.

- Further investigation on the kinetics and mechanisms under NO oxidation since we have only explored the activities under preliminary temperature-effect experiments which then merits for future in-depth investigations. This is important since we have revealed that different active sites are possibly responsible for the enhanced NO oxidation observed by exsolved CoNi systems under low temperatures, in particular.

References

1. Kettler, P.B., *Platinum Group Metals in Catalysis: Fabrication of Catalysts and Catalyst Precursors.* Organic Process Research & Development, 2003. **7**(3): p. 342-354.
2. Wintterlin, J., et al., *Atomic and Macroscopic Reaction Rates of a Surface-Catalyzed Reaction.* Science, 1997. **278**(5345): p. 1931-1934.
3. Engel, T. and G. Ertl, *Elementary steps in the catalytic oxidation of carbon monoxide on platinum metals.* Advances in Catalysis, 1979. **28**: p. 1-79.
4. *Metal prices in the United States through 2010*, in *U.S. Geological Survey Scientific Investigations Report 2012–5188*, U.S.G. Survey, Editor. 2013.
5. Kašpar, J., P. Fornasiero, and N. Hickey, *Automotive catalytic converters: current status and some perspectives.* Catalysis Today, 2003. **77**(4): p. 419-449.
6. Bourges, P., S. Lunati, and G. Mabilon, *N_2O and NO_2 formation during NO reduction on precious metal catalysts*, in *Studies in Surface Science and Catalysis*, A.F. N. Kruse and J.M. Bastin, Editors. 1998, Elsevier. p. 213-222.
7. Erkfeldt, S., E. Jobson, and M. Larsson, *The Effect of Carbon Monoxide and Hydrocarbons on NOx Storage at Low Temperature.* Topics in Catalysis. **16**(1): p. 127-131.
8. Qi, G. and R.T. Yang, *Performance and kinetics study for low-temperature SCR of NO with NH_3 over MnO_x–CeO_2 catalyst.* Journal of Catalysis, 2003. **217**(2): p. 434-441.
9. Xie, X., Li, Y., Liu, Z.-Q., Haruta, M. and Shen, W., *Low-temperature oxidation of CO catalysed by Co_3O_4 nanorods.* Nature, 2009. **458**(7239): p. 746-749.
10. Jansson, J., *On the catalytic activity of Co_3O_4 in low-temperature CO oxidation.* J. Catal., 2002. **211**: p. 387-397.
11. Jansson, J., Skoglundh, M., Fridell, E. and Thormählen, P., *A Mechanistic Study of Low Temperature CO Oxidation over Cobalt Oxide.* Topics in Catalysis, 2001. **16-17**(1-4): p. 385-389.
12. Thormahlen, P., Skoglundh, M., Fridell, E. and Andersson, B., *Low-temperature CO oxidation over platinum and cobalt oxide catalysts.* J. Catal., 1999. **188**: p. 300-310.
13. Irfan, M.F., J.H. Goo, and S.D. Kim, *Co_3O_4 based catalysts for NO oxidation and NO_x reduction in fast SCR process.* Applied Catalysis B: Environmental, 2008. **78**(3–4): p. 267-274.
14. Kim, C.H., Qi, G., Dahlberg, K. and Li, W., *Strontium-Doped Perovskites Rival Platinum Catalysts for Treating NO_x in Simulated Diesel Exhaust.* Science, 2010. **327**(5973): p. 1624-1627.
15. Yu, Y., Takei, T., Ohashi, H., He, H., Zhang, X. and Haruta, M., *Pretreatments of Co_3O_4 at moderate temperature for CO oxidation at −80 °C.* Journal of Catalysis, 2009. **267**(2): p. 121-128.
16. Yao, Y.-F.Y., *The oxidation of hydrocarbons and CO over metal oxides.* Journal of Catalysis, 1974. **33**(1): p. 108-122.
17. Wang, Q., Park, S.Y., Choi, J.S. and Chung, J.S., *$Co/K_xTi_2O_5$ catalysts prepared by ion exchange method for NO oxidation to NO_2.* Applied Catalysis B: Environmental, 2008. **79**(2): p. 101-107.
18. Schlatter, J.C., R.L. Klimisch, and K.C. Taylor, *Exhaust catalysts: appropriate conditions for comparing platinum and base metal.* Science, 1973. **179**(4075): p. 798-800.
19. Voorhoeve, R.J.H., Remeika, J.P., Freeland, P.E. and Matthias, B.T., *Rare-Earth Oxides of Manganese and Cobalt Rival Platinum for the Treatment of Carbon Monoxide in Auto Exhaust.* Science, 1972. **177**(4046): p. 353-354.
20. Twigg, M.V., *Progress and future challenges in controlling automotive exhaust gas emissions.* Applied Catalysis B: Environmental, 2007. **70**(1–4): p. 2-15.

21. Jacobs, G., Das, T.K., Zhang, Y., Li, J., Racoillet, G. and Davis, B.H., *Fischer–Tropsch synthesis: support, loading, and promoter effects on the reducibility of cobalt catalysts.* Applied Catalysis A: General, 2002. **233**(1–2): p. 263-281.
22. Vasilyeva, M.S., Rudnev, V.S., Ustinov, A.Y., Korotenko, I.A., Modin, E.B. and Voitenko, O.V., *Cobalt-containing oxide layers on titanium, their composition, morphology, and catalytic activity in CO oxidation*. Applied Surface Science, 2010. **257**(4): p. 1239-1246.
23. Neagu, D., Oh, T.-S., Miller, D.N., Menard, H., Bukhari, S.M., Gamble, S.R., Gorte, R.J., Vohs, J.M. and Irvine, J.T.S., *Nano-socketed nickel particles with enhanced coking resistance grown in situ by redox exsolution.* Nat Commun, 2015. **6**.
24. Heveling, J., *Heterogeneous Catalytic Chemistry by Example of Industrial Applications.* Journal of Chemical Education, 2012. **89**(12): p. 1530-1536.
25. Davis, M.E. and R.J. Davis, *Fundamentals of Chemical Reaction Engineering*. 2012: Dover Publications.
26. Gao, F. and D.W. Goodman, *Reaction Kinetics and Polarization Modulation Infrared Reflection Absorption Spectroscopy Investigations of CO Oxidation over Planar Pt-Group Model Catalysts†.* Langmuir, 2010. **26**(21): p. 16540-16551.
27. Hagen, J., *Industrial Catalysis: A Practical Approach*. 2015: Wiley.
28. Zaera, F., *Selectivity in hydrocarbon catalytic reforming: a surface chemistry perspective.* Applied Catalysis A: General, 2002. **229**(1–2): p. 75-91.
29. Heck, R.M. and R.J. Farrauto, *Automobile exhaust catalysts.* Appl. Catal. A, 2001. **221**: p. 443-457.
30. Bell, A.T., *The Impact of Nanoscience on Heterogeneous Catalysis.* Science, 2003. **299**(5613): p. 1688-1691.
31. Emsley, J., *The Elements*. 2nd ed, ed. C. Press. 1993, Oxford.
32. Bond, G.C., *General introduction to catalysis by platinum-group metals*, in *Chemistry of the Platinum Group Metals: Recent Developments*, F.R. Hartley, Editor. 1991, Elsevier: New York p. 106–123.
33. Koek, M., Kreuzer, O.P., Maier, W.D., Porwal, A.K., Thompson, M. and Guj, P., *A review of the PGM industry, deposit models and exploration practices: Implications for Australia's PGM potential.* Resources Policy, 2010. **35**(1): p. 20-35.
34. Berger, D.J., *Fuel Cells and Precious-Metal Catalysts.* Science, 1999. **286**(5437): p. 49-49.
35. Service, R.F., *Bringing Fuel Cells Down to Earth.* Science, 1999. **285**(5428): p. 682-685.
36. *PGM Market Report May 2016*, in *Johnson Matthey Technol. Rev.* 2016. p. 209.
37. Balcerzak, M., *Analytical Methods for the Determination of Platinum in Biological and Environmental MaterialsA Review.* Analyst, 1997. **122**(5): p. 67R-74R.
38. *GFMS Platinum & Palladium Survey 2015*, T. Reuters, Editor. 2015: London.
39. Walsh, M.P., *Motor Vehicle Pollution Control: The successes and issues still causing concern as the next millennium begins* in *Platinum Metals Rev.* 2000. p. 22-30.
40. Morgan, C., *40 Years of Cleaner Air: The Evolution of the Autocatalyst.* Johnson Matthey Technol. Rev., 2014. **58**(4).
41. Twigg, M.V., *Critical topics in exhaust gas aftertreatment.* Platinum Metals Rev., 2001. **45**(4): p. 176-178.
42. Heck, R.M. and R.J. Farrauto, *Automobile exhaust catalysts.* Applied Catalysis A: General, 2001. **221**(1–2): p. 443-457.
43. Matsumoto, S.i., *Recent advances in automobile exhaust catalysts.* Catalysis Today, 2004. **90**(3–4): p. 183-190.

44. Lafyatis, D.S., Ansell, G.P., Bennett, S.C., Frost, J.C., Millington, P.J., Rajaram, R.R., Walker, A.P. and Ballinger, T.H., *Ambient temperature light-off for automobile emission control.* Applied Catalysis B: Environmental, 1998. **18**(1–2): p. 123-135.
45. Yung, M.M., E.M. Holmgreen, and U.S. Ozkan, *Cobalt-based catalysts supported on titania and zirconia for the oxidation of nitric oxide to nitrogen dioxide.* Journal of Catalysis, 2007. **247**(2): p. 356-367.
46. Degobert, P., *Automobiles and Pollution*, ed. I. Society of Automotive Engineers. 1995, Warrendale, Pa.
47. Obuchi, A., Kaneko, I., Oi, J., Ohi, A., Ogata, A., Bamwenda, G.R. and Kushiyama, S., *A practical scale evaluation of catalysts for the selective reduction of NOx with organic substances using a diesel exhaust.* Applied Catalysis B: Environmental, 1998. **15**(1): p. 37-47.
48. Taylor, K.C., *Nitric Oxide Catalysis in Automotive Exhaust Systems.* Catalysis Reviews, 1993. **35**(4): p. 457-481.
49. Koltsakis, G.C. and A.M. Stamatelos, *Catalytic automotive exhaust aftertreatment.* Progress in Energy and Combustion Science, 1997. **23**(1): p. 1-39.
50. Després, J., Elsener, M., Koebel, M., Kröcher, O., Schnyder, B. and Wokaun, A., *Catalytic oxidation of nitrogen monoxide over Pt/SiO_2.* Applied Catalysis B: Environmental, 2004. **50**(2): p. 73-82.
51. Takahashi, N., Shinjoh, H., Iijima, T., Suzuki, T., Yamazaki, K., Yokota, K., Suzuki, H., Miyoshi, N., Matsumoto, S.-i., Tanizawa, T., Tanaka, T., Tateishi, S.-s. and Kasahara, K., *The new concept 3-way catalyst for automotive lean-burn engine: NO_x storage and reduction catalyst.* Catalysis Today, 1996. **27**(1): p. 63-69.
52. Fridell, E., Skoglundh, M., Westerberg, B., Johansson, S. and Smedler, G., *NO_x Storage in Barium-Containing Catalysts.* Journal of Catalysis, 1999. **183**(2): p. 196-209.
53. Kishi, H., Oemry, F., Nguyen, T.Q., Kunikata, S., Nakanishi, H., Kasai, H., Maekawa, H. and Osumi, K., *Study of NO oxidation reaction over the Pt cluster supported on γ-Al_2O_3(111) surface.* Current Applied Physics, 2012. **12, Supplement 3**: p. S110-S114.
54. Koebel, M., G. Madia, and M. Elsener, *Selective catalytic reduction of NO and NO_2 at low temperatures.* Catalysis Today, 2002. **73**(3–4): p. 239-247.
55. Song, C., *Fuel processing for low-temperature and high-temperature fuel cells: Challenges, and opportunities for sustainable development in the 21st century.* Catalysis Today, 2002. **77**(1–2): p. 17-49.
56. Hoflund, G.B., Upchurch, B.T., Kielin, E.J. and Schryer, D.R., *Influence of an Fe promoter on silica-supported Pt/SnOx catalysts used for low-temperature CO oxidation.* Catalysis Letters, 1995. **31**(2): p. 133-141.
57. Tanaka, H., Fujikawa, H., and Takahashi, I.,, *Excellent Oxygen Storage Capacity of Perovskite-PD Three way Catalysts.* SAE Technical Paper 950256, 1995.
58. Nishihata, Y., Y., Mizuki, J., Akao, T., Tanaka, H., Uenishi, M., Kimura, M., Okamoto, T. and Hamada, N., *Self-regeneration of a Pd-perovskite catalyst for automotive emissions control.* Nature, 2002. **418**: p. 164-167.
59. Tanaka, H., *An Intelligent Catalyst: The Self-Regenerative Palladium–Perovskite Catalyst for Automotive Emissions Control.* Catalysis Surveys from Asia, 2005. **9**(2): p. 63-74.
60. Tanaka, H., H., Taniguchi, M., Uenishi, M., Kajita, N., Tan, I., Nishihata, Y., Mizuki, J.i., Narita, K., Kimura, M. and Kaneko, K., *Self-Regenerating Rh- and Pt-Based Perovskite Catalysts for Automotive-Emissions Control.* Angewandte Chemie International Edition, 2006. **45**(36): p. 5998-6002.
61. Satsuma, A., Osaki, K., Yanagihara, M., Ohyama, J. and Shimizu, K., *Activity controlling factors for low-temperature oxidation of CO over supported Pd catalysts.* Applied Catalysis B: Environmental, 2013. **132–133**: p. 511-518.

62. Jin, M., Park, J.-N., Shon, J.K., Kim, J.H., Li, Z., Park, Y.-K. and Kim, J.M., *Low temperature CO oxidation over Pd catalysts supported on highly ordered mesoporous metal oxides.* Catalysis Today, 2012. **185**(1): p. 183-190.
63. Meng, L., Jia, A.-P., Lu, J.-Q., Luo, L.-F., Huang, W.-X. and Luo, M.-F., *Synergetic Effects of PdO Species on CO Oxidation over PdO–CeO_2 Catalysts.* The Journal of Physical Chemistry C, 2011. **115**(40): p. 19789-19796.
64. Gulyaev, R.V., Slavinskaya, E.M., Novopashin, S.A., Smovzh, D.V., Zaikovskii, A.V., Osadchii, D.Y., Bulavchenko, O.A., Korenev, S.V. and Boronin, A.I., *Highly active $PdCeO_x$ composite catalysts for low-temperature CO oxidation, prepared by plasma-arc synthesis.* Applied Catalysis B: Environmental, 2014. **147**: p. 132-143.
65. Wang, C., Sasmaz, E., Wen, C. and Lauterbach, J., *Pd supported on SnO_2–MnO_x–CeO_2 catalysts for low temperature CO oxidation.* Catalysis Today, 2015. **258, Part 2**: p. 481-486.
66. Liu, L., Zhou, F., Wang, L., Qi, X., Shi, F. and Deng, Y., *Low-temperature CO oxidation over supported Pt, Pd catalysts: Particular role of FeO_x support for oxygen supply during reactions.* Journal of Catalysis, 2010. **274**(1): p. 1-10.
67. Siani, A., Alexeev, O.S., Lafaye, G. and Amiridis, M.D., *The effect of Fe on SiO_2-supported Pt catalysts: Structure, chemisorptive, and catalytic properties.* Journal of Catalysis, 2009. **266**(1): p. 26-38.
68. Xue, E., K. Seshan, and J.R.H. Ross, *Roles of supports, Pt loading and Pt dispersion in the oxidation of NO to NO_2 and of SO_2 to SO_3.* Applied Catalysis B: Environmental, 1996. **11**(1): p. 65-79.
69. Liu, Y., Meng, M., Li, X.-G., Guo, L.-H. and Zha, Y.-Q., *In situ DRIFTS investigation on the NOx storage mechanisms over Pt/K/TiO_2–ZrO_2 catalyst.* Catalysis Communications, 2008. **10**(2): p. 173-177.
70. Liu, Y., Meng, M., Li, X.-G., Guo, L.-H. and Zha, Y.-Q., *NO_x storage behavior and sulfur-resisting performance of the third-generation NSR catalysts Pt/K/TiO_2–ZrO_2.* Chemical Engineering Research and Design, 2008. **86**(8): p. 932-940.
71. Toops, T.J., D.B. Smith, and W.P. Partridge, *NO_x adsorption on Pt/K/Al_2O_3.* Catalysis Today, 2006. **114**(1): p. 112-124.
72. Yamazaki, K., K., Suzuki, T., Takahashi, N., Yokota, K. and Sugiura, M., *Effect of the addition of transition metals to Pt/Ba/Al_2O_3 catalyst on the NO_x storage-reduction catalysis under oxidizing conditions in the presence of SO_2.* Applied Catalysis B: Environmental, 2001. **30**(3–4): p. 459-468.
73. Vijay, R., Hendershot, R.J., Rivera-Jiménez, S.M., Rogers, W.B., Feist, B.J., Snively, C.M. and Lauterbach, J., *Noble metal free NO_x storage catalysts using cobalt discovered via high-throughput experimentation.* Catalysis Communications, 2005. **6**(2): p. 167-171.
74. Park, J.-H., Cho, H.J., Park, S.J., Nam, I.-S., Yeo, G.K., Kil, J.K. and Youn, Y.K., *Role of cobalt on γ-Al_2O_3 based NO x storage catalyst.* Topics in Catalysis, 2007. **42**(1): p. 61-64.
75. Vijay, R., C.M. Snively, and J. Lauterbach, *Performance of Co-containing NO_x storage and reduction catalysts as a function of cycling condition.* Journal of Catalysis, 2006. **243**(2): p. 368-375.
76. Zou, Z.-Q., Meng, M., Tsubaki, N., He, J.-J., Wang, G., Li, X.-G. and Zhou, X.-Y., *Influence of Co or Ce addition on the NOx storage and sulfur-resistance performance of the lean-burn NO_x trap catalyst Pt/K/TiO_2-ZrO_2.* Journal of Hazardous Materials, 2009. **170**(1): p. 118-126.
77. Lira, E., Merte, L.R., Behafarid, F., Ono, L.K., Zhang, L. and Roldan Cuenya, B., *Role and Evolution of Nanoparticle Structure and Chemical State during the Oxidation of*

NO over Size- and Shape-Controlled Pt/γ-Al_2O_3 Catalysts under Operando Conditions. ACS Catalysis, 2014. **4**(6): p. 1875-1884.
78. Bartholomew, C.H., *Mechanisms of catalyst deactivation.* Applied Catalysis A: General, 2001. **212**(1–2): p. 17-60.
79. Walker, J.S., Straguzzi, G.I., Manogue, W.H. and Schuit, G.C.A., *Carbon monoxide and propene oxidation by iron oxides for auto-emission control.* Journal of Catalysis, 1988. **110**(2): p. 298-309.
80. Heck, R.M. and R.J. Farrauto, *Catalytic Air Pollution Control*. Vol. Ch. 6, 2nd ed. 2002, New York: Wiley.
81. Kummer, J.T., *Use of noble metals in automobile exhaust catalysts.* The Journal of Physical Chemistry, 1986. **90**(20): p. 4747-4752.
82. Nieuwenhuys, B.E., *The Surface Science Approach Toward Understanding Automotive Exhaust Conversion Catalysis at the Atomic Level*, in *Advances in Catalysis*, B.C.G. Werner O. Haag and K. Helmut, Editors. 1999, Academic Press. p. 259-328.
83. Xu, C., Liu, Y., Zhou, C., Wang, L., Geng, H. and Ding, Y., *An In Situ Dealloying and Oxidation Route to Co_3O_4 Nanosheets and their Ambient-Temperature CO Oxidation Activity*. ChemCatChem, 2011. **3**(2): p. 399-407.
84. Cunningham, D.A.H., Kobayashi, T., Kamijo, N. and Haruta, M., *Influence of dry operating conditions: observation of oscillations and low temperature CO oxidation over Co_3O_4 and Au/ Co_3O_4 catalysts.* Catal. Lett., 1994. **25**: p. 257-264.
85. Jansson, J., Palmqvist, A.E.C., Fridell, E., Skoglundh, M., Österlund, L., Thormählen, P. and Langer, V., *On the Catalytic Activity of Co_3O_4 in Low-Temperature CO Oxidation.* Journal of Catalysis, 2002. **211**(2): p. 387-397.
86. Singh, S.A. and G. Madras, *Detailed mechanism and kinetic study of CO oxidation on cobalt oxide surfaces.* Applied Catalysis A: General, 2015. **504**: p. 463-475.
87. Li, J., Lu, G., Wu, G., Mao, D., Guo, Y., Wang, Y. and Guo, Y., *Effect of TiO_2 crystal structure on the catalytic performance of Co_3O_4/TiO_2 catalyst for low-temperature CO oxidation.* Catalysis Science & Technology, 2014. **4**(5): p. 1268-1275.
88. Alvarez, A., Ivanova, S., Centeno, M.A. and Odriozola, J.A., *Sub-ambient CO oxidation over mesoporous Co_3O_4: Effect of morphology on its reduction behavior and catalytic performance.* Applied Catalysis A: General, 2012. **431–432**: p. 9-17.
89. Lv, Y., Y. Li, and W. Shen, *Synthesis of Co_3O_4 nanotubes and their catalytic applications in CO oxidation.* Catalysis Communications, 2013. **42**: p. 116-120.
90. Zheng, X.-C., Wu, S.-H., Wang, S.-P., Wang, S.-R., Zhang, S.-M. and Huang, W.-P., *The preparation and catalytic behavior of copper–cerium oxide catalysts for low-temperature carbon monoxide oxidation.* Applied Catalysis A: General, 2005. **283**(1–2): p. 217-223.
91. Luo, M.-F., Ma, J.-M., Lu, J.-Q., Song, Y.-P. and Wang, Y.-J., *High-surface area CuO–CeO_2 catalysts prepared by a surfactant-templated method for low-temperature CO oxidation.* Journal of Catalysis, 2007. **246**(1): p. 52-59.
92. Pantaleo, G., Liotta, L.F., Venezia, A.M., Deganello, G., Ezzo, E.M., El Kherbawi, M.A. and Atia, H., *Support effect on the structure and CO oxidation activity of Cu-Cr mixed oxides over Al_2O_3 and SiO_2.* Materials Chemistry and Physics, 2009. **114**(2-3): p. 604-611.
93. Tarjomannejad, A., Niaei, A., Farzi, A., Salari, D. and Zonouz, P.R., *Catalytic Oxidation of CO Over $LaMn_{1-x}B_xO_3$ (B = Cu, Fe) Perovskite-type Oxides.* Catalysis Letters, 2016: p. 1-8.
94. Hasegawa, Y., Fukumoto, K., Ishima, T., Yamamoto, H., Sano, M. and Miyake, T., *Preparation of copper-containing mesoporous manganese oxides and their catalytic performance for CO oxidation.* Applied Catalysis B: Environmental, 2009. **89**(3–4): p. 420-424.

95. Hutchings, G.J., Mirzaei, A.A., Joyner, R.W., Siddiqui, M.R.H. and Taylor, S.H., *Effect of preparation conditions on the catalytic performance of copper manganese oxide catalysts for CO oxidation.* Applied Catalysis A: General, 1998. **166**(1): p. 143-152.
96. Jampaiah, D., Venkataswamy, P., Coyle, V.E., Reddy, B.M. and Bhargava, S.K., *Low-temperature CO oxidation over manganese, cobalt, and nickel doped CeO_2 nanorods.* RSC Advances, 2016. **6**(84): p. 80541-80548.
97. Dingsheng, W., Run, X., Xun, W. and Yadong, L., *NiO nanorings and their unexpected catalytic property for CO oxidation.* Nanotechnology, 2006. **17**(4): p. 979.
98. Biabani-Ravandi, A. and M. Rezaei, *Low temperature CO oxidation over Fe–Co mixed oxide nanocatalysts.* Chemical Engineering Journal, 2012. **184**: p. 141-146.
99. Cao, J.-L., Li, G.-J., Wang, Y., Sun, G., Wang, X.-D., Hari, B. and Zhang, Z.-Y., *Mesoporous Co–Fe–O nanocatalysts: Preparation, characterization and catalytic carbon monoxide oxidation.* Journal of Environmental Chemical Engineering, 2014. **2**(1): p. 477-483.
100. Cheng, T., Fang, Z., Hu, Q., Han, K., Yang, X. and Zhang, Y., *Low-temperature CO oxidation over CuO/Fe_2O_3 catalysts.* Catalysis Communications, 2007. **8**(7): p. 1167-1171.
101. Saha, B., Khan, A., Ibrahim, H. and Idem, R., *Evaluating the performance of non-precious metal based catalysts for sulfur-tolerance during the dry reforming of biogas.* Fuel, 2014. **120**(0): p. 202-217.
102. Weiss, B.M., N. Artioli, and E. Iglesia, *Catalytic NO Oxidation Pathways and Redox Cycles on Dispersed Oxides of Rhodium and Cobalt.* ChemCatChem, 2012. **4**(9): p. 1397-1404.
103. Shao, C., C., Liu, X., Meng, D., Xu, Q., Guo, Y., Guo, Y., Zhan, W., Wang, L. and Lu, G., *Catalytic performance of Co-Fe mixed oxide for NH_3-SCR reaction and the promotional role of cobalt.* RSC Advances, 2016. **6**(70): p. 66169-66179.
104. Wang, C.-B., Tang, C.-W., Tsai, H.-C. and Chien, S.-H., *Characterization and Catalytic Oxidation of Carbon Monoxide Over Supported Cobalt Catalysts.* Catalysis Letters, 2006. **107**(3): p. 223-230.
105. Zhou, L., Li, X., Yao, Z., Chen, Z., Hong, M., Zhu, R., Liang, Y. and Zhao, J., *Transition-Metal Doped Ceria Microspheres with Nanoporous Structures for CO Oxidation.* Scientific Reports, 2016. **6**: p. 23900.
106. Salek, G., Alphonse, P., Dufour, P., Guillemet-Fritsch, S. and Tenailleau, C., *Low-temperature carbon monoxide and propane total oxidation by nanocrystalline cobalt oxides.* Applied Catalysis B: Environmental, 2014. **147**: p. 1-7.
107. Chen, G., Xu, Q., Wang, Y., Song, G., Li, C., Zhao, W. and Fan, W., *Solubility product difference-guided synthesis of Co_3O_4-CeO_2 core-shell catalysts for CO oxidation.* Catalysis Science & Technology, 2016. **6**(19): p. 7273-7279.
108. Tuysuz, H., M. Comotti, and F. Schuth, *Ordered mesoporous Co_3O_4 as highly active catalyst for low temperature CO-oxidation.* Chemical Communications, 2008(34): p. 4022-4024.
109. Tschope, A., Liu, W., Flytzanistephanopoulos, M. and Ying, J.Y., *Redox Activity of Nonstoichiometric Cerium Oxide-Based Nanocrystalline Catalysts.* Journal of Catalysis, 1995. **157**(1): p. 42-50.
110. Avgouropoulos, G., Ioannides, T., Matralis, H.K., Batista, J. and Hocevar, S., *CuO–CeO_2 mixed oxide catalysts for the selective oxidation of carbon monoxide in excess hydrogen.* Catalysis Letters, 2001. **73**(1): p. 33-40.
111. Kang, M.Y., Yun, H.J., Yu, S., Kim, W., Kim, N.D. and Yi, J., *Effect of TiO_2 crystalline phase on CO oxidation over CuO catalysts supported on TiO_2.* Journal of Molecular Catalysis A: Chemical, 2013. **368–369**: p. 72-77.

112. Niknahad, B., M. Mohsennia, and A. Eliassi, *Influence of preparation methods on the structure and catalytic performance of nanostructured $La_{0.7}Ba_{0.3}Co_{0.3}Ni_{0.7}O_3$ for CO oxidation.* Reaction Kinetics, Mechanisms and Catalysis, 2016. **117**(2): p. 537-550.
113. Nikolla, E., Holewinski, A., Schwank, J. and Linic, S., *Controlling Carbon Surface Chemistry by Alloying: Carbon Tolerant Reforming Catalyst.* Journal of the American Chemical Society, 2006. **128**(35): p. 11354-11355.
114. Matsuzaki, Y. and I. Yasuda, *The poisoning effect of sulfur-containing impurity gas on a SOFC anode: Part I. Dependence on temperature, time, and impurity concentration.* Solid State Ionics, 2000. **132**(3–4): p. 261-269.
115. Ashrafi, M., Pfeifer, C., Pröll, T. and Hofbauer, H., *Experimental Study of Model Biogas Catalytic Steam Reforming: 2. Impact of Sulfur on the Deactivation and Regeneration of Ni-Based Catalysts.* Energy & Fuels, 2008. **22**(6): p. 4190-4195.
116. Saha, B., Khan, A., Ibrahim, H. and Idem, R., *Evaluating the performance of non-precious metal based catalysts for sulfur-tolerance during the dry reforming of biogas.* Fuel, 2014. **120**: p. 202-217.
117. Misture, S.T., McDevitt, K.M., Glass, K.C., Edwards, D.D., Howe, J.Y., Rector, K.D., He, H. and Vogel, S.C., *Sulfur-resistant and regenerable Ni/Co spinel-based catalysts for methane dry reforming.* Catalysis Science & Technology, 2015. **5**(9): p. 4565-4574.
118. Oleksenko, L.P., *Characteristics of Active Site Formation in Co-Containing Catalysts for CO Oxidation on Chemically Different Supports.* Theoretical and Experimental Chemistry, 2004. **40**(5): p. 331-336.
119. Pinna, F., *Supported metal catalysts preparation.* Catalysis Today, 1998. **41**(1–3): p. 129-137.
120. Campanati, M., G. Fornasari, and A. Vaccari, *Fundamentals in the preparation of heterogeneous catalysts.* Catalysis Today, 2003. **77**(4): p. 299-314.
121. Tsekouras, G., D. Neagu, and J.T.S. Irvine, *Step-change in high temperature steam electrolysis performance of perovskite oxide cathodes with exsolution of B-site dopants.* Energy & Environmental Science. **6**(1): p. 256-266.
122. Vaz, T. and A.V. Salker, *Preparation, characterization and catalytic CO oxidation studies on $LaNi_{1-x}Co_xO_3$ system.* Materials Science and Engineering: B, 2007. **143**(1–3): p. 81-84.
123. Royer, S., Duprez, D., Can, F., Courtois, X., Batiot-Dupeyrat, C., Laassiri, S. and Alamdari, H., *Perovskites as Substitutes of Noble Metals for Heterogeneous Catalysis: Dream or Reality.* Chemical Reviews, 2014. **114**(20): p. 10292-10368.
124. Davies, P.K., Wu, H., Borisevich, A.Y., Molodetsky, I.E. and Farber, L., *Crystal chemistry of complex perovskites: New cation-ordered dielectric oxides.* Annu. Rev. Mater. Res., 2008. **38**: p. 369-401.
125. Kofstad, P., *Nonstoichiometry, Diffusion and Electrical Conductivity in binary Metal Oxides*. 1972, Toronto: Wiley-Interscience.
126. Hashim, S.M., A.R. Mohamed, and S. Bhatia, *Current status of ceramic-based membranes for oxygen separation from air*. Advances in Colloid and Interface Science, 2010. **160**(1–2): p. 88-100.
127. Isupova, L.A., Sadykov, V.A., Tsybulya, S.V., Kryukova, G.N., Ivanov, V.P., Petrov, A.N. and Kononchuk, O.F., *Effect of structural disorder on the catalytic activity of mixed La−Sr−Co−Fr−O perovskites.* Reaction Kinetics and Catalysis Letters, 1997. **62**(1): p. 129-135.
128. Naegu, D., D., Tseukoras, G., Miller, D.N., Menard, H. and Irvine, J.T.S., *In situ growth of nanoparticles through control of non-stoichiometry.* Nature Chemistry 5, 2013(5): p. 916–923.

129. Wen, Y., Zhang, C., He, H., Yu, Y. and Teraoka, Y., *Catalytic oxidation of nitrogen monoxide over La1−xCexCoO3 perovskites.* Catalysis Today, 2007. **126**(3–4): p. 400-405.
130. Nitadori, T. and M. Misono, *Catalytic properties of $La_{1-x}A'_xFeO_3$(A' = Sr,Ce) and $La_{1-x}Ce_xCoO_3$.* Journal of Catalysis, 1985. **93**(2): p. 459-466.
131. Misono, M., *Recent progress in the practical applications of heteropolyacid and perovskite catalysts: Catalytic technology for the sustainable society.* Catalysis Today, 2009. **144**(3–4): p. 285-291.
132. Tanaka, H., Uenishi, M., Taniguchi, M., Tan, I., Narita, K., Kimura, M., Kaneko, K., Nishihata, Y. and Mizuki, J.i., *The intelligent catalyst having the self-regenerative function of Pd, Rh and Pt for automotive emissions control.* Catalysis Today, 2006. **117**(1–3): p. 321-328.
133. Uenishi, M., Taniguchi, M., Tanaka, H., Kimura, M., Nishihata, Y., Mizuki, J. and Kobayashi, T., *Redox behavior of palladium at start-up in the Perovskite-type $LaFePdO_x$ automotive catalysts showing a self-regenerative function.* Applied Catalysis B: Environmental, 2005. **57**(4): p. 267-273.
134. Madsen, B.D., Kobsiriphat, W., Wang, Y., Marks, L.D. and Barnett, S.A., *Nucleation of nanometer-scale electrocatalyst particles in solid oxide fuel cell anodes.* Journal of Power Sources, 2007. **166**(1): p. 64-67.
135. Kobsiriphat, W., Madsen, B.D., Wang, Y., Marks, L.D. and Barnett, S.A., *$La_{0.8}Sr_{0.2}Cr_{1-x}Ru_xO_{3-\delta}$–$Gd_{0.1}Ce_{0.9}O_{1.95}$ solid oxide fuel cell anodes: Ru precipitation and electrochemical performance.* Solid State Ionics, 2009. **180**(2–3): p. 257-264.
136. Bierschenk, D.M., Potter-Nelson, E., Hoel, C., Liao, Y., Marks, L., Poeppelmeier, K.R. and Barnett, S.A., *Pd-substituted (La,Sr)$CrO_{3-\delta}$–$Ce_{0.9}Gd_{0.1}O_{2-\delta}$ solid oxide fuel cell anodes exhibiting regenerative behavior.* Journal of Power Sources, 2011. **196**(6): p. 3089-3094.
137. Katz, M.B., Graham, G.W., Duan, Y., Liu, H., Adamo, C., Schlom, D.G. and Pan, X., *Self-Regeneration of Pd–$LaFeO_3$ Catalysts: New Insight from Atomic-Resolution Electron Microscopy.* Journal of the American Chemical Society, 2011. **133**(45): p. 18090-18093.
138. Neagu, D. and J.T.S. Irvine, *Structure and Properties of $La_{0.4}Sr_{0.4}TiO_3$ Ceramics for Use as Anode Materials in Solid Oxide Fuel Cells.* Chemistry of Materials, 2010. **22**(17): p. 5042-5053.
139. Myung, J.-h., Neagu, D., Miller, D.N. and Irvine, J.T.S., *Switching on electrocatalytic activity in solid oxide cells.* Nature, 2016. **537**(7621): p. 528-531.
140. A. De Souza, R., M. Saiful Islam, and E. Ivers-Tiffee, *Formation and migration of cation defects in the perovskite oxide $LaMnO_3$.* Journal of Materials Chemistry, 1999. **9**(7): p. 1621-1627.
141. Chambers, S.A., Gu, M., Sushko, P.V., Yang, H., Wang, C. and Browning, N.D., *Ultralow Contact Resistance at an Epitaxial Metal/Oxide Heterojunction Through Interstitial Site Doping.* Advanced Materials, 2013. **25**(29): p. 4001-4005.
142. Gohier, A., Ewels, C.P., Minea, T.M. and Djouadi, M.A., *Carbon nanotube growth mechanism switches from tip- to base-growth with decreasing catalyst particle size.* Carbon, 2008. **46**(10): p. 1331-1338.
143. Szot, K. and W. Speier, *Surfaces of reduced and oxidized $SrTiO_3$ from atomic force microscopy.* Physical Review B, 1999. **60**(8): p. 5909-5926.
144. Rostrup-Nielsen, J.R. and I. Alstrup, *Innovation and science in the process industry: Steam reforming and hydrogenolysis.* Catalysis Today, 1999. **53**(3): p. 311-316.
145. Goodhew, P.J., J. Humphreys, and R. Beanland, *Electron Microscopy and Analysis*. Vol. 3rd Edition. 2001, London: Taylor & Francis.

146. Maas, D.J. and R. van Gastel, *Helium Ion Microscopy*, in *Surface Science Techniques*, G. Bracco and B. Holst, Editors. 2013, Springer Berlin Heidelberg: Berlin, Heidelberg. p. 461-497.
147. Fukui, T., Tatami, J., Sakaguchi, S., Wakai, F., Senda, T., Akatsu, T., Baba, T., Noguchi, Y., Miyayama, M., Yamamoto, A., Yonezawa, S., Okamoto, T., Matsuda, M., Awano, M., Katamoto, T., Toda, K., Kirihara, S., Suda, A. and Nogi, K., *Chapter 6 - Evaluation methods for properties of nanostructured body A2 - Yokoyama, Masuo HosokawaKiyoshi NogiMario NaitoToyokazu*, in *Nanoparticle Technology Handbook*. 2008, Elsevier: Amsterdam. p. 317-383.
148. Japan, T.C.o.R.C.o.t.C.S.o. 1989: Shokubai.
149. Mayer, J., Giannuzzi, L.A., Kamino, T. and Michael, J., *TEM sample preparation and FIB-induced damage.* Mrs Bulletin, 2007. **32**(05): p. 400-407.
150. Perego, G., *Characterization of heterogeneous catalysts by X-ray diffraction techniques.* Catalysis Today, 1998. **41**(1–3): p. 251-259.
151. Wender, I., Sternberg, H.W., Friedel, R.A., Metlin, S.J. and Markby, R.E., *The Chemistry and Catalytic Properties of Cobalt and Iron Carbonyls*. 1962: Washington D.C.
152. Yao, Y.Y., *The oxidation of hydrocarbons and CO over metal oxides. III. Co_3O_4.* J. Catal., 1974. **33**: p. 108-122.
153. Neagu, D., Tsekouras, G., Miller, D.N., Ménard, H. and Irvine, J.T.S., *In situ growth of nanoparticles through control of non-stoichiometry.* Nat Chem, 2013. **5**(11): p. 916-923.
154. Freund, H.-J., Meijer, G., Scheffler, M., Schlögl, R. and Wolf, M., *CO Oxidation as a Prototypical Reaction for Heterogeneous Processes.* Angewandte Chemie International Edition, 2011. **50**(43): p. 10064-10094.
155. Yao, Y., Yan, Z., Chen, L., Zhou, Z., Liu, L. and Goodman, D.W., *Nickel Particle Size Effects on Cyclohexane Dehydrogenation: A Combined Reaction Kinetics and Surface Science Study.* Catalysis Letters, 2012. **142**(12): p. 1437-1444.
156. Neagu, D. and J.T.S. Irvine, *Enhancing Electronic Conductivity in Strontium Titanates through Correlated A and B-Site Doping.* Chemistry of Materials. **23**(6): p. 1607-1617.
157. Haneda, M., Watanabe, T., Kamiuchi, N. and Ozawa, M., *Effect of platinum dispersion on the catalytic activity of Pt/Al_2O_3 for the oxidation of carbon monoxide and propene.* Applied Catalysis B: Environmental, 2013. **142–143**(0): p. 8-14.
158. Naik, B., Moon, S.Y., Oh, S., Jung, C.-H. and Park, J.Y., *Titania-Encapsulated Hybrid Nanocatalysts as Active and Thermally Stable Model Catalysts.* Catalysis Letters, 2015. **145**(3): p. 930-938.
159. Papaioannou, E.I., Bachmann, C., Neumeier, J.J., Frankel, D., Over, H., Janek, J. and Metcalfe, I.S., *Role of the Three-Phase Boundary of the Platinum–Support Interface in Catalysis: A Model Catalyst Kinetic Study.* ACS Catalysis, 2016. **6**(9): p. 5865-5872.
160. An, K., Alayoglu, S., Musselwhite, N., Plamthottam, S., Melaet, G., Lindeman, A.E. and Somorjai, G.A., *Enhanced CO Oxidation Rates at the Interface of Mesoporous Oxides and Pt Nanoparticles.* Journal of the American Chemical Society, 2013. **135**(44): p. 16689-16696.
161. Jiang, Y., Liu, B., Yang, L., Yang, B., Liu, X., Liu, L., Weimer, C. and jiang, X., *Size-controllable Ni_5TiO_7 nanowires as promising catalysts for CO oxidation.* Scientific Reports, 2015. **5**: p. 14330.
162. Nikolla, E., J. Schwank, and S. Linic, *Promotion of the long-term stability of reforming Ni catalysts by surface alloying.* Journal of Catalysis, 2007. **250**(1): p. 85-93.
163. Demortiere, A., Panissod, P., Pichon, B.P., Pourroy, G., Guillon, D., Donnio, B. and Begin-Colin, S., *Size-dependent properties of magnetic iron oxide nanocrystals.* Nanoscale, 2011. **3**(1): p. 225-232.

164. Bieniek, B., Pohl, D., Schultz, L. and Rellinghaus, B., *The effect of oxidation on the surface-near lattice relaxation in FeNi nanoparticles.* Journal of Nanoparticle Research, 2011. **13**(11): p. 5935-5946.
165. D'Addato, S., Pasquali, L., Gazzadi, G.C., Verucchi, R., Capelli, R. and Nannarone, S., *Growth of Fe ultrathin films on Ni(111): structure and electronic properties.* Surface Science, 2000. **454–456**: p. 692-696.
166. Tauster, S.J. and S.C. Fung, *Strong metal-support interactions: Occurrence among the binary oxides of groups IIA–VB.* Journal of Catalysis, 1978. **55**(1): p. 29-35.
167. Tauster, S.J., S.C. Fung, and R.L. Garten, *Strong metal-support interactions. Group 8 noble metals supported on titanium dioxide.* Journal of the American Chemical Society, 1978. **100**(1): p. 170-175.
168. An, K. and G. Somorjai, *Nanocatalysis I: Synthesis of Metal and Bimetallic Nanoparticles and Porous Oxides and Their Catalytic Reaction Studies.* Catalysis Letters, 2015. **145**(1): p. 233-248.
169. Berlowitz, P.J., C.H.F. Peden, and D.W. Goodman, *Kinetics of carbon monoxide oxidation on single-crystal palladium, platinum, and iridium.* The Journal of Physical Chemistry, 1988. **92**(18): p. 5213-5221.
170. McClure, S.M. and D.W. Goodman, *New Insights into Catalytic CO Oxidation on Pt-Group Metals at Elevated Pressures.* Chemical Physics Letters, 2009. **469**(1-3): p. 1-13.
171. Wakita, H., T. Takeguchi, and W. Ueda, *Enhancement of selectivity for preferential CO oxidation over SO_2-pretreated Ru/Al_2O_3 catalyst by the presence of sulfur compounds.* Journal of Molecular Catalysis A: Chemical, 2007. **268**(1–2): p. 139-147.
172. Hulteberg, C., *Sulphur-tolerant catalysts in small-scale hydrogen production, a review.* International Journal of Hydrogen Energy, 2012. **37**(5): p. 3978-3992.
173. Yao, H.C., H.K. Stepien, and H.S. Gandhi, *The effects of SO_2 on the oxidation of hydrocarbons and carbon monoxide over Ptγ-Al_2O_3 catalysts.* Journal of Catalysis, 1981. **67**(1): p. 231-236.
174. Chen, I. and D.W. Shiue, *Resistivity to sulfur poisoning of nickel-alumina catalysts.* Industrial & Engineering Chemistry Research, 1988. **27**(8): p. 1391-1396.
175. Ng, C.F. and G.A. Martin, *Poisoning of $NiSiO_2$ catalysts with H_2S: Chemisorption of H_2, CO, C_6H_6, and C_2H_2 studied by magnetic methods.* Journal of Catalysis, 1978. **54**(3): p. 384-396.
176. Moulijn, J.A., A.E. van Diepen, and F. Kapteijn, *Catalyst deactivation: is it predictable?: What to do?* Applied Catalysis A: General, 2001. **212**(1–2): p. 3-16.
177. Kim, M.-Y., Choi, J.-S., Toops, T., Jeong, E.-S., Han, S.-W., Schwartz, V. and Chen, J., *Coating SiO_2 Support with TiO_2 or ZrO_2 and Effects on Structure and CO Oxidation Performance of Pt Catalysts.* Catalysts, 2013. **3**(1): p. 88.
178. Kim, S.H., Nam, S.-W., Lim, T.-H. and Lee, H.-I., *Effect of pretreatment on the activity of Ni catalyst for CO removal reaction by water–gas shift and methanation.* Applied Catalysis B: Environmental, 2008. **81**(1–2): p. 97-104.
179. Singha, R.K., Shukla, A., Yadav, A., Sivakumar Konathala, L.N. and Bal, R., *Effect of metal-support interaction on activity and stability of Ni-CeO_2 catalyst for partial oxidation of methane.* Applied Catalysis B: Environmental, 2017. **202**: p. 473-488.
180. Jansson, J., *Low-temperature CO oxidation over Co_3O_4/Al_2O_3.* J. Catal., 2000. **194**: p. 55-60.
181. Yao, Y., Gu, L.L., Jiang, W., Sun, H.C., Su, Q., Zhao, J., Ji, W.J. and Au, C.T., *Enhanced low temperature CO oxidation by pretreatment: specialty of the Au-Co_3O_4 oxide interfacial structures.* Catalysis Science & Technology, 2016. **6**(7): p. 2349-2360.

182. Lv, S., Xia, G., Jin, C., Hao, C., Wang, L., Li, J., Zhang, Y. and Zhu, J.J., *Low-temperature CO oxidation by Co_3O_4 nanocubes on the surface of $Co(OH)_2$ nanosheets.* Catalysis Communications, 2016. **86**: p. 100-103.
183. McCrea, K.R., J.S. Parker, and G.A. Somorjai, *The Role of Carbon Deposition from CO Dissociation on Platinum Crystal Surfaces during Catalytic CO Oxidation: Effects on Turnover Rate, Ignition Temperature, and Vibrational Spectra.* The Journal of Physical Chemistry B, 2002. **106**(42): p. 10854-10863.
184. Amakawa, K., Sun, L., Guo, C., Hävecker, M., Kube, P., Wachs, I.E., Lwin, S., Frenkel, A.I., Patlolla, A., Hermann, K., Schlögl, R. and Trunschke, A., *How Strain Affects the Reactivity of Surface Metal Oxide Catalysts.* Angewandte Chemie International Edition, 2013. **52**(51): p. 13553-13557.
185. Comotti, M., Li, W.-C., Spliethoff, B. and Schüth, F., *Support Effect in High Activity Gold Catalysts for CO Oxidation.* Journal of the American Chemical Society, 2006. **128**(3): p. 917-924.
186. Kurta, D.L., B.S. Dean, and E.P. Krenzelok, *Acute nickel carbonyl poisoning.* The American Journal of Emergency Medicine, 1993. **11**(1): p. 64-66.
187. Tang, C., C., Li, J., Yao, X., Sun, J., Cao, Y., Zhang, L., Gao, F., Deng, Y. and Dong, L., *Mesoporous NiO–CeO_2 catalysts for CO oxidation: Nickel content effect and mechanism aspect.* Applied Catalysis A: General, 2015. **494**: p. 77-86.
188. Mountapmbeme Kouotou, P., Vieker, H., Tian, Z.Y., Tchoua Ngamou, P.H., El Kasmi, A., Beyer, A., Golzhauser, A. and Kohse-Hoinghaus, K., *Structure-activity relation of spinel-type Co-Fe oxides for low-temperature CO oxidation.* Catalysis Science & Technology, 2014. **4**(9): p. 3359-3367.
189. Jia, C.-J., Schwickardi, M., Weidenthaler, C., Schmidt, W., Korhonen, S., Weckhuysen, B.M. and Schüth, F., *Co_3O_4–SiO_2 Nanocomposite: A Very Active Catalyst for CO Oxidation with Unusual Catalytic Behavior.* Journal of the American Chemical Society, 2011. **133**(29): p. 11279-11288.
190. Hu, L., Sun, K., Peng, Q., Xu, B. and Li, Y., *Surface active sites on Co_3O_4 nanobelt and nanocube model catalysts for CO oxidation.* Nano Research, 2010. **3**(5): p. 363-368.
191. Wang, J., Yang, N., Tang, H., Dong, Z., Jin, Q., Yang, M., Kisailus, D., Zhao, H., Tang, Z. and Wang, D., *Accurate Control of Multishelled Co_3O_4 Hollow Microspheres as High-Performance Anode Materials in Lithium-Ion Batteries.* Angewandte Chemie International Edition, 2013. **52**(25): p. 6417-6420.
192. Qiu, K., Yan, H., Zhang, D., Lu, Y., Cheng, J., Zhao, W., Wang, C., Zhang, Y., Liu, X., Cheng, C. and Luo, Y., *Hierarchical 3D Mesoporous Conch-like Co_3O_4 Nanostructure Arrays for High-Performance Supercapacitors.* Electrochimica Acta, 2014. **141**: p. 248-254.
193. McIntyre, N.S. and M.G. Cook, *X-ray photoelectron studies on some oxides and hydroxides of cobalt, nickel, and copper.* Analytical Chemistry, 1975. **47**(13): p. 2208-2213.
194. Riva, R., Miessner, H., Vitali, R. and Del Piero, G., *Metal–support interaction in Co/SiO_2 and Co/TiO_2.* Applied Catalysis A: General, 2000. **196**(1): p. 111-123.
195. Biesinger, M.C., Payne, B.P., Grosvenor, A.P., Lau, L.W.M., Gerson, A.R. and Smart, R.S.C., *Resolving surface chemical states in XPS analysis of first row transition metals, oxides and hydroxides: Cr, Mn, Fe, Co and Ni.* Applied Surface Science, 2011. **257**(7): p. 2717-2730.
196. Kim, J.G., Pugmire, D.L., Battaglia, D. and Langell, M.A., *Analysis of the $NiCo_2O_4$ spinel surface with Auger and X-ray photoelectron spectroscopy.* Applied Surface Science, 2000. **165**(1): p. 70-84.

197. Railsback, J.G., Johnston-Peck, A.C., Wang, J. and Tracy, J.B., *Size-Dependent Nanoscale Kirkendall Effect During the Oxidation of Nickel Nanoparticles.* ACS Nano, 2010. **4**(4): p. 1913-1920.
198. Wang, H., Chen, C., Zhang, Y., Peng, L., Ma, S., Yang, T., Guo, H., Zhang, Z., Su, D.S. and Zhang, J., *In situ oxidation of carbon-encapsulated cobalt nanocapsules creates highly active cobalt oxide catalysts for hydrocarbon combustion.* Nature Communications, 2015. **6**: p. 7181.
199. Sadasivan, S., R.M. Bellabarba, and R.P. Tooze, *Size dependent reduction-oxidation-reduction behaviour of cobalt oxide nanocrystals.* Nanoscale, 2013. **5**(22): p. 11139-11146.
200. Ha, D.-H., Moreau, L.M., Honrao, S., Hennig, R.G. and Robinson, R.D., *The Oxidation of Cobalt Nanoparticles into Kirkendall-Hollowed CoO and Co_3O_4: The Diffusion Mechanisms and Atomic Structural Transformations.* The Journal of Physical Chemistry C, 2013. **117**(27): p. 14303-14312.
201. Ma, C.Y., Mu, Z., Li, J.J., Jin, Y.G., Cheng, J., Lu, G.Q., Hao, Z.P. and Qiao, S.Z., *Mesoporous Co_3O_4 and Au/Co_3O_4 Catalysts for Low-Temperature Oxidation of Trace Ethylene.* Journal of the American Chemical Society, 2010. **132**(8): p. 2608-2613.
202. Gudyka, S., Grzybek, G., Gryboś, J., Indyka, P., Leszczyński, B., Kotarba, A. and Sojka, Z., *Enhancing the deN_2O activity of the supported Co_3O_4|α-Al_2O_3 catalyst by glycerol-assisted shape engineering of the active phase at the nanoscale.* Applied Catalysis B: Environmental, 2017. **201**: p. 339-347.
203. Deng, J., Feng, S., Zhang, K., Li, J., Wang, H., Zhang, T. and Ma, X., *Heterogeneous activation of peroxymonosulfate using ordered mesoporous Co_3O_4 for the degradation of chloramphenicol at neutral pH.* Chemical Engineering Journal, 2017. **308**: p. 505-515.
204. Sickafus, K.E., J.M. Wills, and N.W. Grimes, *Structure of Spinel.* Journal of the American Ceramic Society, 1999. **82**: p. 3279–3292.
205. Teng, Y., Kusano, Y., Azuma, M., Haruta, M. and Shimakawa, Y., *Morphology effects of Co_3O_4 nanocrystals catalyzing CO oxidation in a dry reactant gas stream.* Catalysis Science & Technology, 2011. **1**(6): p. 920-922.
206. Zhang, X., K.-Y. Tsang, and K.-Y. Chan, *Electrocatalytic properties of supported platinum–cobalt nanoparticles with uniform and controlled composition.* Journal of Electroanalytical Chemistry, 2004. **573**(1): p. 1-9.
207. Wu, J., Xue, Y., Yan, X., Yan, W., Cheng, Q. and Xie, Y., *Co_3O_4 nanocrystals on single-walled carbon nanotubes as a highly efficient oxygen-evolving catalyst.* Nano Research, 2012. **5**(8): p. 521-530.
208. Wang, Z.L., J.S. Yin, and Y.D. Jiang, *EELS analysis of cation valence states and oxygen vacancies in magnetic oxides.* Micron, 2000. **31**(5): p. 571-580.
209. Xia, Y., Dai, H., Jiang, H. and Zhang, L., *Three-dimensional ordered mesoporous cobalt oxides: Highly active catalysts for the oxidation of toluene and methanol.* Catalysis Communications, 2010. **11**(15): p. 1171-1175.
210. Iablokov, V., Barbosa, R., Pollefeyt, G., Van Driessche, I., Chenakin, S. and Kruse, N., *Catalytic CO Oxidation over Well-Defined Cobalt Oxide Nanoparticles: Size-Reactivity Correlation.* ACS Catalysis, 2015. **5**(10): p. 5714-5718.
211. Sun, Y., Lv, P., Yang, J.-Y., He, L., Nie, J.-C., Liu, X. and Li, Y., *Ultrathin Co_3O_4 nanowires with high catalytic oxidation of CO.* Chemical Communications, 2011. **47**(40): p. 11279-11281.
212. Cargnello, M., Doan-Nguyen, V.V.T., Gordon, T.R., Diaz, R.E., Stach, E.A., Gorte, R.J., Fornasiero, P. and Murray, C.B., *Control of Metal Nanocrystal Size Reveals Metal-Support Interface Role for Ceria Catalysts.* Science, 2013. **341**(6147): p. 771-773.

213. Varon, M., Ojea-Jimenez, I., Arbiol, J., Balcells, L., Martinez, B. and Puntes, V.F., *Spontaneous formation of hollow cobalt oxide nanoparticles by the Kirkendall effect at room temperature at the water-air interface.* Nanoscale, 2013. **5**(6): p. 2429-2436.
214. Allian, A.D., Takanabe, K., Fujdala, K.L., Hao, X., Truex, T.J., Cai, J., Buda, C., Neurock, M. and Iglesia, E., *Chemisorption of CO and Mechanism of CO Oxidation on Supported Platinum Nanoclusters.* Journal of the American Chemical Society, 2011. **133**(12): p. 4498-4517.
215. Song, W., Jansen, A.P.J., Degirmenci, V., Ligthart, D.A.J.M. and Hensen, E.J.M., *A computational study of the mechanism of CO oxidation by a ceria supported surface rhodium oxide layer.* Chemical Communications, 2013. **49**(37): p. 3851-3853.
216. Santra, A.K. and D.W. Goodman, *Catalytic oxidation of CO by platinum group metals: from ultrahigh vacuum to elevated pressures.* Electrochimica Acta, 2002. **47**(22-23): p. 3595-3609.
217. McClure, S.M., Lundwall, M., Yang, F., Zhou, Z. and Goodman, D.W., *CO Oxidation on Rh/SiO_2/Mo(112) Model Catalysts at Elevated Pressures.* The Journal of Physical Chemistry C, 2009. **113**(22): p. 9688-9697.
218. McCarthy, E., Zahradnik, J., Kuczynski, G.C. and Carberry, J.J., *Some unique aspects of CO oxidation on supported Pt.* Journal of Catalysis, 1975. **39**(1): p. 29-35.
219. Zhu, Y., Tan, R., Feng, J., Ji, S. and Cao, L., *The reaction and poisoning mechanism of SO_2 and perovskite $LaCoO_3$ film model catalysts.* Applied Catalysis A: General, 2001. **209**(1–2): p. 71-77.
220. Visconti, C.G., Lietti, L., Forzatti, P. and Zennaro, R., *Fischer–Tropsch synthesis on sulphur poisoned Co/Al_2O_3 catalyst.* Applied Catalysis A: General, 2007. **330**: p. 49-56.
221. Royer, S., Van Neste, A., Davidson, R., McIntyre, S. and Kaliaguine, S., *Methane Oxidation over Nanocrystalline $LaCo_{1-x}FeXO_3$: Resistance to SO_2 Poisoning.* Industrial & Engineering Chemistry Research, 2004. **43**(18): p. 5670-5680.
222. Wang, X., W. Zhong, and Y. Li, *Nanoscale Co-based catalysts for low-temperature CO oxidation.* Catalysis Science & Technology, 2015. **5**(2): p. 1014-1020.
223. Zhong, S., Sun, Y., Xin, H., Yang, C., Chen, L. and Li, X., *NO oxidation over Ni–Co perovskite catalysts.* Chemical Engineering Journal, 2015. **275**: p. 351-356.
224. Chen, J., Shen, M., Wang, X., Wang, J., Su, Y. and Zhao, Z., *Catalytic performance of NO oxidation over $LaMeO_3$ (Me = Mn, Fe, Co) perovskite prepared by the sol–gel method.* Catalysis Communications, 2013. **37**: p. 105-108.

A. APPENDICES

1.1 Evolution of exsolved metal systems as CO oxidation catalyst

In Chapter 4 section 2.2, the evolution of the exsolved powder systems were conducted by testing the prepared powder from each batch under the light-off experiments. Eight batches of powder systems were prepared and tested; with the six earlier batches (Batch 1-6) were considered as the screening powders until the most active exsolved powder formulation were found in two final batches (Batch 7 and 8). 60 exsolved metal powder systems were prepared and tested accordingly. **Figure A-1** presents the microstructure of the most active powder systems from each batch as explained in subsection **4.2.2**.

Batch 1

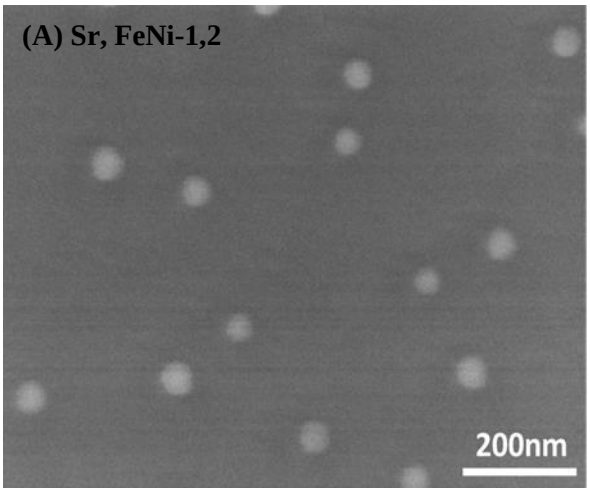

Batch 2

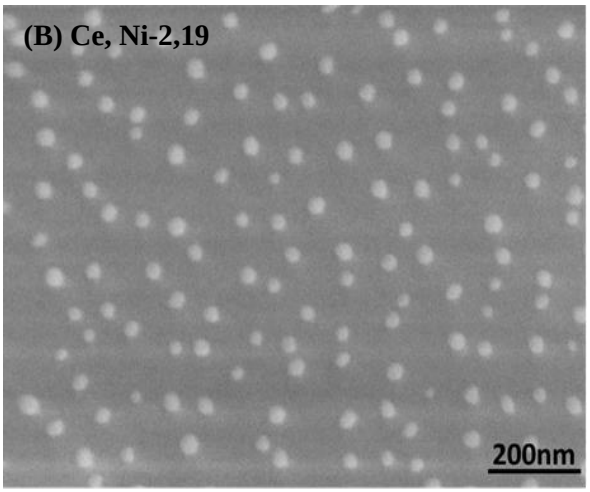

Batch 3

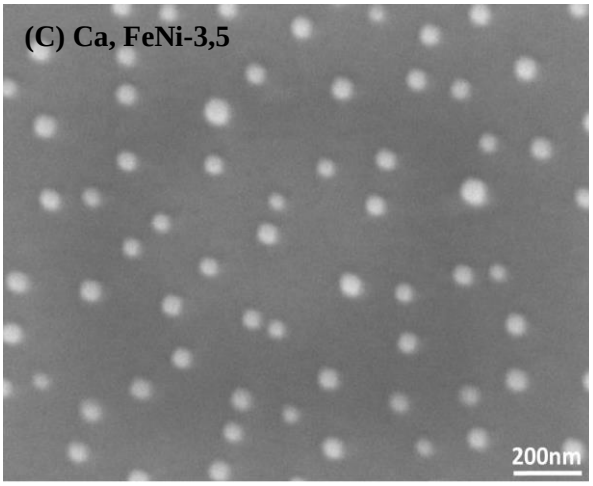

Batch 4

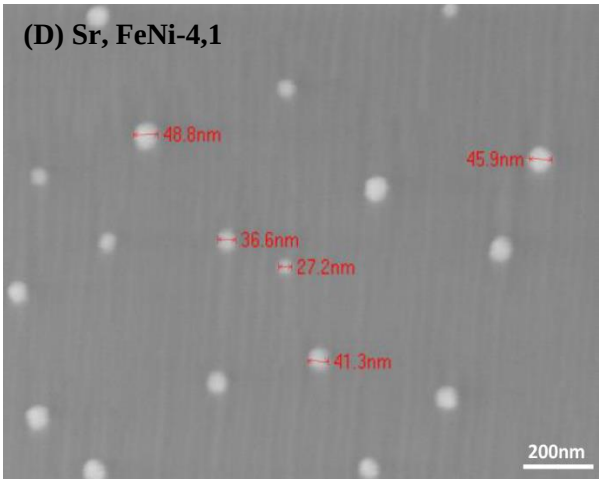

Batch 6 Batch 7

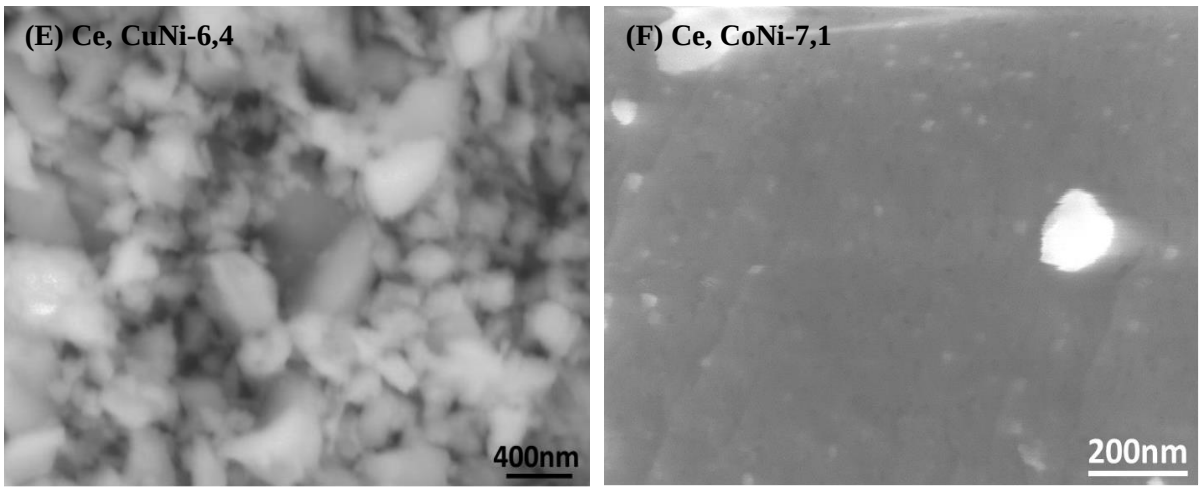

Batch 8

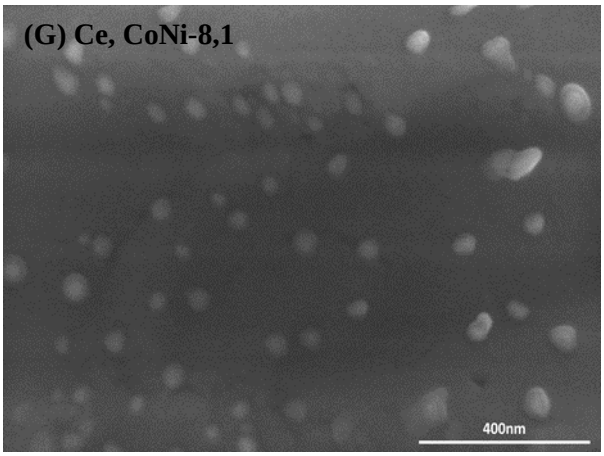

Figure A-1 The different surface metal particles population between the most active exsolved powder systems from each batch; (A) Sr, FeNi-1, 2, (B) Ce, Ni-2, 19, (C) Ca, FeNi-3,5, (D) Sr, FeNi-4,1, (E) Ce, CuNi-6,4, (F) Ce, CoNi-7,1 and (G) Ce, CoNi-8,1

1.1.1 Light-off

In this section, the light-off plots for all powder systems from each batch explained in section **4.2.2** were presented here. The reaction conditions for these light-off were as previously explained in Chapter 4. **Figure A-2** shows the light-off plot for all exsolved Sr, FeNi prepared from Batch 1. In this batch, the preparation parameters were varied from powder to powder, especially in terms of grinding processes and the reducing atmospheres used. Since this was our first attempt in preparing these exsolved metal systems in powder form, hence, the preparation parameters were varied in order to optimise the preparation method. In this batch, three grinding process were employed; i.e. ball milling, crushing and grinding method while two type of reducing atmospheres were used, which include reduction under 5 % of hydrogen and under vacuum. These reducing atmospheres were used to provoke the metal exsolution on

the surface and it was found that the exsolution of FeNi were compromised, with observed low particle population of around 10-15 particles μm^{-2}.

Following this, the exsolution of FeNi were successfully increased in Batch 2, although only up to 30 particles μm^{-2} before the exsolution was restricted by the non-stoichiometry. Several exsolved Ce, Ni powder systems were also successfully prepared with varying grinding processes and reducing atmospheres. **Figure A-3** shows the light-off plot for five exsolved Sr, FeNi and six exsolved Ce, Ni powder systems prepared from Batch 2. The results obtained were explained in subsection 4.2.2. The average particle size of the most active Ce, Ni powder systems (Ce, Ni-2,19 and Ce, Ni-2,18) were around 30-38 nm with 60-67 particles μm^{-2}. It seems that in order to increase the activity of the exsolved Sr, FeNi powder systems, we need to increase the particles population of FeNi on the powder systems. This was successfully done in Batch 3 by replacing the detrimental Sr into Ce or Ca, in which the particles population were improved to around 50 particles μm^{-2}, although at the expense of forming larger particles (> 45 nm) and low activity as shown in **Figure A-4**. Batch 4 and 5 were intended to retest the activity of the most active exsolved Sr, FeNi from Batch 1 and from the screening pellet (FeNi-s). **Figure A-5** presents the reproducibility of these Sr, FeNi systems, in which we weren't able to reproduce the activity, which then raise the reproducibility problem of these systems. System with the exsolution of another active base metals, Cu were also prepared in Batch 6, however, the activities were still low as shown in **Figure A-6**.

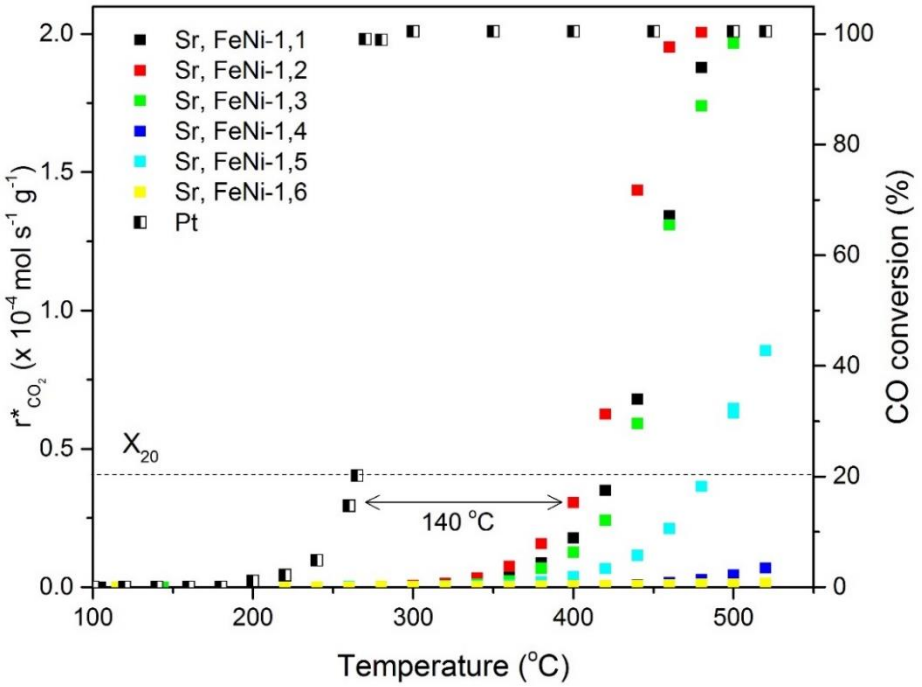

Figure A-2 CO_2 production rates, $r^*_{CO_2}$, and CO conversion as a function of temperatures (light-off) over state-of-the-art Pt/Al_2O_3 and six exsolved Sr, FeNi powder systems from batch 1 under CO oxidation reaction with inlet feed gas mixture of P_{CO} = 0.6 kPa, P_{O2} = 1.0 kPa, F_t = 450 ml min^{-1} and GHSV=26 000 h^{-1}. These exsolved powder systems differ from each other in terms of the difference in grinding methods and the reduction atmospheres employed during preparation.

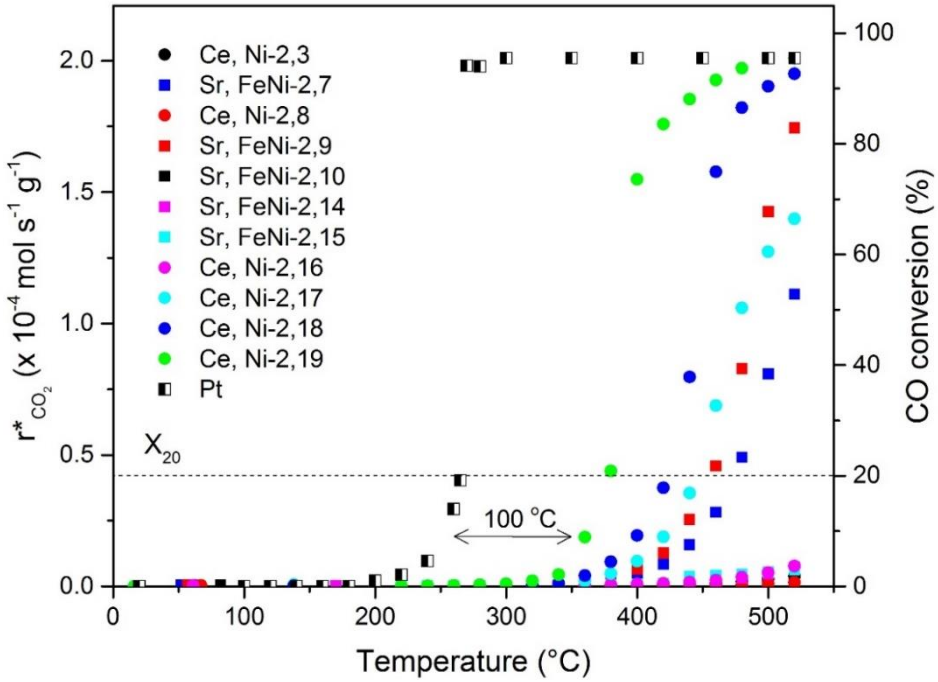

Figure A-3 CO_2 production rates, $r^*_{CO_2}$, and CO conversion as a function of temperatures (light-off) over state-of-the-art Pt/Al_2O_3 and five exsolved Sr, FeNi and six Ce, Ni powder systems from batch 2 under CO oxidation reaction with inlet feed gas mixture of P_{CO} = 0.6 kPa, P_{O2} = 1.0 kPa, F_t = 450 ml min^{-1} and GHSV=26 000 h^{-1}. These exsolved powder systems differ from each other in terms of the difference in grinding methods and the reduction atmospheres employed during preparation.

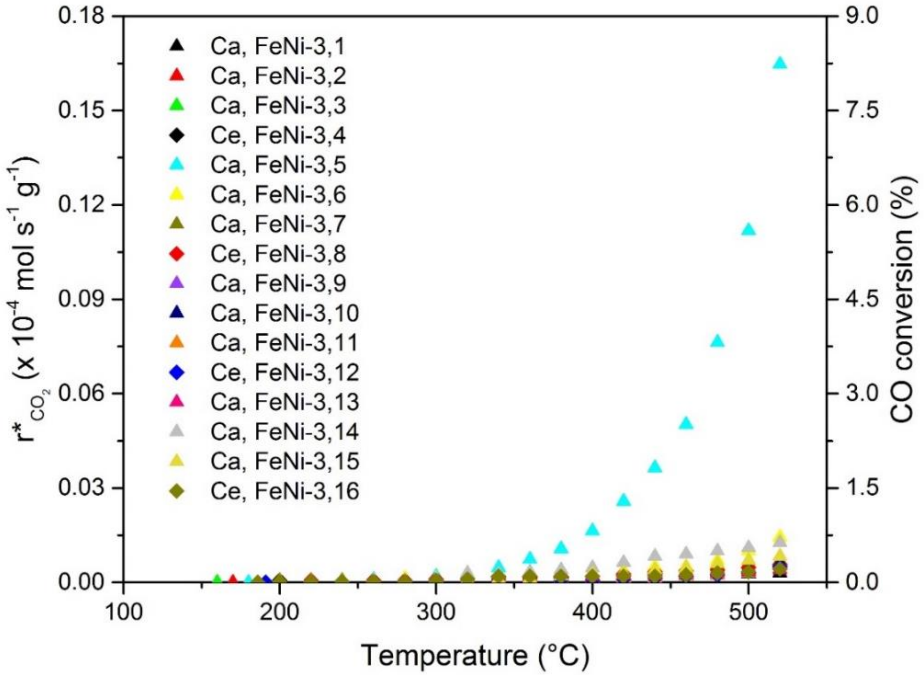

Figure A-4 CO_2 production rates, $r^*_{CO_2}$, and CO conversion as a function of temperatures (light-off) over 12 exsolved Ca, FeNi and four Ce, FeNi powder systems from batch 3 under CO oxidation reaction with inlet feed gas mixture of P_{CO} = 0.6 kPa, P_{O2} = 1.0 kPa, F_t = 450 ml min^{-1} and GHSV=26 000 h^{-1}. These exsolved powder systems differ from each other in terms of the difference in grinding methods and the reduction atmospheres employed during preparation.

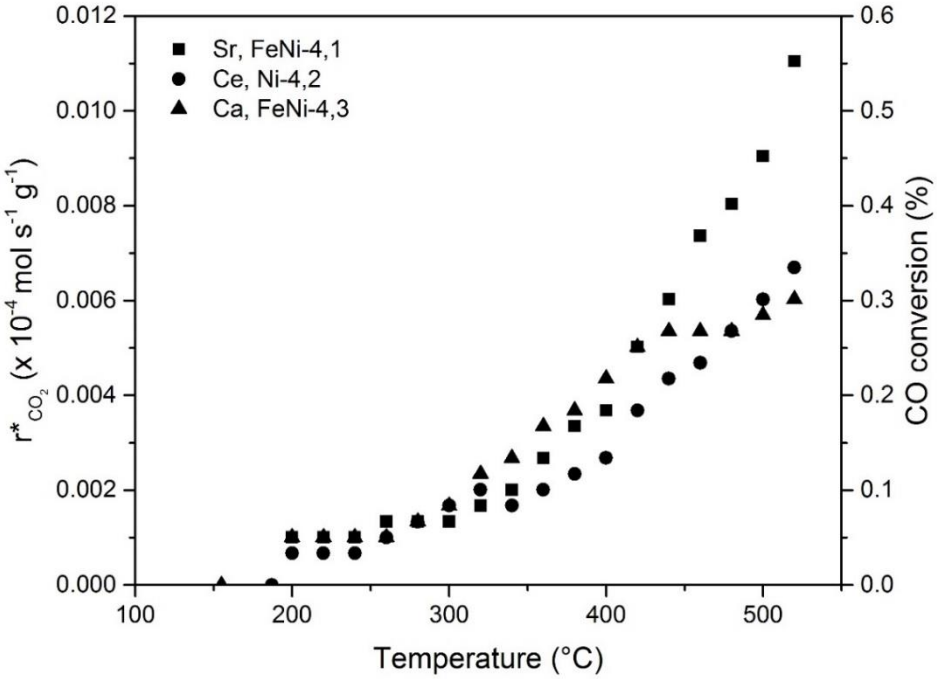

Figure A-5 CO_2 production rates, $r^*_{CO_2}$, and CO conversion as a function of temperatures (light-off) over one Sr, FeNi, one Ce, Ni and one Ce, FeNi powder systems from batch 4 under CO oxidation reaction with inlet feed gas mixture of P_{CO} = 0.6 kPa, P_{O2} = 1.0 kPa, F_t = 450 ml min^{-1} and GHSV=26 000 h^{-1}. These exsolved powder systems differ from each other in terms of the difference in grinding methods and the reduction atmospheres employed during preparation.

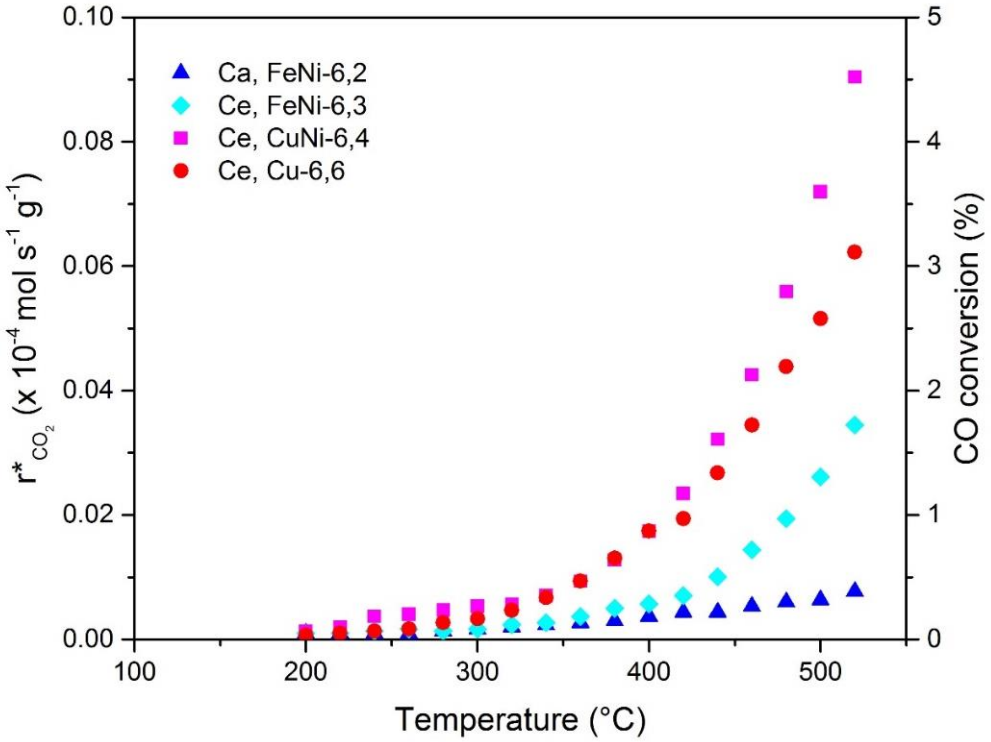

Figure A-6 CO_2 production rates, $r^*_{CO_2}$, and CO conversion as a function of temperatures (light-off) over state-of-the-art Pt/Al_2O_3 and one Ca, FeNi, one Ce, FeNi, one Ce, CuNi and six Ce, Cu powder systems from batch 6 under CO oxidation reaction with inlet feed gas mixture of P_{CO} = 0.6 kPa, P_{O2} = 1.0 kPa, F_t = 450 ml min^{-1} and GHSV=26 000 h^{-1}. These exsolved powder systems differ from each other in terms of the difference in grinding methods and the reduction atmospheres employed during preparation.

The exsolution of Co in exsolved Ce, Ni powder systems were prepared in Batch 7 with altered preparation route, aiming to produce two range of particle sizes (10 and 30 nm). The altered preparation route were altered as shown in **Figure A-7**. The normal preparation route (which were used to prepare the rest of powder systems) were explained in Chapter 3. For exsolved Ce, CoNi in Batch 7, the metal-perovskites mixtures were palletisized following calcination and the exsolution were then provoked on the polished side of the pellet. This then produced the exsolution of larger particles on the surface with smaller particles exsolution within the bulk. The exsolved pellet was then grounded into powder form, which then resulted in different morphology of the powders as shown in the figure below. Ce, CoNi-7,1 powder system exhibited two ranges of particle size with observed empty sockets, resulted from the grinding effect of the bulk metal exsolution, leaving the particles on one part of the breakage and empty socket on the other. This differ from Ce, CoNi-8,1 powder system prepared following the normal preparation route, with only one range of particle size was observed, without the presence of empty sockets. This, however, did not affect the activity of the exsolved Ce, CoNi powder systems since both showed similar activity under the light-off as shown in **Figure A-8**.

Not only that, both were readily activated under CO-rich atmospheres (CO kinetics), in which the activities under light-off were enhanced across all temperatures, as shown by the activated Ce, CoNi-7,1 and Ce, CoNi-8,1 powder systems. Detailed explanation regarding this were explained in Chapter 5.

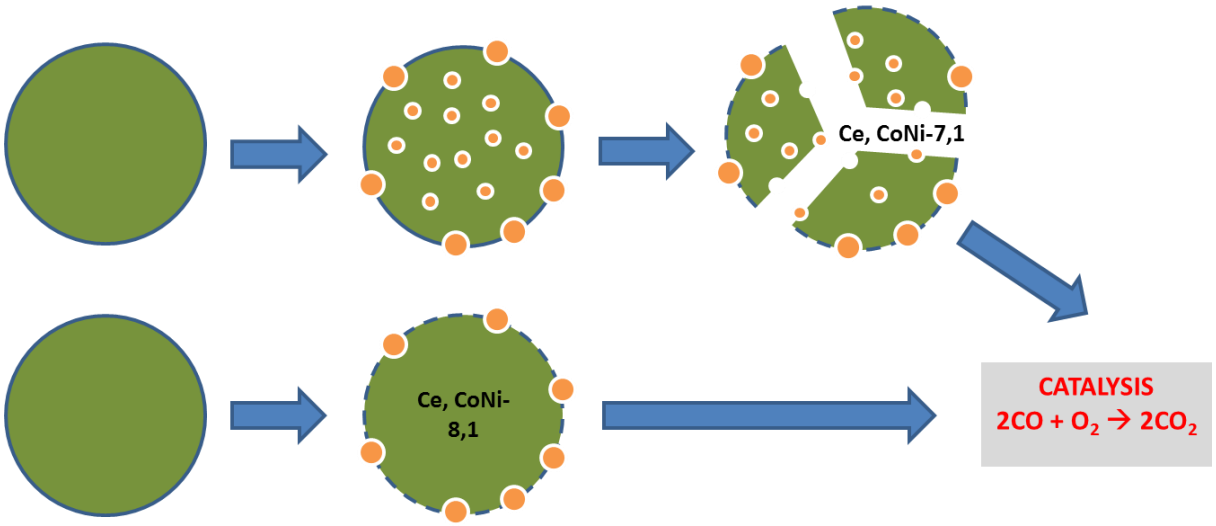

Figure A-7 Schematic diagram of the difference in preparation step between Ce, CoNi-7,1 and Ce, CoNi-8,1 powder systems and the resultant surface morphologies prior and post-experiments. Circles with solid line represent pellet system whilst the circles with dashed line refers to powder system

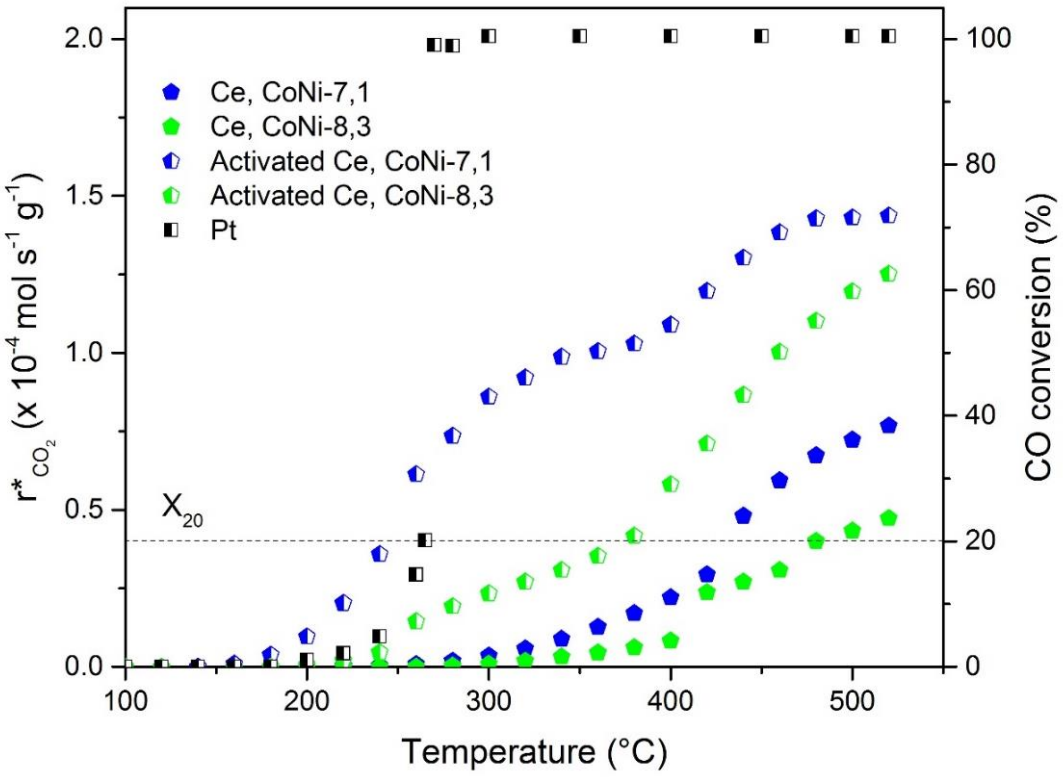

Figure A-8 CO_2 production rates, $r^*_{CO_2}$, and CO conversion as a function of temperatures (light-off) over state-of-the-art Pt/Al_2O_3 and two exsolved Ce, CoNi powder systems from Batch 7 and 8 under CO oxidation reaction with inlet feed gas mixture of P_{CO} = 0.6 kPa, P_{O2} = 1.0 kPa, F_t = 450 ml min^{-1} and GHSV=26 000 h^{-1}. The weight of each powders are similar (weight of powder, w_p = 10 mg), diluted in alumina with a total weight, W_t of 100 mg. These exsolved powder systems differ from each other in terms of the difference in grinding methods and the reduction atmospheres employed during preparation.

Figure A-9 showed the surface morphologies for Ce, CoNi-7,1 powder system after being removed from the reactor. As mentioned previously in subsection **5.4.1**, we were not able to verify the active sites due to the particles being possibly damaged by the alumina balls as seen in **Figure A-9-A,** which then makes the calculation to be inaccurate**.**

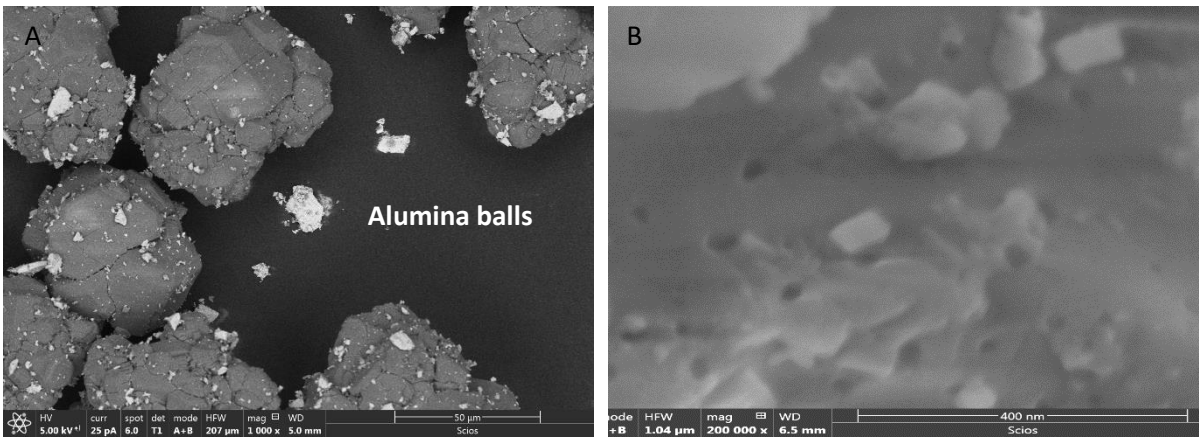

Figure A-9 The surface morphologies for Ce, CoNi-7,1 powder system after being removed from the reactor.

Figure A-10 presents the microstructure of the commercial Ni on alumina silica powder system prior to and following CO kinetics experiment, as explained in subsection **4.3**. we can clearly see that the particles following the CO kinetic experiments were severely agglomerated, hence, blocking the active sites.

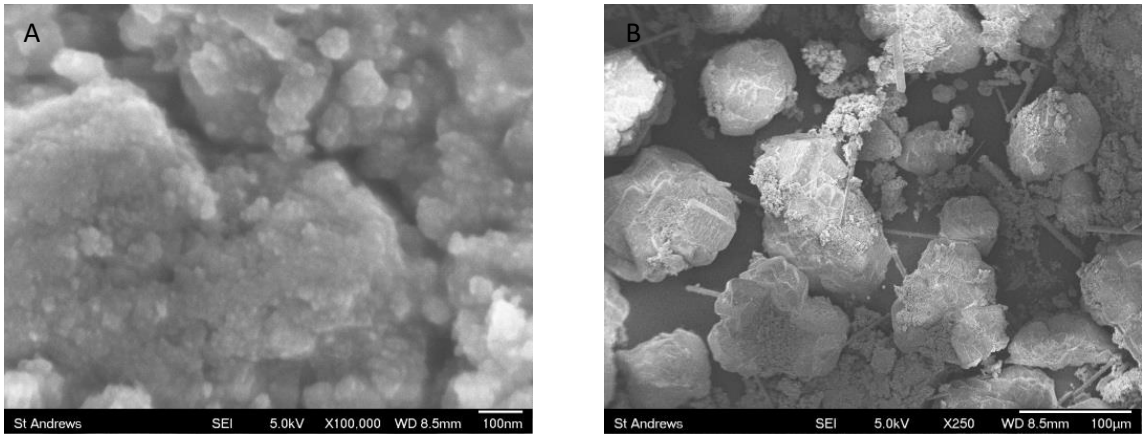

Figure A-10 Comparison of surface morphologies of commercial Ni on alumina silica (A) prior to and (B) following exposure to CO kinetics experiments.

Figure A-11 presents the sulphur poisoning-recovery experiment at 480 °C performed on Ce, Ni-2,19 powder system as comparison to the ones reported in section **4.4**. The experimental conditions were as described in that section. The CO_2 production rates, $r^*_{CO_2}$, were able to recover following sulphur poisoning at two time intervals (30 and 60 minutes) within approximately 2 hours. This also has been previously observed by Sr, FeNi-1,2 powder system.

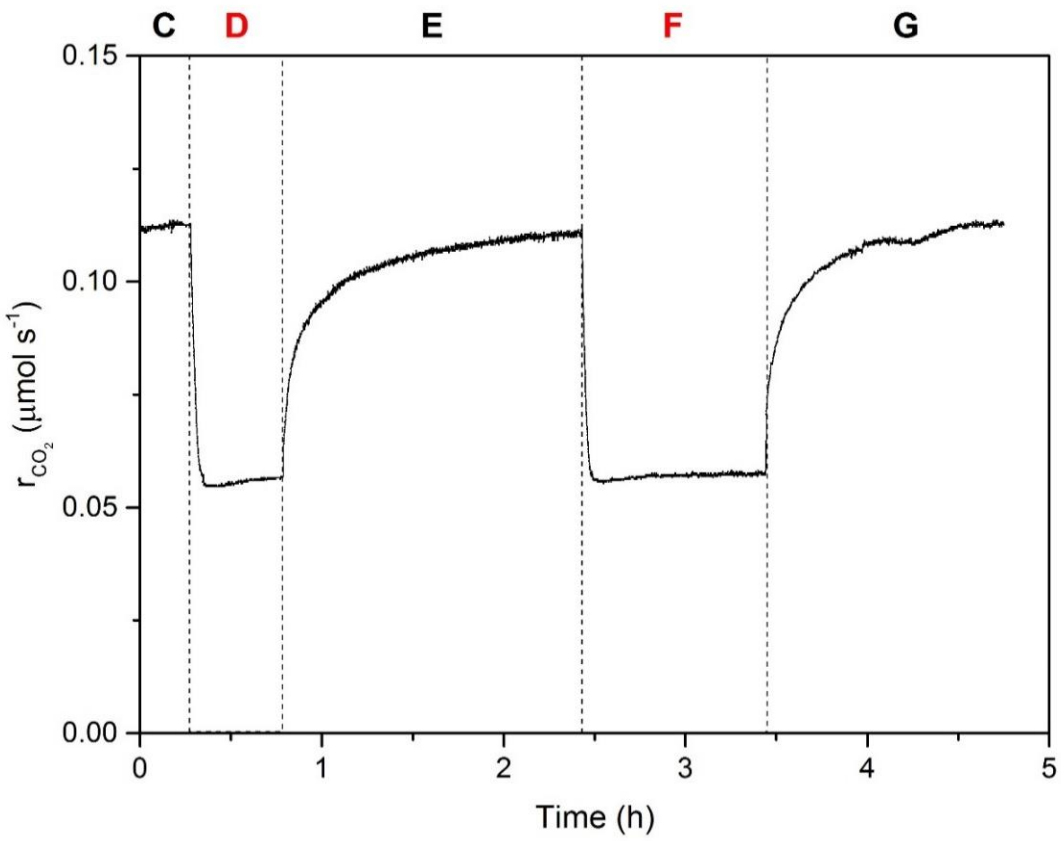

Figure A-11 CO_2 production rates, $r^*_{CO_2}$ and rates recovery during sulphur poisoning (50 ppm SO_2) under differential conditions and the reaction conditions of P_{CO} = 0.6 kPa, P_{O2} = 1.0 kPa, F_t = 450 ml s^{-1} for Ce, Ni-2,19 powder system at T= 480 °C, respectively. The temperatures were chosen in order to operate under differential conditions (20 % of CO conversion or less) for reliable kinetic investigations and sulphur source, SO_2 (50 ppm) was added into the inlet feed gas mixtures in two different time interval; 30 and 60 minutes (Zone D and F).

1.2 Exsolved CoNi as CO and NO oxidation catalysts

Here, the link between the kinetic behaviour and the particle characteristics of exsolved CoNi pellet systems were investigated. The enhanced activities of the nanocubes structures were observed, and in order to pinpoint the origin of the enhanced activities, the mechanical removal of the cubes on another activated exsolved CoNi pellet system were performed and the activities was tested under the light-off. The reaction conditions followed the ones described in subsection **5.3.4**. **Figure A-12** shows the significant drop of activities (r_{CO_2} and TOFs) after the removal of the nanocubes from the pellet surface. The nanocubes present on the pellet surface prior to the removal was similar to the ones exhibited by its predecessor (CoNi-30nm) as shown in **Figure A-14.**

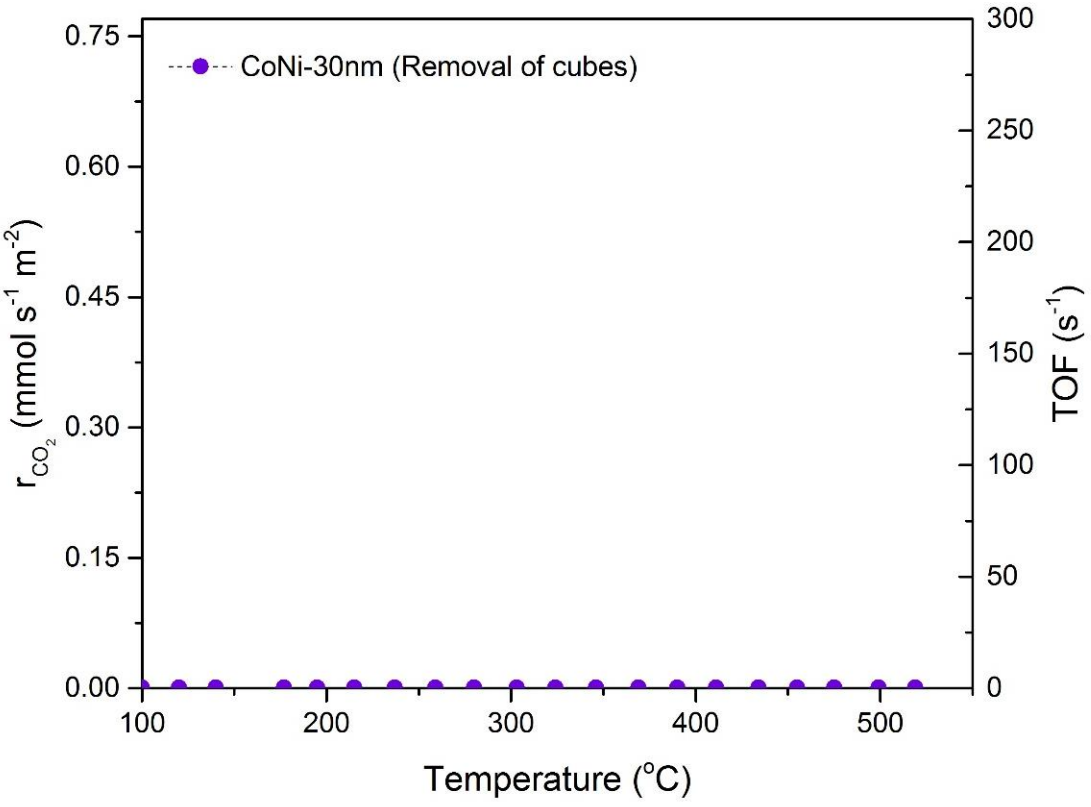

Figure A-12 CO_2 production rates, r_{CO_2}, and TOF values as a function of temperature (light-off) over activated CoNi-30nm pellet system with the cubes were mechanically removed under CO oxidation reaction with inlet feed gas mixture of P_{CO} = 0.6 kPa, P_{O2} = 1.0 kPa, F_t = 150 ml min^{-1}. The rate is normalized with respect to the pellet area decorated with particles (top side in Figure 5-1). Corresponding TOF values are shown on the right axis.

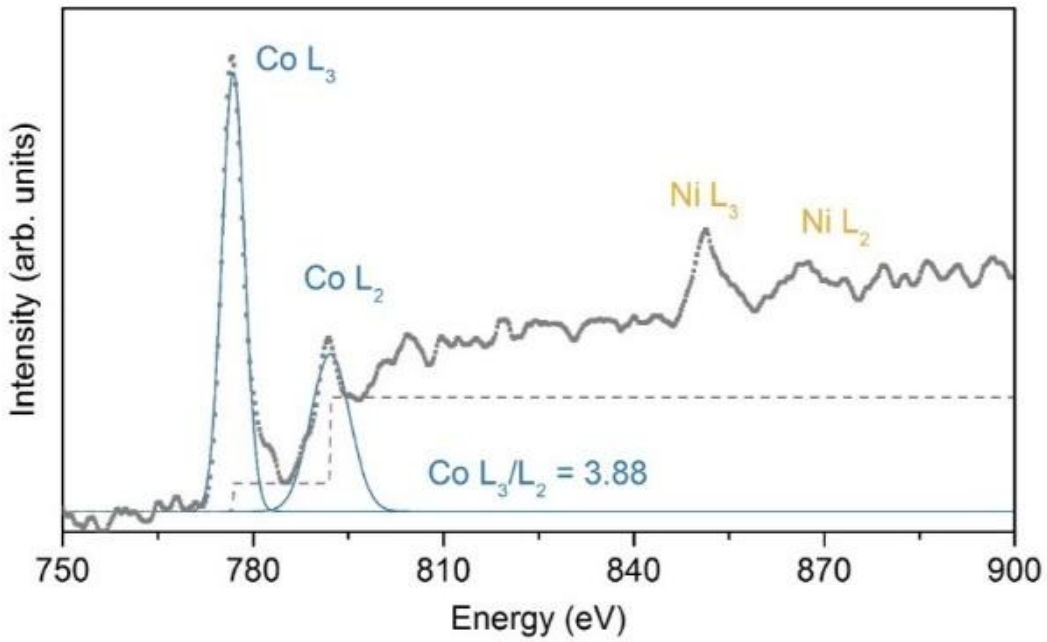

Figure A-13 EELS spectra of the cube structures in **Figure 5.8A**

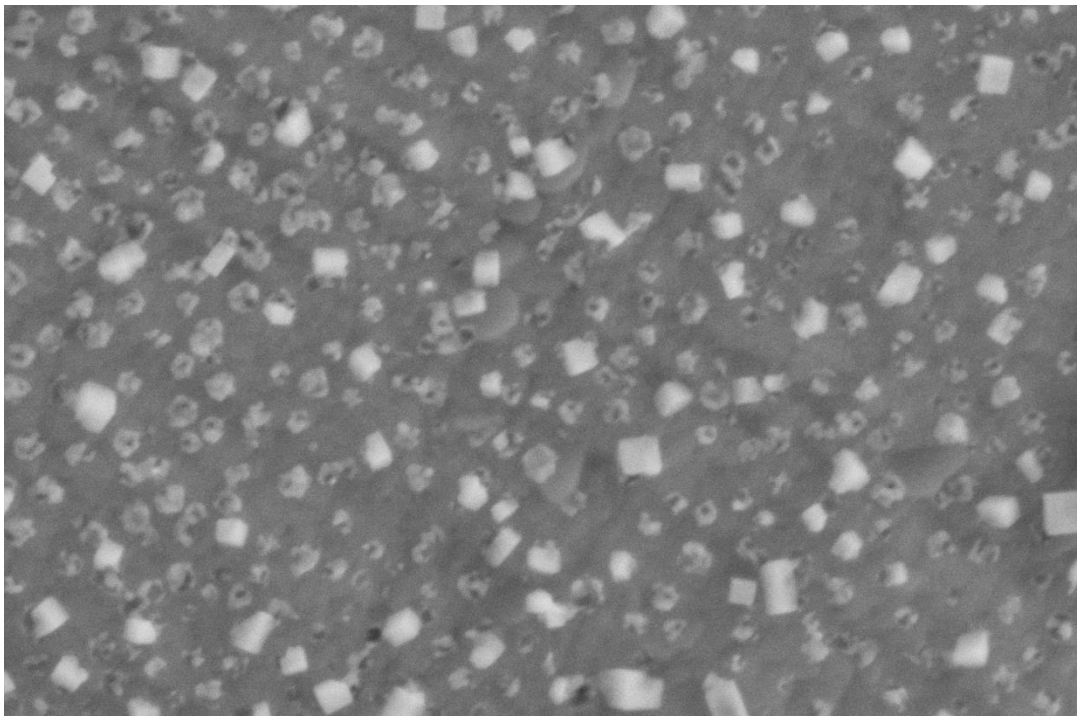

Figure A-14 Microstructure of the CoNi-30nm after activation treatment, extracted using HRSEM after activation.

1.3 Calculation of turnover frequencies (TOFs)

The calculation shown here is for CoNi-30nm pellet system and the calculations are followed for all pellet systems. This calculation was based on the SEM pictures (x40000 magnification level) sent by Dr Dragos Naegu (St Andrews University) as shown in **Figure A-15** below. We have manually calculated the number of nanoparticles and their average diameter on the SEM pictures as to estimate the total surface area and number of moles of the surface nanoparticles on the whole pellet.

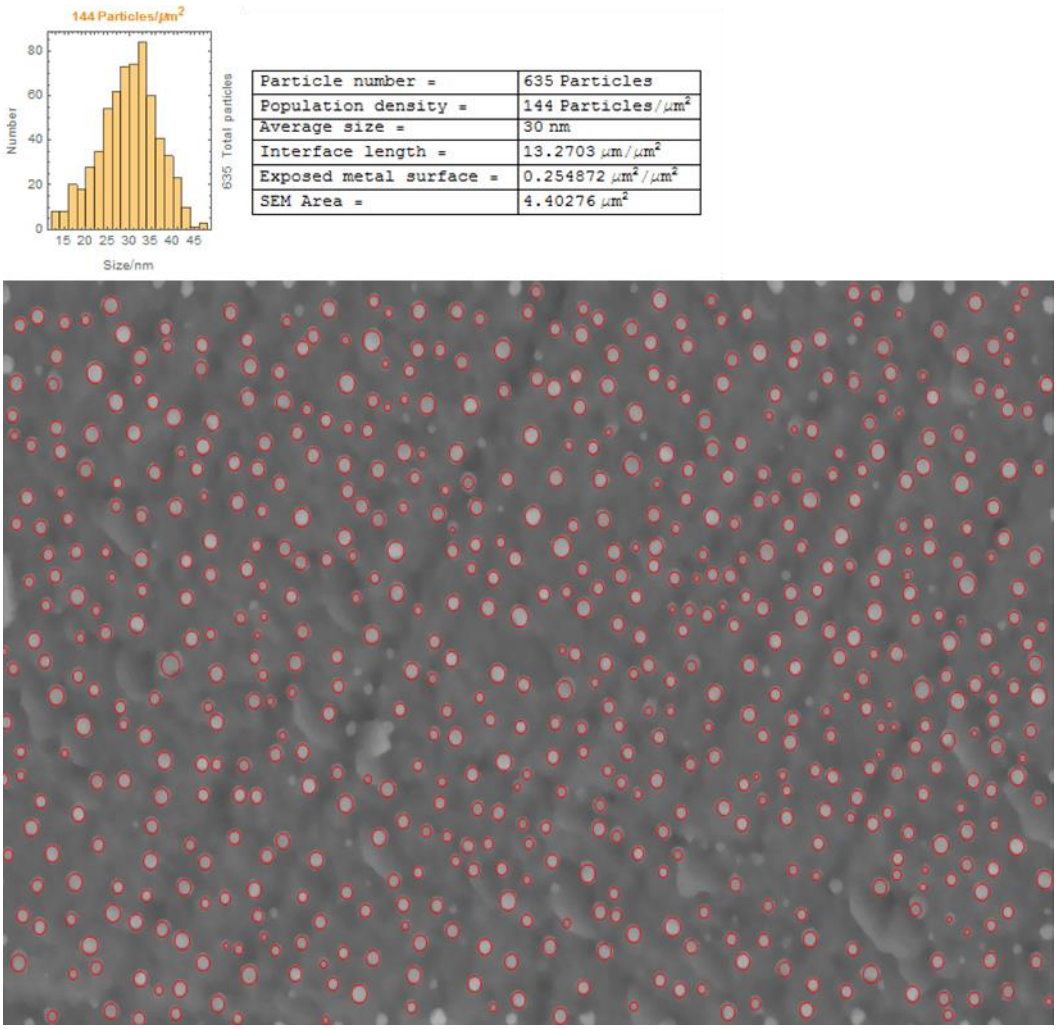

Figure A-15 SEM micrographs of the surface microstructures of fresh CoNi-30nm pellet system with their corresponding particle size histograms obtained.

Area of 1 SEM picture, A_{SEM}

$$A_{SEM}\frac{m^2}{SEMarea} = 4.40276 \text{ x } 10^{-12}\frac{m^2}{SEMarea}$$

Since we do not have any information of the apparent shape of these nanoparticles, we assumed them to be hemispherical. By assuming that these nanoparticles are hemispherical and all the

surface nanoparticle atoms are exposed to the gas phase for reaction, we can calculate the area of one nanoparticle followed by the area covered by all 144 nanoparticles.

Area of one nanoparticle, A_{CoNi}

$$A_{CoNi}\frac{m^2}{CoNi} = 2\pi r^2 = 2\pi(30\text{nm})^2 = 5654.87\text{nm}^2 = 5654.87 \text{ x } 10^{-18}\ \frac{m^2 CoNi}{CoNi}$$

Area of all nanoparticles on the SEM area, A_{CoNit}

$$A_{tCoNI}\frac{m^2 CoNi}{SEM\ area} = No_{CoNi}\frac{CoNi}{SEM\ area} \times A_{CoNi}\frac{m^2 CoNi}{CoNi}$$

$$= 144\frac{CoNi}{SEM\ area} \times 5654.87 \times 10^{-18}\frac{m^2 CoNi}{CoNi}$$

$$= 8.1430 \times 10^{-13}\frac{m^2 CoNi}{SEM\ area}$$

Therefore, we have 8.1430 x 10^{-13} m^2 of CoNi particles in a SEM area of 4.40276 x 10^{-12} m^2.

Since the SEM area is only a part of the whole pellet, we need to calculate the total nanoparticles area on the pellet. For this, the dimension of the pellet was measured and the pellet area was calculated. The pellet provided by Dr. D. Naegu and Prof. J.T.S Irvine from St Andrews University was a disc pellet with one polished surface where the exsoluted nanoparticles were located. Therefore, only the polished surface was taken into account for calculating the total nanoparticles area.

Diameter of pellet, D_{pellet} = 15.39 mm. Thus, r_p = 7.695 mm
Area of pellet, A_{pellet} :

$$A_{pellet}\frac{m^2}{pellet} = \pi r^2 = \pi(7.695\ mm)^2\frac{mm^2}{pellet} = 186\frac{mm^2}{pellet} = 186 \times 10^{-6}\frac{m^2}{pellet}$$

Based on the total area of nanoparticles calculated on the SEM picture, we could then calculate the surface area of these nanoparticles on the whole pellet. Surface area of nanoparticles, A_{tCoNi} on the whole pellet was calculated as follows:

Surface area of CoNi, A_{tCoNi} :

$$A_{tCoNi} = \frac{\left(A_{CoNi_t}\frac{m^2 CoNi}{SEM\ area}\right)}{\left(A_{SEM}\frac{m^2}{SEMarea}\right)} = \frac{\left(8.1430 * 10^{-13}\frac{m^2 CoNi}{m^2\ SEM\ area}\right)}{\left(4.40276 * 10^{-12}\frac{m^2\ SEM\ area}{m^2\ pellet}\right)} = \underline{0.1850\ \frac{m^2 CoNi}{m^2\ pellet}}$$

In order to calculate the number of moles of surface CoNi nanoparticles on the pellet, we need to know the number of CoNi atoms per square meter. Therefore, we need to know the unit cell (a) and the number of active sites per unit cell, k of CoNi particles. From there, we can calculate number of moles by using the total surface area of CoNi nanoparticles, A_{tCoNi} that we have calculated previously. From the results obtained from the XRD analysis, we have calculated the lattice parameters, a of around 0.81 nm for $(CoNi)_3O_4$.

Since we know that most of the particles consisted of Co as shown in the EDX analysis, we can assume that the particles are Co_3O_4. Therefore, we will use the density, $\rho_{Co_3O_4}$ and atomic weight, $A_{Co_3O_4}$ for Co_3O_4 for these calculations.

Given that:

$\rho_{Co_3O_4} = 6.11\ \frac{g}{cm^3}$, $A_{Co_3O_4} = 240.80\frac{g}{mol}$

First, we need to know the volume of one $(CoNi)_3O_4$ unit cell, V_c with a=b=c= $8.1x10^{-8}$ cm

$$\text{Volume of 1 unit cell, } V_c = a^3 = (8.1 \times 10^{-8} cm)^3 = 5.31 \times 10^{-22} cm^3$$

Then, we need to determine the number of $(CoNi)_3O_4$ molecules in 1 cm^3. To do this, we need to first calculate the average mass, $m_{Co_3O_4}$

$$Mass\ of\ Co_3O_4, m_{Co_3O_4} = \frac{A_{Co_3O_4}}{N_A} = \frac{240.80\frac{g}{mol}}{6.022 \times 10^{23}\frac{molecules}{mol}}$$

$$= 4.0\ \times 10^{-22}\frac{molecules}{g}$$

We can then calculate the number of number of $(CoNi)_3O_4$ molecules in 1 cm^3, $N_{Co_3O_4}$ using the following formula:

$$N_{Co_3O_4} = \frac{\rho_{Co_3O_4}}{m_{Co_3O_4}} = \frac{6.11\ \frac{g}{cm^3}}{4.0\ \times 10^{-22}\frac{molecules}{g}} = 1.53 \times 10^{-23}\frac{(CoNi)_3O_4\ molecules}{cm^3}$$

The number of $(CoNi)_3O_4$ molecules per unit cell, $n_{C\ Co_3O_4}$ can then be calculated.

$$n_{C\ Co_3O_4} = N_{Co_3O_4} \times V_c$$
$$= 1.53 \times 10^{-23}\frac{(CoNi)_3O_4\ molecules}{cm^3} \times 5.31 \times 10^{-22}\frac{cm^3}{unit\ cell}$$
$$= 8.11\frac{(CoNi)_3O_4\ molecules}{unit\ cell}$$

The number of metal active sites per unit cell, k can then be calculated.

In one unit cell (a^3), there are 8.11 $(CoNi)_3O_4$ molecules. Therefore, in one unit cell length, a, we have around 2 $(CoNi)_3O_4$ molecules. Hence, k=2 for exsolved CoNi pellet system.

Table A-1 Particle characteristics; the value of a and k, surface metal area and the pellet area which were used for TOFs calculations, with k is the average number of active sites per unit cell, a

System	Temp. (°C)	r_{CO_2} (mol s^{-1})	*a* (nm)	*k*	A_p (μm^2 μm^{-2})	A_{pe} (cm^2)
Ni-30nm	500	0.154	0.41752	1	0.302	1.82
CoNi-30nm	500	0.118	0.80835	2	0.564	1.86
CoNi-30nm (activated)	500	0.294	0.81000	2	0.270	1.86

$$N_{tCoNi/a} = \frac{A_p\frac{m^2\ CoNi}{m^2\ pellet} \times A_{pe} \times 10^{-4}m^2 pellet \times k}{a^2 nm^2}$$
$$= \frac{0.1850\frac{m^2\ CoNi}{m^2\ pellet} \times 186 \times 10^{-6}m^2 pellet \times 2}{0.41752^2 nm^2}$$
$$= 1.9740 \times 10^{14}\ active\ CoNi\ molecule$$

1 mole of CoNi = 6.02 x 10^{23} atoms of CoNi

No of moles of CoNi, $N_{t\ CoNi}$ = 1.9740 x 10^{14} CoNi atoms

No of moles of CoNi in 1.0970 x 10^{14} CoNi atoms:

$$n_{t\ CoNi} = \frac{1.9740 \times 10^{14} \times 1}{6.022 \times 10^{23}} = 3.2779 \times 10^{-10} mole\ of\ active\ CoNi$$

Therefore,

The CO_2 production rates normalised to pellet area, r_{CO_2} and TOFs were calculated

From the experiment at T = 500 °C

CO_2 production rate, r_{CO_2} = 0.154 µmol s^{-1}

$$Rate\left[\frac{mmol}{s\ m^2}\right] = \left(\frac{R_{CO2}\frac{\mu mol}{s}}{\left(A_{pellet} m^2\ pellet\right)}\right) = \frac{0.154\frac{\mu mol}{s}}{(1.86 cm^2\ pellet)} = 0.828\frac{mmol}{s\ m^2}$$

$$TOF[s^{-1}] = \left(\frac{R_{CO2}\frac{\mu mol}{s}}{(n_{t\ CoNi} mol\ of\ active\ CoNi)}\right) = \frac{0.154\frac{\mu mol}{s}}{(3.2779 \times 10^{-10} mol\ of\ active\ CoNi)}$$

$$= 469 s^{-1}$$

For Ni-s

$$A_{tNi} = \frac{\left(A_{Ni_t}\frac{m^2 Ni}{SEM\ area}\right)}{\left(A_{SEM}\frac{m^2}{SEM area}\right)} = \frac{\left(7.0559 * 10^{-12}\frac{m^2 Ni}{m^2\ SEM\ area}\right)}{\left(26.5965 * 10^{-12}\frac{m^2}{m^2\ pellet}\right)} = \underline{0.2653\ \frac{m^2 Ni}{m^2\ SEM}}$$

In order to calculate the number of moles of surface Ni nanoparticles on the pellet, we need to know the number of Ni atoms per square meter. Therefore, we need to know the unit cell (a) and the number of active sites per unit cell, k of Ni particles. From there, we can calculate number of moles by using the total surface area of Ni nanoparticles, A_{tNi} that we calculated previously.

$$N_{tNi/a} = \frac{A_p\frac{m^2\ Ni}{m^2\ pellet} \times A_{pe} \times 10^{-4} m^2 pellet \times k}{a^2 nm^2}$$

$$= \frac{0.2653\frac{m^2\ Ni}{m^2\ pellet} \times 2.0357 \times 10^{-4} m^2 pellet \times 1}{0.41752^2 nm^2}$$

$$= 3.1250 \times 10^{14}\ active\ Ni\ molecule$$

1 mole of Ni = 6.02 x 10^{23} atoms of Ni

No of moles of Ni, N_{tNi} = 3.1250 x 10^{14} Ni atoms

No of moles of Ni in 1.0970 x 10^{14} Ni atoms:

$$n_{tNi} = \frac{3.1250 \times 10^{14} \times 1}{6.022 \times 10^{23}} = 5.189 \times 10^{-10} mole\ of\ active\ Ni$$

The CO_2 production rates normalised to pellet area, r_{CO_2} and TOF were calculated

From the experiment at T = 398 °C

CO_2 production rates = 0.0789 µmol s^{-1}

$$Rate\left[\frac{mmol}{s\ m^2}\right] = \left(\frac{R_{CO2}\frac{\mu mol}{s}}{\left(A_{pellet} m^2\ pellet\right)}\right) = \frac{0.0789\frac{\mu mol}{s}}{(2.0536 cm^2\ pellet)} = 0.384\frac{mmol}{s\ m^2}$$

$$TOF[s^{-1}] = \left(\frac{R_{CO2}\frac{\mu mol}{s}}{(n_{t\ Ni} mol\ of\ active\ Ni)}\right) = \frac{0.0789\frac{\mu mol}{s}}{(5.189 \times 10^{-10} mol\ of\ active\ Ni)}$$

$$= 152.05 s^{-1}$$

1.4 Calculation of NO oxidation Equilibrium Line Using Gibbs Free Energy

1.4.1 Equilibrium line based on concentration

Oxidation reaction of NO

$$NO + \tfrac{1}{2}O_2 \leftrightarrow NO_2 \qquad n_1$$

Conversion of NO_2 to N_2O_4

$$2NO_2 \leftrightarrow N_2O_4 \qquad n_2$$

Equilibrium expression of reaction 1 in terms of concentration

$$K_{c1} = \frac{C_{NO_2}}{C_{NO}C_{O_2}^{1/2}} = \frac{V_T^{3/2}}{V_T}\frac{n_{NO_2}}{n_{NO}n_{O_2}^{1/2}} = \frac{V_T^{1/2}n_{NO_2}}{n_{NO}n_{O_2}^{1/2}} \quad (1)$$

Equilibrium expression of reaction 2 in terms of concentration

$$K_{c2} = \frac{C_{N_2O_4}}{C_{NO_2}^2} = \frac{V_T^2}{V_T}\frac{n_{N_2O_4}}{n_{NO_2}^2} = \frac{V_T n_{N_2O_4}}{n_{NO_2}^2} \quad (2)$$

Convert to NO conversion form assuming only NO and O_2 are present initially.

Mole balance

Extent of reactions 1

$$n_1 = n_{NOi}X_{NO} \quad (3)$$

Extent of reactions 2

$$n_2 = n_{N_2O4} \quad (4)$$

NO

$$n_{NO} = n_{NOi} - n_1 = n_{NOi} - n_{NOi}X_{NO} = n_{NOi}(1 - X_{NO}) \quad (5)$$

O_2

$$n_{O_2} = n_{O_2i} - (1/2)n_1 = n_{O_2i} - (1/2)n_{NOi}X_{NO} = n_{NOi}\left(n_{O_2i}/n_{NOi} - (1/2)X_{NO}\right) \quad (6)$$

NO_2

$$n_{NO_2} = n_1 - 2n_2 = n_{NOi}X_{NO} - 2n_2 \quad (7)$$

N_2O_4

$$n_{N_2O_4} = n_2 \quad (8)$$

Substituting (4) or (8) in (7)

$$n_{NO_2} = n_{NOi}X_{NO} - 2n_{N_2O_4} \tag{9}$$

Total mole

$$n_T = n_{NOi}(1 - X_{NO}) + n_{NOi}\left(n_{O_2i}/n_{NOi} - (1/2)X_{NO}\right) + n_{NOi}\left(X_{NO} - 2\,n_{N_2O_4}/n_{NOi}\right) + n_{N_2O_4} \tag{10}$$

$$n_T = n_{NOi}\left(1 + n_{O_2i}/n_{NOi} - (1/2)X_{NO} - n_{N_2O_4}/n_{NOi}\right) \tag{11}$$

Mole ratio = volume ratio

$$\frac{V_T}{V_{Ti}} = \frac{n_T}{n_{Ti}} = \frac{\left(1+n_{O_2i}/n_{NOi}-(1/2)X_{NO}-n_{N_2O_4}/n_{NOi}\right)}{\left(1+n_{O_2i}/n_{NOi}\right)} \tag{12}$$

Substituting the mole balance into the equilibrium equation (3)

$$K_{c1} = (V_T)^{1/2}\frac{n_{NO_2}}{n_{NO}n_{O_2}^{1/2}} = (V_T)^{1/2}\frac{n_{NOi}X_{NO}-2n_{N_2O_4}}{n_{NOi}^{3/2}(1-X_{NO})\left(n_{O_2i}/n_{NOi}-(1/2)X_{NO}\right)^{1/2}} \tag{13}$$

$$K_{c1} = \left(\frac{V_T}{V_{Ti}}\right)^{1/2}\frac{X_{NO}-2n_{N_2O_4}/n_{NOi}}{C_{Noi}^{1/2}(1-X_{NO})\left(n_{O_2i}/n_{NOi}-(1/2)X_{NO}\right)^{1/2}} \tag{14}$$

Substituting the volume ratio from equation (12) into the equilibrium equation (14)

$$K_{c1} = \frac{\left(1+n_{O_2i}/n_{NOi}-(1/2)X_{NO}-n_{N_2O_4}/n_{NOi}\right)^{1/2}\left(X_{NO}-2n_{N_2O_4}/n_{NOi}\right)}{C_{Noi}^{1/2}\left(1+n_{O_2i}/n_{NOi}\right)^{1/2}(1-X_{NO})\left(n_{O_2i}/n_{NOi}-(1/2)X_{NO}\right)^{1/2}} \tag{15}$$

or

$$K_{c1} = \frac{(RT)^{1/2}\left(1+n_{O_2i}/n_{NOi}-(1/2)X_{NO}-n_{N_2O_4}/n_{NOi}\right)^{1/2}\left(X_{NO}-2n_{N_2O_4}/n_{NOi}\right)}{p_{Noi}^{1/2}\left(1+n_{O_2i}/n_{NOi}\right)^{1/2}(1-X_{NO})\left(n_{O_2i}/n_{NOi}-(1/2)X_{NO}\right)^{1/2}} \tag{16}$$

Substituting the mole balance into the equilibrium equation (4)

$$K_{c2} = \frac{V_T n_{N_2O_4}}{n_{NO_2}^2} = V_T\frac{n_{NOi}\left(n_{N_2O_4}/n_{NOi}\right)}{n_{NOi}^2\left(X_{NO}-2n_{N_2O_4}/n_{NOi}\right)^2} \tag{17}$$

$$K_{c2} = \left(\frac{V_T}{V_{Ti}}\right)\frac{\left(n_{N_2O_4}/n_{NOi}\right)}{C_{NOi}\left(X_{NO}-2n_{N_2O_4}/n_{NOi}\right)^2} \tag{18}$$

Substituting the volume ratio from equation (12) into the equilibrium equation (18)

$$K_{c2} = \frac{\left(1+n_{O_2i}/n_{NOi}-(1/2)X_{NO}-n_{N_2O_4}/n_{NOi}\right)\left(n_{N_2O_4}/n_{NOi}\right)}{C_{NOi}\left(1+n_{O_2i}/n_{NOi}\right)\left(X_{NO}-2n_{N_2O_4}/n_{NOi}\right)^2} \tag{19}$$

or

$$K_{c2} = \frac{RT\left(1+n_{O_2i}/n_{NOi}-(1/2)X_{NO}-n_{N_2O_4}/n_{NOi}\right)\left(n_{N_2O_4}/n_{NOi}\right)}{p_{NOi}\left(1+n_{O_2i}/n_{NOi}\right)\left(X_{NO}-2n_{N_2O_4}/n_{NOi}\right)^2} \tag{20}$$

1.4.2 Equilibrium line based on partial pressure

Equilibrium expression in terms of partial pressures

$$K_{p1} = \frac{p_{NO_2}}{p_{NO}p_{O_2}^{1/2}} \tag{21}$$

Convert to NO conversion form using equations (2) – (5)

Assume ideal gas

$$K_{p1} = \left(\frac{V_T}{RT}\right)^{1/2}\frac{n_{NO_2}}{n_{NO}n_{O_2}^{1/2}} \tag{22}$$

Substitute mole balance from equations (5) – (11) and Ideal Gas Law

$$K_{p1} = \left(\frac{V_T}{RT}\right)^{1/2}\frac{n_{NOi}X_{NO}-2n_{N_2O_4}}{n_{NOi}^{3/2}\left(1-X_{NO}\right)\left(n_{O_2i}/n_{NOi}-(1/2)X_{NO}\right)^{1/2}} \tag{23}$$

Or

$$K_{p1} = \left(\frac{V_T}{V_{Ti}}\right)^{1/2}\frac{X_{NO}-2n_{N_2O_4}/n_{NOi}}{p_{Noi}^{1/2}\left(1-X_{NO}\right)\left(n_{O_2i}/n_{NOi}-(1/2)X_{NO}\right)^{1/2}} \tag{24}$$

Substituting volume ratio

$$K_{p1} = \frac{\left(1+n_{O_2 i}/n_{NOi}-(1/2)X_{NO}-n_{N_2O_4}/n_{NOi}\right)^{1/2}\left(X_{NO}-2n_{N_2O_4}/n_{NOi}\right)}{p_{Noi}^{1/2}\left(1+n_{O_2 i}/n_{NOi}\right)^{1/2}(1-X_{NO})\left(n_{O_2 i}/n_{NOi}-(1/2)X_{NO}\right)^{1/2}} \quad (25)$$

Check by comparing equation (16) and (25).

$$K_{c1} = (RT)^{1/2}K_{p1} \quad (26)$$

In the same way

$$K_{p2} = \frac{\left(1+n_{O_2 i}/n_{NOi}-(1/2)X_{NO}-n_{N_2O_4}/n_{NOi}\right)\left(n_{N_2O_4}/n_{NOi}\right)}{p_{NOi}\left(1+n_{O_2 i}/n_{NOi}\right)\left(X_{NO}-2n_{N_2O_4}/n_{NOi}\right)^2} \quad (27)$$

1.4.3 Gibbs Free Energy and Equilibrium Constant

Equilibrium constant 1 in terms of Gibbs free energy

$$K_{p1} = exp\left(-\frac{\Delta G_{r1}(T)}{RT}\right) = \frac{\left(1+n_{O_2 i}/n_{NOi}-(1/2)X_{NO}-n_{N_2O_4}/n_{NOi}\right)^{1/2}\left(X_{NO}-2n_{N_2O_4}/n_{NOi}\right)}{p_{Noi}^{1/2}\left(1+n_{O_2 i}/n_{NOi}\right)^{1/2}(1-X_{NO})\left(n_{O_2 i}/n_{NOi}-(1/2)X_{NO}\right)^{1/2}} \quad (28)$$

Equilibrium constant 2 in terms of Gibbs free energy

$$K_{p2} = exp\left(-\frac{\Delta G_{r2}(T)}{RT}\right) = \frac{\left(1+n_{O_2 i}/n_{NOi}-(1/2)X_{NO}-n_{N_2O_4}/n_{NOi}\right)\left(n_{N_2O_4}/n_{NOi}\right)}{p_{NOi}\left(1+n_{O_2 i}/n_{NOi}\right)\left(X_{NO}-2n_{N_2O_4}/n_{NOi}\right)^2} \quad (29)$$

Taking natural log on both sides

$$-\frac{\Delta G_{r1}(T)}{RT} = ln\left[\frac{\left(1+n_{O_2 i}/n_{NOi}-(1/2)X_{NO}-n_{N_2O_4}/n_{NOi}\right)^{1/2}\left(X_{NO}-2n_{N_2O_4}/n_{NOi}\right)}{p_{Noi}^{1/2}\left(1+n_{O_2 i}/n_{NOi}\right)^{1/2}(1-X_{NO})\left(n_{O_2 i}/n_{NOi}-(1/2)X_{NO}\right)^{1/2}}\right] \quad (30)$$

$$-\frac{\Delta G_{r2}(T)}{RT} = ln\left[\frac{\left(1+n_{O_2 i}/n_{NOi}-(1/2)X_{NO}-n_{N_2O_4}/n_{NOi}\right)\left(n_{N_2O_4}/n_{NOi}\right)}{p_{NOi}\left(1+n_{O_2 i}/n_{NOi}\right)\left(X_{NO}-2n_{N_2O_4}/n_{NOi}\right)^2}\right] \quad (31)$$

Gibbs free energy for reaction 1 at any temperature T can be calculated by

$$\Delta G_{r1}(T) = \Delta H_{r1}(T) - T\Delta S_{r1}(T) \quad (32)$$

$$\Delta H_{r1}(T) = \Delta H_{r1}^{o} + \int_{298}^{T}\left[\sum_i^m \nu_{iP}C_{piP}(T) - \sum_i^n \nu_{iR}C_{piR}(T)\right]dT \quad (33)$$

$$\Delta H_{r1}(T) = \Delta H_{r1}^{o} + \int_{298}^{T}\left(C_{pNO_2} - C_{pNO} - 0.5C_{pO_2}\right)dT \quad (34)$$

$$\Delta S_{r1}(T) = \Delta S_{r1}^{o} + \int_{298}^{T}\frac{\left[\sum_i^m \nu_{iP}C_{piP}(T) - \sum_i^n \nu_{iR}C_{piR}(T)\right]}{T}dT \quad (35)$$

$$\Delta S_{r1}(T) = \Delta S_{r1}^{o} + \int_{298}^{T} \frac{\left(C_{pNO_2} - C_{pNO} - 0.5C_{pO_2}\right)}{T} dT \quad (36)$$

Gibbs free energy for reaction 2 at any temperature *T* can be calculated by

$$\Delta G_{r1}(T) = \Delta H_{r2}(T) - T\Delta S_{r2}(T) \quad (37)$$

$$\Delta H_{r2}(T) = \Delta H_{r2}^{o} + \int_{298}^{T} \left[\sum_i^m \nu_{iP} C_{piP}(T) - \sum_i^n \nu_{iR} C_{piR}(T)\right] dT \quad (38)$$

$$\Delta H_{r2}(T) = \Delta H_{r2}^{o} + \int_{298}^{T} \left(0.5C_{pN_2O_4} - C_{pNO_2}\right) dT \quad (39)$$

$$\Delta S_{r2}(T) = \Delta S_{r2}^{o} + \int_{298}^{T} \frac{\left[\sum_i^m \nu_{iP} C_{piP}(T) - \sum_i^n \nu_{iR} C_{piR}(T)\right]}{T} dT \quad (40)$$

$$\Delta S_{r1}(T) = \Delta S_{r1}^{o} + \int_{298}^{T} \frac{\left(0.5C_{pN_2O_4} - C_{pNO_2}\right)}{T} dT \quad (41)$$

1.4.4 Results of Calculation

Data:

Table A-2 Standard Heat, Entropy and Gibbs Free Energy of Formation and of NO Oxidation Reaction

Component	NO	O_2	NO_2	NO Oxidation Reaction	
ΔH_f^o (kJ/mole)	90.30	0	33.20	ΔH_r^o (kJ/mol)	-57.1
ΔS_f^o (kJ/mole/K)	0.21	0.205	0.24	ΔS_r^o (kJ/mol K)	-0.0732
ΔG_f^o (kJ/mole)	86.57	0	51.3	ΔG_r^o (kJ/mol)	-35.27

Table A-3 Standard Heat, Entropy and Gibbs Free Energy of Formation of Conversion of NO_2 to N_2O_4 Reaction

Component	NO_2	N_2O_4	Conversion NO_2 to N_2O_4 Reaction	
ΔH_f^o (kJ/mole)	33.20	9.1	ΔH_r^o (kJ/mol)	-28.65
ΔS_f^o (kJ/mole/K)	0.24	0.30429	ΔS_r^o (kJ/mol K)	-0.087855
ΔG_f^o (kJ/mole)	51.3	97.8	ΔG_r^o (kJ/mol)	-4.8

Table A-4 Specific Heat Capacities [C_p (J/mole/K) and T (K)]

Component	*A*	*B*	*C*	*D*
NO	29.35	9.38×10^{-4}	9.75×10^{-6}	4.19×10^{-9}
O_2	29.1	0.01158	6.08×10^{-6}	1.31×10^{-8}
NO_2	24.233	4.84×10^{-2}	-2.08×10^{-5}	2.93×10^{-10}
N_2O_4	34.0527	0.1919845	-1.510575×10^{-4}	4.439350×10^{-8}

Source: Introductory Chemical Engineering Thermodynamics, J. R. Elliott and C. T. Lira, Prentice-Hall, 1999; Perry's Chemical Engineers' Handbook, 6th ed.; and Lange's Ha4dbook of Chemistry, 14th ed.

Table A-5 Gas Constant, Partial Pressures and Mole Ratio Used in Experiment

R (J/K/mol)	8.31451
p_{NOi} (kPa)	0.04
p_{O2i} (kPa)	8
p_T (kPa)	8.04
Mole ratio	10

Gibbs Free Energy and Equilibrium Constant Calculation

The Heat, Entropy and Gibbs Free Energy of NO oxidation reaction is calculated using Equations (32), (34) and (36).

The Heat, Entropy and Gibbs Free Energy of Formation and of Conversion of NO_2 to N_2O_4 Reaction is calculated using Equations (37), (39) and (41). The results are shown in Table 4 and 5.

Equilibrium Line Calculation

Equations (8) is rewritten as

$$\frac{\Delta G_{r1}(T)}{RT} - ln\left[\frac{\left(1+n_{O_2i}/n_{NOi}-(1/2)X_{NO}-n_{N_2O_4}/n_{NOi}\right)^{1/2}\left(X_{NO}-2n_{N_2O_4}/n_{NOi}\right)}{p_{Noi}^{1/2}\left(1+n_{O_2i}/n_{NOi}\right)^{1/2}(1-X_{NO})\left(n_{O_2i}/n_{NOi}-(1/2)X_{NO}\right)^{1/2}}\right] = 0 \quad (42)$$

$$\frac{\Delta G_{r2}(T)}{RT} - ln\left[\frac{\left(1+n_{O_2i}/n_{NOi}-(1/2)X_{NO}-n_{N_2O_4}/n_{NOi}\right)\left(n_{N_2O_4}/n_{NOi}\right)}{p_{NOi}\left(1+n_{O_2i}/n_{NOi}\right)\left(X_{NO}-2n_{N_2O_4}/n_{NOi}\right)^2}\right] = 0 \quad (43)$$

Equation (42) and (43) are used to force the LHS of both equations to diminish to zero at any given temperature, T by changing conversion of NO, X_{NO} and the selectivity of N_2O_4 in moles of per mole of initial NO, n_{N2O4}/n_{NOi} using the Solver in MS Excell. The results are shown in **Table A-7** and **Figure A-16**. The curves are almost identical because the conversion of NO_2 to N_2O_4 reaction has a lot smaller equilibrium constant and rate of N_2O_4 production is higher at lower temperature and taper off quickly to a negligible rate.

Table A-6 Heat, Entropy, Gibbs Free Energy of Formation and Equilibrium Constant of NO Oxidation Reaction

Temperature (K)	$\Delta H_{r1}(T)$ (J/mole)	$\Delta S_{r1}(T)$ (J/mole/K)	$\Delta G_{r1}(T)$ (J/mole)	K_{p1}	K_{c1}
273.15	-56608.32666	-72.76848427	-36731.61518	10568950.18	503675450.1
323.15	-57566.61616	-73.52534535	-33806.90081	291393.6753	15104297.51
373.15	-58406.52468	-73.91479022	-30825.22071	20648.88816	1150155.935
423.15	-59137.50506	-74.05154271	-27802.59476	2703.53313	160360.425
473.15	-59768.64243	-74.01090633	-24750.38209	539.9016763	33863.54561
523.15	-60308.65424	-73.84467703	-21676.81145	145.9811639	9627.826753
573.15	-60765.89026	-73.58975764	-18587.92067	49.42962983	3412.242096
623.15	-61148.33255	-73.27315538	-15488.16578	19.87193523	1430.391078
673.15	-61463.5955	-72.91504451	-12380.83329	9.134721781	683.3915106
723.15	-61718.92579	-72.5307287	-9268.329333	4.67147431	362.2317301
773.15	-61921.20242	-72.13194591	-6152.388434	2.604053243	208.785373
775.15	-61928.28331	-72.11582957	-6027.698023	2.547857795	204.5438332
777.15	-61935.29019	-72.09970535	-5903.004177	2.493153656	200.4101906
779.15	-61942.22346	-72.08357377	-5778.306958	2.439894633	196.3812135
779.65	-61943.94532	-72.07953978	-5747.132133	2.426800419	195.389955
779.75	-61944.28914	-72.07873293	-5740.897143	2.42419202	195.1924606
779.85	-61944.63279	-72.07792606	-5734.662145	2.421587088	194.9952178
779.95	-61944.97624	-72.07711918	-5728.427139	2.41898562	194.7982262
780.05	-61945.31952	-72.07631228	-5722.192124	2.416387609	194.6014853
780.15	-61945.66261	-72.07550537	-5715.957102	2.413793051	194.4049948
781.15	-61949.08352	-72.06743531	-5653.606426	2.388036156	192.4537805
783.15	-61955.87077	-72.05129047	-5528.902641	2.337535213	188.6248763
793.15	-61988.72893	-71.97048725	-4905.336968	2.103989754	170.8596903
803.15	-62019.82664	-71.88959497	-4281.698439	1.898727857	155.1598617
813.15	-62049.21304	-71.80866941	-3657.993508	1.717805769	141.2465082

823.15	-62076.93669	-71.7277636	-3034.228084	1.557895036	128.8831122
873.15	-62192.27223	-71.32520944	85.33439616	0.988314463	84.20888366
923.15	-62272.98496	-70.92972626	3205.791837	0.658583893	57.69863934
973.15	-62324.48311	-70.54550673	6326.876757	0.457517979	41.15441085

Table A-7 Heat, Entropy, Gibbs Free Energy of Formation and Equilibrium Constant of Conversion of NO_2 to N_2O_4 Reaction

Temperature (K)	$\Delta H_{r2}(T)$ (J/mole)	$\Delta S_{r2}(T)$ (J/mole/K)	$\Delta G_{r2}(T)$ (J/mole)	K_{p2}	K_{c2}
273.15	-57045.92515	-176.2832179	-8894.164177	50.21037943	114033.2148
323.15	-57406.47034	-175.1130932	-818.6742789	1.356216051	3643.927271
373.15	-57654.63843	-173.902382	7237.035394	0.09704294	301.0814871
423.15	-57803.28526	-172.6896699	15270.34855	0.013032853	45.85328925
473.15	-57864.44526	-171.4987193	23280.17378	0.002691465	10.58825161
523.15	-57849.33151	-170.344453	31266.36908	0.000755518	3.286302131
573.15	-57768.33568	-169.2361935	39229.3886	0.000265998	1.267601456
623.15	-57631.02805	-168.1795421	47170.0536	0.000111209	0.57619308
673.15	-57446.15752	-167.1775309	55089.39738	5.31273×10^{-5}	0.297348949
723.15	-57221.6516	-166.2313603	62988.55662	2.82046×10^{-5}	0.1695838
773.15	-56964.61641	-165.3408901	70868.69279	1.62995×10^{-5}	0.104779163
775.15	-56953.75007	-165.3064166	71183.51873	1.59703×10^{-5}	0.102928518
777.15	-56942.84223	-165.2720303	71498.31612	1.56495×10^{-5}	0.101120954
779.15	-56931.89325	-165.2377312	71813.08502	1.53367×10^{-5}	0.099355262
779.65	-56929.14962	-165.22917	71891.77281	1.52598×10^{-5}	0.098920244
779.75	-56928.60059	-165.2274585	71907.51015	1.52445×10^{-5}	0.098833544
779.85	-56928.05146	-165.2257471	71923.24742	1.52292×10^{-5}	0.098746945
779.95	-56927.50223	-165.224036	71938.98462	1.52139×10^{-5}	0.098660447
780.05	-56926.95289	-165.222325	71954.72175	1.51986×10^{-5}	0.098574049

780.15	-56926.40345	-165.2206143	71970.45881	1.51833×10^{-5}	0.098487752
781.15	-56920.90351	-165.2035192	72127.82551	1.50319×10^{-5}	0.097630276
783.15	-56909.87337	-165.1693942	72442.53767	1.47347×10^{-5}	0.095944866
793.15	-56854.12952	-165.0000696	74015.67572	1.33554×10^{-5}	0.088074383
803.15	-56797.42987	-164.8329022	75588.11555	1.21362×10^{-5}	0.081043228
813.15	-56739.81813	-164.6678764	77159.86559	1.10554×10^{-5}	0.074745211
823.15	-56681.33669	-164.5049758	78730.93413	1.00948×10^{-5}	0.069089456
873.15	-56377.27578	-163.7217058	86576.3316	6.61997×10^{-6}	0.048059769
923.15	-56057.07564	-162.9885725	94405.8251	4.55371×10^{-6}	0.034952192
973.15	-55724.55685	-162.3025986	102220.217	3.26124×10^{-6}	0.026387559

Table A-8 Equilibrium Conversion of NO in NO Oxidation Only and Combined NO Oxidation Reaction and Conversion of NO_2 to N_2O_4 Reaction

Temperature (K)	NO Oxidation Only	Combined NO Oxidation Reaction and Conversion of NO_2 to N_2O_4 Reaction	
	X_{NO}	X_{NO}	n_{N2O4}/n_{NOi}
273.15	0.99999985	0.999999947	0.31
323.15	0.999994561	0.999995000	0.05
373.15	0.999923248	0.999922000	0.00432
423.15	0.999414148	0.999400000	0.00060
473.15	0.997074667	0.9971	0.00011
523.15	0.989257341	0.988452993	0.000034
573.15	0.968911107	0.968935063	0.00001045
623.15	0.92608676	0.926147901	0.00000398
673.15	0.852150763	0.853	0.0000015
723.15	0.746719535	0.745	0.0000007
773.15	0.621763873	0.62	0.00000025
775.15	0.616622421	0.615	0.00000025
777.15	0.611481383	0.613	0.00000026
779.15	0.606341966	0.605	0.00000025
779.65	0.605057505	0.603	0.00000023
779.75	0.604800636	0.6026	0.000000226
779.85	0.604543774	0.6023	0.00000023
779.95	0.604286921	0.602	0.000000226
780.05	0.604030076	0.602	0.00000025
780.15	0.603773239	0.602	0.00000023
781.15	0.601205364	0.6	0.000000225
783.15	0.596072753	0.595	0.000000215
793.15	0.570509575	0.57	0.000000177
803.15	0.545228444	0.545	0.00000015
813.15	0.520283056	0.52	0.00000013
823.15	0.495717904	0.496	0.000000105
873.15	0.384246222	0.385	0.000000042
923.15	0.293800121	0.292	0.000000015
973.15	0.224168388	0.225	0.000000007

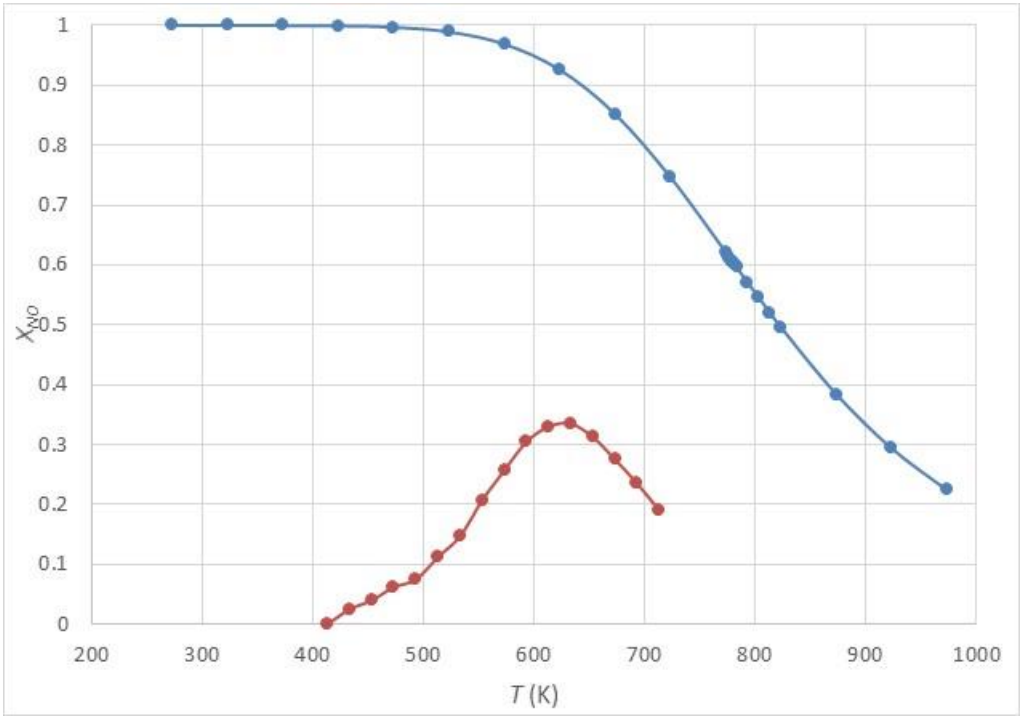

Figure A-16 Equilibrium Line of NO Oxidation Only

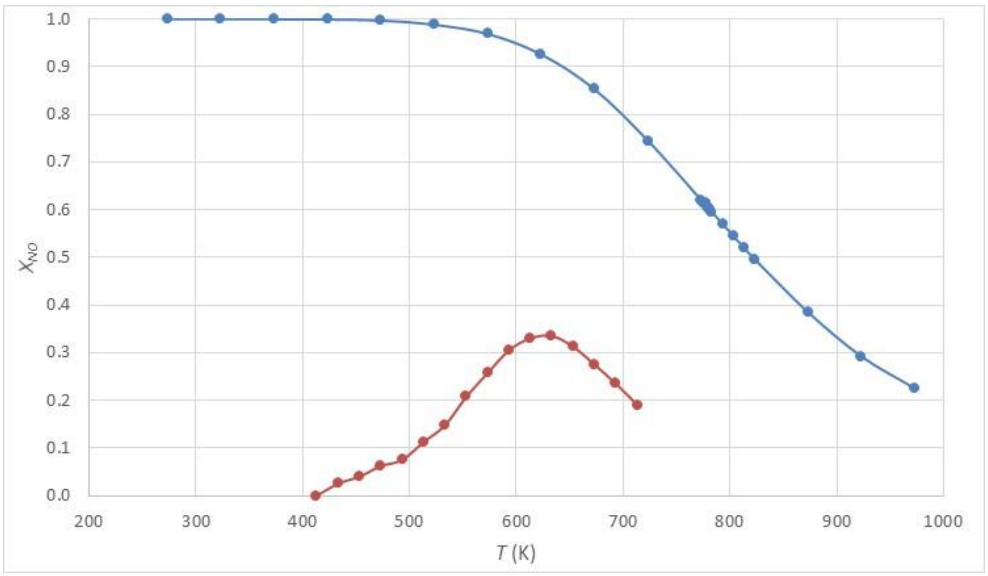

Figure A-17 Equilibrium Line of Combined NO Oxidation Reaction and Conversion of NO_2 to N_2O_4 Reaction